Living Lasers: Lasing from Biological and Biocompatible Soft Matter

Markus Karl

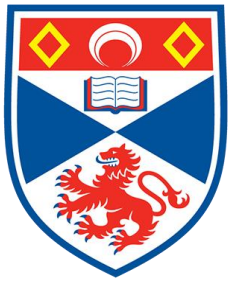

University of
St Andrews

This thesis is submitted in partial fulfilment for the degree of

Doctor of Philosophy (PhD)

at the University of St Andrews

April 2018

Candidate's declaration

I, Markus Karl, do hereby certify that this thesis, submitted for the degree of PhD, which is approximately 45,000 words in length, has been written by me, and that it is the record of work carried out by me, or principally by myself in collaboration with others as acknowledged, and that it has not been submitted in any previous application for any degree.

I was admitted as a research student at the University of St Andrews in September 2014.

I received funding from an organisation or institution and have acknowledged the funder(s) in the full text of my thesis.

Date Signature of candidate

Supervisor's declaration

I hereby certify that the candidate has fulfilled the conditions of the Resolution and Regulations appropriate for the degree of PhD in the University of St Andrews and that the candidate is qualified to submit this thesis in application for that degree.

Date Signature of supervisor

Permission for publication

In submitting this thesis to the University of St Andrews we understand that we are giving permission for it to be made available for use in accordance with the regulations of the University Library for the time being in force, subject to any copyright vested in the work not being affected thereby. We also understand, unless exempt by an award of an embargo as requested below, that the title and the abstract will be published, and that a copy of the work may be made and supplied to any bona fide library or research worker, that this thesis will be electronically accessible for personal or research use and that the library has the right to migrate this thesis into new electronic forms as required to ensure continued access to the thesis.

I, Markus Karl, confirm that my thesis does not contain any third-party material that requires copyright clearance.

The following is an agreed request by candidate and supervisor regarding the publication of this thesis:

Printed copy

Embargo on all of print copy for a period of 1 year on the following ground(s):

- Publication would preclude future publication

Supporting statement for printed embargo request

Not all the material presented in this thesis has been published at the current stage.

Electronic copy

Embargo on all of electronic copy for a period of 1 year on the following ground(s):

- Publication would preclude future publication

Supporting statement for electronic embargo request

Not all the material presented in this thesis has been published at the current stage.

Title and Abstract

- I agree to the title and abstract being published.

Date Signature of candidate

Date Signature of supervisor

Underpinning Research Data or Digital Outputs

Candidate's declaration

I, Markus Karl, understand that by declaring that I have original research data or digital outputs, I should make every effort in meeting the University's and research funders' requirements on the deposit and sharing of research data or research digital outputs.

Date Signature of candidate

Permission for publication of underpinning research data or digital outputs

We understand that for any original research data or digital outputs which are deposited, we are giving permission for them to be made available for use in accordance with the requirements of the University and research funders, for the time being in force.

We also understand that the title and the description will be published, and that the underpinning research data or digital outputs will be electronically accessible for use in accordance with the license specified at the point of deposit, unless exempt by award of an embargo as requested below.

The following is an agreed request by candidate and supervisor regarding the publication of underpinning research data or digital outputs:

Embargo on all of electronic files for a period of 1 year on the following ground(s):

- Publication would preclude future publication

Supporting statement for embargo request

Not all the material presented in this thesis has been published at the current stage.

Title and Description

- I require an embargo on the description only

Date Signature of candidate

Date Signature of supervisor

Abstract

In recent years, the study of stimulated emission from and by biological systems has gained wide spread attention as a promising technology platform for novel biointegrated laser. However, the photonic properties and the associated physics of many biological laser systems are not yet fully understood and many promising resonator architectures and laser classes have not yet transitioned into the biological world.

In this thesis, we investigate the fundamental photonic properties of lasers based on single biological cells and explore the potential of distributed feedback (DFB) gratings as novel biointegrated laser resonators. We show how the easy and flexible fabrication of DFB resonators helps to realize optofluidic and solid-state biological lasers. Lasing characteristics, such as tunable and single mode emission, are investigated and different applications are explored. Fourier-space emission studies on different biological lasers give insight into the photonic dispersion relation of the system and the fundamental creation of lasing modes and their confinement in living systems.

The first purely water based optofluidic DFB laser is demonstrated and novel sensing applications are suggested. This device shows low threshold lasing due to an optimized mode shape, which is achieved by a low refractive index substrate and the use of a mixed-order grating. Next, by integrating a high refractive index interlayer on a DFB resonator, a laser device incorporating the novel solid-state biological gain material green fluorescent protein (GFP) is realized. Lastly, we show how the thickness of organic polymer lasers can be reduced to its fundamental limit ($< 500\,\mathrm{nm}$) and the resulting membrane like laser devices can be applied to and operated on various body parts to potentially complement biometric identification.

Acknowledgements

General Acknowledgements

First, I would like to express my sincere gratitude to Prof. Malte C. Gather who gave me the opportunity to join his group and to work on this exciting topic. During my PhD he gave me all the freedom and trust I could wish for with outstanding support and help whenever I needed it. I admire your infectious enthusiasm for science which has always inspired me to give my best. Your scientific intuition amazed me numerous times and you truly are the best mentor I could have asked for. I learned a lot from you and working with you has shaped me both as a scientist and as a person. Thanks Malte!

Secondly, I am indebted to my second supervisor Prof. Graham A. Turnbull who always provided a relaxed and motivating working atmosphere for me. I also want to express my great appreciation for his excellent support and the trust he put in me and my research over the past years.

Next, I would like to thank Prof. Ifor D. W. Samuel for all the fruitful and stimulating discussions, his great scientific input and many ideas during our regular meetings.

Moreover, I would like to thank all my colleagues and friends at the School of Physics and Astronomy at the University of St Andrews. Especially, I would like to thank everyone in the Gather Lab and the Organic Semiconductor Optoelectronics group for providing help and support.

In particular, I am very grateful to Dr Marcel Schubert for constantly pushing my work on biological lasers and providing guidance and help. I enjoyed our discussions about science and life and the fruitful work we did together. Working with you certainly helped me to become a better scientist. A special thanks goes to Dr Nils M. Kronenberg for his support in the lab, his many critical questions and for just being the most pleasant person to share a desk with. Thank you, Marcel and Nils, not just for being great colleagues but also good friends.

I would like to thank Dr Guy L. Whitworth and Dr Christof P. Dietrich for providing training and support in laser fabrication and characterization during the early stages of my PhD.

I am thankful to Dr Andrew Morton and Dr Anja Steude for introducing me to the world of biology, providing a well working biology lab and helping me with any biological problems I encountered. I am further grateful to James M. E. Glackin for his help with PLQY measurements and the support in fabricating membrane lasers. Laura Tropf deserves my gratitude for always performing ellipsometry measurements when I needed it.

I also want to acknowledge all the staff, technicians and secretaries in the department for their support. In particular, Callum Smith, Steve Balfour and Graeme Beaton for keeping the cleanroom and all its equipment in good working order at all times.

My gratitude also goes to Dr David N. Miller for performing SEM and FIB imaging/etching experiments, Dr Simon Powis for providing access to and training on the flow cytometer and Prof. Frank Gunn-Moore for providing access to the Nucleofector.

Further, I would like to thank everyone else from the Gather Lab for creating the most pleasant work environment and being such a fun group: Thank you Arko, Alasdair, Andrew (Meek), Elena, Caro, Changmin, Philipp, Andreas, Joe, Ana, Yali, Soraya, and Dinesh.

A big thank you goes to all my friends here in St Andrews, back in Germany and anywhere in the world. I would further like to thank my family and in particular my parents Horst and Petra Karl as well as my grandparents Theodor and Rosa Karl. Without your support and encouragement in all my endeavors, I would not be where I am today. Last but not least, I would like to thank Melina for her constant support and for sharing her life with me.

Funding

This work was supported by the Engineering and Physical Sciences Research Council [grant number EP/M506631/1]

Research Data/Digital Outputs Access Statement

Research data underpinning this thesis are available at:
http://dx.doi.org/10.17630/12494f21-52d1-426a-8377-908c6c60be83

List of Publications and Patents

Publications

1. Hannes Klumbies, Markus Karl, Martin Hermenau, Roland Rösch, Marco Seeland, Harald Hoppe, Lars Müller-Meskamp & Karl Leo "Water ingress into and climate dependent lifetime of organic photovoltaic cells investigated by calcium corrosion tests", *Solar Energy Materials and Solar Cells* **120**, 685-690 (2014)

2. Marcel Schubert, Anja Steude, Philipp Liehm, Nils M. Kronenberg, Markus Karl, Elaine C. Campbell, Simon J. Powis & Malte C. Gather "Lasing within live cells containing intracellular optical microresonators for barcode-type cell tagging and tracking", *Nano letters* **15**, 5647-5652 (2015)

3. Markus Karl, Guy L. Whitworth, Marcel Schubert, Christof P. Dietrich, Ifor D. W. Samuel, Graham A. Turnbull & Malte C. Gather "Optofluidic distributed feedback lasers with evanescent pumping: Reduced threshold and angular dispersion analysis", *Applied Physics Letters* **108**, 261101 (2016)

4. Markus Karl, Christof P. Dietrich, Marcel Schubert, Ifor D. W. Samuel, Graham A. Turnbull & Malte C. Gather "Single cell induced optical confinement in biological lasers", *Journal of Physics D: Applied Physics* **50**, 084005 (2017)

5. Christof P. Dietrich, Markus Karl, Jürgen Ohmer, Utz Fischer, Malte C. Gather & Sven Höfling "Molding Photonic Boxes into Fluorescent Emitters by Direct Laser Writing", *Advanced Materials* **29**, 1605236 (2017)

6. Marcel Schubert, Klara Volckaert, Markus Karl, Andrew Morton, Philipp Liehm, Gareth B. Miles, Simon J. Powis & Malte C. Gather "Lasing in Live Mitotic and Non-Phagocytic Cells by Efficient Delivery of Microresonators", *Scientific Reports* **7**, 40877 (2017)

7. Markus Karl, James M. E. Glackin, Marcel Schubert, Nils M. Kronenberg, Graham A. Turnbull, Ifor D. W. Samuel & Malte C. Gather "Flexible and ultra-lightweight polymer membrane lasers", *Nature Communications* **9**, 1525 (2018)

Patents

1. Markus Karl, Graham A. Turnbull, Ifor D. W. Samuel & Malte C. Gather “Laser Device”, GB1711097.4 (10 July 2017)

Contents

1 Introduction

Stimulated emission was first postulated by Albert Einstein in 1917 [1, 2] but it took almost 40 years to realize a device based on this principle. In 1953, Charles H. Townes and co-workers succeeded in fabricating the first maser[1], a device amplifying microwave radiation through stimulated emission [3]. Shortly after their initial success, Townes and Arthur Schawlow conceived the idea for a similar device but instead of using microwave radiation, planned to amplify visible light [4]. Eventually, in 1960, Theodore Maiman realized the first laser[2] using a synthetic ruby crystal pumped by an intense flashtube [5]. The unique properties of lasers - spectrally narrow emission, small divergence angle of emission, high spatial and temporal coherence and high energy and power density - quickly made them an indispensable tool in many areas of research and later also daily life. Areas of applications today include medical treatment, chemical analysis, material machining, quality inspection, optical communication and data storage. Even the latest technological developments of our society such as self driving cars rely on laser based distance measurements [6].

[1]The word "MASER" is an acronym for "Microwave Amplification by Stimulated Emission of Radiation".
[2]The word "LASER" is an acronym for "Light Amplification by Stimulated Emission of Radiation".

Shortly after the invention of the laser, the first laser in which emission was generated by fluorescent organic molecules was realized with the development of the liquid dye laser [7, 8]. These lasers had a tremendous impact on industrial and academic research, due to the possibility of tuning the emission from the ultra violet to the near infrared with a broad gain bandwidth in either continuous or pulsed mode operation [9]. However, liquid dye lasers are expensive and complex systems requiring a high level of maintenance and are therefore nowadays commonly replaced by fiber lasers and optical parametric oscillators. The discovery of electrical conductivity [10] and efficient electroluminescence [11] in thin films of organic polymers and molecules laid the foundation for the development of optoelectronic devices based on solid-state organic materials. These materials are electrical insulators but become semiconducting upon injection of charges and are therefore called organic semiconductors. Devices such as organic light emitting diodes (OLEDs) constitute an industry worth billions of dollars and are commonly used as technology platforms for displays and illumination [12, 13]. Organic solar cells [14] and field effect transistors [15] are other prime examples for devices based on organic semiconductors. Similarly to organic dyes, solid-state organic semiconductors show broad absorption and emission spectra and can have high quantum efficiencies. In contrast to their inorganic counterparts, low-cost and large area fabrication using thermal evaporation or solution processing is readily achievable with organic materials. These achievements together with the demonstration of stimulated emission in optically pumped organic semiconductors [16] paved the way for the development of the first solid-state organic lasers in 1996 and 1997 [17, 18]. Organic lasers combine the emission tunability and broad spectral range of liquid dye lasers with the cheap manufacturing and simplicity of other organic opotoelectronic devices [19, 20]. Distributed feedback (DFB) gratings are a particularly useful resonator structure for organic lasers since single mode operation and controlled emission tuning are readily achievable [21].

Lasers are an integral part of modern medicine and biology in application and fundamental research. In medicine, the use of lasers in photodynamic therapy (PDT) aids to treat skin cancer [22] by supplying high intensity light to activate a photosensitizer in the vicinity of cancerous tissue. Other examples for medical applications include cosmetic dermatology via laser surgery [23], (*in vivo*) confocal scanning microscopy [24] and diagnostic imaging of the human eye via laser ophthalmoscopy [25]. A fascinating biological application is the use of lasers as optical stretchers [26] where the mechanical strength and morphology of single cells

is probed to monitor the progression from a normal to a cancerous and a metastatic state. Most laser based diagnostic, therapeutic and surgical techniques, however, rely on the delivery of externally generated laser light to the cell or tissue of interest.

This dogma has recently been challenged by the development of laser devices where stimulated emission is generated within or by biological systems. These biological lasers exist in a vast variety of forms and incorporate biomaterials, ranging from molecules such as vitamins [27, 28], proteins [29–31] or DNA [32] to more complex biological hierarchies such as cells [33, 34] or tissue [35]. Biomaterials can be utilized directly as the gain material or as optical resonator providing feedback. Most biological lasers rely on the use of an organic light emitting material for providing gain and therefore the development of biological lasers has greatly benefited from the advances in the field of organic semiconductor lasers. Biological processes often occur in aqueous environments, which renders optofluidic biological lasers, where the gain material and cavity are placed in a fluidic environment, a particularly interesting sensing platform. Utilizing these devices, minute changes in the fluorescence signal originating from molecular interactions during a biological event are greatly enhanced by optical feedback and the emission properties can be related to the characteristics of the biological host material [36]. However, while the extensive research in conventional optofluidic lasers based on organic dyes has provided a viable playground [37], some resonator structures commonly used for optofluidic dye lasers require high refractive index solvents and do not support lasing from aqueous environments. For optofluidic biological lasers, the biological material needs to be extracted from cells or tissue which does not reflect the complex environment in which most biological events occur. In 2011, Gather and Yun reported the first biological single cell laser [34], where stimulated emission is generated within a living cell placed inside a planar Fabry-Pérot cavity and where this cell produces its own gain material - the green fluorescent protein (GFP). First applications for single cell lasers have been suggested and include the monitoring of osmotic pressure within live cells by recording the spectral position of different lasing modes [38]. Single cell lasers further provide an interesting playground for sophisticated biological photonic systems which has not been exploited so far. Other cell laser systems include dye stained tissue slabs sandwiched between two highly reflective mirrors for cancer screening [39] and intracellular lasers, where a micron sized whispering gallery mode (WGM) laser is internalized by a cell and can be used for cell tracking, tagging and sensing applications [40–42]. Furthermore, using GFP as the gain material in single live cells has trig-

gered the interest of many groups worldwide to explore the potential of this novel biological material as a solid-state gain material in lasers and a multitude of different GFP based laser systems have been developed lately [29, 43, 44].

In this thesis, we develop novel biological lasers incorporating a variety of different gain media, in solid-state and fluidic phase as well as within single biological cells. We further investigate the fundamental photonic properties of biological laser systems and enhance their biointegration with the aim to advance biological lasers for practical applications.

This dissertation is structured in eight chapters, Chapter 2 explains the physical fundamentals of this work and introduces the materials, resonator architectures and optical processes utilized in biological laser devices. First, the chemical and physical properties of three different organic light emitting materials used throughout this thesis are explained and the optical processes rendering them interesting gain materials for lasers are identified. Secondly, the basic processes within optically active materials are discussed and the necessary prerequisites for active materials to provide optical gain are introduced. Next, the fundamentals for light propagation in dielectric materials are explored and the concept of optical waveguides is discussed. Lastly, the state of the art in biological lasers and their relation to conventional organic lasers is examined.

Chapter 3 describes the experimental methodologies and materials that are common throughout the entire thesis. This includes the fabrication and characterization of solid-state thin films, nanostructured gratings and laser devices. Lastly, the relevant gain materials are introduced and the methods for their optical characterization are explained.

In Chapter 4, the photonic properties of single cell lasers are investigated in detail and the potential of fluorescent biological cells as refractive index landscapes and active optical elements within a planar cavity is explored. It is shown, that the inherent refractive index contrast between a biological cell and its surrounding leads to 3D confinement of photons within the cell. Fourier- and hyperspectral-imaging techniques are used to explore the origin for photonic confinement in single cells and the unqiue mode structure observed above threshold.

A novel optofluidic biological laser platform based on an evanescently pumped DFB laser is demonstrated in Chapter 5. It is shown that with the aid of optical simulations, an optimized waveguide structure incorporating a low refractive index substrate can be constructed, facilitating laser emission from dye molecules dissolved in biocompatible solvents such as water.

The optimized waveguide design in combination with the use of a mixed-order DFB grating further promotes low threshold lasing. Lastly, the DFB Fourier emission below threshold is investigated for potential biosensing applications.

In Chapter 6, the potential of integrating a solid-state fluorescent protein film as gain material with a DFB resonator is investigated for a novel biological laser. It is explained how a high refractive index interlayer can help to overcome optical design challenges and facilitate lasing action. Further, a high degree of control over different lasing modes and their spectral tunability is demonstrated. Lastly, the peculiar far field emission of different lasing modes is investigated.

Lastly, in Chapter 7, the biointegration of conventional organic semiconductor lasers is explored by drastically altering their design and fabricating thin, lightweight and flexible organic membrane lasers which may be used as versatile security labels. The design and fabrication of polymer membrane DFB lasers is discussed and the devices are optically characterized. The concept of using membrane lasers as barcode-like labels is introduced and their performance is tested on banknotes. Lastly, it is demonstrated how the lightweight and thin design of membrane lasers can be utilized to exploit applications as wearable security tags to augment biometric authentication. In a proof of principle experiment, it is shown how membrane lasers could be safely operated on the finger or even on the human eye by integration with a contact lens.

2

Theory and Background

2.1 Organic Light Emitting Materials

This section introduces organic light emitting materials which constitute the basic building block of most biological lasers. The basic chemical and optical properties are discussed and three different classes of organic light emitting materials used throughout this thesis are described.

First, in Section 2.1.1, the basic principles, chemical structure and properties of organic light emitting materials are introduced. This work features small molecules, conjugated polymers and fluorescent proteins as organic light emitting materials and their properties are discussed in more detail in Section 2.1.2, 2.1.3 and 2.1.4, respectively. A special emphasis on fluorescent proteins is given since they only emerged recently as an attractive and novel material class for laser devices. Lastly, in Section 2.1.5, light is shed on the optical properties of organic materials that are utilized in biological laser devices.

2.1.1 Basics of Organic Light Emitting Materials

Most biological and biocompatible lasers use organic light emitting materials as the gain material. In chemistry, the term "organic" typically relates to hydrocarbon bonds. Organic light emitters, more specifically, are π-bonded molecules or polymers consisting of mainly carbon and hydrogen atoms. As an example, the molecular properties of the simple organic molecule benzene shall be discussed.

Figure 2.1a shows the chemical structure of benzene, consisting of six carbon and six hydrogen atoms. Each carbon atom in benzene has four valence electrons of which three of them covalently bind with neighboring carbon or hydrogen atoms via sp^2-orbitals. These are so called σ-bonds, which due to their high binding energy define the structure of the molecule. The remaining valence electron of each carbon atom forms a $2p_z$-orbital in the orthogonal plane, as depicted in Fig. 2.1b. The $2p_z$-orbitals overlap mutually with the neighboring orbital and form so called π-bonds. All orbitals together form a conjugated system in which the electrons are delocalized over the entire molecule instead of being localized on a single bond (see Fig. 2.1c). The conjugated system can exist as binding π-orbital and antibinding π^*-orbital [45]. These states differ in energy and the binding π-orbital energetically describes the highest occupied molecular orbital (HOMO) while the antibinding π^*-orbital describes the lowest unoccupied molecular orbital (LUMO). Hence, the HOMO has a lower energy than the LUMO with a energy difference of typically a few eV. Optically, this corresponds to photons in the visible range and the transition is exploited in biological lasers for the absorption and emission of photons. The absorption of a photon leads to the excitation of electrons into the LUMO level of the molecule leaving a hole in the HOMO level. Due to the relatively low dielectric constant of organic molecules and hence a weak intermolecular interaction, these electron hole pairs are strongly bound to the molecule. The Coulomb interaction between electrons in the LUMO and holes in the HOMO leads to the formation of a neutral bound quasiparticle, called Frenkel exciton. Compared to their inorganic counterparts (Wannier-Mott excitons, $\sim 10\,\text{meV}$), excitons in most organic semiconductors typically have binding energies of $0.3 - 1.6\,\text{eV}$ [46], exceeding the thermal energy at room temperature ($\sim 25\,\text{meV}$). This renders organic materials ideal light emitting and absorbing materials for devices operated at room temperature.

The different organic light emitting materials utilized in this work can be classified as, conjugated small molecules, conjugated polymers and fluorescent proteins. While small molecules

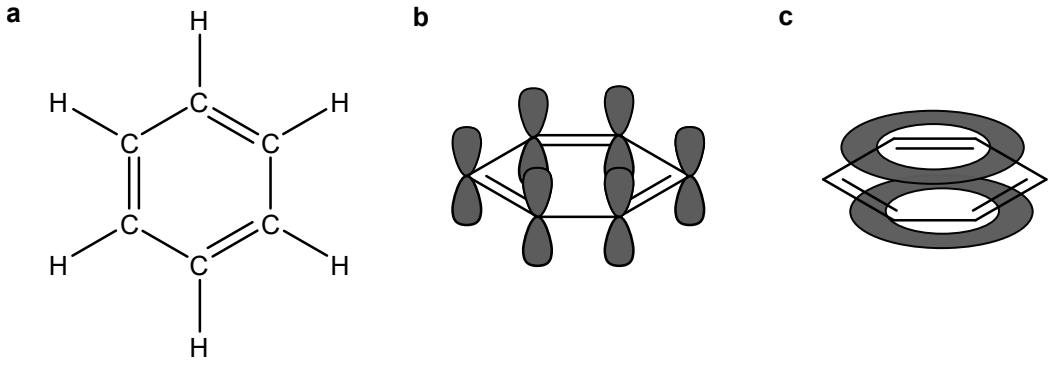

Figure 2.1: **a**, Chemical structure of benzene (C_6H_6). **b**, Illustration of the $2p_z$-orbitals formed by the unbound valence electron of the individual carbon atoms of benzene. **c**, Illustration of the conjugated system formed by π-bonds leading to a delocalization of electrons over the molecule.

and conjugated polymers are well studied and commonly used organic gain materials for laser devices, fluorescent proteins only recently emerged as novel gain materials and will be discussed in more detail.

2.1.2 Small Molecules

Small molecules show a lower molecular weight, compared to conjugated polymers and fluorescent proteins (typically $M_w \sim 10 - 250\,\text{kDa}$) and thin films can be fabricated by a variety of thermal evaporation techniques. Conveniently, since the intermolecular van der Waals interaction between organic small molecules is weak, only moderate processing temperatures are needed to evaporate the material and hence to grow thin solid-state films. Within these films, high material purities can be achieved by repeated vacuum sublimation of the organic material prior to evaporation. When used as active material in organic lasers, the emissive moieties of small molecules are often physically separated by a host material to prevent concentration quenching [21]. This is also the case for fluidic organic and biological lasers, where small molecules are dissolved in organic solvents or water.

2.1.3 Conjugated Polymers

Conjugated polymers, in contrast, are long chain-like molecules consisting of alternating single and double bonds. The conjugated system and hence the delocalization of π-electrons stretches along the backbone of the polymer. The distance over which π-electrons are delocalized usually does not cover the entire polymer chain. Instead, the chain is subdivided into chromophore segments which are individually optically active [47]. The molecular weight

of conjugated polymers (typically $M_w > 10\,\text{kDa}$) is usually orders of magnitudes larger than the weight of small molecules and therefore thermal evaporation for device fabrication is not feasible. Most commonly, wet processing techniques, such as inkjet printing and spin coating, are used to produce conjugated polymer solid-state thin films [48–50].

Furthermore, similarly to small molecules, conjugated polymers show semiconducting properties and are widely used in organic light emitting diods (OLEDs) and organic solar cells (OSCs) [11, 51, 52]. In fact, it was a conjugated polymer (polyacetylene) in which semiconducting properties were first identified in an organic material. The scientists Alan J. Heeger, Alan G. MacDiarmid and Hideki Shirakaw were awarded the 2000 Nobel Prize in Chemistry for this discovery [10].

2.1.4 Fluorescent Proteins

Small molecules and conjugated polymers are well studied in the context of organic light emitting devices. Only in recent years, fluorescent proteins have emerged as a novel organic material class for laser devices. Therefore, the origin and properties of fluorescent proteins are less well known in the organic laser community and shall be discussed in more detail.

Traditionally, fluorescent proteins are used as a marker to study proteins, cells and even whole organisms in eukaryotic and prokaryotic life [53–55]. The superiority of fluorescent proteins when compared to other fluorescent markers, is the fact that the fluorescence does not require any additional co-factors but that the fluorophore produced by the cells under investigation, following routine genetic modification, is formed exclusively by the aromatization of the peptide backbone and hence fluorescent proteins do generally not significantly alter the function or position of their fusion partners. Furthermore, the emission is stable and can be recorded non-invasively and species independently bacterial and mammalian cells [56].

Within this section, the focus will be on the wild type green fluorescent protein (GFP) found in the jellyfish *Aequorea victoria*. This GFP type is widely studied and its properties are well understood. Nevertheless, most practical studies rely on the use of specifically designed mutants of fluorescent proteins from the GFP family. The best example is enhanced GFP (eGFP) which is primarily used as a research tool and shares most of its basic properties with the wild type GFP.

GFP was first discovered by Johnson and Shimomura on a field trip to the Northwest Pacific

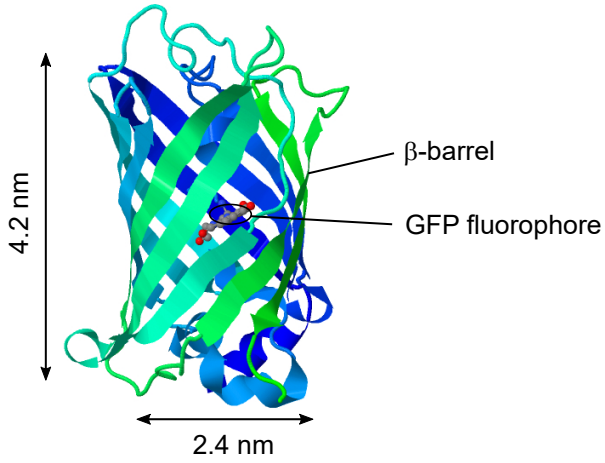

Figure 2.2: Illustration of the enhanced green fluorescent protein (eGFP) structure with a size of 2.4 nm by 4.8 nm. The fluorophore is surrounded by the 11-stranded β-sheet forming a nano-barrel. Adapted from Ref. [59].

in 1962, where they studied the luminescence of the jellyfish *Aequorea victoria*. Their findings suggested that the green light emitted by the jellyfish is generated in a two step process [57]. In a first step, a bioluminescent protein (later called aequorin) emits blue light in the presence of Ca^{2+}. Next, a secondary fluorescent protein absorbs the blue light and emits in the green. This protein was later called GFP. It is hypothesized, that the reason for the red shift induced by GFP is for enhancing the penetration of light in the ocean which could give an evolutionary advantage [58]. However, it is still unknown why nature designed this two step process, rather than evolving a primary green bioluminescent protein.

The vast scientific interest in GFP only started three decades later and was triggered by the first cloning of the wild type GFP in 1992 and expression as a transgene in *C. elegans* in 1996, respectively [60, 61]. Hence, it is important to understand the chemical and physical processes of GFP and its fluorophore. Photophysical studies revealed that the wild type GFP has a main absorption peak at 475 nm and a minor absorption peak at 395 nm. To generate its luminescence, the jellyfish *Aequorea victoria* uses the main absorption peak since the peak bioluminescence emission of aequorin is at 470 nm [62]. The relative ratio between the main and minor absorption peak is dependent on environmental factors such as illumination history or pH level [63]. The main emission peak of wild type GFP is stable at 508 nm. The mutant type eGFP is exclusively used throughout this thesis and its photo physical properties are discussed in detail in Section 3.3.3. The main differences are, a red shifted absorption, a higher absorption cross section at the peak absorption wavelength, a more efficient protein folding

and consequently an increase in fluorescence intensity [64].

The 3D structure of GFP was discovered in 1996 by means of crystallography [63, 65]. This aided to understand the autocatalytic formation of the fluorophore and the fluorescence properties in the mature protein [56]. GFP consists of 238 amino acids which form a structure comprising five α-helices and an 11-stranded β-sheet [60]. As shown in Fig. 2.2, the β-sheet wraps up to form an almost seamless symmetrical cylinder, known as β-barrel structure [65]. The full protein is 4.2 nm long and 2.4 nm in diameter with a molecular weight of 21 kDa [60, 63]. The green emitting GFP fluorophore is formed at the center of the tightly packed β-barrel which provides stability and resistance to unfolding by temperature increase and denaturation. Figure 2.3 shows the formation of the fluorophore which happens spontaneously by folding of the peptide chain and involves the three amino acids Ser^{65}, Tyr^{66} and Gly^{67} [62, 66]. In a first step, due to rapid cyclization, the C-terminus of Ser^{65} and the N-terminus of Gly^{67} bind to form a five membered ring. Next, a second conjugated π-system is formed on the 3 membered polypeptide chain due to dehydration. Lastly, the fluorophore is formed by linkage of the separate conjugated π-systems via a double bond due to oxidation. The last step requires the presence of oxygen and it was shown that GFP is non-fluorescent in an anaerobic environment [67]. However, as oxygen is generally present, the formation of the fluorophore is normally described as autocatalytic with no additional co-factors required.

Other organic light emitting materials, such as small molecules, typically show a decrease in fluorescence brightness at high molecular concentrations due to self aggregation and consequently intermolecular quenching [68]. This effect is mostly absent in solid-state GFP, where the β-barrel diameter defines the distance between two neighboring fluorophores. Many years of evolutionary optimization may have engineered GFP such that an optimal balance between high protein density and low energy transfer self quenching is reached [29]. Hence, a high emission brightness is retained even at maximum density of solid-state films which makes GFP an interesting light emitting material for lasers. It has been shown that dried GFP films allow for strong optical amplification, providing gain of $g = 22\,\mathrm{cm}^{-1}$ while the fluorescence signal is reduced by only 7 dB due to concentration quenching [29]. Interestingly, the gain properties can be altered by changing the humidity level. It is assumed that changes in humidity lead to a variation of the β-barrel diameter which in turn changes the interfluorophore distance and hence the selfquenching rate.

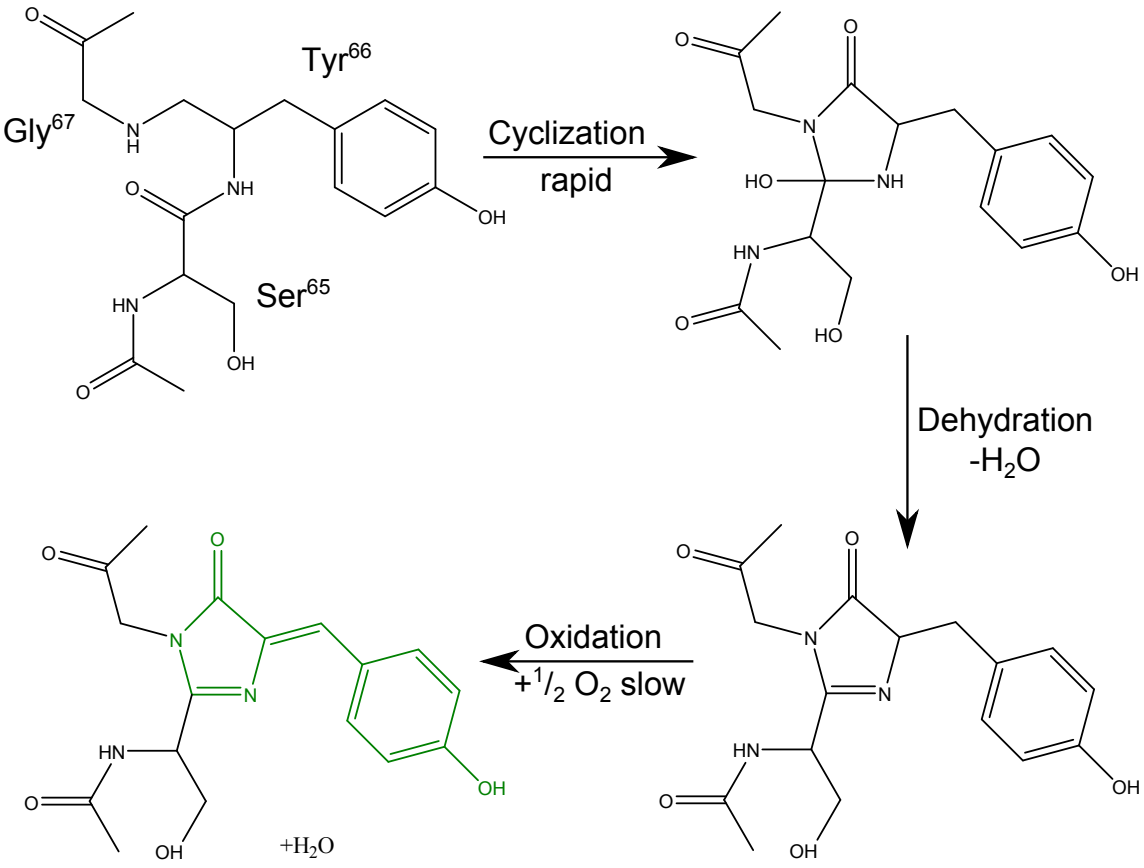

Figure 2.3: Formation of the GFP fluorophore from the polypeptide sequence $Ser^{65}Tyr^{66}Gly^{67}$. The formation process is governed by the three steps, cyclization, dehydration and oxidation. The chemical structure marked in green indicates the fluorophore.

2.1.5 Optical Properties of Organic Light Emitting Materials

We have already identified that the binding energy of Frenkel excitons in organic light emitting materials ($0.3-1.6\,\text{eV}$) is just below the energy of a photon in the visible spectrum (typically $> 2\,\text{eV}$). However, the optical properties of organic light emitting materials show further unique features, especially when compared to their inorganic counterparts. For example, the absorption and emission spectra of organic light emitting materials are not single Lorentzian transitions but rather consist of multiple broad bands. Another feature is the substantial energy shift between absorption and emission spectrum, which is known as the Stokes shift. These properties are directly related to vibronic interactions influencing the electron cloud on the molecule and can be explained by the Franck-Condon principle [69].

The energetic state of an organic emitter that is relevant for light interaction is the singlet ground state, called S_0. Singlet means that the spin directions of the two energetically highest electrons oppose each other. In the first electronic excited state S_1, there is one electron in the previously introduced π^*-orbital and hence a hole in the π-orbital. As a molecule transitions from one state to another, the electron density distribution changes and leads to a displacement of charges which gives rise to a shift in atomic coordinates on the molecule. All states feature a unique electron density distribution which is influenced by vibronic interactions. This causes vibronic modes which can be approximated by harmonic oscillations. Figure 2.4 shows an illustration of the characteristic potential wells forming the ground and first excited electronic state of a molecule and the vibronic levels (ν for S_0 and ν' for S_1) within them. The energy difference between two vibronic levels is typically in the order of 100 meV and hence the probability for thermal excitation to a higher lying vibronic level at room temperature is low. Therefore, most organic molecules reside in the ground state at room temperature (S_0, $\nu = 0$).

The Born-Oppenheimer approximation states that electrons, due to their small mass, move faster than atoms [70]. This results in a time scale for electronic transitions (1 fs) orders of magnitude shorter than for vibronic transitions (0.1 ps) which are effectively reorganizations of the spatial location of atoms within the molecule. Consequently, during electronic transitions the atomic coordinates do not change. The Franck-Condon principle further states that the strength of an electronic transition is proportional to the overlap of the vibronic wave functions. The timescale for radiative transitions back to the ground state is in the order of 1 ns and hence much slower than vibronic transitions. Therefore, the re-emission of photons takes place by

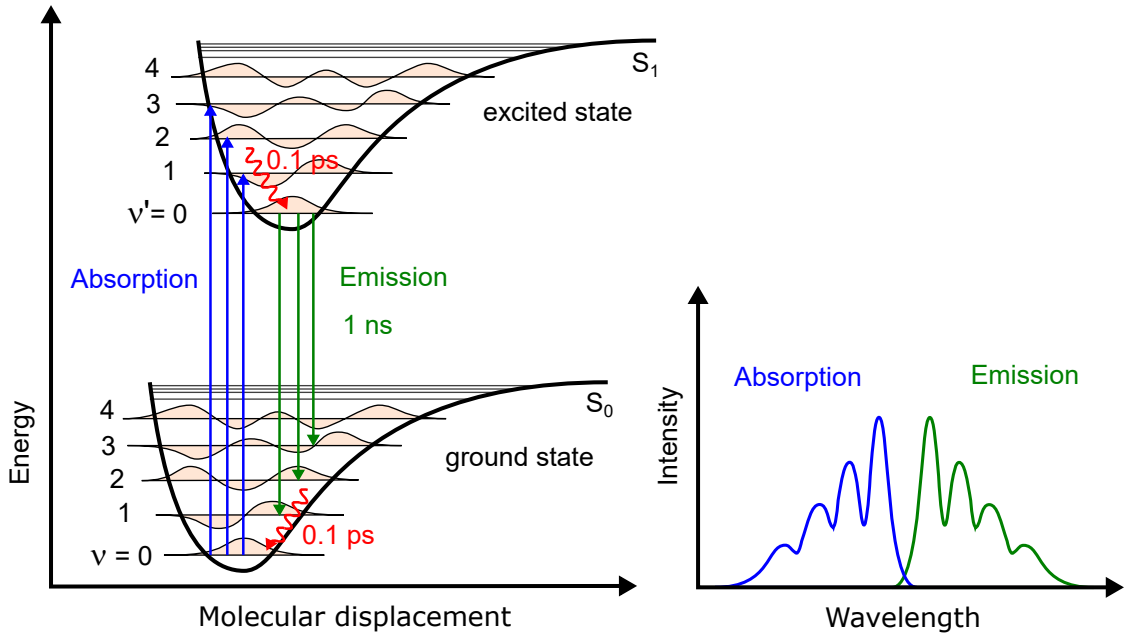

Figure 2.4: Illustration of the potential energy of a molecule as a function of molecular displacement. The vibronic levels are indicated by ν and ν'. The straight vertical arrows mark the Franck-Condon transitions for absorption (blue) and emission (green) of photons. The red oscillating arrows mark the non-radiative relaxation to the lowest vibronic level (ν and ν'). The associated absorption and emission spectrum is shown on the right hand side.

electronic transition from the lowest vibronic energy level of the excited state. As a result, the wavelength of the emitted light is red-shifted compared to the absorption wavelength which explains the Stokes shift. As we will see later on (Section 2.2.2), the fast absorption, followed by a fast vibronic relaxation, slow fluorescence emission and again a fast vibronic relaxation to the ground state constitutes a nearly ideal quasi 4-level system needed for laser gain materials.

2.2 Basics of Laser Operation

In this section, the basic processes within optically active materials are discussed. Furthermore, the necessary prerequisites for active materials to provide optical gain are introduced.

The different optical processes that can occur in active media, such as organic light emitting materials, are identified and elucidated in Section 2.2.1. Subsequently, in Section 2.2.2 the crucial conditions for lasing action, such as gain and population inversion, are derived and their realization in a 4-level energy system is discussed.

2.2.1 Optical Processes in Active Media

The working principle of a laser relies on the interaction of a strong photon field with an optically active material. Incident photons are coupled to the energy distribution of the material via a process called stimulated emission. Typically, bound electron-hole pairs or excited electrons are stimulated by incident photons and undergo a transition to a lower energetic level while emitting a "copy" of the initial photon with the same energy, phase, directionality and polarization. For laser operation, stimulated emission has to be the dominating optical process in the system. The material supporting this process is called an optically active or gain material. For dominant stimulated emission, this material needs to be placed inside a cavity providing resonant confinement of the photon field and hence optical feedback. Furthermore, an external pump source needs to supply the necessary amount of excited states in the active material. A large variety of optically active materials can be used for different laser applications. These include gaseous, liquid, solid-state and semiconductor materials. All active materials used in this work are organic light emitters that rely on fluorescence.

In all of the aforementioned active materials, three fundamental optical processes can occur. These are depicted in Fig. 2.5a-c and can be classified as stimulated absorption, spontaneous emission and stimulated emission. Considering an idealized quantized two-level system

with a ground state E_1 populated by a certain number of electrons N_1 and an excited state E_2 (population number N_2), stimulated absorption occurs when an incident photon with a resonance energy equal to the energy difference between the two states $\hbar\omega = E_2 - E_1$ is absorbed in the system and promotes an electron from E_1 to E_2. The rate of this transition is described by the Einstein coefficient B_{12} in the form

$$\frac{dN_1}{dt} = -\frac{dN_2}{dt} = -B_{12}N_1u_\omega \ , \tag{2.1}$$

where u_ω is the photon density at the resonance frequency ω. The excited electron has a certain mean lifetime τ_{21} after which it spontaneously decays down to the ground state E_1 while emitting a photon with an energy $\hbar\omega$. The rate of this transition is described by the Einstein coefficient $A_{21} = 1/\tau_{21}$ in the form

$$\frac{dN_2}{dt} = -\frac{dN_1}{dt} = -A_{21}N_2 \ . \tag{2.2}$$

In contrast to stimulated absorption, the spontaneous emission process is not influenced by the surrounding photon field. Lastly, within the mean lifetime τ_{21}, an electron can transition downwards from E_2 to E_1 due to stimulation from an incoming photon with an energy $\hbar\omega$. This process is called stimulated emission and an exact copy of the initial photon is created. The rate of the transition is described by the Einstein coefficient B_{21} in the form

$$\frac{dN_2}{dt} = -\frac{dN_1}{dt} = B_{21}N_2u_\omega \ . \tag{2.3}$$

An idealized quantized two-level system is in thermodynamic equilibrium if the Boltzmann equation applies and the system obeys

$$\frac{N_2}{N_1} = \frac{\exp(-E_2/k_BT)}{\exp(-E_1/k_BT)} \ , \tag{2.4}$$

where k_B is Boltzmann's constant and T is the temperature. If we assume energetic states with $E_2 > E_1$ (see Fig. 2.5), then $N_2 < N_1$. Furthermore, for a system under equilibrium conditions, the net rate between downward and upward transitions must be the same:

$$B_{12}N_1u_\omega = A_{21}N_2 + B_{21}N_2u_\omega \ . \tag{2.5}$$

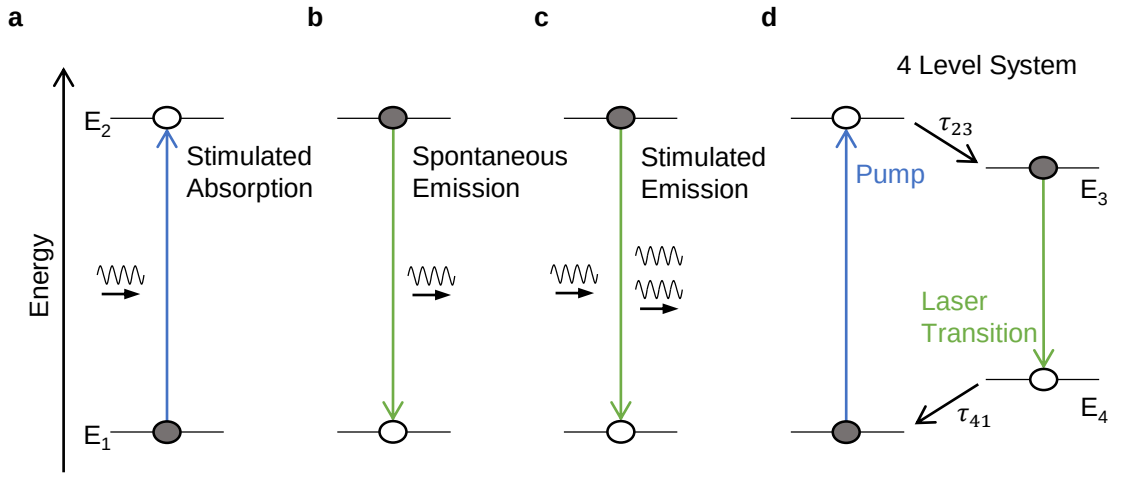

Figure 2.5: Schematic energy diagram of the fundamental optical processes in active media. Stimulated absorption (**a**), spontaneous emission (**b**) and stimulated emission (**c**) of photons in a quantized two-level system with an energy separation of $\hbar\omega = E_2 - E_1$. **d**, Schematic energy diagram of a 4-level system required for population inversion and lasing, with τ_{23} and τ_{41} indicating the non-radiative decay rates from E_2 to E_3 and from E_4 to E_1, respectively.

By combining Eq. 2.4 and 2.5 and solving for the photon density u_ω one obtains

$$u_\omega = \frac{A_{21}}{B_{21}} \frac{1}{(B_{12}/B_{21})\exp(\hbar\omega/k_B T) - 1} \,. \tag{2.6}$$

Comparing this equation to Planck's radiation law [71]

$$u_\omega = \frac{\hbar\omega^3}{\pi^2 c^3} \frac{1}{\exp(\hbar\omega/k_B T) - 1} \,, \tag{2.7}$$

yields that the Einstein coefficients for absorption and stimulated emission relate to one another by

$$\frac{A_{21}}{B_{21}} = \frac{\hbar\omega^3}{\pi^2 c^3} \qquad \text{and} \qquad B_{12} = B_{21} \,, \tag{2.8}$$

where c is the speed of light in the active medium.

2.2.2 Gain in Active Media

In order to quantitatively determine the amplification in an active medium, it is important to take a closer look at the details of stimulated absorption and emission. Considering a photon field that passes through an active medium along the z-direction, we know that each upward transition subtracts a photon from the initial photon field. Conversely, each downwards tran-

sition adds a photon to the field. Hence, considering Eq. 2.1 and 2.3, the change in the photon field density u_ω, as it passes through an active material along the z-direction, can be expressed as

$$\frac{du_\omega}{dt} = c\frac{du_\omega}{dz} = (B_{21}u_\omega N_2 - B_{12}u_\omega N_1)\hbar\omega l(\omega)\,, \tag{2.9}$$

where $l(\omega)$ is the spectral line shape (in seconds) of the optical transition in the gain material. Considering that the active material has a finite length L and substituting Eq. 2.8 into Eq. 2.9 and integrating along the z-direction yields,

$$u_\omega(L) = u_\omega(0)\exp(\frac{\hbar\omega}{c}B_{21}u_\omega\Delta N l(\omega)L) = u_\omega(0)\exp(g_\omega L)\,, \tag{2.10}$$

where $\Delta N = N_2 - N_1$ and the gain coefficient g_ω is defined as

$$g_\omega = \sigma_{SE}(\omega)\Delta N = \frac{\hbar\omega}{c}B_{21}u_\omega\Delta N l(\omega)\,, \tag{2.11}$$

where $\sigma_{SE}(\omega)$ is the stimulated emission cross section of the excited state which quantifies the likelihood of a stimulated emission event. Interestingly, optically excited organic gain materials achieve stimulated emission cross sections of $10^{-17} - 10^{-16}$ cm^{-2} [72]. This exceeds the cross sections typically achieved in inorganic Nd:YAG (neodymium-doped yttrium aluminum garnet) crystals $\sim 10^{-19}$ cm^{-2} [73].

Previously we have found (see Eq. 2.4) that for a two level system in thermal equilibrium $N_2 < N_1$ and hence such a system is always a net absorber with $g_\omega < 0$ (see Eq. 2.10). This in turn means that for laser operation and hence net gain ($g_\omega > 0$), the population of the excited state N_2 needs to surpass the population of the ground state N_1. This situation is called population inversion and in order to achieve it, active media with multiple energetic levels are selected. One example is the 4-level system depicted in Fig. 2.5d which shall be discussed here. In addition to the ground and excited state, two intermediate energetic states (E_3 and E_4) are part of the system. Here, electrons are pumped via stimulated absorption from the ground state E_1 to the excited state E_2. Next, the electrons decay non-radiatively with a rate τ_{23} to the energetic state E_3. The radiative transition from E_3 to E_4 is utilized as the laser transition via stimulated emission and finally the electrons decay non-radiatively with a rate τ_{41} from E_4 to E_1. Hence, the pumping is decoupled from the laser transition and a population inversion between E_3 and E_4 can be achieved. A good active material shows fast decay rates

τ_{23} and τ_{41}, which leads to efficient population of the upper laser level (E_3) and depopulation of the lower laser level (E_4). This ensures that the population inversion $N_3 > N_4$ is reached easily and that there are enough electrons in the ground state available to be pumped in the excited state. In real lasers the transition to and from the laser level are considered a bottle neck which introduces energy losses. This is particularly pronounced in CO_2 lasers where He is added to the gas in order to enhance the decay rates [74]. Conveniently, organic emitters which are typically the gain material of choice for biological lasers, intrinsically show a quasi 4-level system as already discussed in Section 2.1.5.

2.3 Optics in Dielectric Media

Since organic materials are dielectric media and the propagation of light is essential for the operation of lasers, the basic optical principles involved in light propagation within dielectric media are introduced in this section.

Starting with Maxwell's equations in dielectric media, the principle fields are introduced in Section 2.3.1. After the derivation of the wave equation for the electric field and the general dispersion relation of photons, the concept of polarization and total internal reflection is introduced. In Section 2.3.2, this theory is applied to an asymmetric waveguide structure which is a key optical element in this thesis and light is shed on the propagation and field distribution of optical modes within these structures.

2.3.1 Maxwell Equations in Dielectric Media

Electro-magnetic fields in isotropic dielectric materials can be described by Maxwell's equations, which in a source, current and charge free medium can be expressed as

$$\nabla \times \vec{H} = \frac{\partial \vec{D}}{\partial t} \tag{2.12}$$

$$\nabla \times \vec{E} = -\frac{\partial \vec{B}}{\partial t} \tag{2.13}$$

$$\nabla \cdot \vec{D} = 0 \tag{2.14}$$

$$\nabla \cdot \vec{B} = 0\,, \tag{2.15}$$

where $\vec{E}$ is the electric and $\vec{H}$ is the magnetic vector field which are functions of position and time. The electric flux density (also called the electric displacement) $\vec{D}$ is related to the elec-

tric field $\vec{E}$ via the electric properties of the material, which are described by the polarization density $\vec{P}$. This is the sum of all macroscopic dipole moments induced by the electric field. Similarly, the magnetic flux density $\vec{B}$ is related to the magnetic field $\vec{H}$ via the magnetic properties of the materials, embodied by the magnetization density $\vec{M}$. The equations relating the fields and flux densities are

$$\vec{D} = \epsilon_0 \vec{E} + \vec{P} = \epsilon \vec{E} \tag{2.16}$$

$$\vec{B} = \mu_0(\vec{H} + \vec{M}) = \mu \vec{H} \ , \tag{2.17}$$

with ϵ_0 and ϵ describing the electric permittivity of the field in vaccum and in the material, respectively. Similarly, μ_0 and μ describe the magnetic permeability in vacuum and in the material, respectively. The material dependent electric permittivity ϵ and magnetic permeability μ are scalar quantities in isotropic media. With Maxwell's equations at hand, we know how the different electro-magnetic fields are related, but in oder to describe the propagation of light it is necessary to know the electromagnetic wave equation. Taking the curl of Maxwell's second equation (Eq. 2.13), together with Eq. 2.12, the constitutive relations Eq. 2.16 and 2.17 and using a known vector identity [1] one can write

$$\nabla \times \nabla \times \vec{E} = \nabla(\nabla \cdot \vec{E}) - \nabla^2 \vec{E} = -\frac{\partial(\nabla \times \vec{B})}{\partial t} = -\epsilon\mu \frac{\partial^2 \vec{E}}{\partial t^2} \ . \tag{2.18}$$

From Eq. 2.14 we know that the dielectric flux density and hence the electric field has no sources in the material and Eq. 2.18 simplifies to the Hemholtz wave equation

$$\nabla^2 \vec{E} - \frac{1}{c^2} \frac{\partial^2 \vec{E}}{\partial t^2} = 0 \quad \text{with} \quad c = \frac{1}{\sqrt{\epsilon\mu}} \ . \tag{2.19}$$

This equation relates the spatial contribution of the electric field with the time dependent contribution. The material dependent constant c describes the speed of light within the medium. For light propagating in vacuum the fundamental speed of light is thus

$$c_0 = \frac{1}{\sqrt{\epsilon_0 \mu_0}} \approx 3 \times 10^8 \mathrm{m\,s^{-1}} \ . \tag{2.20}$$

The ratio between the speed of light in vacuum and the medium is defined as the refractive index $n = c_0/c = \sqrt{\epsilon\mu/\epsilon_0\mu_0}$ of the medium. For the dielectric nonmagnetic materials inves-

[1] $\nabla \times \nabla \times \vec{A} = \nabla(\nabla \cdot \vec{A}) - \nabla^2 \vec{A}$

tigated in this thesis, we can set the magnetic permeability to unity and denote the refractive index as a complex quantity $n \rightarrow n + i\kappa$, where n describes the real part and κ the imaginary part of the refractive index.

The simplest solution to the wave equation (Eq. 2.19) for the electric field is the harmonic plane wave

$$\vec{E} = \vec{E_0} \exp i(\omega t - \vec{k}\vec{r}) \,, \tag{2.21}$$

where ω is the oscillation frequency in time and $\vec{k}$ is the propagation vector. By plugging the equation for the harmonic plane wave into the wave equation, we arrive at the dispersion relation for photons in dielectric media

$$k^2\vec{E} + \frac{1}{c^2}\omega^2\vec{E} = 0 \quad \Rightarrow \quad \omega = ck = c_0 nk \,, \tag{2.22}$$

which is valid in most macroscopic systems where the light is not confined and interference does not occur. We will see later on, that for light propagation in optical resonators and nano patterned structures this dispersion relation needs to be modified. The above derivation can be executed for the magnetic field $\vec{H}$ in a similar fashion.

Polarization

We can see from Eq. 2.21 that the electric field vector $\vec{E}$ has a defined direction depending on $\vec{E_0}$. In fact, by inserting the expression describing a harmonic plane wave into Maxwell's third equation (Eq. 2.14), we can conclude $\vec{k}\vec{E_0} = 0$ which can be interpreted as the electric field oscillating perpendicular to the wave vector and hence the direction of light propagation. In a similar fashion, the solution to the wave equation can be inserted into Maxwell's second equation (Eq. 2.13) and we can see that $\vec{k} \times \vec{E} = \omega\vec{B}$, which tells us that the magnetic field direction is perpendicular to the wave vector and the electric field direction. This restricts the electric field to three different types of oscillations. First, the linear polarization of light, where the electric field oscillates in a plane along the propagation direction. Secondly, the circular polarization, described by a rotating electric field with a constant amplitude and lastly, the elliptical polarization, where the electric field is rotating and oscillating simultaneously.

The concept of polarization will get important again when talking about different modes in a planar waveguide in Section 2.3.2.

Snell's Law

Relation 2.19 implies that the speed of light c changes as light propagates from one medium with a refractive index n_1 to another medium with a different refractive index n_2. When the light impinges onto the material interface under a certain angle of incidence θ_1 (with respect to the surface normal), the change in c induces a refraction of the light under a transmission angle θ_2. The relation between the angles and refractive indices is described by Snell's law in the form

$$n_1 \sin\theta_1 = n_2 \sin\theta_2 \ . \tag{2.23}$$

Total Internal Reflection

Snell's law (Eq. 2.23) implies that light passing from a higher refractive index material to a lower refractive index material is bent away from the surface normal. Vice versa, light propagating from a lower refractive index material to a higher refractive index material is bent towards the surface normal. Consequently, there must exist a critical angle of incidence θ_{crit} for which light that is propagating from a higher refractive index material n_1 to a lower refractive index material n_2 (with $n_1 > n_2$), is refracted along the material interface ($\theta_2 = 90°$). This yields the general expression for the critical angle

$$\theta_{\text{crit}} = \arcsin(\frac{n_2}{n_1}\sin\theta_2) = \arcsin(\frac{n_2}{n_1}) \quad \text{with} \quad \theta_2 = 90° \ . \tag{2.24}$$

Consequently, for any incidence angle $\theta_1 > \theta_{\text{crit}}$, Snell's law does not provide a solution for the refraction angle θ_2 and the light is totally reflected at the materials interface. This is a core principle for waveguides as will be discussed next.

2.3.2 Guided-Wave Optics

The theory introduced in Section 2.3.1 is generally valid in any photonic system consisting of dielectric materials. One of these systems is the dielectric planar slab waveguide in which photonic modes propagate over macroscopic distances. As we will see below (Section 2.4.3), photonic waveguides are also the fundamental structure for distributed feedback (DFB) lasers which are an important part of this work. Figure 2.6 shows an illustration of a simple three layer planar waveguide consisting of a slab of thin, dielectric layers where the light is confined in the core layer of a thickness d sandwiched in between two cladding layers.

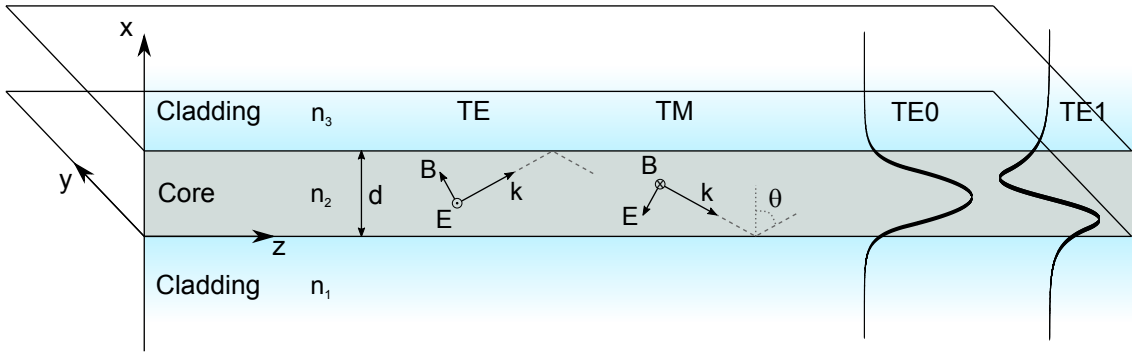

Figure 2.6: Schematic drawing of a three layer waveguide structure consisting of a core layer with a thickness d and a refractive index n_2 and two semi-infinite cladding layers with refractive index n_1 and n_3. The possible propagation direction and electromagnetic field orientation for TE and TM modes is indicated and the electric field distribution for $TE0$ and $TE1$ is shown.

To find the allowed modes within a three-layer waveguide structure, it is possible to utilize a simple ray optics picture. For confinement in the core layer, the light must be reflected from both boundaries under an angle θ larger than the critical angle for total internal reflection (*cf.* Section 2.3.1). This is only possible if the refractive indices n_1, n_2 and n_3 of the waveguide obey $n_1,\ n_3 < n_2$. Additionally, the waveguided mode can only exist if a standing wave pattern emerges from constructive interference of the incident wave and the corresponding reflections on each boundary. Both requirements are fulfilled for

$$\frac{4\pi d}{\lambda_0}\sqrt{n_2^2 - n_{\text{eff}}^2} = \phi_1 + \phi_3 + M2\pi \quad \text{with} \quad M \in \mathbb{N}\,, \tag{2.25}$$

where $n_{\text{eff}} = n_2 \sin\theta$ is the effective refractive index of the guided mode, ϕ_1 and ϕ_3 are the Goos-Hänchen phase shifts at the boundaries between waveguide core and cladding layers. Both phase shifts depend on the polarization of the mode, the refractive indices $n_{1/3}$ and the effective refractive index n_{eff}. An exact expression for the Goos-Hänchen phase shift can be found in Ref. [75]. The effective refractive index n_{eff} is a property associated with each individual mode and has an allowed range,

$$\max(n_1, n_3) \leq n_{\text{eff}} \leq n_2\,. \tag{2.26}$$

The modal Equation 2.25 is transcendental and has therefore no analytical solutions. Utilizing, either numerical or graphical solvers yields the polarization (TE or TM), the mode order M

and the effective refractive index n_{eff} of supported modes in a waveguide structure. Figure 2.7a shows a graphical method to solve Eq. 2.25 for a typical waveguide stack consisting of e.g. an organic layer ($n_2 = 1.7$, $d = 600\,\text{nm}$) on top of a carrier glass substrate ($n_1 = 1.5$) enclosed by air ($n_3 = 1.0$) as the top cladding layer. The term on the left-hand side of Eq. 2.25 (gray line in Fig. 2.7a), depends directly on the core layer thickness d and is mainly defined by the waveguide architecture. In contrast, the polarization dependent term on the right-hand side (blue and red lines in Fig. 2.7a) mainly describes the light propagation and replicates with phase shift multiples M of 2π. Utilizing this method, it is possible to obtain the effective refractive index n_{eff} for different guided modes for a range of different core layer thicknesses (see Fig. 2.7b). The onset for guided modes within the simulated asymmetric waveguide is at a core layer thickness $d = 101\,\text{nm}$ for the example shown here. This feature can not be found in symmetrical waveguides ($n_1 = n_3$) where a cut-off thickness does not exist and Eq. 2.25 can be solved for infinitesimal thin core layers. For thin core layers, in the simulated structure, $TE0$ and $TM0$ modes are supported and higher order modes only exist for a layer thickness $d \geq 434\,\text{nm}$. Furthermore, TE modes generally show a higher effective refractive index n_{eff} than the associated TM modes over the entire simulation range. This confirms that TE modes, with an electric field oscillating in plane, are more strongly confined in the higher refractive index core layer. The electric field of TM modes in contrast, is probing more into the adjacent layers and hence the mode confinement is weaker. Therefore, TE modes usually experience a stronger interaction with the core layer material. In lasers devices based on waveguide structures where the core layer comprises a gain material, this can lead to an increase in modal gain for TE modes compared to TM modes and thus lower lasing threshold requirements.

Equation 2.25 allows to determine which optical modes can be supported by a waveguide but the exact electric field distribution is unknown. To determine the fields, the simple ray optics picture is not sufficient and the more general theory introduced in Section 2.3.1 needs to be utilized. The fields propagating in a waveguide in z-direction are governed by Maxwell's equations (2.12 to 2.15) and in the case of a planar waveguide have no y-dependency ($\partial \vec{E}/\partial y = 0$) since the structure is translation invariant in y- and z-direction. This allows simplifying Maxwell's equations to derive a scalar second-order differential Helmholtz like equation of the form

$$\frac{\partial^2 E_y}{\partial x^2} + k_x^2 E_y = 0\,, \tag{2.27}$$

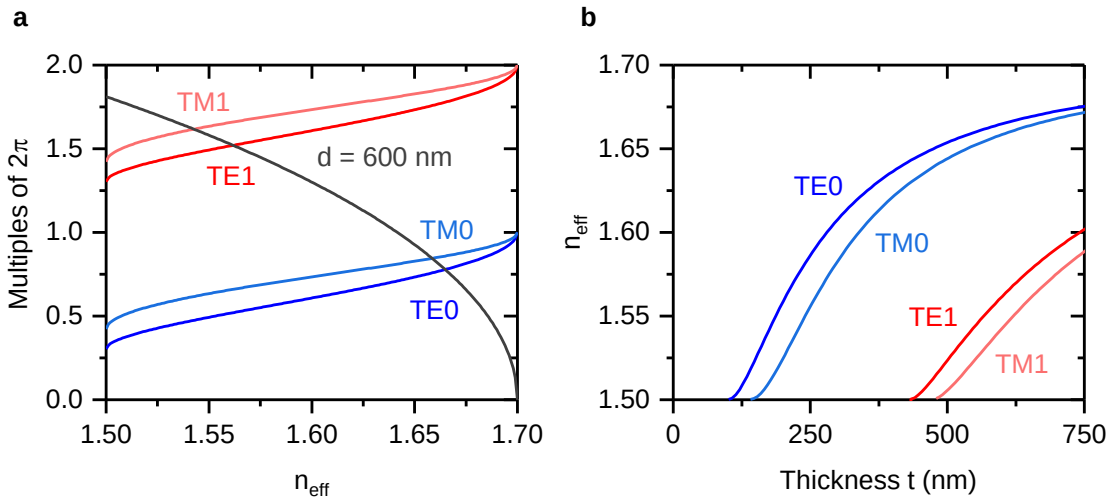

Figure 2.7: **a**, Number and polarization of allowed modes with corresponding effective refractive index. The crossing points indicate allowed modes for a waveguide structure with a lower cladding layer with a refractive index $n_1 = 1.5$, a core layer with a refractive index $n_2 = 1.7$ and a thickness of 600 nm, and an upper cladding layer with a refractive index $n_3 = 1.0$, for a mode wavelength $\lambda = 530$ nm. **b**, Effective refractive index n_{eff} depending on the core layer thickness d for different TE and TM modes within the same waveguide structure.

where k_x describes the projection of the wave vector $\vec{k}$ in x-direction with

$$k_x^2 = k_0^2 n_2^2 - k_0^2 n_{\text{eff}}^2 = |\vec{k}|^2 - k_z^2 \,. \tag{2.28}$$

This yields solutions for E_y of the form,

$$E_y = \begin{cases} A\exp(+\sqrt{k_0^2(n_{\text{eff}}^2 - n_1^2)}x), & \text{for } x < 0 \\ B\exp(ik_x x) + C\exp(-ik_x x), & \text{for } 0 < x < d \\ D\exp(-\sqrt{k_0^2(n_{\text{eff}}^2 - n_3^2)}x), & \text{for } x > d \,, \end{cases} \tag{2.29}$$

where the coefficients A, B, C and D are constants that need to be determined from the boundary conditions that apply to each region. The range of allowed values for n_{eff} defined by Eq. 2.26 yields that the arguments in the exponential terms for the substrate ($x < 0$) and cover ($x > d$) in Eq. 2.29 are real and hence the field is decaying to zero in this region. The respective boundary conditions are the continuity of the field and its first derivation,

$$\begin{aligned} E_y\Big|_{x=0_-} &= E_y\Big|_{x=0_+} & \qquad E_y\Big|_{x=d_-} &= E_y\Big|_{x=d_+} \\ \frac{\partial E_y}{\partial x}\Big|_{x=0_-} &= \frac{\partial E_y}{\partial x}\Big|_{x=0_+} & \qquad \frac{\partial E_y}{\partial x}\Big|_{x=d_-} &= \frac{\partial E_y}{\partial x}\Big|_{x=d_+} \end{aligned} \quad . \tag{2.30}$$

This approach allows to determine the electric field distribution within an asymmetric three layer waveguide structure. As an example, the $TE0$ and $TE1$ mode profile is shown in Fig. 2.6. A similar derivation can be executed for TM modes where the refractive index of the different layers is included explicitly.

The mode profile and distribution is particularly important for the work presented on DFB lasers (Chapter 5, 6 and 7), which can be regarded as waveguides with an additional corrugation at one interface. Knowing the field distribution within the waveguide further allows to determine the overlap of the guided mode with a specific region of the waveguide. For example, if a gain material is only present in the waveguide core $0 < x < d$ it is important to assess and maximize the modal overlap Γ of waveguided mode and core layer,

$$\Gamma = \frac{\int_0^d |E_y|^2 dx}{\int_{-\infty}^{+\infty} |E_y|^2 dx} \, . \tag{2.31}$$

A MATLAB script based on the derivation above to find modes and their respective field distribution within a three layered dielectric waveguide slab can be found in Appendix A.

2.4 Basics of Resonator Physics

In this section, the previously derived fundamentals in optics are utilized to introduce the concept of optical resonators which are the structure responsible for providing optical feedback in lasers.

Key properties of resonator structures, such as resonant amplification and the quality factor, are introduced in Section 2.4.1 using a Fabry-Pérot cavity as an example. Next, in Section 2.4.2 whispering gallery mode (WGM) resonators are introduced. These resonator structures are not utilized in this work but have proven to be an indispensable resonator architecture for biological lasers in general and are therefore discussed briefly. Most resonator structures presented in this thesis are distributed feedback (DFB) resonators which are introduced in Section 2.4.3. The peculiar photonic dispersion relation of these periodic structures is investigated and subsequently the necessary conditions to achieve Bragg scattering and lasing in a variety of different DFB lasers

are introduced. This is followed by discussing the coupled wave theory, a mathematical model describing the basic light propagation, scattering and amplification processes within DFB lasers.

2.4.1 Fabry Pérot Resonators

Apart from the gain material, the key element of most lasers is a resonator which is responsible for providing optical feedback. Due to the versatile fabrication techniques for organic light emitting materials, it is possible to realize lasers with a variety of different resonator architectures [76]. Devices based on organic light emitting materials often rely on light confinement within a dielectric material which enables the fabrication of lasers with dimensions on the order of a couple of wavelengths of the emitted light [77]. The basic principle of an optical resonator relies on trapping and enhancement of light with a certain resonance wavelength, while light with a non-resonant wavelength is diminished and leaves the resonator. In the context of organic lasers, resonators are often called cavities and both expressions are used interchangeably in this thesis.

In Chapter 4, lasers based on coplanar Fabry-Pérot resonators are investigated. This resonator structure consists of two planar highly reflective mirrors (with reflectivity R_1 and R_2) that are facing each other and are separated by a distance l_c. Typically, distributed Bragg reflectors (DBRs) consisting of alternating layers of low and high refractive index materials are used as mirrors in this resonator architecture. In order to introduce a simplified model of a Fabry-Pérot resonator, we assume the resonator is filled with an optically active dielectric material (e.g. an organic light emitting material) of refractive index n forming a waveguide core between the two mirrors (see Fig. 2.8a). A plane wave E, propagating vertically in the Fabry-Pérot resonator, will be reflected from one mirror and can interfere with itself. Constructive interference occurs when the electric field amplitude E_0 returns to its initial value after one round trip in the resonator according to [77]

$$E_0\sqrt{R_1R_2}\exp([G_m-\alpha]l_c)\exp(i4\pi nl_c/\lambda_0)=E_0\ , \tag{2.32}$$

where G_m describes the modal gain, α the propagation losses along the cavity normal and λ_0 the vacuum wavelength. A standing wave forms, if the imaginary exponent in Eq. 2.32 is an

integer multiple m of 2π and hence the resonance condition for Fabry-Pérot resonators is

$$nl_c = m\frac{\lambda_0}{2} \quad \text{with} \quad m \in \mathbb{N} \, . \tag{2.33}$$

The resonance condition further dictates a free spectral range $\Delta\lambda_{\mathrm{FSR}} = \lambda_0^2/2nl_c$ between consecutive longitudinal modes in the cavity (see Fig. 2.8b). Each longitudinal mode can further be subdivided into several transverse modes, not only differing in resonance wavelength but also in their spatial intensity pattern.

The second condition that can be deduced from Eq. 2.32 is that the intra-cavity losses α and mirror losses must be exceeded by the modal gain G_m in one round trip with a length l_c and hence

$$G_m l_c = \frac{\ln(R_1 R_2)}{2} + \alpha l_c \, . \tag{2.34}$$

If Eq. 2.33 is fulfilled a standing wave between the two mirrors is created and oscillates in time. Due to the resonance condition (Eq. 2.33), this effect only applies to light with a certain resonance wavelength and hence leads to mode selectivity. If an excited gain material is present in the resonator, the standing wave is enhanced due to stimulated emission. Further, if one of the mirrors exhibits a certain degree of transmission, this leads to monochromatic and coherent lasing emission. The modal gain G_m can be calculated from the material gain coefficient g (Eq. 2.11) and the modal overlap Γ of the waveguided mode with the gain material (according to Eq. 2.31)

$$G_m = \Gamma g \, . \tag{2.35}$$

The quality of a laser resonator can be assessed by investigating the lifetime τ_c of a photon within a resonator where no optical gain is present. This is typically quantified by the quality factor Q which is defined as

$$\frac{1}{\tau_c} = c_0 \frac{\alpha - (1/[2l_c])\ln(R_1 R_2)}{n} = \frac{2\pi c_0}{Q\lambda_0} \, , \tag{2.36}$$

where c_0 is the speed of light in vacuum. For the above derivation, it was assumed that the group and phase velocity within the resonator are identical.

Due to conservation of momentum and energy, the resonance wavelength exhibits an angle dependency within the Fabry-Pérot resonator which is described as the dispersion relation of the system. Consequently, the wave vector $\vec{k}$ is a superposition of a vertical component k_z and

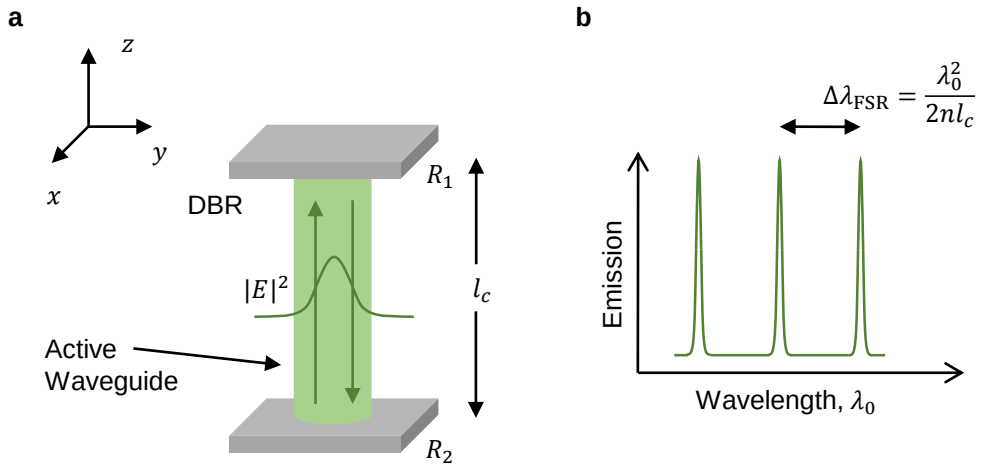

Figure 2.8: **a**, Illustration of a Fabry-Pérot resonator formed by two distributed Bragg reflectors (DBR) with a reflectivity R_1 and R_2 separated by a distance l_c and connected by an optically active waveguide. **b**, Typical emission spectrum of Fabry-Pérot laser comprising longitudinal modes separated by the free spectral range $\Delta\lambda_{\mathrm{FSR}}$.

a lateral in-plane component $k_{||} = \sqrt{k_x^2 + k_y^2}$ and can be expressed as $|\vec{k}| = k_z/\cos\theta$ where θ is the angle to the normal of the resonator plane. Using Eq. 2.33 we can obtain the general dispersion relation for photonic modes in a Fabry-Pérot resonator

$$E = \hbar c_0 |\vec{k}| = \hbar c_0 \sqrt{k_z^2 + k_{||}^2} = \hbar c_0 \frac{m\pi}{l_c n} \cos\theta \ , \tag{2.37}$$

which reveals that resonant modes with a finite in-plane wave vector $k_{||}$ are blue shifted.

2.4.2 Whispering Gallery Mode Resonators

Whispering Gallery Mode (WGM) resonators are not featured in this work, however they constitute an important resonator family for biological and biocompatible lasers and therefore their main concept shall be briefly introduced here. WGM resonators are circularly symmetric resonators that trap light of a certain resonance wavelength along their periphery. The trapping mechanism along the circumference with a radius r relies on repeated total internal reflection (Eq. 2.24) at the resonator surface. Hence, the resonator (usually a dielectric material) in which the light is confined, exhibits a higher refractive index n_i than the surrounding material n_o. If the angle of incidence between trapped light and resonator surface is below the critical angle, total internal reflection occurs. Consequently, due to the circular symmetry of

the resonator, all subsequent reflection events will obey total internal reflection and a standing wave can form if the light is in phase after a round trip. If the optical path length per round trip ($\approx 2\pi n_i r$) is an integer multiple m of the wavelength λ_0, the resonance condition

$$m\lambda_0 \approx 2\pi n_i r \quad \text{with} \quad m \in \mathbb{N}\,, \tag{2.38}$$

is fulfilled. This simple derivation gives a good approximation for resonant modes, however, it does not account for the full electro-magnetic field propagation within the resonator. A more scrutinized approach to this problem can be found in Ref. [78–80], where the Helmholtz equation is analytically solved in spherical coordinates and the contribution of the surrounding refractive index n_o is included.

For large resonators ($r \gg \lambda_0$) the light impinges onto the resonator surface at near glancing incidence ($\theta \approx 90°$) and hence most evanescent losses are small. This gives rise to a comparably large Q-factor for WGM resonators which is desirable for resonators supporting low threshold lasing. Within WGM resonators the Q-factor mainly depends on radiative losses, material absorption, surface scattering and surface contamination [79]. High Q-factors of $> 10^{11}$ have been experimentally reported for spheres acting as WGM resonators [81]. Similarly to guided modes in a dielectric waveguide, the modes within WGM resonators can be of transverse electric (TE) and transverse magnetic (TM) nature which corresponds to the electric field oscillating primarily in the radial and azimuthal direction, respectively. A direct consequence is that TM modes extend further into the surrounding media and are therefore more susceptible to e.g. a refractive index change in the surrounding material. This feature is regularly used for sensing applications [78].

2.4.3 Distributed Feedback Resonators

A popular resonator architecture for both organic and inorganic semiconductor lasers are distributed feedback (DFB) structures. A DFB laser consists of a simple waveguide structure (see Section 2.3.2) in which optical feedback is achieved due to light scattering on an adjacent diffractive structure. This gives rise to an exceptional mode selectivity and offers many pathways for tuning the laser emission wavelength. Furthermore, the fabrication of DFB resonators for lasers based on organic materials is compatible with most solution processing techniques.

DFB Dispersion

A surface grating, as depicted in Fig. 2.9a, can act as a scattering element in combination with a waveguide, coupling in-plane modes into free space. Due to conservation of momentum, the in-plane component (z-component) of the wave vector of the radiated wave k_0 is a superposition of the in-plane modal wave vector k_{mode} and a multiple m of the reciprocal grating lattice wave vector k_G and hence obeys

$$k_z = k_0 \sin\theta = \pm k_{\text{mode}} \pm m k_G \quad \text{with} \quad m \in \mathbb{N}\,, \tag{2.39}$$

where θ describes the scattering angle with respect to the normal of the waveguide surface. Eq. 2.39 is the general dispersion relation for a grating structure and can be expressed in the form

$$\frac{2\pi}{\lambda_0}\sin\theta = \pm\frac{2\pi n_{\text{eff}}}{\lambda_0} \pm m\frac{2\pi}{\Lambda} \quad \text{with} \quad m \in \mathbb{N}\,, \tag{2.40}$$

where λ_0 is the wavelength of the scattered light in free space and Λ the grating period. Eq. 2.40 directly shows a relation between the scattering angle θ and the wavelength λ_0 and hence relates the energy and momentum of scattered light. The photonic dispersion relation of a grating structure can be experimentally determined, by measuring the angle dependent reflection of light from or transmission through it. Two methods for combined angle and spectrally resolved measurements are discussed in detail in Section 3.2. Figure 2.9b shows the calculated dispersion relation for a grating structure with $\Lambda = 350\,\text{nm}$ and $n_{\text{eff}} = 1.60$. The dispersion relation is approximately linear at small angles and mirror-symmetric around 0°. It is important to note that the experimentally determined dispersion relation would differ slightly since the refractive index of the grating and hence the effective refractive index $n_{\text{eff}}(\lambda_0)$ of the mode is dispersive and depends on the wavelength λ_0.

DFB Lasers

The basic principle of DFB lasers relies on the constructive interference of periodically scattered modes within a waveguide. There are two different possibilities to achieve a modulation with a periodicity Λ in a DFB laser. Either through a periodic variation in the refractive index or in the gain profile. Usually, a change in gain profile also induces a change in refractive index and vice versa and therefore in a fabricated DFB laser one typically observes a combination of both.

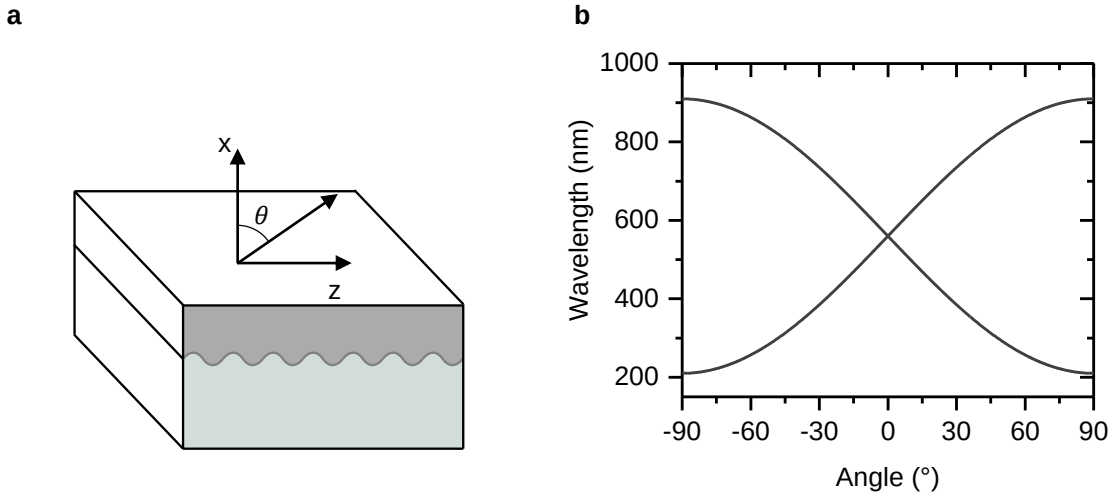

Figure 2.9: **a**, Illustration of a corrugated waveguide structure. The grating couples in-plane modes propagating in z-direction into free space under an angle θ and is known as a distributed feedback (DFB) grating **b**, Dispersion relation for a DFB grating with a period $\Lambda = 350\,\text{nm}$ and a mode propagating with an effective refractive index $n_{\text{eff}} = 1.60$.

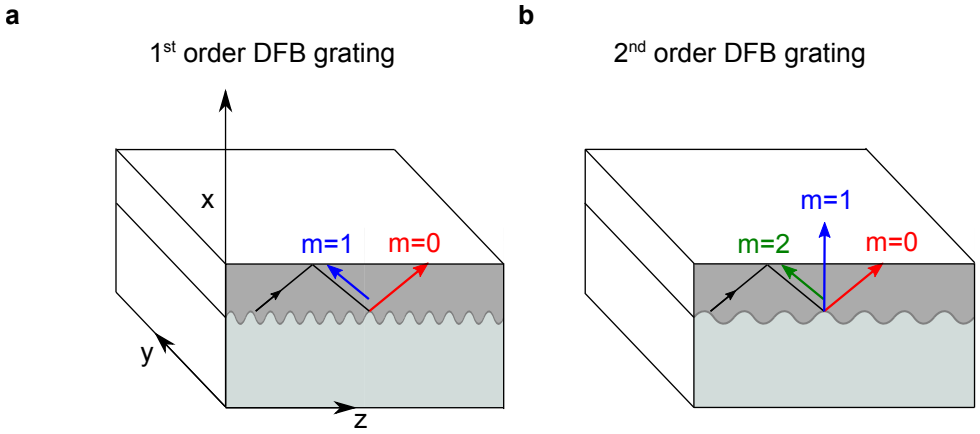

Figure 2.10: Illustration of a first- (**a**) and second-order (**b**) distributed feedback grating. The modulation in a second-order grating is double the period as in a first-order grating. The individual scattering order is denoted as m and the approximate directions are indicated by colored arrows. The second-order grating facilitates out of plane coupling ($m = 1$) whereas the first-order grating only supports in-plane scattering events.

For waveguided modes, constructive interference occurs if the optical path length of the corrugation period in the corrugated waveguide structure is a multiple of half the wavelength of the modes. Thus, the modes undergo Bragg scattering and this can be described by the Bragg condition,

$$m\lambda_B = 2n_{\text{eff}}\Lambda, \quad m \in \mathbb{N}, \tag{2.41}$$

where m is an integer describing the scattering order and λ_B is the wavelength for which the Bragg condition is fulfilled. As already described in Section 2.3.2, the effective refractive index n_{eff} describes the different possible modes in the waveguide structure. The polarization (TE or TM) of a given mode is not specifically addressed in Eq. 2.41 but accounted for within the effective refractive index n_{eff} and the wavelength λ_B. It is possible to estimate the laser emission wavelength λ_{lase} of a DFB laser by $\lambda_{\text{lase}} \approx \lambda_B$. The reason for possible deviations between the lasing wavelength and the Bragg wavelength are discussed below. When designing a DFB laser it is further important that λ_B is within the spectral gain region of the active material. In contrast to lasers based on Fabry-Pérot cavities and WGM resonators, single mode operation in DFB lasers is achievable by relatively simple optical design according to Eq. 2.41. The emission wavelength can be tailored by changing the effective refractive index n_{eff}, the grating period Λ and the spectral gain region of the active material. Especially the effective refractive index n_{eff} depends on many device parameters, such as the thickness t and refractive index n of the individual layers as well as the wavelength and polarization of the resonant wave and can thus be used to precisely control the emission wavelength.

The two most common DFB laser designs are based on so called first- and second-order DFB gratings. Figure 2.10a shows an illustration of a first-order DFB laser where light that undergoes first-order diffraction ($m = 1$) is backscattered into the waveguide. This process is known as distributed feedback and gives rise to counterpropagating waves within the waveguide structure, which grow in the presence of gain and feed energy into each other by means of Bragg scattering. In organic semiconductor lasers, the core layer typically consists of a light emitting organic semiconductor which is deposited on top of e.g. a polymer grating structure. By optically exciting the organic semiconductor, gain is provided and light amplification is supported by the DFB structure. The laser emission generated in a first-order DFB laser is intrinsically guided to the end facets of the waveguide. This is desirable for integrated photonics applications of organic DFB lasers where light needs to be coupled to an adjacent waveguide [82–84].

Figure 2.10b shows an illustration of a second-order DFB laser. This structure relies on a similar feedback mechanism when compared to a first-order grating. However, in this structure the first-order ($m = 1$) diffraction is perpendicular to the waveguide surface and the second-order diffraction ($m = 2$) is responsible for counterpropagating modes and hence feedback. The first-order diffraction in a second-order DFB laser therefore constitutes a loss channel since light is effectively extracted from the waveguide. By combining first- and second-order DFB laser sections, it is possible to fabricate a so called mixed-order grating. Here, a small section of a grating that is resonant in second-order is placed in the center and surrounded by a grating structure with half the period that is hence resonant in first-order. Following this strategy, the low losses from first-order lasers are combined with efficient light extraction from second-order devices [85, 86]. The work presented in this thesis mainly features second-order and mixed-order DFB gratings.

Coupled Wave Theory

Equation 2.41 shows how different device parameters can be used to tune the emission wavelength of a DFB laser. However, it does not describe the actual feedback mechanism nor reveal the prerequisites for low thresholds lasing. A mathematical description of distributed feedback laser modes has been presented by Kogelnik and Shank in 1972 and is called coupled wave theory [87]. This approach does not describe all the processes found in real DFB laser device but offers an intuitive and simplified description of the the complex interplay between a corrugated structure and its emission characteristics. One important simplification is the assumption of an almost homogeneous propagation medium that only shows a periodic perturbation. In other words, the model does not describe the presence of an underlying waveguide structure. Considering a mode propagating in the z-direction, a spatial variation of the refractive index $n(z)$ is described by the periodic perturbation expression

$$n(z) = n + \Delta n \cos\left(\frac{2\pi}{\Lambda} z\right) , \tag{2.42}$$

where n is the average refractive index of the medium and Δn the amplitude of the spatial modulation of the refractive index. Similarly, a periodic spatial variation in the gain profile $g(z)$ can be expressed as

$$g(z) = g + \Delta g \cos\left(\frac{2\pi}{\Lambda} z\right) , \tag{2.43}$$

where g is the average gain of the medium and Δg the amplitude of the spatial modulation of the gain profile. Taking Eq. 2.19 and assuming a harmonic time varying field $E(z,t) = E(z)\exp(i\omega t)$ yields the Helmholtz equation

$$\partial_z^2 E + k^2 E = 0 \,. \tag{2.44}$$

If the Bragg condition Eq. 2.41 is fulfilled with substituting $n \rightarrow n + igc_0/\omega$, the periodic variation of refractive index (Eq. 2.42) and gain (Eq. 2.43) are contained in the wave vector k by

$$k^2 = \beta^2 + 2ig\beta + 4\kappa_{\mathrm{DFB}}\beta\cos\left(\frac{2\pi}{\Lambda}z\right) , \tag{2.45}$$

where $\beta = n\omega/c_0 = 2\pi n/\lambda_0$ and we assumed that the gain is small over distances of the order of a wavelength ($g \ll \beta$) and that the perturbation of refractive index ($\Delta n \ll n$) and gain ($\Delta g \ll \beta$) are small. The coupling coefficient κ_{DFB} is defined by

$$\kappa_{\mathrm{DFB}} = \pi\frac{\Delta n}{\lambda_0} + i\frac{\Delta g}{2} , \tag{2.46}$$

and is a measure for the strength of the backward Bragg scattering process and hence the amount of feedback (per unit length) provided by the grating. The electric field E within the DFB structure is composed of two counterpropagating waves R and S which grow due to the presence of gain and exchange energy by means of Bragg scattering. Hence, the electric field in the DFB structure can be written as the sum

$$E(z) = R(z)\exp(-i\beta z) + S(z)\exp(i\beta z) \,. \tag{2.47}$$

For further calculations, we assume that the amplitude of these waves are varying slowly and hence their second derivatives $\partial_z^2 R$ and $\partial_z^2 S$ can be neglected. Inserting Eq. 2.47 into the wave equation (Eq. 2.44) yields a pair of coupled wave equations of the form

$$\begin{aligned} -\partial_z R(g - i\delta)R &= i\kappa_{\mathrm{DFB}} S \\ \partial_z S(g - i\delta)S &= i\kappa_{\mathrm{DFB}} R \,, \end{aligned} \tag{2.48}$$

where $\delta \approx \beta - \pi/\Lambda$ is a measure for the deviation of the wavelength from the Bragg resonance. Assuming a structure with a length L (for example by optical excitation with a pump spot of

diameter L), the set of differential equations 2.48 yields a resonance condition

$$\kappa_{\mathrm{DFB}} = \pm i \frac{\gamma}{\sinh(\gamma L)} , \tag{2.49}$$

where γ is the complex propagation constant of a mode and for each eigenvalue γ a corresponding threshold gain constant g and resonance frequency can be found from the relation

$$g - i\delta = \pm i \kappa_{\mathrm{DFB}} \cosh(\gamma L) . \tag{2.50}$$

Hence, for a given coupling κ_{DFB} and device length L, the above equation yields a characteristic threshold gain and resonance frequency for each mode.

For a DFB structure entirely based on refractive index modulation ($\Delta g = 0$), the allowed modes are clustered symmetrically around the Bragg wavelength λ_B with a mode spacing $\Delta\lambda_{\mathrm{FSR}} \approx \lambda_0^2/2nL$. This is similar to the free spectral range for the aforementioned Fabry-Pérot resonator. Interestingly, at the Bragg wavelength λ_B no mode is supported due to the formation of a photonic stop band of width [88]

$$\Delta\lambda_{\mathrm{gap}} = \frac{\kappa_{\mathrm{DFB}} \lambda_B^2}{\pi n_{\mathrm{eff}}} . \tag{2.51}$$

It is further found that the threshold condition Eq. 2.50 for the case of pure refractive index modulation can be simplified to

$$\frac{\exp(2g_M) M^L}{g_M^2 + \delta_M^2} = \frac{4}{\kappa_{\mathrm{DFB}}^2} , \tag{2.52}$$

where M describes the mode number. The above equation suggests that modes with the same deviation from the Bragg resonance $|\delta_M|$ have the same threshold gain. In this case, the two modes appearing symmetrically on either side of the stop band are closest to the Bragg resonance and show the lowest threshold. Furthermore, Eq. 2.52 indicates an increase in threshold with increasing mode number M [88]. For pure gain modulation ($\Delta n = 0$), no stop band exists and hence the mode with the lowest threshold appears exactly at the Bragg resonance. Similarly, to DFB lasers with index coupling, the free spectral range is $\Delta\lambda_{\mathrm{FSR}} \approx \lambda_0^2/2nL$.

In real DFB lasers the modulation is neither purely based on gain nor refractive index mod-

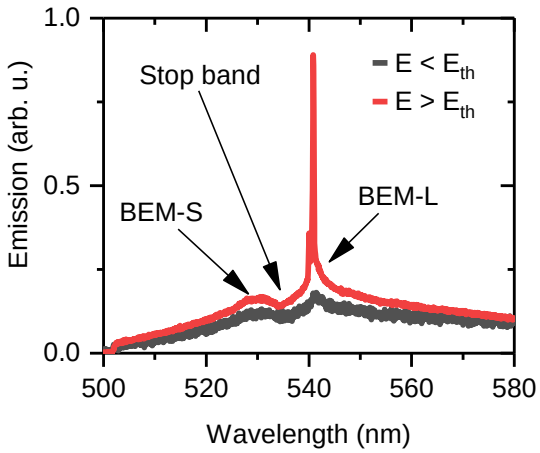

Figure 2.11: Typical emission spectrum from a second-order distributed feedback (DFB) laser below (gray) and above (red) the lasing threshold. The spectral position of the stop band, the band edge mode at the short wavelength edge (BEM-S) and at the long wavelength edge (BEM-L) of the stop band are marked. These example spectra were obtained from a second-order DFB membrane laser based on the conjugated polymer $F8_{0.9}BT_{0.1}$ as described in Chapter 7.

ulation but a combination of both. Hence, due to the presence of refractive index modulation a stop band appears. Kazarinov and Henry presented an equivalent DFB theory for second-order waveguide structures in 1985 [89].

The creation of a stop band in a second-order DFB laser can also be understood by considering the interference effects within the DFB structure. At the Bragg resonance, the counterpropagting modes interfere and build a standing wave with a periodicity $\Lambda/2$. Due to symmetry considerations, two standing wave patterns are supported that have nodes at either the maxima and minima, or at the shoulders, of the periodic components of the grating [90]. Hence, the two modes have a different energy and the energy difference is equal to the width of the stop band $\Delta\lambda_{gap}$. Within the stop band, guided modes always interfere destructively and hence can not propagate in the waveguide [91]. As an example, Figure 2.11 shows an emission spectrum of an organic DFB laser based on a conjugated polymer gain material. The spectrum features a stop band, a band edge mode at the short wavelength edge of the stop band (BEM-S) and a band edge mode at the long wavelength edge of the stop band (BEM-L). The occurrence of the laser mode at the long wavelength edge of the stop band and hence reduced gain requirements at this energy can be attributed to the difference in spatial distribution of the standing wave fields relative to the corrugation. For the higher energy mode

(BEM-S), the field maxima are vertically displaced, while for the lower energy mode (BEM-L), the maxima lie in the same horizontal plane compared to the average grating plane [90]. The difference in spatial distribution leads to a preferred outcoupling of the higher energy mode whereas the lower energy mode couples less well to radiation and thus experiences higher net gain [91].

2.5 Biological Lasers

A general overview of the basic properties and recent developments of biological lasers is given in this section.

First, in Section 2.5.1, a brief introduction to organic lasers, which provide the basis for most biological lasers, is given. Next, typical resonator architectures and gain materials, utilized for biological lasers are introduced in Section 2.5.2. Subsequently, in Section 2.5.3, optofluidic biological lasers are discussed which are the most common biological laser type to date and are operated in a fluidic environment typical for biological processes. Many biological events, however, happen within cells or organizational units of cells and therefore single cell and tissue lasers and their applications are introduced in Section 2.5.4. Many of the aforementioned biological lasers rely on fluorescent proteins as the gain material. In the context of lasers they constitute a novel and interesting solid-state gain material class, as will be discussed in Section 2.5.5.

2.5.1 Organic Lasers

While this thesis relies on laser devices based on organic light emitting materials, the main motivation was not to further develop and improve conventional organic lasers but to investigate their potential in the realm of biology. Therefore, only a brief overview on the state-of-the-art in organic lasers shall be given.

Shortly after the first demonstration of lasing action in a ruby crystal by Maiman [5], the first organic light emitting materials were utilized as gain materials in optically pumped dye lasers [8]. These devices required a constant dye flow to replenish photo bleached molecules or those in long-lived triplet states with unexcited molecules in the pump spot region [92]. Despite being relatively complex and expensive systems, dye lasers have played a key role in many research fields and amongst other achievements have contributed significantly to the generation of ultra short pulses [93]. In recent years, the advances in microfabrication and

microfluidic techniques [94, 95] has fostered the emergence of much smaller and cheaper optofluidic dye lasers which show great potential for lab on a chip devices [37, 96, 97] and even allow for continuous wave (CW) lasing operation without externally driven dye circulation [98].

The earliest demonstration of an optically pumped solid-state organic laser dates back to the 1990s [16–18]. These lasers have attracted substantial interested due to some interesting properties and applications, such as tunable lasing emission by altering the resonator [99, 100] and the chemical composition of the gain material [19]. Here, the broad gain spectrum of organic light emitting materials facilitates wavelength tuning and allows higher tolerances in the fabrication of resonator structures when compared to narrow band inorganic emitters. Furthermore, the required pump powers to reach lasing operation can be extremely low [101–104], which can in part be attributed to the good photoluminescence quantum yield of the organic light emitting materials [20, 21]. Despite relying on highly efficient organic gain materials, most organic lasers have to be optically pumped by external inorganic laser devices. However, a few low threshold solid-state organic laser excited by an integrated inorganic nitride light emitting diode have been demonstrated, e.g. Ref. [105].

A long-standing pursuit is to build an electrically driven organic laser, which is also considered the holy grail in the field of solid-state organic lasers. Among other factors, the required high excitation rates which result from short excited-state life times and a low charge carrier mobility in organic materials have so far prevented the implementation of electrical pumping in organic lasers [106]. Continuous wave operation is considered a stepping stone towards electrically driven organic laser devices since both excitation pathways share common challenges, such as extensive triplet creation due to intersystem crossing [107]. Recently, Jia *et al.* [108] provided evidence for real continuous wave lasing operation for up to one hour from a DFB laser incorporating an organic-inorganic lead halide perovskite gain material that undergoes a dynamic phase change. While the demonstration of continuous wave operation is exciting, the device required cooling to roughly 100 K, limiting real life applications.

While organic lasers show only modest output powers compared to their inorganic counterparts, they are potentially useful in analytical systems. For example, organic laser devices have been used as light sources for on chip Raman spectroscopy [84, 109]. Furthermore, organic lasers can be used as chemosensors that react to minute traces of explosives and

drugs [110, 111], effectively quenching excitons and reducing the gain. In the future, organic lasers may be used in integrated photonic circuits [112] and for short distance, light based data communication [113]. The possibility of producing organic lasers on a large scale [114] further offers the possibility for potentially cheap and disposable devices.

2.5.2 Biological Gain Materials and Resonators

Biological lasers are devices that incorporate biological materials as the gain material or resonator structure. Furthermore, there are also laser devices which rely on gain materials or resonators that are not biorelated but which can be used in close proximity to biological media without altering their functionality and are therefore called biocompatible lasers. All biological gain materials reported so far are based exclusively on organic light emitting materials while gain materials for biocompatible lasers can be made of organic or inorganic materials. Advanced micro-fabrication technologies have enabled the realization of a broad range of biological and biocompatible cavities for laser devices, such as planar Fabry-Pérot resonators based on dielectric [115] and metal mirrors [116], micro-sphere resonators [31], micro-ring resonators [117], DFB resonators [27, 118], photonic crystals [119] and random feedback structures [120, 121]. Figure 2.12 shows a selection of feedback structures that can be combined with biological gain materials or can be fabricated from biological materials and be used as biological or biocompatible lasers. Lasing has been shown from natural biological gain materials, such as fluorescent proteins [29–31], pigments [117, 122], luciferins [123] and vitamins [27, 28]. Furthermore, quantum dots [124, 125], dyes [97], and even fluorescently labeled DNA strands [32] have been used as a gain material for bioinspired and biocompatible laser devices.

Most examples mentioned above either incorporate a resonator structure or a gain material consisting of a biological material. In order to facilitate an increased biointegration, considerable efforts have been made to demonstrate laser systems that are fully biological. For example, a silk based DFB resonator with riboflavin (vitamin B_2) as the gain material and biodegradable fluoresceine salt stained protein microsphere lasers have been developed [126, 127]. All biological lasers introduced so far are optically pumped, typically utilizing an inorganic pump laser source. Recently, it was attempted to realize a biological laser device where even the excitation energy is provided by an integrated biomaterial. Humar *et al.* [128] coated a polystyrene microsphere with bioluminescent luciferins acting as the gain material. However,

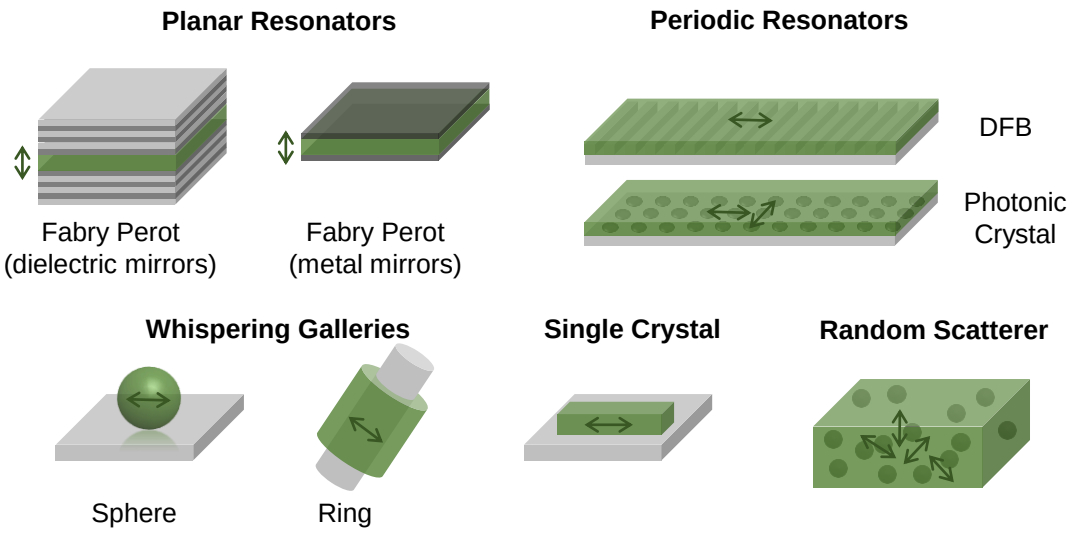

Figure 2.12: Illustration of different feedback structures used for biological lasers. In planar resonators the gain material is sandwiched between two highly reflective dielectric or metal mirrors. At least one mirror is partially transparent in the spectral gain range to allow for light extraction from the resonator. In periodic structures, such as distributed feedback gratings or photonic crystals, feedback is generated by regular and repeated scattering due to gain or refractive index modulation. Whispering gallery resonators are the most common resonator class for biological lasers and so far show the highest Q-factors of all resonators presented. The ring resonator can also be operated evanescently, with a fluidic gain material being pumped through the center. Single crystals rely on the same feedback mechanism as planar resonators but the reflecting surfaces are formed directly between crystal and surrounding. Random scatterer structures can facilitate lasing via random scattering of light rather than by deterministic resonant feedback.

the light emitted from the luciferins did not provide sufficient energy to achieve lasing in the microspheres but only supported relatively noisy sub-threshold emission from WGMs.

2.5.3 Optofluidic Biological Lasers

Depending on the application, the gain material for biological lasers can be in a condensed solid-state or in a fluidic phase. The fluidic phase is the natural environment for most biological processes and experiments, and consequently fluidic biolasers may be used for sensitive bioanalysis. Many bioanalysis assays rely on the fluorescence signal emitted by dyes and fluorescent proteins that are fused to certain biomolecules. Upon molecular interaction of the host molecule, the intensity or spectral position of the emission originating from the fluorescent probes is altered and hence can be studied to investigate the underlying biological process. The fluorescence signal, however, might often not be detectable due to an omnipresent autofluorescence background [36]. Figure 2.13a shows that a typical fluorescence signal increases linearly with the excitation signal and the emitted spectrum is rather broad, making it difficult to detect minute spectral changes. To overcome this limitation, the fluorescent biological material can be placed inside a resonator structure and hence due to stimulated emission and optical feedback the sensing signal is converted into laser emission (see Fig. 2.13b). The enhanced laser sensing signal is more susceptible to small changes in the gain material induced by the underlying biological processes when compared to the fluorescence signal. In fact, due to the enhanced signal-to-noise ratio, the dynamic range of a laser-based detection scheme is increased by $1-3$ orders of magnitude when compared to fluorescence-based detection schemes [129, 130]. Observing and recording characteristic laser properties such as the emission spectrum, transverse mode profile, threshold behavior, stability and directionality gives key insight into the laser system and hence the biological host material.

One of the earliest examples of a fluidic biological laser device, has been realized by Hänsch *et al.* [131] by dissolving fluorescein disodium in a droplet of gelatin. Optical excitation of the fluorescein led to the creation of lasing WGMs in the gelatin droplet. In fact, this was the first “edible” laser. While this project was mostly curiosity driven and had no immediate applications, biological lasers developed in the last decade are getting increasingly relevant for biomedical research purposes and clinical applications. An interesting example is an optofluidic Förster resonance energy transfer (FRET) laser based on protein pairs linked by length tunable peptides [30]. In this device, a solution containing the linked protein pairs is pumped

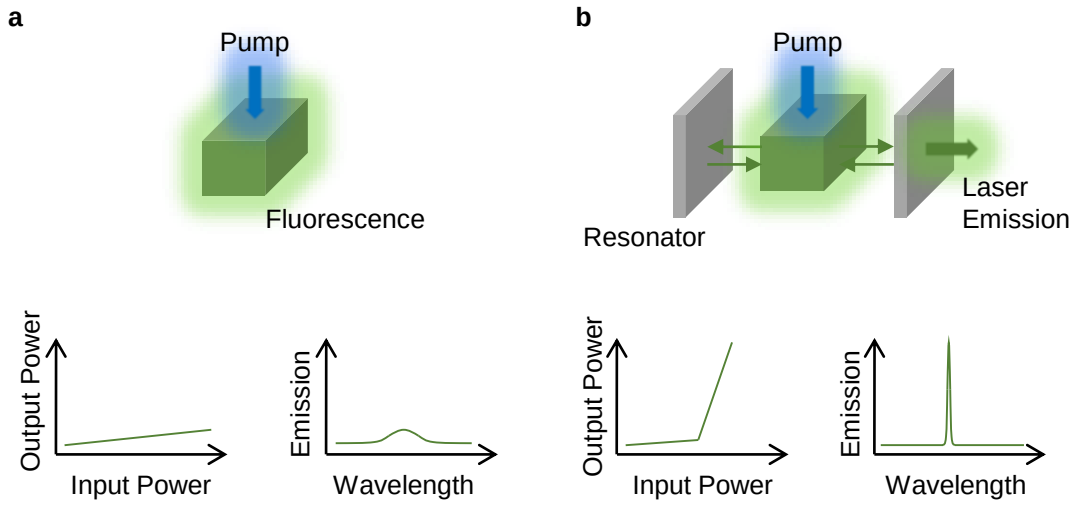

Figure 2.13: Illustration of the general set up, typical input-output characteristics and emission spectra of **a** fluorescence and **b** laser based detection schemes for bioanalysis. Adapted from Ref. [36].

through a ring resonator ($Q > 10^7$) and the lasing emission upon excitation is investigated. This work constitutes a new approach to quantify protein interactions and - with further development - may provide important insight into protein-protein interactions and protein-drug interactions. Using a similar resonator structure, Chen *et al.* [132] developed a laser based on an U.S. Food and Drug Administration (FDA) approved near-infrared dye dissolved in whole human blood which can be used to discriminate between and investigate the major serological components of blood. This work may mark a critical step toward biomedical clinical applications of optofluidic biological lasers.

2.5.4 Cell and Tissue Lasers

The laser devices discussed above rely on the generation of laser light from biological molecules that are extracted from cells or tissue. However, the study of stimulated emission directly from more complex biological hierarchies, such as cells or tissue, has gained substantial interest in the last two decades and evolved from random lasing in dye stained animal tissue [133] to the development of a single cell biological laser [33, 34]. The latter is a laser based on a single live cell that produces its own gain medium (eGFP) and is suspended between two highly reflective mirrors forming a Fabry-Pérot resonator. Since the resonator structure is located outside the cell, this single cell laser can be classified as an extracellular laser. To generate laser emission, the structure is optically excited with ns-pulses for which the required threshold pump

energy to achieve lasing is in the nJ-range and therefore orders of magnitude below the onset for photo-induced damage to the cell [33, 134]. The obtained laser emission originating from the cell shows all characteristics expected from a Fabry-Pérot resonator architecture and can be used to study intracellular properties. For example, the spectral position of different longitudinal and transverse laser modes can be monitored to analyze changes in the osmotic pressure of a cell [38]. Interestingly, due to the refractive index contrast between cell and the surrounding medium, the cell acts as a biological convex lens and stabilizes the resonator configuration [38]. Very recently, an integrated microwell array platform based on the extracellular single cell laser concept was realized for automated cell laser studies [135]. The previously introduced biological cell laser devices are based on laser emission from individual single cells. However, in reality, cells are embedded into an extracellular matrix forming cell compounds and tissues. In a recent study, a new biological tissue laser was realized by placing dye stained tissue pieces into a Fabry-Pérot cavity [35]. A subsequent study investigated the feasibility of this structure for a laser emission based cancer screening and immunodiagnosis involving nuclear biomarkers [39].

By utilizing more compact resonator architectures it is further possible to introduce the resonator inside the cell. Since the resonator is internalized by the cell, this single cell laser can be classified as an intracellular laser. It was shown that the spherical dye stained polystyrene WGM resonators discussed in Section 2.4.2 can be introduced into live cells via a natural cellular process called phagocytosis and be operated as optically pumped intracellular lasers. The formation of lasing in WGM resonators relies on the refractive index contrast between polystyrene (1.6) and cell ($1.37-1.39$) and is supported even in spheres with diameters below $15\,\mu$m under optical excitation with sub nJ-pulses. The emitted laser spectrum is strongly dependent on the size of the sphere and small inherent size differences between spheres lead to unique emission spectra which can be exploited for cell tagging. If a sphere is internalized by a cell, the emission spectrum can be used as an optical barcode label for reidentification among a culture of other tagged cells [40]. It was further shown, that the spheres can be introduced into many different cell types and be used for tagging several generations of cells [42]. Next to their tagging capability, intracellular microsphere resonators can also be used for sensing the intracellular refractive index [41]. Lasing emission was further demonstrated from adipocytes (fat cells) without the need for introducing a resonator structure. These cells naturally contain a large lipid vesicle which can be stained with a lipophilic dye and be operated

as an intracellular WGM laser [41].

2.5.5 Solid State Biological Lasers

The biological laser devices discussed above are operated in aqueous or at least fluidic environments, mimicking biologically relevant settings. However, some biological materials additionally offer unique solid-state photo physical properties interesting for laser devices and thus present an alternative material platform when compared to conventional organic semiconductors (e.g. conjugated polymers or small molecules). Especially, solid-state fluorescent protein films show unique light emitting properties in terms of concentration and bi-molecular quenching. This has been exploited to build a bio-integrated eGFP humidity laser sensor in which the gain is altered by a change of the intermolecular separation due to variations in humidity [29]. The resonator architecture for this type of laser sensor is a ring resonator simply formed by coffee stain effect based self assembly [136].

Using a solid-state eGFP film as the gain material in a Fabry-Pérot resonator (formed by two highly reflective DBR mirrors) results in a > 100 fold reduction in laser threshold (82 pJ) when compared to solution based eGFP [29, 33, 137] in the same cavity, providing evidence for stable fluorescence emission even at high concentrations. These devices can be conveniently used for on-demand fabrication of complex photonic structures by controlled and spatially confined photobleaching of the fluorescent protein solid-state film with a high power laser. It was shown that this approach allows for stimulated emission from solid-state fluorescent proteins in three-dimensionally confined photonic boxes with lasing thresholds outperforming unstructured planar resonator architecture [44]. Recently, fluorescent protein solid-state films in Fabry-Pérot cavities have been utilized to facilitate strongly coupled systems [138]. Here, excitons couple to cavity photons, forming new quasiparticles (polaritons) which are able to relax into a Bose Einstein condensate even at room temperature [43]. Furthermore, there is experimental evidence for lasing from fluorescent protein crystals [139].

3

Experimental Methods and Materials

In this chapter, the experimental practices and methodologies that are common throughout the thesis are introduced and discussed. This includes the fabrication and characterization of solid-state thin films and nanostructured gratings. Furthermore, the relevant gain materials and common methods for their optical characterization are described.

In Section 3.1.1, a widely used method to produce solid-state thin films is discussed and Section 3.1.2 describes, how optical and structural properties of the aforementioned thin films can be obtained. Next, in Section 3.1.3, it is shown how these methods together with ultraviolet nanoimprint lithography (UV-NIL) can be used for fabricating nanostructured polymer gratings. The optical and structural properties of fabricated polymer gratings are discussed in Section 3.1.4. The gratings are used as an integral part of distributed feedback (DFB) lasers and Section 3.2 introduces the optical characterization setup for these devices. Lastly, the processing parameters and chemical and optical properties for different gain materials used throughout this thesis are summarized in Section 3.3.

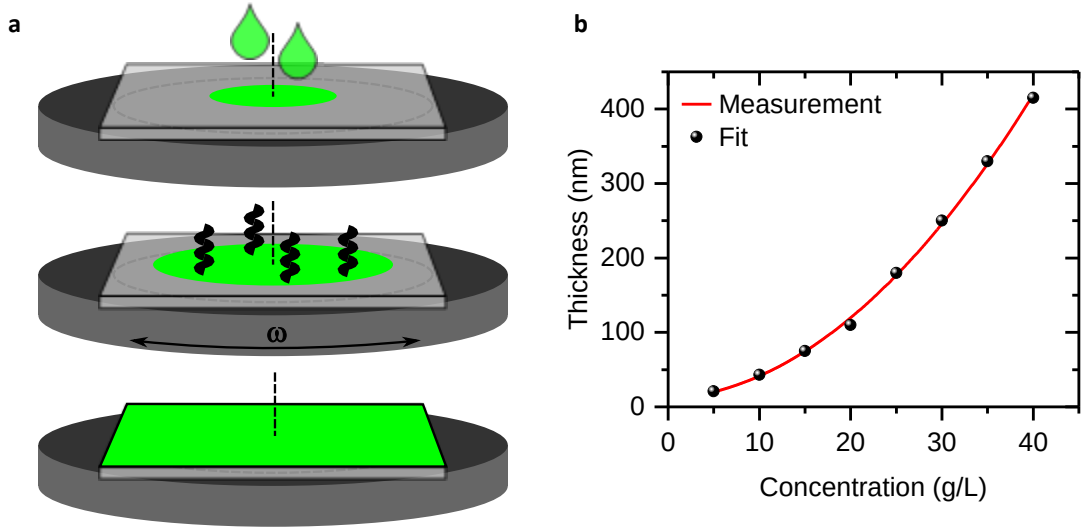

Figure 3.1: Spin-coating procedure. **a**, Illustration of the spin-coating process where an organic semiconductor solution is deposited on a substrate. A thin film is formed by rotating the substrate with an angular frequency ω while the solvent evaporates. **b**, Thickness of a spin-coated conjugated polymer film (polyfluorene co-polymer, F8BT) depending on the concentration of the initial polymer solution.

3.1 Fabrication of Organic Thin Films and Resonator Structures

3.1.1 Solution Processing

Depending on the organic material, there are a variety of different methods to obtain solid-state thin films. For example, small molecule thin films can be conveniently grown by organic vapor phase deposition or thermal evaporation in high vacuum [140]. Most materials used in this work, however, are conjugated polymers or fluorescent proteins, which have molecular weights that are too high to allow transition into gas phase. Instead, solid-state thin films are usually obtained by solution processing techniques. This is possible since most polymers have long hydrocarbon side chains, which make them soluble in a large variety of organic solvents. Fluorescent proteins in contrast are water soluble since H_2O molecules bind to the protein. Throughout this thesis most solid-state thin films were deposited by spin-coating. This is a widely applied method for small scale production especially in experimental research since it allows reproducible production of thin films with a thickness of $\sim 5\,\text{nm}$ accuracy. Other commonly used wet processing techniques for polymers from solution are inkjet printing and blade coating [141, 142].

Figure 3.1a shows an illustration of the spin-coating process. A flat square glass substrate

(1 cm × 1 cm) is placed on a metal chuck and fixed in place by a vacuum pump. Depending on the polymer solution, $\sim 100\,\mu$L are deposited on top of the substrate. In a next step, the substrate is rotated at an angular frequency ω (typically between 1000−4000 rpm, revolutions per minute) for a fixed period of time (typically between $30-120$ s). During the spin-coating process, due to centrifugal forces, the material spreads out on the substrate surface and excess solution flies off the substrate at the edges. At the same time, the organic solvent evaporates and after spin-coating the substrate is coated with a thin solid-state polymer film. Usually, spin-coated films show a uniform thickness across the central region with an edge bead forming at the perimeter of the substrate [143].

The thickness d of the polymer film depends on the angular frequency ω, the concentration C and the viscosity η of the initial solution by [144]

$$d \sim C\sqrt{\frac{\eta}{\omega}}\,, \tag{3.1}$$

which is an empirically found relation. Since the thickness of the polymer film depends on the square root of the angular frequency, this parameter can be used to accurately control the thickness. The linear relation between thickness and concentration gives a coarse adjustment of the thickness. It is important to point out, that this dependency is not exactly linear since a change in concentration also influences the viscosity of the solution. This can be seen in Fig. 3.1b where the thickness of a polyfluorene co-polymer (F8BT) film spin-coated from a toluene solution with different concentrations is shown. The fit to the data points suggests a square root dependency rather than a linear dependency between film thickness and solution concentration, confirming the influence of the change in viscosity with concentration.

Spin-coating was used throughout this work to fabricate all polymer films. Furthermore, we used spin-coating to obtain solid-state fluorescent protein films from an aqueous solution. Spin-coating was performed in air in a clean room environment to improve the film quality by avoiding particle defects.

3.1.2 Thin Film Characterization

Stylus Profilometer

In order to obtain the thickness of various polymer and fluorescent protein films, a Dektak 150 Surface Profilometer (Veeco) was used. This method relies on a needle with a diamond

tip that is brought into contact with the sample surface under a controlled force. By scanning the needle across the sample surface, piezo-motors and a feedback loop are used to achieve a constant contact force and adjust the height of the tip yielding a topological height map of the thin film. In order to measure the thickness of individual layers, the polymer film needs to be scratched prior to the measurement. The depth of the scratch can be measured with an accuracy of $\sim 5\,\text{nm}$.

Since this is an invasive method, it is usually performed on reference samples or on samples that have been optically characterized and are not needed anymore. Further, it is important to point out, that the direct contact with the diamond tip may introduce additional scratches into a soft thin film, yielding an incorrect height measurement. This effect can be observed in particularly soft samples like fluorescent protein solid-state films. The validity of a height measurement can be assessed by performing multiple subsequent line measurements at the same sample position.

Spectroscopic Ellipsometry

An alternative method to measure the thickness of thin films is variable angle spectroscopic ellipsometry (VASE). In addition to the film thickness, VASE provides the optical properties (refractive index and extinction coefficient) of thin films. These are particularly important for optical modeling of devices. In contrast to the surface profilometer, VASE is a non-destructive contactless method [145]. It relies on a linearly polarized beam of monochromatic light which is reflected by the thin film and collected by a photodetector with a rotating polarizer attached to it. Hence, the change in amplitude and phase of the polarization of the reflected light can be measured. Using a broadband light source in combination with a monochromator allows to tune the wavelength of light, here between $200-1700\,\text{nm}$. One can also accurately adjust the angle of incidence. Using optical modeling and data-fitting, the complex refractive index $\tilde{n} = n + i\kappa$ of the material can be calculated. Generally, in a first step the film thickness is fitted using a Cauchy model and subsequently the optical constants are fitted utilizing a general oscillator model [146]. Furthermore, VASE can be used to determine the optical anisotropy of thin films, which provides information on the alignment of molecules. Typically, thin films composed of small molecules and fluorescent proteins are isotropic whereas polymer thin films are anisotropic. This can be explained by the tendency of polymer chains to lie in-plane due to shear alignment during the spin-coating process [147].

All VASE measurements presented in this thesis were carried out on a J. A. Woolam Co. Inc. M2000-DI ellipsometer by Laura Tropf and Guy Whitworth.

3.1.3 Grating Fabrication

Polymer DFB gratings (see Section 2.4) were produced using ultraviolet nanoimprint lithography (UV-NIL) in a clean room environment. UV-NIL is a low-cost soft lithography process which can be used to fabricate 1D and 2D sub-wavelength polymer structures in a reproducible manner [148, 149]. The grating fabrication was predominantly performed on an EVG620 (EV group) photomask aligner with a custom nanoimprint unit.

Figure 3.2 shows the two-step process flow for grating fabrication. In a first step, a soft nanostructured stamp is fabricated from a master grating ($1.1-1.3$ in Fig. 3.2) containing the final structure. The master grating was fabricated on a silicon wafer by a commercial provider (Kelvin Nanotechnology Ltd), using electron beam lithography and fluorine based ion etching to define the sub-wavelength structures. To prepare the soft stamp, a thin primer layer (3-(Trimethoxysilyl)propyl acrylate, 4045X, Solvay) is spin-coated on an oxygen plasma cleaned glass carrier substrate. This layer increases the adhesion between soft stamp material and glass substrate. Next, a UV curable perfluoropolyether (MD700, Solvay) is drop casted onto the primer layer and pressed into the master grating structure by hand before being exposed to UV light ($\lambda = 365\,\text{nm}$, dose $56\,\text{mW}\,\text{cm}^{-2}$) for 250 s. The soft stamp thickness ($\sim 0.2\,\text{mm}$) was controlled using metal spacers (three washers) and the final stamp can be used to fabricate multiple grating samples.

In a next step, the soft stamp is used to replicate the master grating into a nanoimprint resist ($2.1-2.3$ in Fig. 3.2). First, a thin adhesion promoter (mr-APS1, Micro Resist Technology, $10-20\,\text{nm}$) is spin-coated onto an oxygen plasma cleaned transparent substrate and baked at 150 °C for 60 s. As will be presented in Chapter 5, the substrate material is either glass, MgF_2 or SiO_2. In a next step, a liquid UV curable polymer solution is spin-coated onto the adhesion promoter and subsequently baked. The spin-coating and baking parameters and hence the layer thickness depend on the type of polymer resist. For this work, mr-UVCur06, mr-UVCur21 and mr-NIL210 (all Micro Resist Technology) were used according to the manufacturer's guidelines (in brief, mr-UVCur06 was spin coated at 4000 rpm for 60 s and baked at 100 °C for 20 s, mr-UVCur21 was spin coated at 3000 rpm for 60 s and baked at 100 °C for 20 s and mr-NIL210 was spin coated at 3000 rpm for 30 s and baked at 100 °C for 60 s). Next,

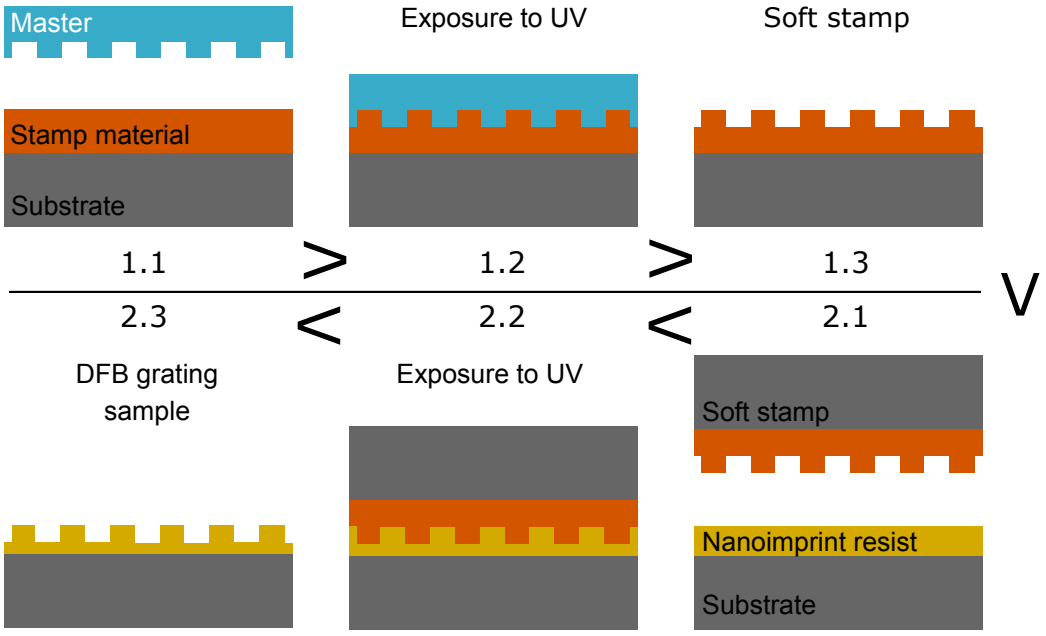

Figure 3.2: Illustration of the two step UV nanoimprint lithography process. In the first step 1.1 – 1.3, a soft stamp containing a negative of a nanostructured grating master is formed. In the second step 2.1 – 2.3, this soft stamp is used to imprint the grating structure into a UV curable polymer resist.

the soft stamp is pressed into the polymer resist layer with a constant pressure of 950 mbar and cross-linked by UV exposure ($\lambda = 365\,\text{nm}$, dose $56\,\text{mW}\,\text{cm}^{-2}$) at room temperature for 250 s. Lastly, the soft stamp is separated from the polymer resist post exposure, leaving a copy of the silicon master structure. The thickness of the residual layer can be controlled by mixing a thinner material (mr-T 1070, Micro Resist Technology) to the initial polymer resist solution, effectively reducing the initial concentration.

In order to use the polymer gratings as a resonator structure for laser devices, a gain material needs to be added. In this thesis three different options are explored. The results presented in Chapter 5, rely on depositing an aqueous solution of a liquid gain material (a laser dye as discussed in Section 3.3.2) directly on top of the grating structures. In Chapter 7 and 6, a solid-state film consisting of light emitting conjugated polymers and fluorescent proteins, respectively, is spin-coated onto the gratings. In either case, the periodic structure defined by the polymer grating is also resembled in the gain material.

3.1.4 Grating Properties

The optical and structural properties of the grating structures directly influence the properties of the emitted light. For example, the refractive index of the grating structure effects the effective refractive index of the waveguided mode and hence the wavelength of the emitted light. This work features the three different photo-curable resist formulations, mr-UVCur06 (Chapter 5), mr-UVCur21 (Chapter 7) and mr-NIL210 (Chapter 6). They are all purely organic components with no silicon content. The reason for using different materials was mainly due to discontinuation of product lines by the manufacturer. Next to a difference in fabrication parameters, the three materials also differ in their optical properties and final film thickness. Especially, the refractive index and the layer thickness are crucial parameters for the device design and simulations and were determined by using a combination of the aforementioned VASE and profilometer measurements. Figure 3.3 shows the wavelength dependent refractive index for all three cross-linked materials. We find a refractive index $n_{\text{UVCur21}} = 1.52$, $n_{\text{UVCur06}} = 1.54$ and $n_{\text{NIL210}} = 1.55$ at a wavelength $\lambda = 530\,\text{nm}$ for UVCur21, UVCur06 and NIL210 respectively. The measured extinction coefficient at the important visible wavelength range ($400 - 700\,\text{nm}$) was at maximum 0.01 for all three materials post curing, confirming good optical transparency. Furthermore, for each material the grating was imprinted into the top side of the respective polymer film, leaving a certain residual layer with no grating struc-

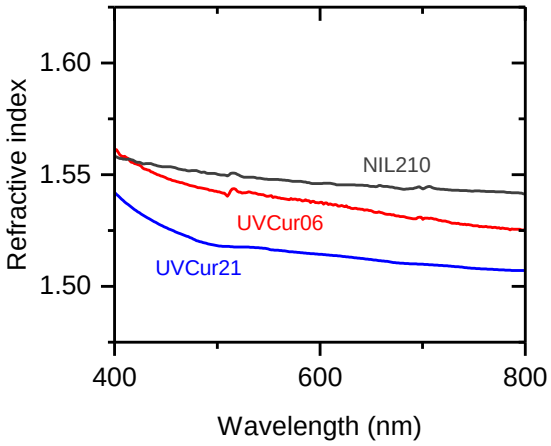

Figure 3.3: Refractive index vs. wavelength for three different UV curable polymer resists. The resists were used to fabricate grating structures and the refractive index was measured using variable angle spectroscopic ellipsometry (VASE). The VASE measurements were performed by Guy Whitworth and Laura Tropf.

ture. The residual layer thickness after grating fabrication was 50 nm, 250 nm and 170 nm for UVCur21, UVCur06 and NIL210, respectively.

As explained in Section 3.1.3, a master grating structure is imprinted into the photo-curable resist. Many of the DFB results presented in this thesis are based on the same master grating structure which is a structure that contains several one-dimensional first-, second- and mixed-order gratings. Figure 3.4 shows a map of the master grating structure incorporating gratings with periods of $\Lambda = 340\,\text{nm}$ (blue), 350 nm (green) and 360 nm (yellow) in second-order. The total area for each grating was $1\,\text{mm} \times 1\,\text{mm}$. The top left panel in Fig. 3.4 shows an atomic force measurement (AFM, Flex-Bio, Nanosurf) of a section of a one-dimensional second-order grating with a groove depth of $(106 \pm 5)\,\text{nm}$. As explained in Section 2.4 a second-order grating allows for simultaneous in-plane and out-of-plane scattering. The top right panel of Fig. 3.4, furthermore, shows an AFM measurement of the center region of a mixed-order grating with a groove depth of $(86 \pm 4)\,\text{nm}$ (first-order region). The grating period of the first-order region $\Lambda = 175\,\text{nm}$ is half the period of the second-order region and allows for in-plane scattering. If a gain material is present in the grating structure, in-plane Bragg scattering can lead to stimulated emission and feedback in the first-order region. In this example, 4 periods of second-order in the grating center are used to couple out the light which is generated in the larger first-order region. Furthermore, the master structure contains mixed-order gratings

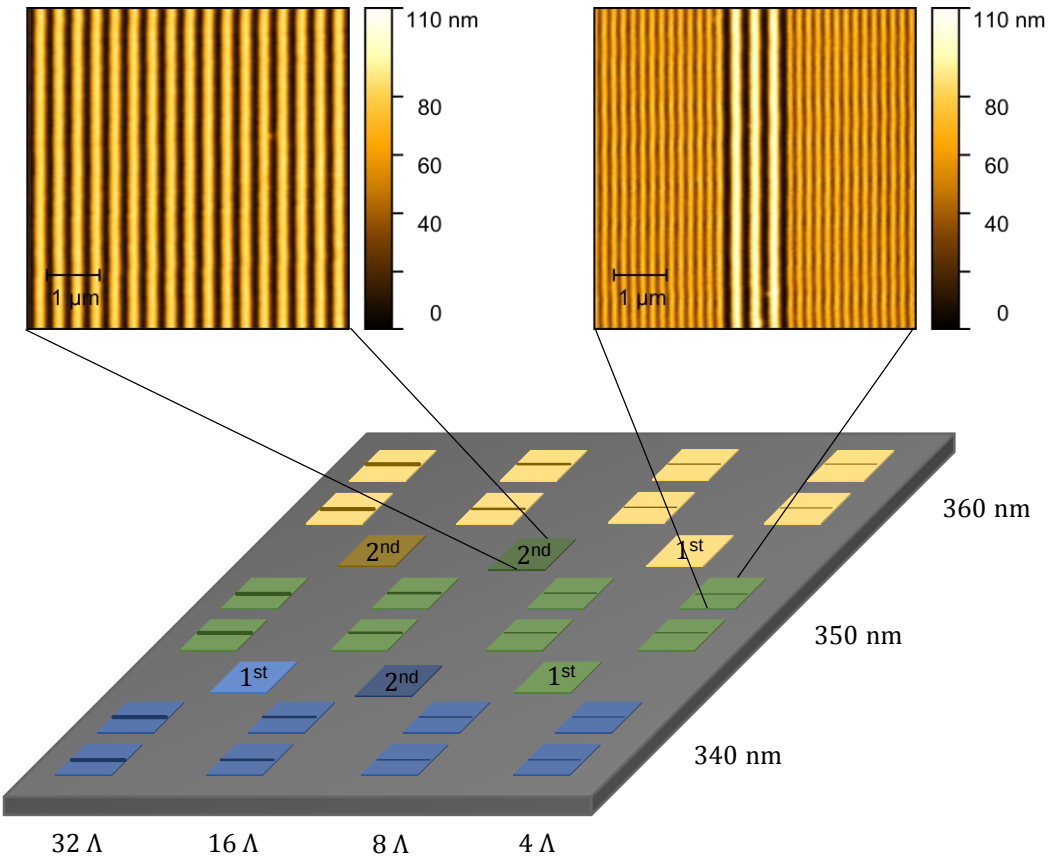

Figure 3.4: Atomic force measurements (AFM) of a second-order (top left) and a mixed-order grating (top right). The grating period for both gratings was $\Lambda = 350\,\text{nm}$ in second-order and the mixed-order grating contains 4 second-order periods to couple out the in-plane waveguided light. Bottom: Map of a master grating structure containing first- (1^{st}-), second- (2^{nd}-) and mixed-order (rest) gratings. The gratings have a period of $\Lambda = 340\,\text{nm}$ (blue), $350\,\text{nm}$ (green) and $360\,\text{nm}$ (yellow) in second-order. The outcoupling regions of the mixed-order gratings consist of 4, 8, 16 and 32 periods of second-order and are indicated by lines with increasing thickness. The total area of one grating is $1\,\text{mm} \times 1\,\text{mm}$ and the total size of the master substrate is $\sim 2\,\text{cm} \times 2\,\text{cm}$.

containing second-order sections with a length of 8, 16 and 32 periods (indicated by lines with increasing thickness).

The results presented in Chapter 6 were obtained with a two-dimensional grating structure. The properties of this structure are discussed in Chapter 6.

3.2 Optical Characterization Setup

Samples were optically investigated on a custom-built inverted fluorescence microscope. The excitation pulses were provided by an optical parametric oscillator (OPO; Opolette 355, Opotek Inc.). This OPO has a maximum tuning range of $410 - 2400\,\text{nm}$ with a peak energy of 5.1 mJ

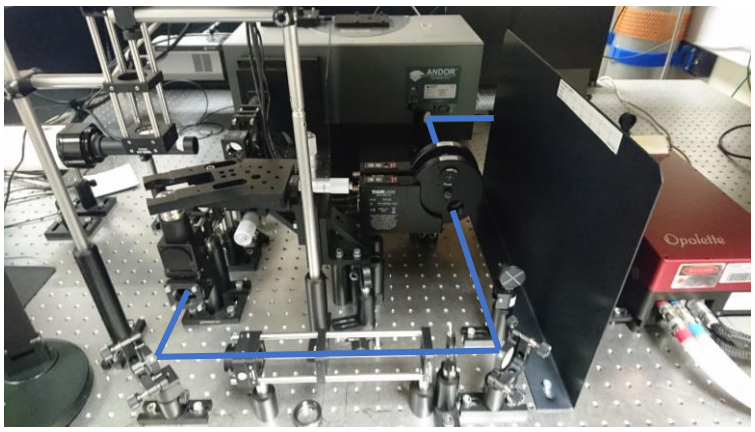

Figure 3.5: Photograph of the custom-built inverted fluorescence microscope for optical characterization. The excitation laser beam (indicated as a blue line) originates from the optical parametric oscillator (OPO) and passes through a custom-built optical attenuator consisting of a set of rotation stages containing neutral density filters. Next, the beam is guided through a lens and coupled into a microscope objective via a dichroic beam splitter. The collection arm of the setup is hidden behind the sample holder on top of the microscope objective.

and a maximum repetition rate of 20 Hz. In addition to the OPO output, it is also possible to access the fundamental wavelength of the Nd:YAG pump laser (1064 nm) and the frequency doubled (532 nm) and tripled (355 nm) output. The frequency tripled output of the Nd:YAG laser is used to pump the OPO.

Figure 3.5 shows a photograph of the experimental setup mounted on an optical table and the same setup is schematically shown in Fig. 3.6a. The OPO output (blue beam path) was passed through a custom-built optical attenuator consisting neutral density filters mounted on two rotational stages to control the excitation energy. Next, it was passed through a dichroic beam splitter (DBS; onset 500 nm) into a microscope objective (MO; 40 X, $NA = 0.55$ or 10 X, $NA = 0.25$). A lens $L1$ was used to increase the divergence of the excitation beam before it enters the MO. Hence, the pump spot at the focal plane of the objective was not perfectly focused but its size could be varied depending on the position of $L1$. At the focal plane of the objective, the sample S was excited. It was further possible to illuminate the sample with an LED light source through a Köhler illumination scheme from the top (not shown in Fig. 3.6a). The emission was collected through the same microscope objective and the longer wavelength part (> 500 nm) was passed into a separate collection arm by the DBS. The beam path in the collection arm is shown in more detail in Fig. 3.6b. Here, a long pass filter (LPS; onset 500 nm)

was used to filter out any remaining pump light. All work presented in this thesis, relied on excitation below 500 nm and emission above 500 nm but the setup can be adapted to operate at different wavelengths. Next, a projection lens (PL), positioned one focal length away from the entrance slit of the spectrograph, was used to focus the emission onto the entrance slit of the spectrograph (Shamrock 500i, Andor). This resulted in a spectrally decomposed emission profile on the electron multiplying cooled charged coupled device (EM-CCD) array detector (active pixels 1600×400; Newton 971, Andor) coupled to the spectrograph. To simply obtain the emission profile, the spectrally resolved emission was vertically binned on the EM-CCD detector. The spectrograph was equipped with three interchangeable gratings with groove densities of $150\,\mathrm{l\,mm^{-1}}$, $600\,\mathrm{l\,mm^{-1}}$ and $1800\,\mathrm{l\,mm^{-1}}$. Using the grating with the highest resolution, a peak width of 50 pm could be resolved on the EM-CCD detector. It was further possible, to obtain bright field images or near-field emission information of the sample by inserting a flip mirror (FP) into the collection arm and imaging directly onto a separate CCD detector using a camera projection lens (CL).

The results presented in Chapter 4, show spectrally resolved near-field emission information. These could be obtained by using a technique called hyperspectral imaging, where the slit of the spectrometer was opened to generate an image of the near-field emission at the different wavelength components.

The results presented in Chapter 4 and 5, contain spectrally resolved far-field emission measurements obtained by Fourier-imaging. Figure 3.6c shows that, compared to the setup described above, only one additional lens (Fourier lens, FL) needs to be inserted between microscope objective and projection lens in the collection arm to obtain angular resolved emission information [137, 151]. The collection beam path is shown in more detail in Fig. 3.6d. In this configuration, the collection arm consisted of a so called $4f$-correlator comprising two lenses with the same focal length. Light that is emitted from the sample at a certain angle is focused on the back aperture of the microscope objective (Fourier-plane). The Fourier lens (FL) was positioned one focal length away from the back aperture of the microscope objective and hence imaged the Fourier-plane (far-field) of the emission onto the entrance slit of the spectrograph via a projection lens (PL). This resulted in an angle dependent and spectrally decomposed emission profile on the EM-CCD detector. The maximum angular range was defined by the numerical aperture NA of the microscope objective and $\theta_{10\,\mathrm{X}} = \arcsin(NA/n)_{\mathrm{air}} \approx 14°$ and $\theta_{40\,\mathrm{X}} \approx 33°$ (half angle to the normal, as depicted in Fig. 3.6d) for the 10 X and 40 X objective,

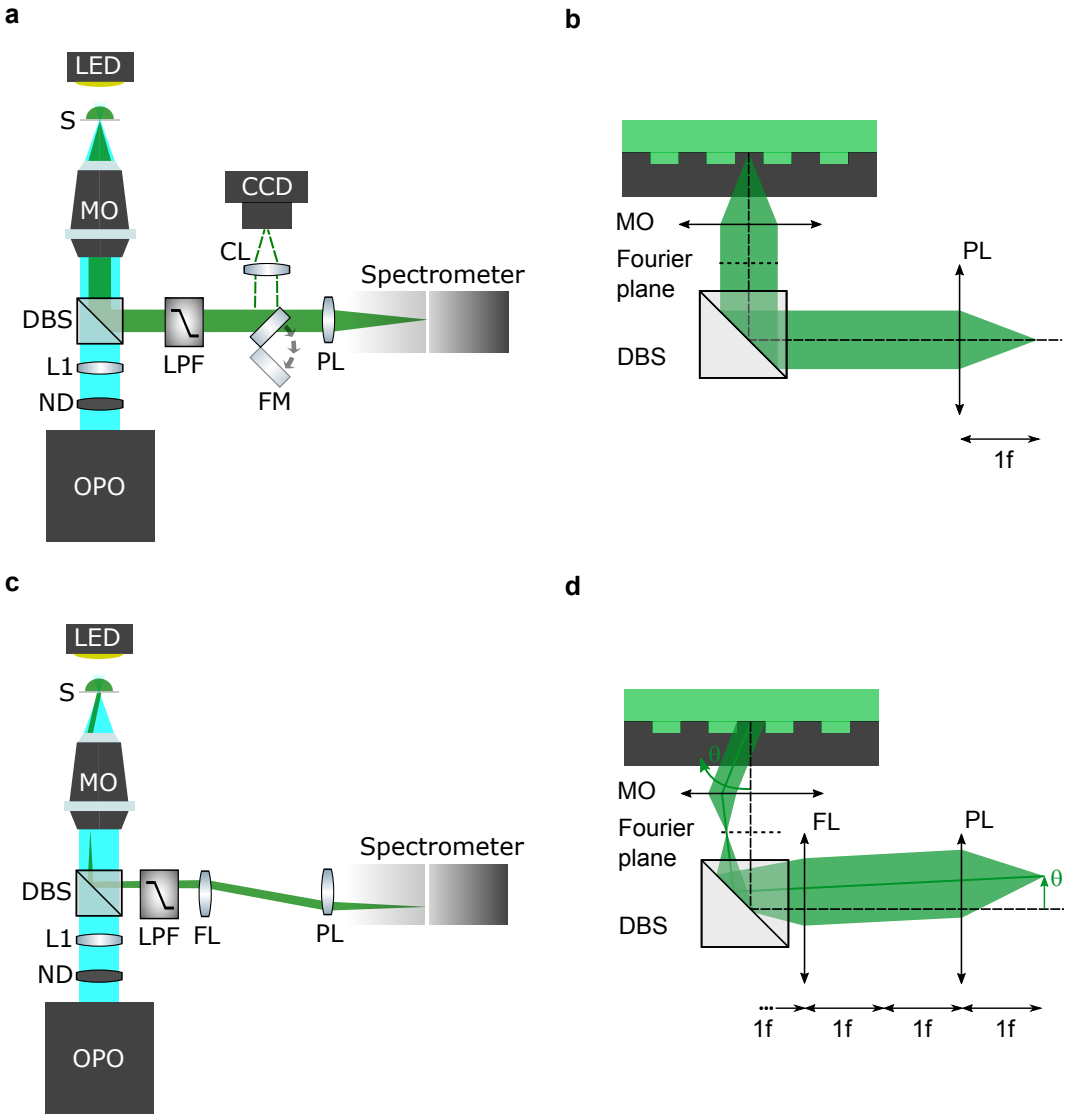

Figure 3.6: **a**, Illustration of the custom-built inverted microscope for optical characterization. The blue beam represents the excitation pump beam that is generated in an optical parametric oscillator (OPO). The excitation light is passed through an optical attenuator (ND), a divergence lens ($L1$), a dichroic beam splitter (DBS) and a microscope objective (MO) to excite the sample S. The green beam represents the fluorescence signal emitted from the sample and is collected by the same MO and passed into the collection arm by the DBS. Remaining pump light is filtered with a long pass filter (LPS) and the emission is focused onto the entrance slit of the spectrometer using a projection lens (PL). A flip mirror (FM) can be used to image directly onto a CCD camera via a camera lens (CL). **b**, Illustration of the optical beam path in the collection arm for the setup shown in a. **c** Illustration of the optical characterization setup for Fourier-imaging. Compared to the setup shown in a, an additional Fourier lens (FL) is inserted into the collection arm to collect the light from the back aperture of the MO and image the angular resolved emission onto the entrance slit of the spectrometer. **d**, Illustration of the optical beam path in the collection arm for the setup shown in c (adapted from Ref. [150]).

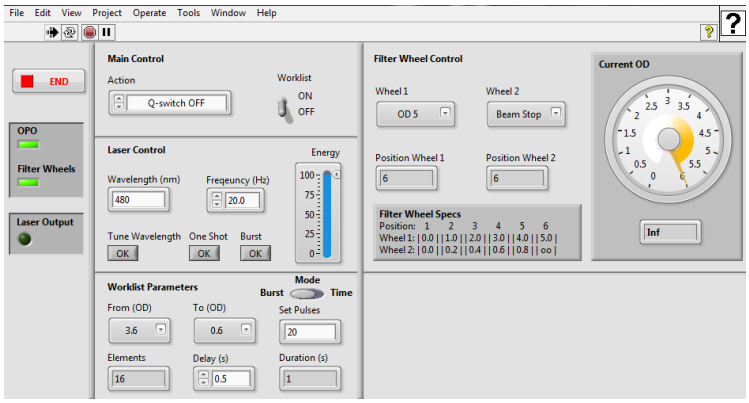

Figure 3.7: LabVIEW user interface to control the pump laser and the optical attenuator simultaneously. The "Worklist" section allows to define attenuator settings for automated threshold measurements.

respectively. To resolve the far-field pattern along both axes, the spectrograph was operated in zero-order reflection, e.g. without any wavelength dispersion. Another method to obtain angular resolved emission is by using a goniometer, where the emission is collected at different discrete angles one at a time [152]. However, compared to the Fourier-imaging technique, this is usually more time consuming and requires a more elaborate experimental setup.

The pump laser and optical attenuator of the optical characterization setup were controlled via a self written LabVIEW (National Instruments) script. Figure 3.7 shows the user interface which allows to select the wavelength and repetition rate of the pump laser as well as the settings of the optical attenuator. Furthermore, it was possible to define a worklist with different settings of the optical attenuator and the number of pump pulses given at a certain combination of neutral density filters. In combination with a hardware trigger between pump laser and spectrometer EM-CCD detector, this was used to automatically acquire pump power dependent emission information from laser samples.

3.3 Gain Materials

3.3.1 Conjugated Polymers

One class of gain materials presented in this work (see Chapter 7) are conjugated polymers. As state-of-the-art fluorescent emitters, we selected two different polyfluorene co-polymers and

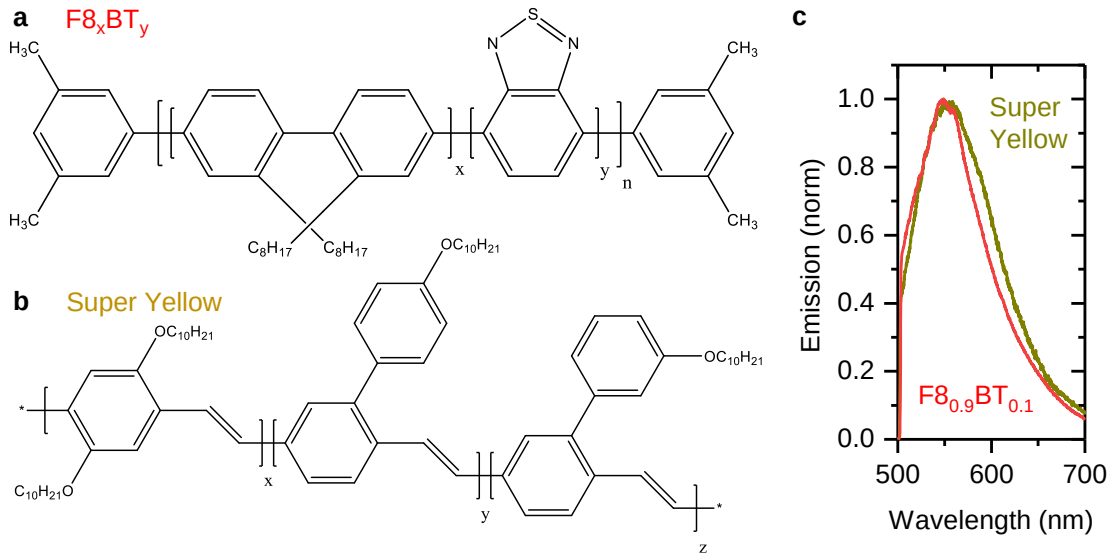

Figure 3.8: Chemical structure of the polyfluorene co-polymer $F8_xBT_y$ (**a**, x and y define the statistical ratio between fluorene (F8) and benzothiadiazole (BT) units, respectively) and the phyenylenevinylene polymer Super Yellow (**b**). **c**, Emission spectra for the conjugated polymers $F8_{0.9}BT_{0.1}$ (red) and Super Yellow (yellow). A long pass filter (onset, 500 nm) was used to filter out the excitation.

a phyenylenevinylene polymer (PPV) to be used as a solid-state polymer film providing gain.

Figure 3.8a shows the chemical structure of a polyfluorene co-polymer, known as poly(9,9-dioctylfluorene-co-benzothiadiazole) (F8BT), i.e. a polymer consisting of alternating fluorene (F8) and benzothiadiazole (BT) units. This polymer is of particular interest for laser applications since it shows high gain, a broad gain spectrum and long gain lifetimes [153]. The gain of F8BT can be enhanced further by changing the ratio of fluorene (F8) and benzothiadiazole (BT) units from 1:1 (F8BT) to 9:1 ($F8_{0.9}BT_{0.1}$), which reduced amplified spontaneous emission thresholds in thin films to values as low as $2\,\mu J\,cm^{-2}$ [154]. This effect was attributed to an improved chain isolation by the increased number of octyl side chains effectively preventing exciton annihilation processes [20]. The other conjugated polymer used in this work is the PPV derivative poly(paraphenylene-vinylene) and is known under the trade name Super Yellow. The chemical structure is shown in Fig. 3.8b. This polymer is routinely used in organic light emitting diodes [155] and organic lasers [103] due to its relatively high PLQY when compared to other PPV derivatives [156]. A typical fluorescence emission spectrum obtained from $F8_{0.9}BT_{0.1}$ and Super Yellow solid-state films is shown in Fig. 3.8c. While the peak shape is similar for both materials, the emission of Super Yellow is slightly red shifted ($\lambda_{max} \approx 553\,nm$) compared to $F8_{0.9}BT_{0.1}$ ($\lambda_{max} \approx 548\,nm$). The refractive index of all fabricated solid-state conjugated polymer films was found to be similar ($n \approx 1.7$) [72, 103].

We purchased poly(9,9-dioctylfluorene-co-benzothiadiazole) with a statistical 9:1 ratio of F8 to BT units ($F8_{0.9}BT_{0.1}$; $M_w = 52 \times 10^3$ Da; ADS233YE, American Dye Source Inc.), poly(9,9-dioctylfluorene-co-benzothiadiazole) with a 1:1 ratio of F8 to BT units (F8BT; $M_w = 61 \times 10^3$ Da; ADS133YE, American Dye Source Inc.) and the poly(paraphenylene vinylene) copolymer (Super Yellow; $M_w = 1.7 \times 10^6$ Da; PDY-132, Merck). The conjugated polymers were delivered in powder form and were dissolved in toluene at a concentration of 25 mg mL^{-1} ($F8_{0.9}BT_{0.1}$ and F8BT) and 10 mg mL^{-1} (Super Yellow), respectively. The polymer solutions were spin-coated at 2000 rpm for 60 s, yielding a solid-state film of (180 ± 10) nm (for $F8_{0.9}BT_{0.1}$ and F8BT, see also Fig. 3.1b) and (250 ± 10) nm (Super Yellow).

3.3.2 Dyes

In contrast to the aforementioned conjugated polymers, most laser dyes have a molecular weight < 900 Da and no repeated subunits; they hence fall into the category of small molecules. Some of the results presented in Chapter 4 and 5 are based on the commercially available synthetic laser dye Pyrromethene 556 (PM556, Disodium-1,3,5,7,8-pentamethyl-pyrromethene-2,6-disulfonate-difluoro-borate, Exciton Inc.). The fluorescence of this dye originates from the fluoroboration (BF_2 complex) of two pyrrole rings linked by a conjugated π-system (see Fig. 3.9a). This dye has a molecular weight of 466.19 Da and is delivered in powder form. It is particularly well suited for the presented experiments since it is soluble in water and has similar spectral properties (see Fig. 3.9b) when compared to other green emitters, routinely used in biological experiments (e.g. CMF or eGFP). Table 3.1 summarizes the most important photophysical properties for PM556 dissolved in water at a concentration of 2 mM [157]. The highest fluorescence intensities were recorded for a concentration $c_{max} \approx 5$ mM, with higher concentrations inducing self-quenching and hence a reduction in fluorescence signal. Although high concentrations gave the brightest emission, they also led to a red shift of emission due to self absorption, compared to low aqueous PM556 concentrations ($c \approx 2\,\mu$M), where the maximum emission wavelength is $\lambda_{max} \approx 518$ nm [157]. Furthermore, this dye is particularly well suited for laser experiments due to a good photostability and a reduced dye aggregation at high concentrations when compared to conventional rhodamine dyes [158, 159].

In Chapter 4 the synthetic dye 5-chloromethyl-fluorescein diacetate (CMFDA, Life Technologies) was selected for cell staining and as intracellular gain material. This dye is widely used to stain cells for tracking and monitoring in biological experiments [162]. Furthermore,

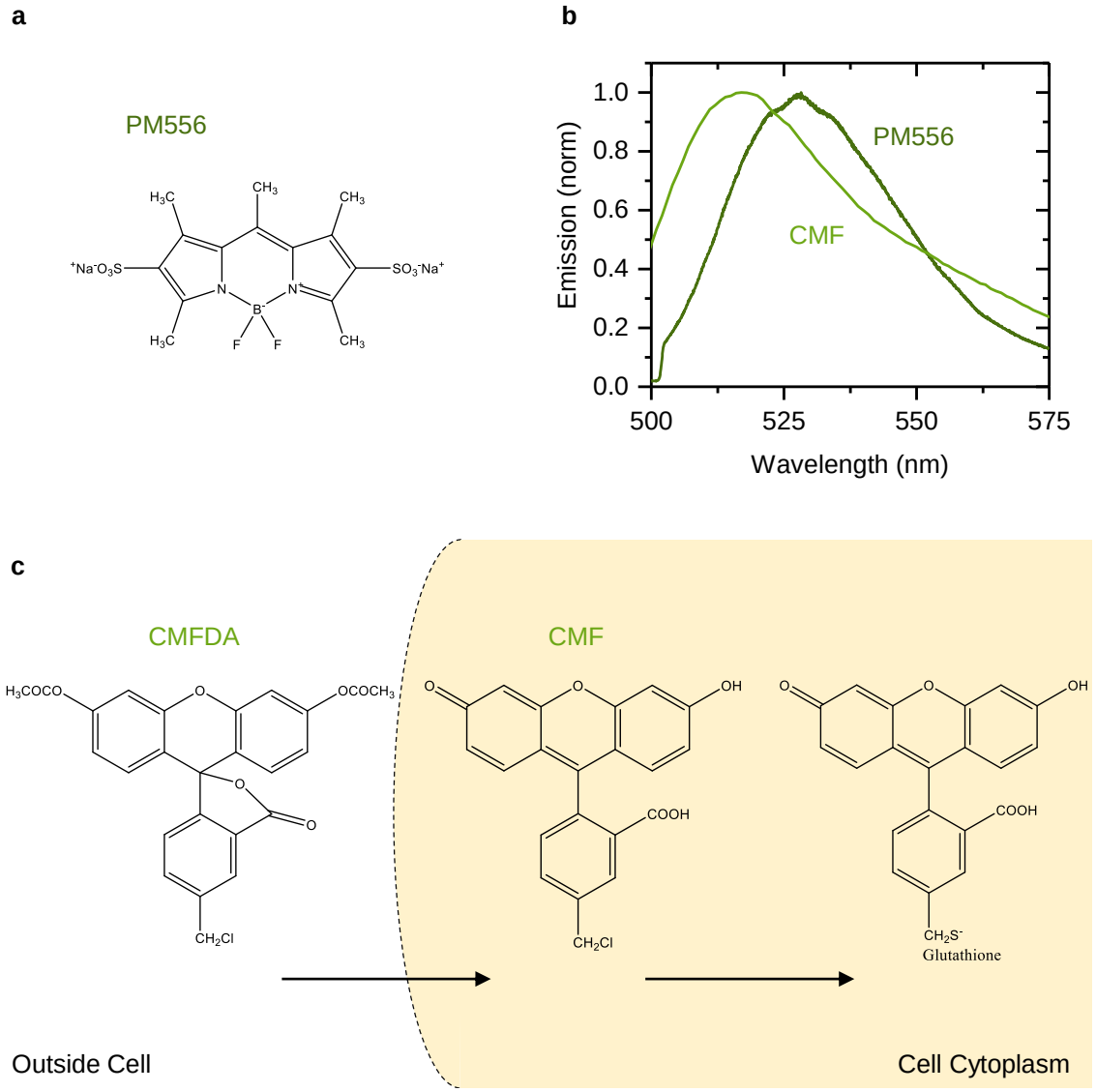

Figure 3.9: **a**, Chemical structure of the laser dye Pyrromethene 556. **b**, Emission spectra for Pyrromethene 556 (PM556, dark green) and the fluorescent molecule fluoresceine (CMF, bright green). The emission spectrum for fluoresceine was obtained from Ref. [160]. **c**, Chemical structure of the cell tracker dye CMFDA and the structural changes upon contact with cell cytoplasm (adapted from Ref. [134]).

Table 3.1: Summary of photophysical properties of aqueous solutions of Pyrromethene 556 (PM556) [157] and fluoresceine (CMF) [161].

Photophysical property	PM556	CMF
Absorption maximum (nm)	491	493
Emission maximum (nm)	525	522
Extinction coefficient ($M^{-1}\,cm^{-1}$)	98 600	76 900
Photoluminescence quantum yield	0.83	0.93

it has been shown that it can be used as a convenient synthetic alternative to biologically produced fluorescent proteins as a gain material in single cell lasers [134]. The fluorescent product of this dye is a fluorescein derivative and as such, shows bright fluorescence and good photostabilty. The photophysical properties of fluorescein are summarized in Table 3.1 [161] and the emission spectrum is shown in Fig. 3.9b [160]. In contrast to fluorescein, the dye CMFDA only becomes fluorescent when it interacts with the cytoplasm of a cell and this interaction also modifies the dye to become membrane-impermeable [163]. Figure 3.9c shows the changes in the chemical structure of CMFDA during this process. The initial CMFDA molecule is non-fluorescent and non-absorbing but due to intracellular esterases, the acetate groups are cleaved from the molecule once it enters the cell cytoplasm. The product is the brightly fluorescent fluorescein derivative 5-chloromethylfluorescein (CMF). In a subsequent reaction, thiol groups from intracellular proteins interact with the chloromethyl group of CMF (via a glutathione S-transferase-mediated reaction) which renders the molecule non-membrane permeable. This feature can lead to an accumulation of intracellular fluorescent molecules, exceeding the initial staining concentration [134].

The staining procedure and initial CMFDA concentration are discussed in Chapter 4.

3.3.3 Fluorescent Proteins

For the experiments presented in Chapter 4 and 6, we selected eGFP as the fluorescent gain material. While the experiments in Chapter 4 are performed using eGFP in solution within biological cells, the results obtained in Chapter 6 are based on eGFP solid-state films.

In Chapter 4, eGFP is transiently expressed within cells using different transfection methods. In order to initiate the intracellular eGFP expression, a DNA strand encoding for eGFP that is not present in the original cell must be transferred into the nucleus of the cell. In an additional step, the protein will be produced by means of transcription and translation. The delivery of the DNA plasmid into the nucleus of a cell is a complex but widely studied process [164] and the different methods can be broadly classified into two main categories. First, viral vector-mediated systems which routinely show a delivery and expression efficiency $> 90\,\%$ but are costly and sometimes toxic [164, 165]. Second, the non-viral (synthetic) vector-mediated systems which show lower efficiencies but are feasible in standard biology laboratories and are hence the method of choice for the presented work. Two prominent synthetic transfection methods are Lipofection [166] and Nucleofection [167]. While both

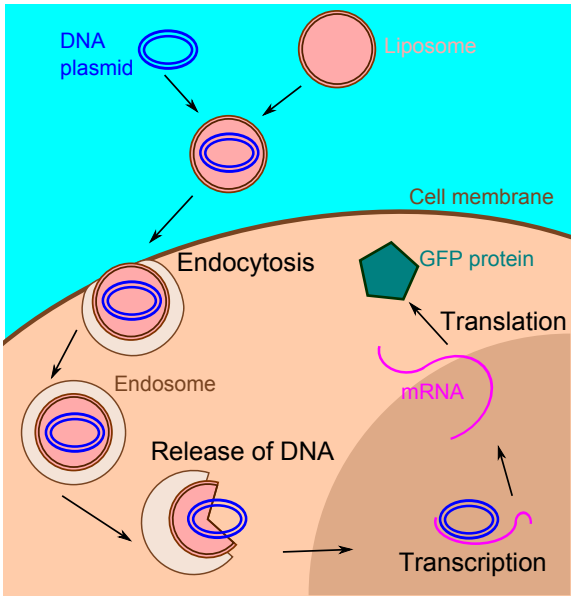

Figure 3.10: Principle of Lipofection. A DNA plasmid encoding for a specific protein (e.g. eGFP) is packed inside a liposome. The liposome containing the DNA plasmid enters the cell cytoplasm via endocytosis. Next, it releases the DNA plasmid which diffuses into the nucleus of the cell. Messenger RNA (mRNA) is formed via transcription. Lastly, the protein is expressed by translating the specific mRNA code into a sequence of amino acids.

methods rely on different procedures, their basic principle is the same here.

Figure 3.10 shows an illustration of the Lipofection process where in a first step, external DNA is packed inside a cationic liposome. This is a positively charged spherical vesicle consisting of a lipid bilayer. The cell membrane is negatively charged and hence the liposome can attach to the outside of the cell via electrostatic interaction. Next, the vesicle enters the cell via a process called endocytosis. This is a fundamental cellular process to transfer external objects inside the cell via membrane bound vesicles. Once into the cell, the liposome disassembles and the DNA plasmid is released and can diffuse into the nucleus. From thereon, the information contained on the DNA strand is read out and the protein is expressed via transcription and translation (see Ref. [168] for further details). The Nucleofection process is based on the same biological principles but instead of relying on endocytosis, external DNA enters the cell through membrane pores opened due to electroporation, a process in which a short pulse of an intense electric field is applied to a cell culture which in turn opens pores on the cell membrane and increases the transient permeability of the cell wall. The transfection protocols and specific materials are summarized in Appendix C.

For the experiments on solid-state eGFP films (Chapter 6), the initial eGFP was expressed

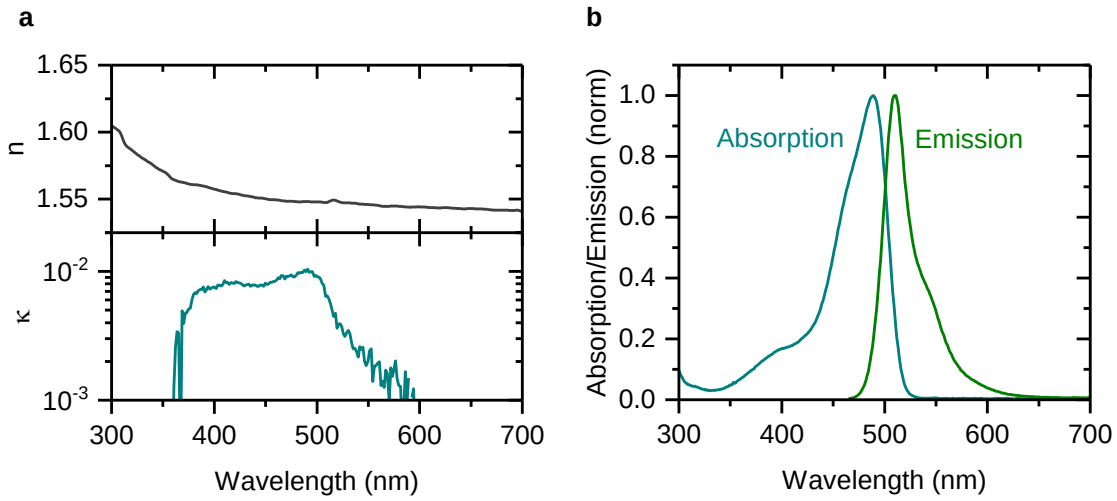

Figure 3.11: **a**, Refractive index (n) and imaginary part of the refractive index (κ) for a solid-state eGFP film, measured using variable angular spectroscopic ellipsometry (VASE). The VASE measurement was performed by Laura Tropf. **b**, Absorption and emission spectrum of an aquaeus solution of eGFP. The absorption and emission spectrum for eGFP was obtained from [169].

in and harvested from biological cells. The protein extraction was carried out by K. Ostermann (TU Dresden) and details on the procedure can be found in Ref. [43]. The provided eGFP was dissolved in water, filtered and subsequently centrifuged to remove buffer salts and increase the protein concentration. To obtain solid-state films, the aqueous eGFP solution (concentration of 100 mM) was spin-coated at 1500 rpm for 120 s, yielding a solid-state eGFP film with a thickness of $\approx 1\,\mu$m. Figure 3.11a shows the optical properties of a solid-state eGFP film. A refractive index $n = 1.55$ is obtained at a wavelength $\lambda = 530$ nm. As expected, the imaginary part of the refractive index κ for eGFP is particularly pronounced at a wavelength range where the material shows a high absorption (see Fig. 3.11b, absorption peak at $\lambda = 489$ nm). Furthermore, the emission spectrum shows a maximum intensity at $\lambda = 511$ nm. While the presented data was measured on an aqueous solution of eGFP (obtained from [169]), the spectral position of the main emission peak in a solid-state film is the same [170]. The high PLQY $\approx 0.6-0.8$ of eGFP is close to state-of-the art conjugated polymers and engineered laser dyes (see Table 3.1), which makes it particularly interesting as a laser gain material.

4

Single Cell Induced Optical Confinement

In this chapter, the potential of fluorescent biological cells as refractive index landscapes and active optical elements is investigated using a combined Fourier- and hyperspectral-imaging technique.

The general structure of single cell lasers and the motivation for studying their photonic properties are introduced in Section 4.1. To investigate the characteristics of single cell lasers, reliable laser components supporting a stable laser emission need to be selected. The properties of two different intracellular gain materials are assessed in Section 4.1.1. Having found a suitable gain material, the fabrication of the cavity system and their basic optical characterization is explained in Section 4.1.2. To understand and validate the laser operation of single cell lasers, the emission properties are compared to two simpler microcavity structures in Section 4.2. In Section 4.3, the three cavity systems are further investigated using Fourier- and hyperspectral-imaging techniques and evidence for 3D photonic confinement inside the living cells is presented. The origin for photonic confinement in single cell lasers and their unique mode structures are shown in Section 4.4. Lastly, Section 4.5 investigates the fundamental creation of transverse and longitudinal lasing modes in single cell lasers.

The flow cytometer and nucleofection experiments described in this chapter were carried out in the lab of Dr Simon Powis and Prof. Frank Gunn-Moore, respectively.

The contents of this chapter have in parts been published in Ref. [171]

4.1 The Single Cell Laser

In 2011 Gather and Yun demonstrated the first biological laser in which lasing is achieved directly within a single living biological cell or bacterium by using the green fluorescent protein (GFP) as the gain material [33, 34]. Figure 4.1 shows a schematic of the single cell laser. Here, lasing is typically obtained from fluorescent living cells embed between two highly reflective distributed Bragg reflector (DBR) mirrors forming a Fabry-Pérot cavity. The cells are floating in the cavity suspended in a non fluorescent cell medium (not shown). The intracellular fluorophores can be optically excited with nanosecond pulses (blue beam path) to achieve population inversion in the fluorescent material and hence lasing (green beam path). The required pump energy to achieve lasing (threshold) is typically in the nJ-range. It has been shown that cells sustain these pump conditions and that photo-induced damage is only observed at pump energies orders of magnitude above typical threshold values [33, 134].

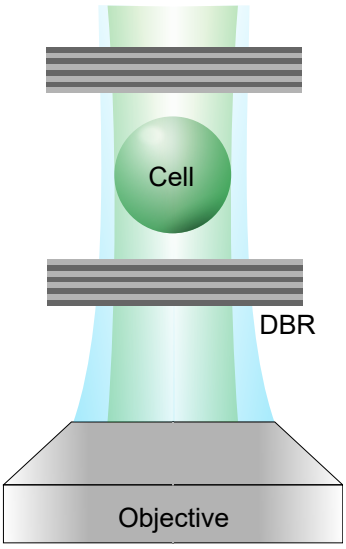

Figure 4.1: Illustration of a single cell laser based on an external cavity. The external cavity is formed by two highly reflective distributed Bragg reflector (DBR) mirrors. The cell is suspended in a cell medium and floating between the two DBR mirrors. The intracellular gain material is optically excited (blue beam path) and the emission (green beam path) is collected through the same microscope objective.

The refractive index contrast between the cell ($n \approx 1.37$) and the surrounding medium (e.g. phosphate buffered saline solution, PBS, $n \approx 1.33$) together with the spherical shape of the cell make it possible to accommodate certain tilts between the two DBR mirrors and therefore prevent spatial beam walk off and a destabilized cavity [38]. In a simplified picture, the cell acts as a convex lens within the Fabry-Pérot cavity. While lasing from single cells has been reported and first applications have been suggested, the effects of the unique refractive index

landscape introduced by the presence of the cell on the electromagnetic field in the cavity have not been studied in detail. Microcavity systems based on organic or inorganic emitter materials offer a powerful toolkit to investigate light-matter interaction [76]. In a simple microcavity photons are only confined in one dimension and are able to propagate freely in-plane. Introducing lateral discontinuities into the refractive index landscape of the microcavity leads to further optical confinement in two or even three dimensions. This strategy is often applied to study coherent light emission over macroscopic distances [172]. In laser devices based on organic emitters this studies can even be performed at room temperature [173]. So far, however, the introduction of lateral discontinuities typically relies on lithographic patterning of a dielectric or metal in the microcavity system [104]. In the following sections we will investigate whether the inherent refractive index contrast between cell and surrounding medium in a biological single cell laser can be harnessed for trapping photons and studying the light-matter interaction in a biological system.

4.1.1 Intracellular Gain Material

To study the photonic properties of a single cell laser in a reliable manner, a stable laser system and hence the right biological laser components are needed. As the host for the gain material we choose cells from the HEK 293 cell line (derived from human embryonic kidney cells, Sigma Aldrich) due to their reliable growth characteristics and amenability to transfection [174]. The cells were cultured in DMEM (Dulbecco's Modified Eagle Medium) with 10 % (v/v) fetal bovine serum (FBS) and 1 % penicillin-streptomycin (PS) under standard incubation conditions (37 °C, 5 % CO_2) until about 50 % confluency. The next important component is the gain material.

To achieve lasing, enough gain must be provided within the cell to overcome any optical losses of the resonator [175]. In the original work by Gather & Yun, cells were transiently transfected with a plasmid encoding for eGFP (enhanced GFP) to provide sufficient gain. In order to initiate the transient eGFP expression, a DNA strand coding for eGFP - not present in the original cell - was transferred into the cell. In a next step, the cell produced the specific protein (in this case eGFP) through transcription and subsequent translation. The basics and different techniques of cell transfection are discussed in Section 3.3.3.

We followed the same eGFP transfection approach as described in the original report [33] and observed that not only the available gain and hence the intracellular fluorophore concen-

tration in a single isolated cell is a crucial parameter but also the number of cells containing the gain material. This is important since during an actual experiment there is not only one but $> 100\,000$ cells floating within the cavity. If only a small number is transfected, the chances of finding a cell containing enough fluorophores (or fluorescent proteins) providing sufficient gain to overcome the cavity losses is small. In cell biology the fraction of successfully transfected cells is known as transfection efficiency. We studied two different non-viral transfection methods to introduce the DNA plasmid into the nucleus of the cell:

Lipofection: External DNA is packaged inside a cationic liposome and enters the cell via endocytosis, which is a cellular process to transfer external objects inside the cell via membrane bound vesicles called endosomes.

Nucleofection: External DNA enters the cell through membrane pores opened due to electroporation. The open pores and hence the increased transient permability of the cell membrane is achieved by applying a short pulse of an intense electric field (electroporation).

The optimized staining protocols for both techniques can be found in the Appendix C. The transfection efficiency was studied for certain time intervals after introducing the DNA plasmid using a flow cytometer (Guava easyCyte HT Sampling Flow Cytometer). Flow cytometry is a laser based biophysical technique, in which cells are suspended in a stream of fluid and passed through the optical path of an excitation laser cell by cell [176]. The emission intensity of each individual cell is spectrally resolved and recorded. Figure 4.2a shows a histogram of the green fluorescence intensity (spectral band, (525 ± 30) nm) of nucleofected HEK 293 cells 8 h after transfection. We can distinguish two distinct populations showing different fluorescence properties in the histogram. The first population on the left hand side originates from cells that are not expressing eGFP and only showing auto fluorescence. The second population on the right hand side originates from cells expressing eGFP and therefore showing an increased fluorescence intensity. The percentage ratio between the two peaks is defined as the fraction of positively eGFP labeled (eGFP+) cells. In this example 72.1 % of the cells are positively eGFP labeled 8 h after nucleofection. We conducted this experiment for lipofected and nucleofected HEK 293 cells 4 h, 8 h, 24 h, 48 h and 72 h after transfection. For each measurement a control sample containing non-transfected cells was measured as well. In each case the control sample only showed an auto fluorescence peak. Figure 4.2b shows the fraction of positively eGFP

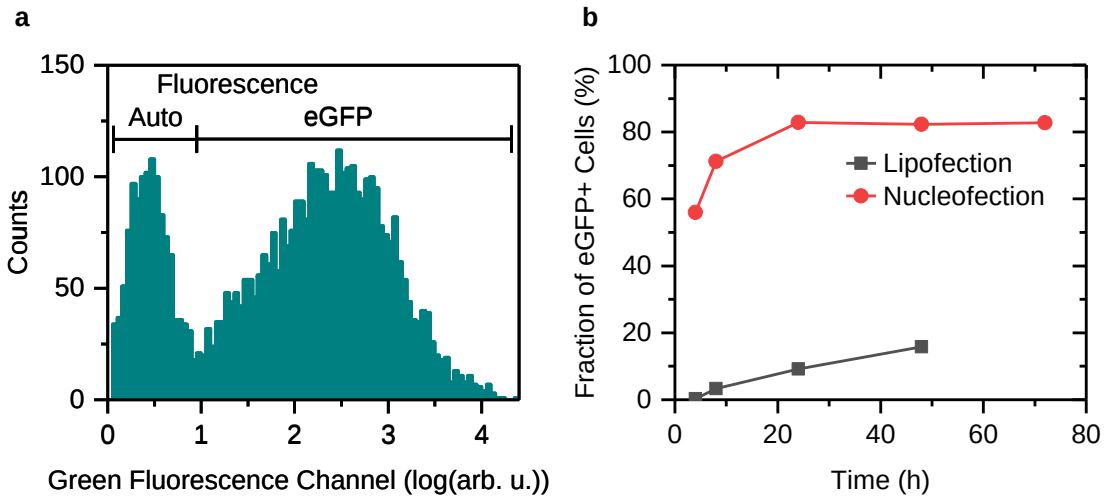

Figure 4.2: eGFP transfection efficiency of HEK 293 cells. **a**, Histogram showing the green fluorescence intensity emitted from individual cells on a logarithmic scale. The cell sample had a size of 4752 cells and was investigated 8 h after nucleofection. The two populations originated from auto and eGFP fluorescence and are labeled accordingly. **b**, Fraction of eGFP+ cells for lipofected (gray symbols) and nucleofected (red symbols) over time. The "+" indicates that eGFP fluorescence above the autofluorescence background level can be observed from the cells.

labeled (eGFP+) cells for both techniques over time. The gray data points show the fraction of eGFP+ lipofected cells. Initially (after 4 h), only 0.2 % of the cells have expressed sufficient eGFP to cause fluorescence above the autofluorescence background level. The fraction of eGFP+ cells slowly increases to 15.8 % after 48 h. For nucleofected cells, however, the initial fraction of positively eGFP labeled cells after 4 h is already at 56.0 % and increases rapidly to 82.8 % at 24 h when it saturates. The saturated fraction of eGFP+ cells (at longer times) is equal to the transfection efficiency since the cells had enough time to produce an amount of eGFP sufficient to cause fluorescence above the autofluorescence background. At times shortly after the transfection process, however, it is likely that some transfected cells with a slow eGFP production rate fall into the autofluorescence population. We conclude that nucleofection is superior to lipofection in terms of transfecting a large fraction of the cell population. In fact 4 out of 5 cells are expressing eGFP after only 24 h.

After having established a technique to efficiently transfect a large fraction of cells, it was important to validate the available gain within the cell. The gain per cavity round trip depends on the number of fluorophores within the cavity and hence on the intracellular fluorophore concentration. We estimated the concentration by measuring the emitted green fluorescence intensity of individual cells upon excitation with blue light under an inverted fluorescence mi-

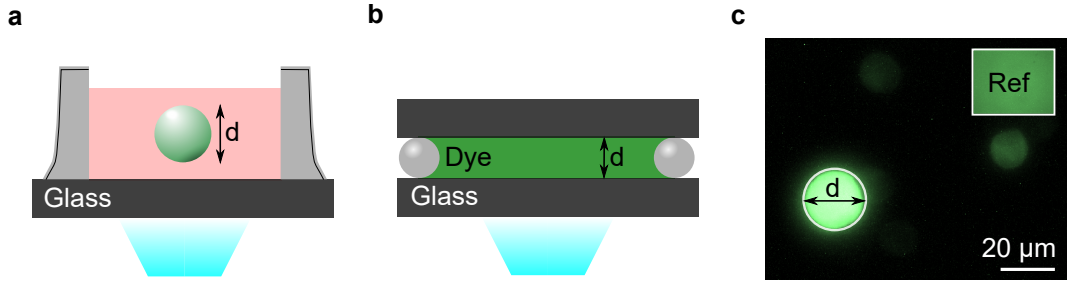

Figure 4.3: Fluorescence microscopy method to estimate the intracellular fluorophore concentration. **a**, Illustration of a floating fluorescent cell with diameter d excited with blue light. **b**, Illustration of a reference sample containing a fluorescent dye solution with a defined optical path length d excited with blue light. The two glass slides are separated by glass beads (gray circles) with a defined diameter d. **c**, Fluorescence microscopy image of a cell containing eGFP with diameter d. The inset shows a fluorescence microscopy image of the reference dye sample illustrated in b.

croscope. This method, rather than the brightness information in arbitrary units obtained by the flow cytometer, was used to get a quantitative measurement of intracellular fluorophore concentrations. Figure 4.3 shows a schematic illustration of the method used to determine the concentration. In a first step, cells were trypsinized (detached from the bottom of the culture dish) and suspended in a phenol-red free cell medium (FluoroBrite DMEM). Phenol-red free medium is used to minimize the effect of background fluorescence introduced by the surrounding medium (see Fig. 4.3a for an illustration). To minimize their surface area, the trypsinized cells form spherical objects with a diameter d and are floating in the cell medium. The fluorescence intensity was measured by exciting the cells with blue light through a microscope objective and recording the green emission with a scientific CMOS detector (Zyla 5.5 sCMOS, Andor) through the same objective. Excitation (450 nm to 490 nm) and emission (500 nm to 550 nm) were spectrally separated using a beam splitter. This experiment was performed using a commercial epi-fluorescence microscope (Eclipse Ti-S,Nikon). To get a trustworthy estimate of the fluorescence intensity, it was crucial to only analyze cells in the focal plane of the objective. Cells out of focus might appear dimmer due to blurring, i.e. divergence of the emission. An example image recorded with this setup is shown in Fig. 4.3c. In this example only the brightest cell is in focus. From this image we can deduce two important quantities of the cell. The fluorescence intensity F emitted by the cell and the cell diameter d corresponding to the optical path length within the cell. The fluorescence intensity F was obtained by integrating all pixel counts within a circular area around the cell defined by the diameter d. We can relate the fluorescence intensity F and the intracellular concentration c by using the

following equation:

$$F = I_0 \phi (1 - \exp(-\epsilon d c)), \tag{4.1}$$

where I_0 is the excitation intensity, ϕ the photoluminescence quantum yield and ϵ the absorption coefficient intrinsic to the fluorophore. The photoluminescence quantum yield ϕ and absorption coefficient ϵ for eGFP can be found in Section 3.3.3. This equation, however, can not be solved without knowing the excitation intensity I_0. We could estimate I_0 and thus calibrate this method by taking a reference measurement of a fluorescent sample with a defined concentration c where all parameters are known. This is schematically shown in Fig. 4.3b where a solution of fluorescent dye is suspended between two glass cover slides separated by 20 µm using glass spheres as spacers to define the optical path length d. For the calibration measurement, the excitation and acquisition settings need to be the same as for the cell samples. A microscopy image of a reference sample containing the fluorescent dye Pyrromethene 556 (PM556, Disodium-1,3,5,7,8-pentamethylpyrromethene-2,6-disulfonate-difluoro-borate, Exciton Inc.) dissolved in deionized water at a concentration $c = 50\,\mu\text{M}$ is shown in the inset of Fig. 4.3c. The photoluminescence quantum yield ϕ and absorption coefficient ϵ for PM556 can also be found in Table 3.9. Calculating I_0 from the reference measurement and analyzing the microscopy images of the cells using Eq. 4.1 yielded a distribution of intracellular fluorophore concentration c. Utilizing this method, the intracellular fluorophore concentration of HEK 293 cells with the highest transfection efficiency was investigated. Figure 4.4 shows the intracellular fluorophore concentration distribution of eGFP nucleofected cells 72 h after transfection. A median concentration $c_{\text{med}} = (5 \pm 1)\,\mu\text{M}$ was obtained for a sample containing 700 cells. Since the intracellular concentration does not show a normal distribution but is skewed towards lower concentration values, the median rather than the mean is a better representative of the central location of the data. As indicated by the box plot, 50 % of the cells (the so called interquartile range which is defined as the 25 to 75 percentile) fall into a narrow concentration range from 3.7 µM to 8.4 µM. However, there are also some outliers with a maximum intracellular concentration $c_{\text{max}} = (115 \pm 13)\,\mu\text{M}$. In the original work by Gather & Yun [33] a required intracellular eGFP concentration $c \approx 300\,\mu\text{M}$ for a working single cell laser is experimentally found. However, the cells used in the original work were obtained by running fluorescently activated cell sorting (FACS) after the transfection. This technique sorts cells depending on their fluorescence intensity and is similar to the aforementioned flow cytometer but incorporates an additional sorting unit based on electrostatic deflection [177].

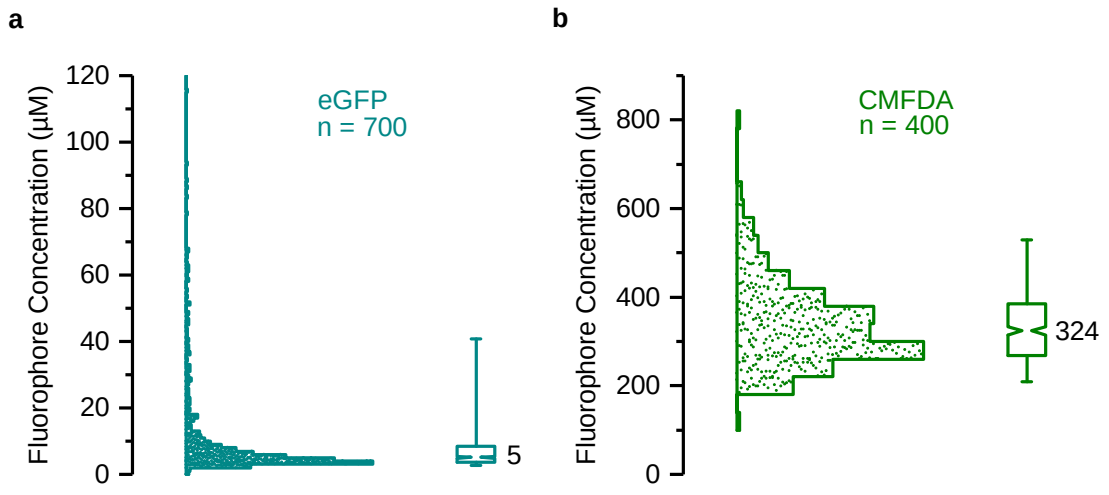

Figure 4.4: Distribution histogram of intracellular fluorophore concentration for **a**, eGFP nucleofected cells 72 h after transfection and **b**, CMFDA stained HEK 293 cells. *n* gives the number of investigated cells (sample size). The median value is listed next to the notched box. Whiskers extend to 5 % and 95 % of the data.

Using this technique, only the brightest cells providing the maximum gain are selected for the experiment. We partially attribute the two order of magnitude range of intracellular fluorophore concentration to the unavailability of FACS in our experiments. In conclusion, even after optimizing the transfection procedure it was not possible to obtain a cell population with a intracellular fluorophore concentration distribution suitable for a single cell laser. Only a small number of cells in a population appear to reach sufficient brightness for lasing. A FACS system might have helped to select only the brightest cells and hence achieve a concentration distribution with a significantly higher median value. Since a FACS machine was not available, we explored a different strategy.

Another way to obtain a population with higher intracellular fluorophore concentration distribution is to change the gain material. In many biological experiments, synthetic dyes rather than fluorescent proteins are used to label cells. This approach is less time consuming and in many cases yields brighter fluorescence emission [178]. For further experiments the synthetic dye 5-chloromethyl-fluorescein diacetate (CMFDA, Life Technologies) was selected for cell staining. This fluorescein derivate only becomes fluorescent when it interacts with the cytoplasm and this interaction also modifies the dye to become membrane-impermeable [163]. Furthermore, the slightly higher quantum yield ϕ and extinction coefficient ϵ of the CMFDA compared to the fluorescent protein eGFP contribute to a more efficient fluorescence emission

Table 4.1: Maximum and median intracellular fluorophore concentration c of nucleofected (eGFP) and stained (CMFDA) cells.

Fluorescent Material	c_{max} [µM]	c_{med} [µM]
eGFP	115 ± 13	5 ± 1
CMFDA	782 ± 93	324 ± 6

and therefore even relax the requirements for intracellular fluorophore concentrations. HEK 293 cells were incubated in a CMFDA solution with a concentration of 200 µM for 30 min. This staining concentration exceeds the suppliers recommendation (25 µM) by almost one order of magnitude. However, a cell viability test proved, that the higher concentration had no detrimental effect on the cells. A sample of 400 CMFDA stained cells was investigated using the fluorescence microscopy method explained above. Figure 4.4b shows the intracellular fluorophore concentration distribution directly after the staining procedure. The median concentration $c_{med} = (324 \pm 6)\,\mu M$ is significantly higher compared to eGFP transfected cells and even exceeds the concentration of the staining solution. We attribute this increase in concentration over the original CMFDA staining solution to an intracellular accumulation of non-membrane-permeable dye. The box plot indicates that 50 % of the data fall in a concentration range from 268.4 µM to 385.4 µM and are therefore close to the anticipated 300 µM. The brightest cell in this cell sample showed an intracellular fluorophore concentration of $c_{max} = (782 \pm 93)\,\mu M$. Table 4.1 summarizes the median and maximum intracellular fluorophore concentration for eGFP transfected and CMFDA stained HEK 293 cells. For the CMFDA stained cells, the staining efficiency (percentage of stained cells in a culture) was not measured using a flow cytometer but estimated to be $\approx 100\,\%$ using a fluorescence microscope. The staining process is based on the diffusion of initially membrane-permeable fluorophores into the cell cytoplasm and hence the high staining concentration (200 µM) and long staining time (30 min) are responsible for the high staining efficiency. To conclude, due to a significantly higher fluorescence signal achieved with staining compared to transfecting cells, the CMFDA dye is used as an intracellular gain medium further on. Moreover, the CMFDA staining process is less time consuming, simpler and cheaper compared to eGFP transfection. However, if there is the need for an even more biologically compatible laser it may be required to return to cell produced eGFP as the gain material.

4.1.2 Cavity Fabrication and Optical Investigation

Having found a suitable intracellular gain material, this section will focus on the the fabrication of three different microcavity systems and the optical setup to investigate them. The three microcavity systems are the aforementioned single cell lasers, a cavity structure containing fluorescent microspheres mimicking the geometrical properties of cells and an unstructured microcavity filled with only a fluorescent dye solution as a reference. All cavity systems rely on the use of two highly reflective circular DBR mirrors with a diameter of 25.4 mm (purchased from Melles Griot). The stop band with a reflectivity $R > 99\,\%$ of each mirror is centered at 532 nm and extents from 480 nm to 590 nm. The cavity separation was controlled by sprinkling glass beads with a well-defined diameter of $(10.0 \pm 1.0)\,\mu$m (Thermo Scientific 9010) on the bottom mirror and gluing the second mirror on top using an adhesive polymer. For the single cell laser, 20 µL of cell solution was introduced into the cavity via capillary forces through the cavity void from the edges. The cell solution consisted of fluorescent HEK 293 cells suspended in phosphate buffered saline solution (PBS) to provide physiological osmolarity and ion concentration as well as reduce the background fluorescence (see Fig. 4.5a and b). The fluorescent micorsphere cavity was fabricated in a similar fashion. Here, internally dye doped (Firefli Green, $\lambda_{\text{max}} = 540$ nm) polystyrene divinylbenzene (PS-DVB) microspheres with a refractive index $n = 1.60$ (purchased from Fisher Scientific) were used to mimic the geometrical properties of cells. The microspheres with an average diameter of 15 µm were suspended in immersion oil ($n = 1.51$) and introduced into a microcavity using the same technique as for the cell solution. In this case the two DBR mirrors were separated by glass beads with a nominal diameter of 20 µm. Lastly, as a reference and to study the emission without in-plane confinement, a microcavity containing the fluorescent dye PM556 dissolved to a concentration of 5 mM in deionized water was fabricated. A refractive index of $n = 1.342 \pm 0.015$ was measured for the dye solution using a diffraction grating (see Section 5.3).

All three cavity systems were optically characterized using the custom built inverted microscope introduced in Section 3.2. Laser beam pulses were generated in the optical parametric oscillator (OPO) tuned to 465 nm (pulse duration, 5 ns; repetition rate, 5 Hz) and passed into a 40× microscope objective ($NA = 0.55$) to excite the microcavity samples. The setup was used in standard configuration (see Fig. 3.6a and b) to record spectrally resolved emission profiles. For hyperspectral-imaging, the slit of the spectrometer was opened to decompose the near-

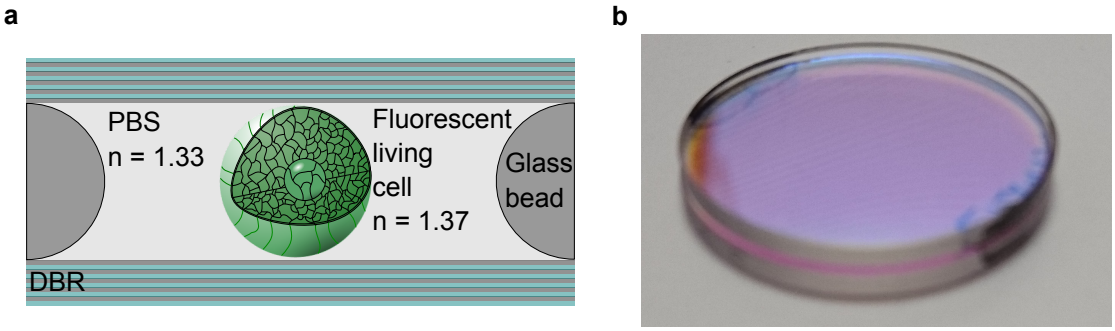

Figure 4.5: Illustration (**a**) and photograph (**b**) of a microcavity containing fluorescent cells suspended in phosphate buffered saline solution (PBS). The distributed Bragg reflector (DBR) mirrors are separated by glass beads and glued together using an adhesive polymer (black stains). Adapted from Ref. [171].

field emission into the different wavelength components. To record the near-field emission and bright field images of the microcavity, the light was passed to a separate collection arm via a flip mirror and projected onto a CCD camera using a lens. In order to obtain angle dependent and spectrally decomposed emission profiles, the setup was used in Fourier-imaging mode (see Fig. 3.6c and d).

4.2 Basic Laser Characterization

While the laser emission of single cell lasers has been described in the literature [33, 38, 134, 179], for context and completeness we summarize the basic laser characterization of single cell lasers based on CMFDA here and compare them to similar microcavity structures not incorporating biological cells. Figure 4.6a shows a schematic representation of the investigated single cell laser together with an example bright-field image of HEK 293 cells within the cavity and a typical near-field emission pattern upon optical excitation of these cells. The near-field emission shows a superposition of multiple modes. Furthermore, the input-output characteristics of a single cell laser is shown. Above a threshold pump pulse energy of 25 nJ a superlinear increase in the output signal can be observed. This is an indication for laser emission and this claim is further supported by the appearance of narrow emission peaks in the spectrum. These peaks are clustered in three groups and previous work has shown that within each group the peaks originate from multiple transverse lasing modes whereas the splitting between the groups can be attributed to different longitudinal lasing modes [33]. At low pump pulse energies (< 25 nJ), only a weak and spectrally broad fluorescence signal originating from the

intracellular CMFDA fluorophores was observed.

To further understand and study the laser emission of a single cell laser, we designed a simplified cavity model with similar geometrical and optical properties. Here, dye doped green fluorescent polystyrene beads with diameters similar to trypsinized HEK 293 cells were placed in a Fabry-Pérot cavity (see Fig. 4.6b). These microspheres are similar to those used for intracellular lasers discussed in Section 2.5 and can be operated as lasers even outside a Fabry-Pérot cavity under optical excitation. This process relies on total internal reflection and the formation of whispering gallery modes with high Q-factors for which a substantial refractive index contrast between polymer bead and surrounding medium (e.g. air with $\Delta n \approx 0.6$ or water with $\Delta n \approx 0.27$) needs to be achieved. For the purpose of mimicking a single cell laser with a refractive index contrast of $\Delta n \approx 0.04$ between cell interior and surrounding medium (PBS), this situation is not desirable. By dispersing the microspheres in a high refractive index immersion oil rather than in PBS, we achieved an estimated refractive index contrast of $\Delta n \approx 0.09$ and therefore circumvented the formation of whispering gallery modes with high Q-factors. Figure 4.6b shows a bright-field image and the near-field lasing emission of a fluorescent microsphere with a diameter of 12.5 µm embedded in a microcavity. The input-output characteristics show a superlinear increase of output power at pump pulse energies above 4 nJ. This is a $\approx$ 6-fold pump threshold reduction compared to the single cell laser, which can be attributed to the higher accumulation of dye molecules within the polystyrene bead, less intracavity scattering due to a higher optical uniformity of the bead and the slightly higher refractive index contrast Δn. This results in an increased lensing effect compared to the single cell laser. However, it is not possible to rule out that there is also an effect of the longer cavity and the use of a different dye on the threshold. The appearance of multiple peaks in the emission spectrum is similar to the previously discussed situation for a single cell laser and expected for an in-plane structured Fabry-Pérot-like cavity. Again, the clusters can be explained by the formation of multiple transverse modes for each longitudinal laser mode. The separation of longitudinal modes is called the free spectral range (FSR) of the laser cavity and is $\Delta\lambda_{\mathrm{FSR}} = (4.1 \pm 0.2)\,\mathrm{nm}$. This corresponds to a geometrical cavity length of $l_c = \lambda_0^2/2n_c\Delta\lambda_{\mathrm{FSR}} = (20.5 \pm 1.6)\,\mu\mathrm{m}$, consistent with the 20 µm glass beads used as spacers for the cavity separation. Here, λ_0 is the vacuum wavelength and n_c the average intracavity refractive index.

Both cavities discussed above incorporated structures leading to an in-plane refractive index contrast. To further understand the emission properties of the single cell and the micro-

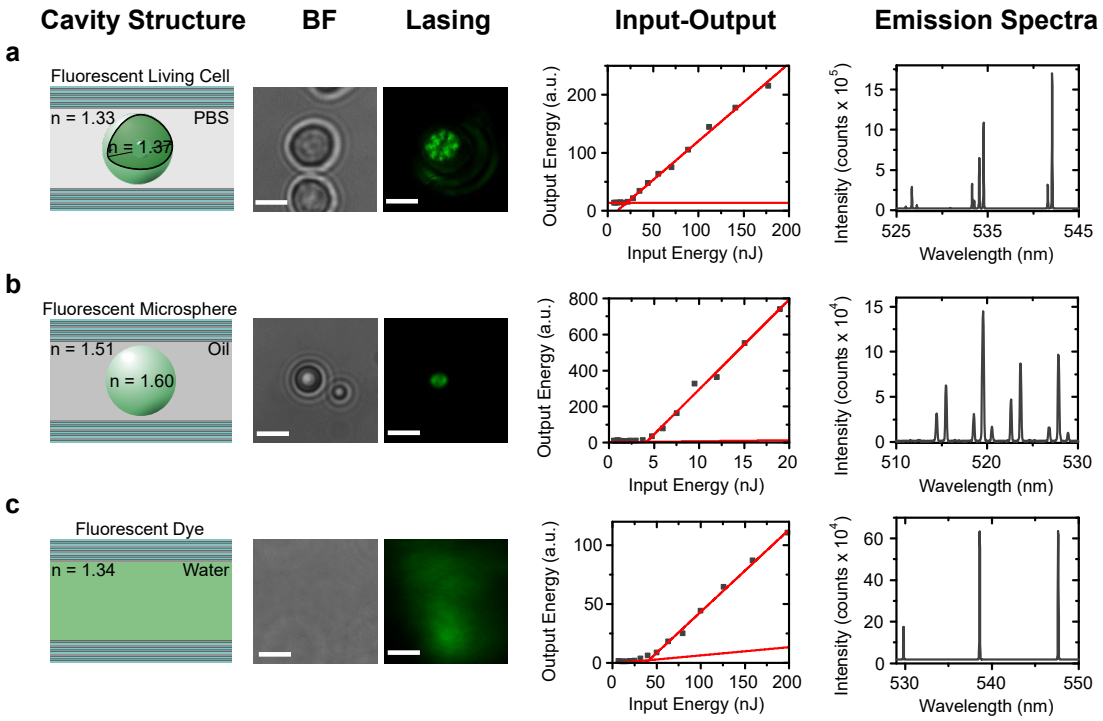

Figure 4.6: Basic laser characterization of three different microcavity structures based on **a**, a fluorescent living cell in phosphate buffered saline (PBS) solution, **b**, a fluorescent polystyrene microsphere in immersion oil and **c**, a fluorescent dye solution. From left to right, shown are an illustration , a bright-field (BF) image, the near-field lasing emission, the input-output characteristics (red lines, linear fit to measured data points) and an emission spectrum above threshold of the respective microcavity structure. Scale bars, 20 µm. Adapted from Ref. [171].

sphere laser, a simple cavity structure filled with only a fluorescent dye solution showing a uniform in-plane refractive index was investigated (see Fig. 4.6c). Compared to the previous cavities, the bright-field image does not show any distinct features but only the dye solution filled cavity. The near-field emission originates from the entire pump spot (diameter, $\approx 15\,\mu m$) and some in-plane scattering due to the absence of in-plane confinement. The onset for lasing at a pump pulse energy of 50 nJ is higher than for the cavity structures with in-plane photonic confinement. Similar to the other cavities the emission spectrum above threshold is composed of a series of sharp peaks. However, in this case, the peaks appear as individual peaks separated by the FSR ($\Delta\lambda_{FSR} = (9.1 \pm 0.2)\,nm$) and do not show a splitting into multiple transverse modes. Consistent with the 10 µm glass beads used to separate the mirrors, the FSR corresponds to a cavity length of $l_c = (11.5 \pm 0.9)\,\mu m$.

4.3 Cell Induced Optical Confinement

For the understanding of the following sections, it is important to be familiar with the available imaging possibilities and how the obtained data can be interpreted. Figure 4.7a shows a typical emission spectrum of a single cell laser consisting of a series of multiple narrow-band peaks. To identify the spectrally decomposed peaks as longitudinal and transverse modes and assign the respective mode numbers, it is possible to use a technique called hyperspectral-imaging. Here, the slit of the spectrometer is opened to decompose the near-field emission pattern of a single cell laser (see Fig. 4.7b) in to its spectral components (for further details see Section 4.1.2). Figure 4.7c shows an example hyperspectral-image associated to the spectrum shown above (Fig. 4.7a) and the near-field emission shown on the left hand side (Fig. 4.7b). Using this technique we can conclude that the seemingly random pattern in the near-field emission is actually an overlay of multiple lasing modes operating simultaneously. To label the different modes, the transverse mode numbers p and q and the longitudinal mode number m are given as $(p,q)_m$. It is further possible to conclude that all modes marked with a bracket belong to the same longitudinal mode family comprising the same collection of multiple transverse modes. In this example we can identify the mode family m ranging from 545 nm to 549 nm and the mode family $m-1$ ranging from 538 nm to 542 nm. The transverse modes are of Ince-Gaussian nature and can be identified as as e.g. $(0,0)_m$ to $(3,0)_m$ modes with increasing photon energy. It was shown that this imaging technique can also be used to study the osmotic pressure of single cells by recording the spectral position of individual lasing modes over time [38].

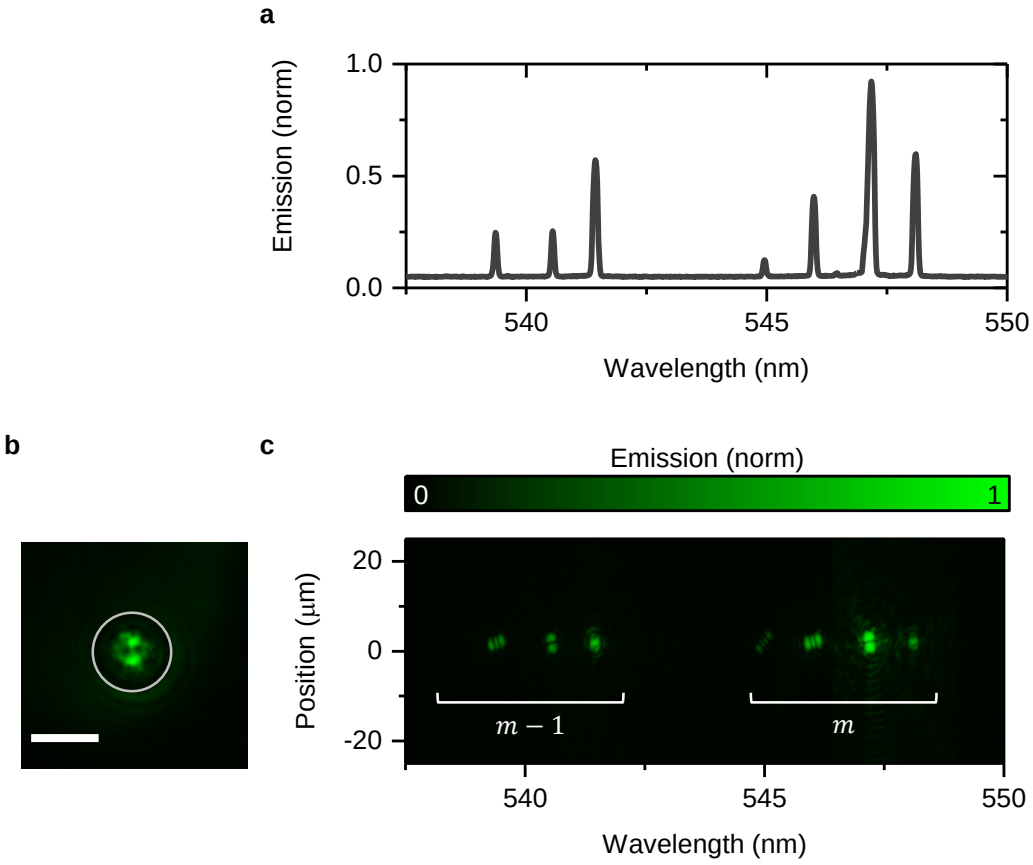

Figure 4.7: Single cell laser emission. **a**, Spectrally decomposed emission spectrum of a single cell laser. **b**, Near-field emission image of the same single cell laser. The cell boundary is marked with a white line. Scale bar 10 μm. **c**, Hyperspectral emission image of the same single cell laser. The longitudinal mode families (m and $m-1$) are marked with white brackets. Adapted from Ref. [171].

To explore the refractive index landscape of single cell lasers and understand the cavity physics in more detail, a combined hyperspectral- and Fourier-imaging system is used to investigate the relation between real-and momentum-space emission from the microcavities. Within a Fabry-Pérot-like microcavity, standing waves form at normal incidence whenever the optical path length of the cavity $l_c n_c$ is an integer multiple m of half the wavelength $\lambda_c/2$ of the emitted light

$$l_c n_c = m\frac{\lambda_c}{2}; \quad m \in \mathbb{N}. \tag{4.2}$$

m is also referred to as the longitudinal mode number. The conservation of energy and momentum dictates that photons within the microcavity can only attain a specific wave vector $\boldsymbol{k}$ which is related to the photon energy E by the general dispersion relation

$$E = \hbar c|\boldsymbol{k}| = \hbar c\sqrt{k_z^2 + k_x^2 + k_y^2}, \tag{4.3}$$

where $\hbar$ is the reduced Planck constant, c the speed of light and k_j the projection of the wave vector $\boldsymbol{k}$ into the j-direction ($j = x, y, z$). The projection of the wave vector in z-direction is defined normal to the mirror surface and the projection in x and y-direction is tangential to the mirror surface (in-plane). Figure 4.8 shows the Fourier- and real-space emission for the three investigated microcavity configurations. The Fourier-space emission for the microcavity filled with only a solution of fluorescent dye (see Fig. 4.8c) shows a nearly parabolic cavity mode. This cavity mode originates from the $1D$ photonic confinement in z-direction given by the mirrors. The absence of in-plane photonic confinement allows the wave vector in x and y-direction (k_x, k_y) to take arbitrary values. Defining θ as the angle to the normal of the cavity plane allows to approximate the angle dependence of the wave vector $|\boldsymbol{k}| = k_z/\cos(\theta) \approx (2\pi/\lambda_c)(1 + \theta^2/2)$ for small θ. This allows to rewrite an approximation for Eq. 4.3

$$E \approx \hbar c\frac{m\pi}{l_c n_c}\left(1 + \frac{\theta^2}{2}\right). \tag{4.4}$$

A fit of Eq. 4.4 to the Fourier-space emission data in Fig. 4.8c yields a cavity mode (white dashed line) with a longitudinal mode number $m = 73$. Above threshold the lasing emission starts to emerge from the lowest energy point on the nearly parabolic cavity mode at $\theta = 0°$. Additionally to the main emission at $\theta = 0°$ some laser light with the same energy (or wavelength) is scattered towards larger angles, into cavity modes with a lower longitudinal mode number. Figure 4.8c further shows the real-space emission of the same cavity. The emission

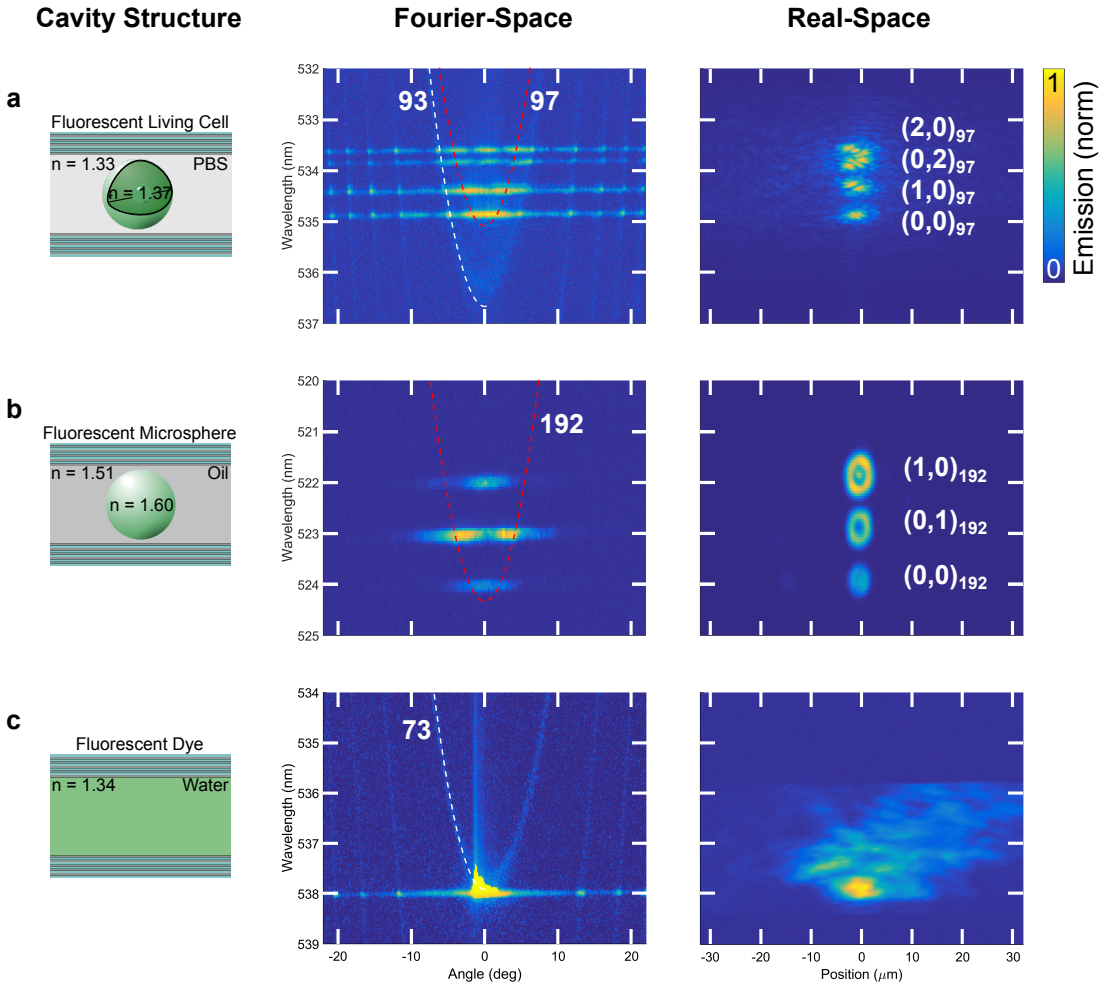

Figure 4.8: Fourier- and real-space lasing characterization from **a**, a single cell laser, **b**, a microsphere cavity laser and **c**, a dye solution in a microcavity. From left to right, shown are an illustration, the normalized Fourier-space and the normalized real-space emission of the respective cavity system. The Fourier-space emission shows the dependence of the in-plane angle on the emission wavelength. The red dashed lines represent a parabolic fit to the data, assuming a dispersion for an unstructured cavity with a refractive index equal to the refractive index of the cell or microsphere. The white dashed lines represent a fit to the data with the same cavity dispersion but assuming a bare cavity mode (refractive index of the medium). The numbers indicate the longitudinal mode number m. The real-space emission shows a spectrally decomposed heatmap of the near-field emission for the three cavity systems. The transverse mode numbers p and q and the longitudinal mode number m are given as $(p,q)_m$. Adapted from Ref. [171].

profile resembles the Gaussian-profile of the pump spot with some additional unstructured scattering away from the main emission spot. This can be attributed to in-plane scattering induced by the surface roughness of the mirrors and some tilt between the mirrors leading to laser beam walk-off in the absence of in-plane photonic confinement.

Placing a fluorescent cell suspended in PBS into the microcavity changes the emission properties in Fourier- and real-space. Figure 4.8a shows that there are now several discrete energetic lasing states in the Fourier-space emission. These states can be assigned to a specific cavity mode (red dashed line, longitudinal mode number $m = 97$) describing the propagation of a mode through an unstructured cavity with an intracavity refractive index equal to the refractive index of a cell. The refractive index difference between cell and surrounding (PBS) creates a unique refractive index landscape within the microcavity and introduces a refractive index contrast in the x-y-plane. This causes the wave vector projections k_x and k_y to take discrete values and therefore violates the assumptions for Eq. 4.4. Hence, the dispersion relation (Eq. 4.3) for this microcavity system does not resemble a nearly parabolic shape but takes on a series of discrete modes that are blue shifted in energy compared to the ground state energy of the corresponding virtual parabolic cavity mode.

The Fourier-space emission further shows a faint trace of the parabolic dispersion originating from the bare cavity mode (white dashed line, longitudinal mode number $m = 93$). The parabola can be fitted to the data by assuming the refractive index of the surrounding medium. This can be attributed to a small number of photons being scattered by intracellular structures into the bare cavity filled with PBS. Similar to the cavity filled with a fluorescent dye solution the laser emission is also scattered towards larger angles into lower order cavity modes.

The real-space emission of the single cell laser Fig. 4.8a, (Real-space) shows the transverse mode nature of the discrete lasing states. The elliptically shaped transverse modes can be identified as so called Ince-Gaussian modes (IGMs). IGMs are generalized orthogonal paraxial modes in elliptical coordinates. They describe the transition between Hermite-Gaussian modes (HGMs) with rectangular symmetry and Laguerre-Gaussian modes (LGMs) with circular symmetry. The appearance of IGMs can be attributed to the slightly elliptical shape of the cells and possibly the spatial variation of refractive index within the cell [180]. The observed modes can be labeled according to their shape and energetic position with mode indices from $(0,0)_{97}$ to $(2,0)_{97}$ (as before, the transverse mode numbers p and q and the longitudinal mode

number m are given as $(p,q)_m$). According to theory modes with the same longitudinal mode number m and the same transverse mode numbers p,q = const. are degenerated and hence have the same discrete energetic position. The slight energetic shift between the $(2,0)_{97}$ and $(0,2)_{97}$ mode is most likely a result of the elliptical shape of the cell and possibly some tilt between the two cavity mirrors.

Since the number of nodes and energetic position for a specific mode is identical in Fourier- and real-space, it is possible to predict e.g. the transverse mode number and wavelength of a certain mode in real-space from the energetic state in Fourier-space. As an example, the $(0,0)_{97}$ IGM in-real space shows one peak and zero nodes at the same energy in Fourier-space and the $(1,0)_{97}$ IGM in real-space shows two peaks and one node at the same energy in Fourier-space, etc.

Lastly, to mimic the single cell laser with almost perfect sphericity and reduced scattering, the emission from a dye doped polystyrene microsphere in immersion oil between two DBR mirrors was investigated. The discrete energetic states in Fourier-space are similar to the single cell laser emission. However, the faint emission originating from the bare cavity mode is absent. This can be attributed to the reduced internal scattering together with the slightly enhanced photonic confinement due to the increased refractive index contrast between microsphere and surrounding medium compared with the single cell laser. The microsphere laser modes in real-space can be identified as the first three fundamental LGMs (from $(0,0)_{192}$ to $(1,0)_{192}$). The creation of LGMs rather than IGMs or HGMs can be attributed to the more spherical symmetry of the microspheres compared to the cells. Similarly to the single cell laser, the energetic position and transverse mode shape of the real-space emission can be predicted from the Fourier-space emission.

4.4 Single Cell Real- vs Fourier-space Emission

Devices based on organic or inorganic semiconductors are often engineered and optimized to support certain photonic modes. Including for example the photonic structures discussed in Chapters 5-7. The rather uniform and predictable refractive index distribution together with the precise control of spatial extend (e.g. layer thickness) makes it possible to create a refractive index landscape perfectly matched to desired photonic modes. The large variability of cells in shape and size, however, makes it challenging to predict specific photonic modes that

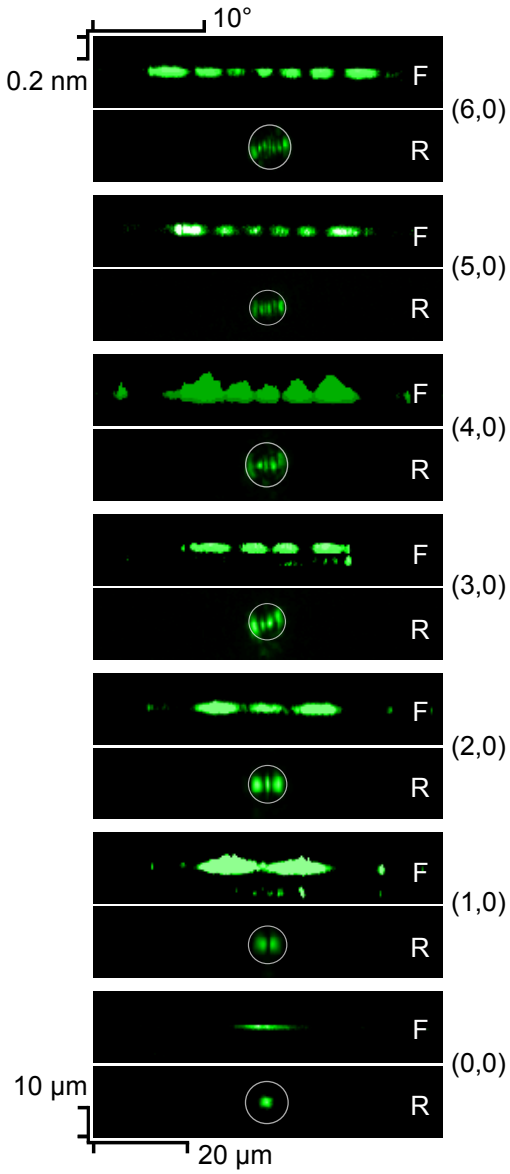

Figure 4.9: Fourier-space (F) and real-space (R) lasing emission images from seven different HEK 293 cells. The Ince-Gaussian modes (IGMs) are ordered by their corresponding mode number from $(0,0)$ to $(6,0)$. The cell boundary of each individual cell is indicated by a white line in the real-space emission. The corresponding scale is given in µm × µm in real-space and nm × degree angle in Fourier-space. Adapted from Ref. [171].

are created and supported by biological lasers based on individual single cells. This seemingly apparent drawback can however be utilized to distinguish individual cells from each other, just by observing their unique transverse mode pattern.

Figure 4.9 shows the unique transverse mode patterns and energetic states created in seven different lasing cells in real- and Fourier-space. Even though the cell boundary (indicated as a white line in the real-space emission image) for all seven cells and hence the size and shape

of each cell is very similar, and make them hardly distinguishable using standard microscopy techniques, the lasing modes in Fourier- and real-space emission are all different and can be used as an identifier for a certain cell.

As before, the number of nodes in the energetic states in Fourier-space is the same as the number of nodes in the transverse modes (IGMs) in real-space. Furthermore, while modes with high transverse mode numbers (e.g. $(6,0)$) are still spatially confined by the cell boundary in real space, the same modes are emitted into a large range of angles due to their energetically higher position in the cavity dispersion. As an example, mode number $(6,0)$ and $(0,0)$ originate from cells with approximately the same spatial extent in real-space but show a different divergence of $\Delta\theta = (21 \pm 1)^\circ$ and $\Delta\theta = (5 \pm 1)^\circ$, respectively. The introduction of photonic confinement due to the refractive index contrast at the cell boundary can further be assessed by the spatial extent of higher mode numbers in real-space. For example, the two outer emission peaks originating from the cell supporting mode $(3,0)$ follow the slightly elliptical shape of the cell.

4.5 Input-Output Analysis in Fourier-space

To further explore the fundamental creation of different lasing states/modes in a single cell laser, the pump energy dependent Fourier-space emission is investigated. This makes it possible to assess the lasing threshold for different states/modes at different energies and momenta. To avoid confusion, the phrase “state” is used from now on when talking about a certain emission peak at a specific point in energy and momentum. As before, “mode” describes the entire mode present at a constant energy over the whole angle range in Fourier-space. Figure 4.10a shows the Fourier-space emission of a single cell laser at a fixed pump pulse energy of 150 nJ operating at the longitudinal mode numbers $m = 111$ and $m = 112$. Again, the nearly parabolic cavity dispersion expected for an unstructured cavity with an intracavity refractive index equal to the refractive index of the cell is indicated with a red dashed line.

For this single cell laser the threshold behavior of four different lasing states is analyzed. The states are marked with white boxes (region of interest, ROI) and are labeled with the respective mode numbers in the Fourier-space emission image (see Fig. 4.10a). To assess the energy dependent emission of a certain lasing state, the corresponding ROI at different pump pulse energies was integrated on the EM-CCD detector attached to the spectrometer.

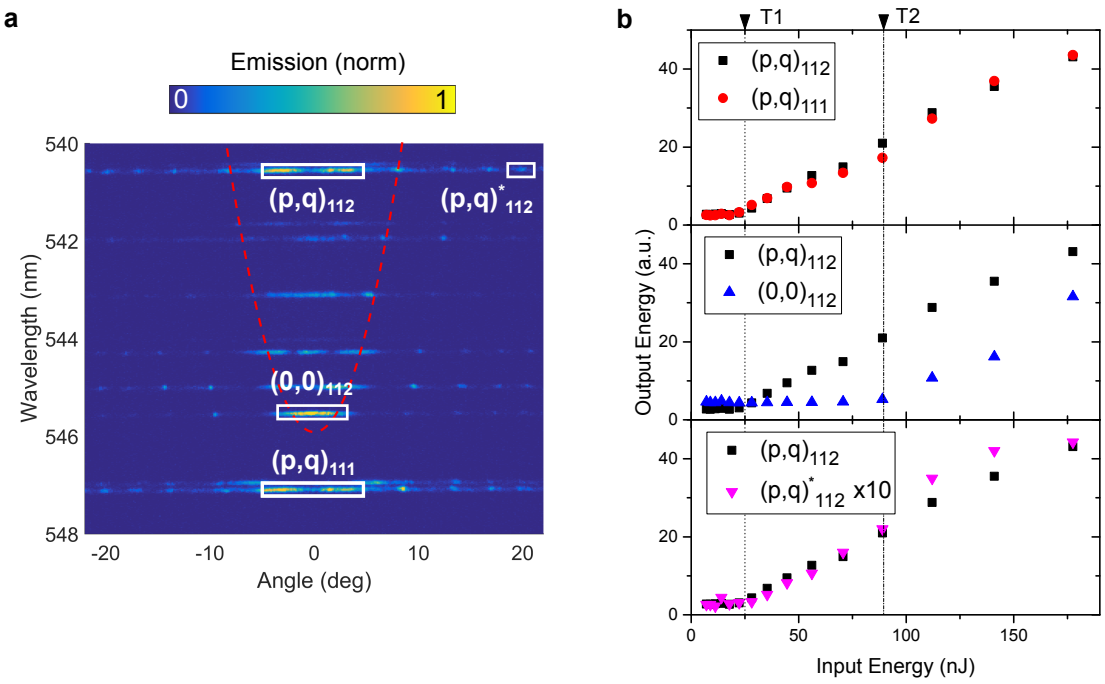

Figure 4.10: Input-output characteristics of a single cell laser for different lasing modes at different energies and momenta in Fourier-space. **a**, Fourier-space emission of a single cell laser at a fixed pump pulse energy of $\approx 140\,\mathrm{nJ}$. The white boxes indicate the different region of interest (ROI) where the pump energy dependent emission of individual modes was analyzed (labeled with the respective mode number). The red dashed line indicates the cavity dispersion with a longitudinal mode number 112 experienced by photons propagating through an unstructured cavity with an intracavity refractive index equal to the refractive index of the cell. **b**, Input-output curves for different mode energies and momenta corresponding to the ROIs in a. The lasing threshold of mode $(p,q)_{112}$ (black symbols) is compared to the same transverse mode in the adjacent longitudinal mode family $(p,q)_{111}$ (red symbols), to the fundamental $(0,0)_{112}$ in the same longitudinal mode family (blue symbols) and to an emission state within the same mode but at larger angles ($(p,q)^*_{112}$, purple symbols, output energy scaled by $\times 10$ for better visibility). Distinct threshold values are indicated with $T1$ and $T2$. Adapted from Ref. [171].

Firstly, the threshold for the state with the highest energetic position (emission wavelength, $\lambda = (540.6 \pm 0.2)\,\mathrm{nm}$) labeled $(p,q)_{112}$ is analyzed. The top panel in Fig. 4.10b (black symbols) shows the input-output characteristics of this state with a superlinear growth above a threshold pump pulse energy of 25 nJ (indicated as $T1$). Similarly, the threshold for an emission state with the same transverse mode number but in an adjacent longitudinal mode family (labeled $(p,q)_{111}$ in Fig. 4.10a and represented as red symbols in the top panel of Fig. 4.10b) is analyzed. The input-output data and threshold for the lasing state $(p,q)_{111}$ match well with those found for state $(p,q)_{112}$. Since both states are of the same transverse mode nature, they take on the same spatial profile and hence overlap similarly with the gain landscape inside the cell as well as with any scattering or absorbing particles in the cavity, presenting them with a similar gain and loss environment and hence leading to a similar threshold. Furthermore, the small difference in emission wavelength/energy and hence a similar spectral position in the gain spectrum does not lead to a significant reduction of available gain.

The fundamental $(0,0)_{112}$ mode appears at the low-energy end at the bottom of the cavity dispersion. The input-output characteristics are shown in the central panel of Fig. 4.10b (blue symbols) and the threshold pump pulse energy is 89 nJ (indicated as $T2$) and hence almost three times higher than for the $(p,q)_{112}$ state. Therefore, in complex biological photonic structures the lasing mode with the lowest threshold is not necessarily a simple fundamental mode but can be of higher order and complexity. This situation is, for example, different in precisely fabricated vertical-cavity surface-emitting lasers (VCSELs) where the most favorable lasing mode is the fundamental mode [181]. This suggests that the refractive index and gain landscape defined by the cell can provide more gain to a mode with a larger spatial extent and complex structure.

Lastly, we analyzed the influence of the momentum position on the input-output characteristics of a specific lasing state within a transverse mode with constant energy. Here, the two different emission states $(p,q)_{112}$ emitting around 0° and $(p,q)^*_{112}$ emitting at higher angles are investigated. Their corresponding input-output characteristics are shown in the bottom panel of Fig. 4.10b (purple symbols for state $(p,q)^*_{112}$). Firstly, it is evident that the emission intensity from the higher momentum state $(p,q)^*_{112}$ is considerably weaker than for the emission close to zero in-plane momentum. The onset for lasing at 25 nJ, is similar for both emission states. This suggests that both emission states are originating from the same transverse mode and that the emission at larger momentum is indeed due to a linear scattering process from

the small momentum states into lower energy cavity dispersions. Interestingly, this is different to earlier findings on microcavities filled with the eGFP where the scattering from the emission state at zero momentum served as a catalyst to induce emission states at higher momentum showing increased thresholds [137].

4.6 Discussion

The results presented in this chapter provide direct evidence for $3D$ photonic confinement induced by a fluorescent cell placed into a microcavity utilizing combined Fourier- and hyper-spectral-imaging techniques. Comparing the emission properties of a biological single cell laser to those of a microcavity filled with only a fluorescent dye solution and a mirocavity filled with fluorescent microspheres as an idealized model system for the single cell laser, confirmed that the photonic confinement is introduced by the refractive index contrast between cell and surrounding medium. Furthermore, the emission states in Fourier-space allow a direct prediction of the unique transverse mode nature of a single cell laser in real-space. Those are unique for different cells and can hence be used as an easily accessible label or identifier for cells that are hardly distinguishable just by shape or size in real-space. The data also showed that the lasing emission is less directional with an increasing transverse mode number while the cell boundary confines the light in real-space. Lastly, the formation of different energy and momentum emission states and modes was investigated by analyzing their input-output characteristics.

This chapter shed light on the fundamental processes involved in the creation of stimulated emission and hence lasing in single biological cells. Especially the dependence of the transverse mode nature on the unique refractive index and gain landscape created by the cell, may in the future be used for sensing and monitoring intracellular processes by means of a cell laser based cytometer. In fact, after our results were published, first applications into this direction have been attempted [135].

5

Water-based Optofluidic DFB Lasers

Optofluidic distributed feedback (DFB) lasers have emerged as a cost-effective tool enabling lab-on-a-chip diagnostics and spectroscopy applications by combining optics and microfluidics. However, due to their current design limitations, high refractive index solvents are needed which reduces their biocompatibility.

The design considerations and limitations of the most important optofluidic waveguide lasers and possible ways of improving them, including evanescent pumping schemes, are discussed in Section 5.1. Next, in Section 5.2, these possible improvements are applied to a water based optofluidic DFB laser design where evanescent pumping is inevitable and simulations showing how a low refractive index substrate improves the waveguide quality and the amount of available modal gain are presented. The results discussed in Section 5.3 reveal the characteristic photonic band of the aforementioned devices via a passive and active angular dispersion analysis. This allows to determine crucial device parameters such as the thickness of the waveguide core or the refractive index of the fluidic gain material. Having full knowledge of the devices at hand, we tested their lasing performance. The results are shown in Section 5.4, and indicate that the optimized waveguide

design together with the use of a mixed-order grating facilitated low-threshold lasing action in the water based DFB lasers. Furthermore, a convenient way of tailoring the divergence of the vertically emitted output beam is discussed. Lastly, in Section 5.5 the results obtained in the previous sections are discussed and possible applications are suggested.

The contents of this chapter have in parts been published in Ref. [182].

5.1 Optofluidic DFB Lasers

Optofluidic lasers are microfabricated coherent light sources incorporating a liquid gain material [37]. In contrast to their bulky ancestors, namely dye jet lasers of the last century [183], optofluidic lasers are much smaller in size and therefore easy and cheap to fabricate [97]. Besides providing optical gain, the liquid medium can be used to manipulate the optical properties of the emitted laser light. For example, the emission wavelength can be tuned by changing the solvent and hence the refractive index or by switching between different dye molecules [184, 185]. Furthermore the emission is more robust when compared to e.g. organic solid-state lasers since the liquid gain material is constantly replenished. This happens either by active circulation through a microfluidic system or simply diffusion, effectively reducing the accumulation of triplet states or photobleaching in the laser active region [20]. In combination with DFB resonators providing single mode operation, optofluidic DFB lasers are a perfect candidate for cost-effective integration on lab-on-a-chip devices for e.g. spectroscopy applications [186, 187]. Since most biological processes are taking place in a liquid environment, optofluidic DFB lasers are furthermore well suited for bio-sensing applications [184, 188, 189]. The low refractive index of the liquid gain material, however, imposes a challenge on the laser design.

Most commonly, optofluidic DFB lasers are fabricated following a liquid core waveguide (LCW) design. Figure 5.1a shows an illustration of a possible LCW device comprising a substrate and two low refractive index cladding layers with a high refractive index fluidic core layer sandwiched in between. Due to the higher refractive index of the fluidic core compared to the cladding layers, the electro-magnetic mode is waveguided in the core and only the evanescent part of the mode extends into the cladding layers. In such structures, the gain material is typically dissolved in the high index core solvent or buffer and hence a substantial overlap of the mode with the gain material is readily achieved [96]. Two common high refrac-

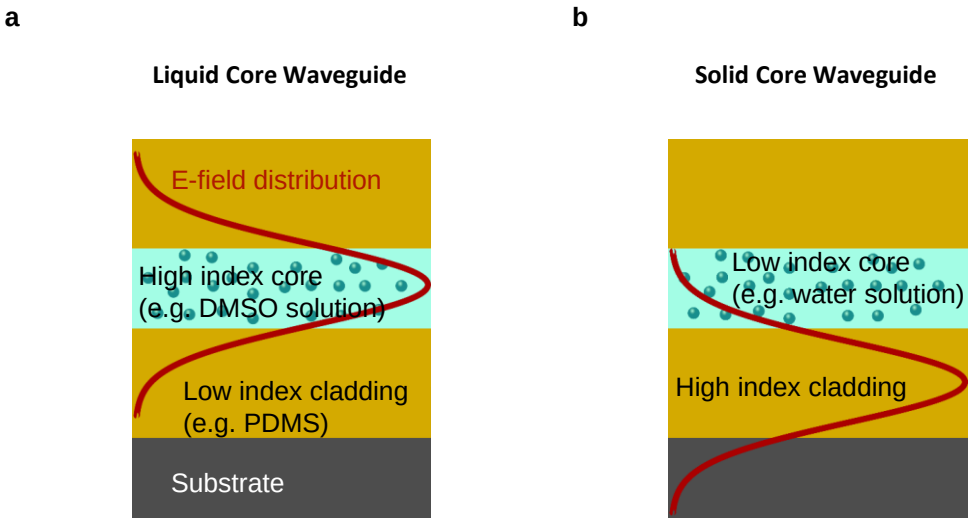

Figure 5.1: Illustration of two possible design considerations for optofluidic DFB lasers. **a**, The liquid core waveguide (LCW) design, where a high refractive index fluidic core surrounded by lower refractive index cladding layers acts as the waveguide confining the electric field (represented by a red solid line). **b**, The solid core waveguide (SCW) design, where a solid layer with a higher refractive index acting as the waveguide is positioned next to a fluidic layer with a lower refractive index. In both structures the DFB grating imprinted in the lower cladding layer is not shown.

tive index buffers are ethylene glycol and dimethyl sulfoxide (DMSO) [184, 185, 188–190]. These solvents are not biocompatible [191] and hence limit the application of optofluidic DFB lasers based on the LCW design in bio-sensing [36].

In order to overcome this limitation, it is possible to change the design of the optofluidic device to a solid core waveguide (SCW, see Fig. 5.1b). Here, the mode is confined in a polymer based high index waveguide adjacent to a lower index gain doped fluidic layer. The decoupling of waveguide layer and gain material relaxes the requirements on the refractive index of the fluidic component and allows the use of biocompatible low refractive index gain solvents, such as water. However, this design has the inherent drawback of reducing the modal gain since only the evanescent field of the laser-active waveguided mode overlaps with the gain region and hence contributes to the stimulated emission rate. This configuration is called evanescent pumping scheme and was first proposed by Ippen & Shank in 1972 [192] but has only been demonstrated experimentally recently by Song *et al.* in 2009 [190]. Even though it was possible to built a working laser device, the gain fluid needed to be doped with a high index fluid (DMSO) to obtain a sufficiently high mode overlap with the gain region. Furthermore, lasing thresholds have remained high (9.5 µJ [190]) compared to other optofluidic DFB lasers (90 nJ to 157 nJ [193]) which prevented a more wide spread use for bio applications.

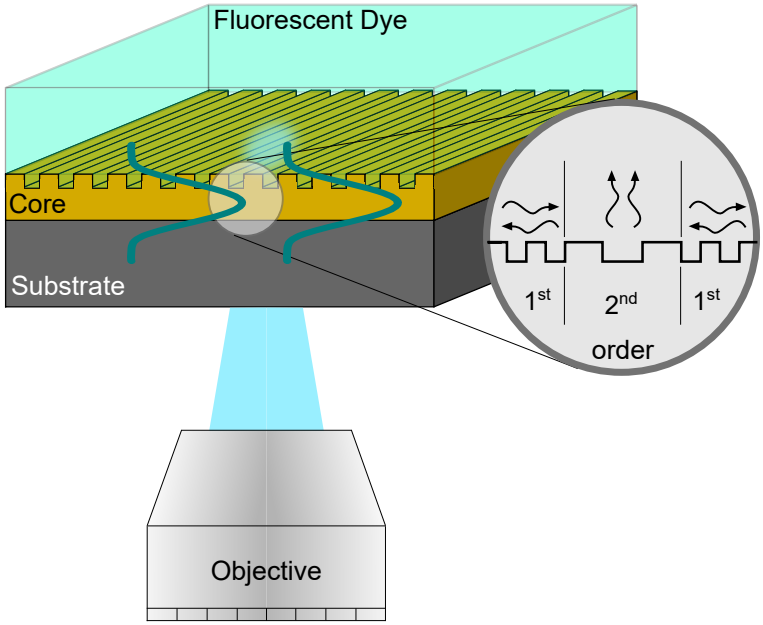

Figure 5.2: Illustration of the evanescently-pumped water based optofluidic DFB laser. The waveguide stack comprises a transparent substrate, a waveguide core incorporating an imprinted DFB grating and a fluorescent dye as the gain material. The structure is pumped through the transparent substrate and the waveguide core using a microscope objective. In order to confine the light, the waveguide core (thickness, several 100 nm) has a higher refractive than the adjacent cladding layers. The grating is a mixed-order grating, consisting mainly of first-order periods for in-plane feedback and a small section of second-order periods in the center to extract the light perpendicular to the surface. Adapted from Ref. [182].

To overcome these problems, we designed an optofluidic DFB laser as illustrated in Fig. 5.2. Here, a DFB grating was imprinted into a polymer waveguide on top of a rigid substrate and the fluorescent gain fluid was added as the upper cladding layer. From an optics point of view, the mode confinement in the bottom layer makes the use of a polymer upper cladding layer as shown in Fig. 5.1b redundant. Furthermore, using this configuration the gain fluid could be convientently added as a droplet on top of the DFB structure and an elaborate microfluidic channel system was not needed. A pumping scheme through the transparent substrate was applied to efficiently excite the fluorescent molecules close to the DFB structure. A microscope objective was used to simultaneously deliver the excitation pump beam and collect the emission. In order to obtain reduced laser thresholds, we used mixed-order gratings as discussed in Section 2.4. Further details on the grating production and the different grating structures used can be found in Section 3.1.3.

5.2 Laser Design and Mode Profile

In order to build an optofluidic DFB laser with reduced threshold, the overall goal is to optimize the structure such that the overlap of the waveguided mode with the gain layer is maximized. The structure and location of the waveguided mode depends mainly on the refractive index and the thickness of the different layers in the waveguide stack. In order to find suitable materials and corresponding layer thicknesses for our optofluidic DFB laser, we modeled and simulated the photonic properties using a self written MATLAB script (see Appendix A). For the simulations, it is possible to decompose the structure into an asymmetric three layer waveguide and a grating structure. Furthermore, the planar structure of the waveguide slab allows to use a two-dimensional simulation approach where the thickness of the two cladding layers is assumed to be semi-infinite. A rigorous mathematical derivation that describes the problem is given in Section 2.3.2. For the given dielectric asymmetric three layer waveguide slab, the photonic modes fulfill the relation

$$\frac{4\pi d}{\lambda_0}\sqrt{n_g^2 - n_{\text{eff}}^2} = \phi_s + \phi_d + 2M\pi, \quad M \in \mathbb{N}, \tag{5.1}$$

where d is the layer thickness of the core layer, λ_0 the vacuum wavelength, n_g the refractive index of the core layer, n_{eff} the effective refractive index of the confined mode, $\phi_{s/d}$ the Goos-Hänchen phase shift induced between the core layer and the substrate / dye cladding layer

and M an integer. The refractive index of each cladding layer (in our case, the substrate (s) and the dye (d) gain fluid) is incorporated in the Goos-Hänchen phase shift $\phi_{s/d}$. This is a transcendental equation which can not be solved analytically. The MATLAB script applies a numerical solver to find the effective refractive index n_{eff} for all TE and TM modes supported by the waveguide structure. In a next step, this result can be used and fed into the Helmholtz Equation with appropriate boundary conditions (a set of second-order differential equations) to obtain the electric field distribution and hence the mode profile for the given waveguide structure.

This approach was used to simulate the mode profile for a waveguide stack comprising a glass substrate, a polymer grating and a water based cladding layer. Fabricating the polymer grating on a glass substrate is a common material choice and routinely used for DFB lasers based on organic semiconductors. The assumed refractive indices are $n_s = 1.52$, $n_g = 1.54$ and $n_d = 1.33$ (all at $\lambda_0 = 530\,\text{nm}$) for the glass substrate, the polymer grating and the fluidic gain material, respectively. Using these parameters and an assumed waveguide thickness of $d = 500\,\text{nm}$, yields a mode overlap between gain region and photonic mode of only 2.2 %. This can be explained, by the close refractive index of the glass substrate and the polymer grating and subsequently a highly asymmetrical mode that is shifted away from the gain region and towards the substrate.

One strategy to improve the mode overlap with the gain region is to introduce a substrate with a lower refractive index and hence render the mode more symmetrical and reduce the fraction of the mode in the substrate. Figure 5.3a shows the $TE0$ mode profile of a photonic mode in a waveguide with a SiO_2 substrate ($n_{SiO_2} = 1.46$) and a core layer thickness of $d = 300\,\text{nm}$. The mode is still asymmetrical with a significant fraction being present in the substrate and hence a small overlap factor Γ of only 11.7 % (dashed area in Fig. 5.3a). However, compared to the glass substrate the mode overlap with the gain region is increased. This is achieved for an even thinner core layer d, for which modes would not be supported when using glass as a substrate. Changing the substrate material to MgF_2 with an even lower refractive index ($n_{MgF_2} = 1.39$) leads to a more symmetrical $TE0$ mode with an increased overlap factor $\Gamma = 18.4\,\%$ (see Fig. 5.3b). This can be attributed to the lower refractive index of MgF_2 compared to SiO_2. In fact, the structure based on a MgF_2 substrate is close to a symmetric waveguide.

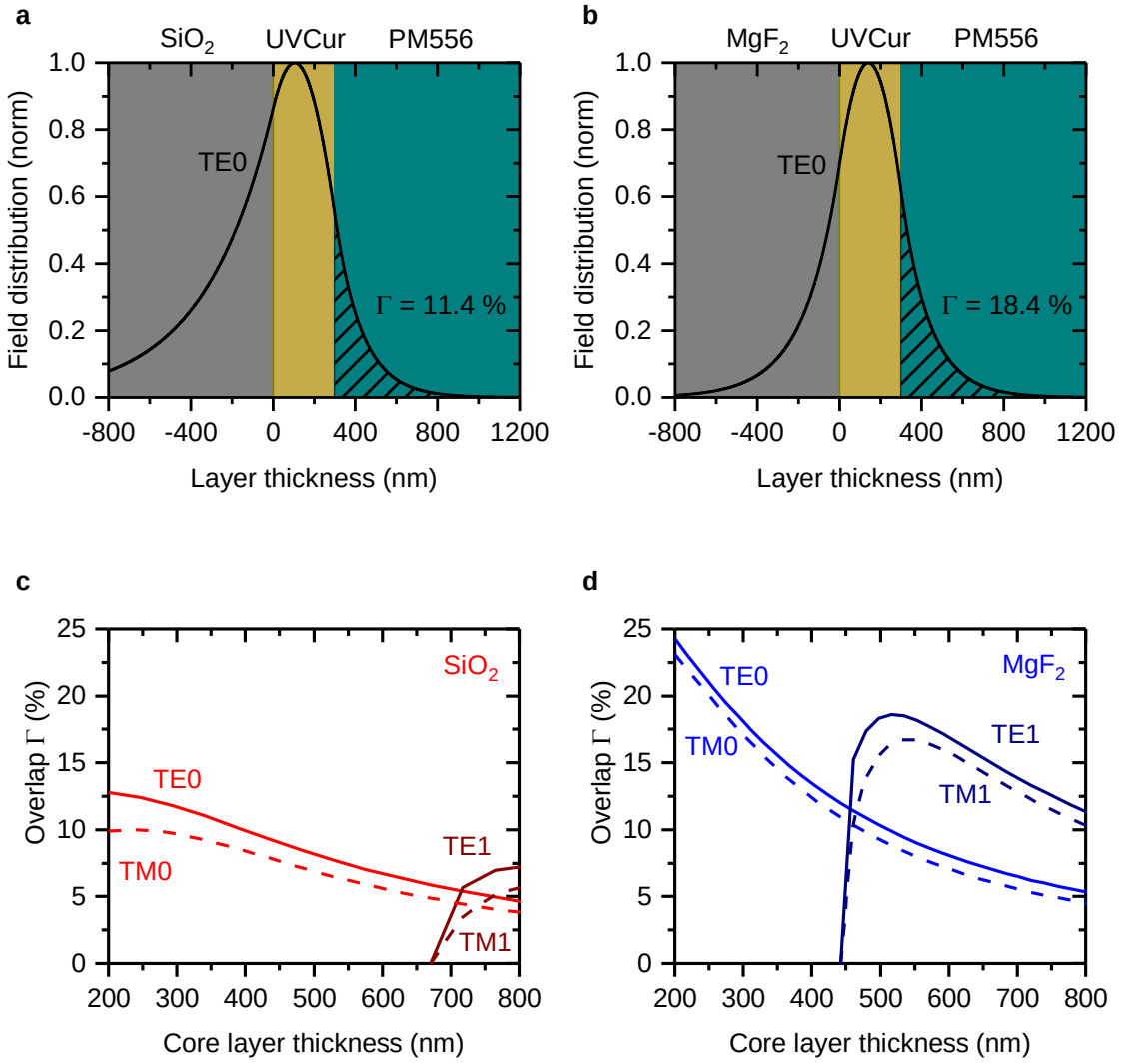

Figure 5.3: Waveguide simulations for the optofluidic DFB laser. **a** and **b**, $TE0$ mode simulations for a waveguide stack comprising a low refractive index SiO_2 (a) or MgF_2 (b) substrate, a higher refractive index UV curable resist (UVCur06) core and a fluidic gain layer (PM556). The solid line represents the $TE0$ mode for a core layer thickness of 300 nm. The dashed area represents the overlap of the $TE0$ mode with the gain layer and the overlap factor is $\Gamma = 11.4\%$ and $\Gamma = 18.4\%$ for the device based on a SiO_2 and MgF_2 substrate, respectively. **c** and **d**, Simulated overlap factors Γ for different core layer thicknesses d, different polarizations (TE and TM) and either SiO_2 (c) or MgF_2 (d) substrates. The highest overlap factors can be achieved with MgF_2 substrates and thin core layers. Adapted from Ref. [182].

The refractive index of the substrate layer is not the only parameter to influence the mode overlap. Changing the thickness d of the core layer also influences the mode shape and overlap factor Γ. Figure 5.3c shows the overlap factor Γ depending on the core layer thickness d for SiO_2 based devices. Higher order modes (e.g. $TE1$ or $TM1$) are only supported by waveguide structures with an increased core layer thickness ($> 700\,\text{nm}$) which limits their overlap with the gain region and is not desirable because it could lead to multi-mode lasing and mode beating. The overlap for $TE0$ and $TM0$ modes increases slightly with decreasing core layer thickness down to $d < 300\,\text{nm}$ where it saturates. The cut-off thickness for this structure is $d_{\text{cut}} = 168\,\text{nm}$. For MgF_2 based devices (see Fig. 5.3d), the overlap factor over the entire simulation range is higher than for devices based on SiO_2. Modes are supported by the MgF_2 substrate based waveguides for core layer thicknesses above 66 nm. Also, $TE0$ modes always show a higher overlap compared to $TM0$ modes and are thus expected to lase at lower thresholds.

5.3 Angular Dispersion of Optofluidic DFB Gratings

So far, we only assumed a waveguide device consisting of multiple planar dielectric layers and neglected the presence of the DFB grating. However, at the interface between solid waveguide and fluidic gain layer the light is Bragg scattered by the corrugation. The scattering angle θ depends on the wavelength λ, the effective refractive index n_{eff} of the propagating mode and the grating period Λ and can be described by

$$\frac{2\pi}{\lambda}\sin\theta = \pm\frac{2\pi n_{\text{eff}}}{\lambda} \pm m\frac{2\pi}{\Lambda}, \quad m \in \mathbb{N}, \tag{5.2}$$

where m is an integer. The resonance condition is fulfilled and distributed feedback can occur when the incident mode is diffracted into a counterpropagating mode with a phase shift of π. This yields the so called Bragg condition $m\lambda_B = 2n_{\text{eff}}\Lambda$ for second-order gratings. Light with the Bragg wavelength λ_B is scattered into counterpropagating modes within the waveguide and stimulated emission can occur. In order to determine the effective refractive index n_{eff} for a mode in a second-order DFB laser device, it is common practice to identify the lasing mode wavelength above threshold and consequently utilize the Bragg condition [194]. However, it is also possible to use the angle dependent emission from the DFB grating below threshold and fit the data to the dispersion relation described by Eq. 5.2.

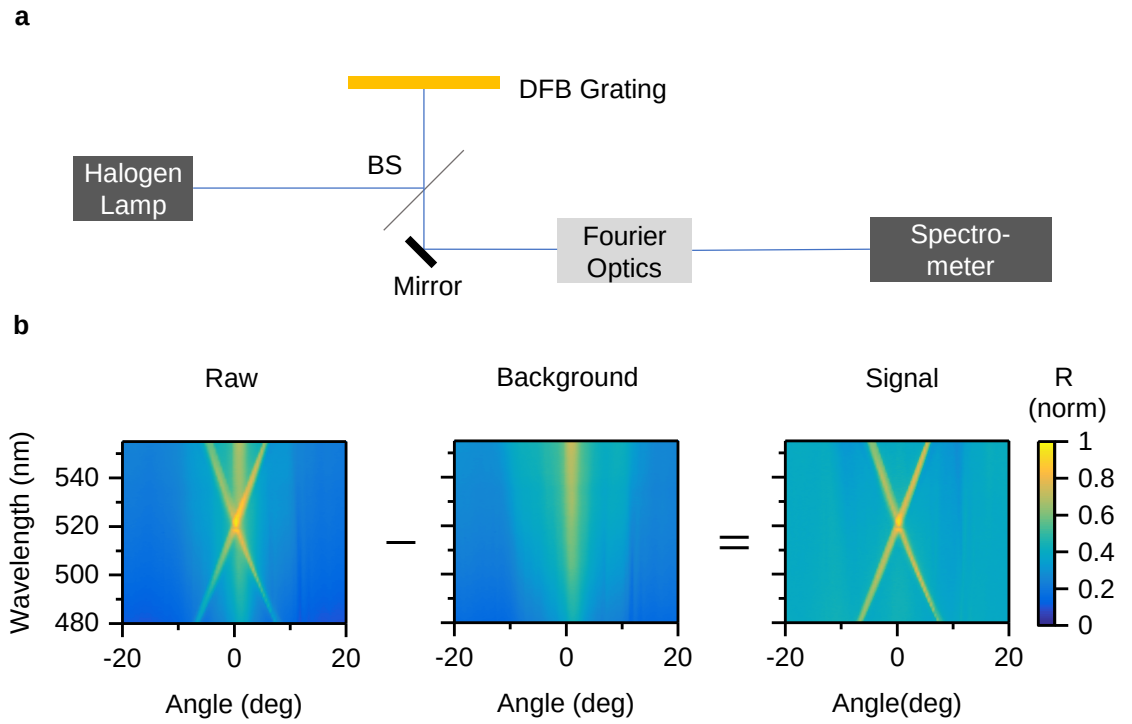

Figure 5.4: Passive angluar dispersion characterization of the DFB gratings. **a**, Sketch of the optical characterization set-up used to measure the angle dependent reflection from a DFB grating. A halogen lamp was used to illuminate the DFB grating via a beam splitter (BS) and a microscope objective (not shown). The angle-dependent far-field reflection was imaged onto the entrance slit of a spectrometer by the same microscope objective together with a $4f$-correlator (Fourier Optics). **b**, Image data processing steps. The recorded raw data consisted of an overlay of the reflection signal originating from the DFB grating and a background signal originating from direct illumination and other reflection pathways in the set-up. A background image was acquired on a grating free area on the sample and subtracted from the raw image data to obtain the dispersion relation (Signal).

In a first step, we investigated the dispersion relation of a second-order DFB grating without the presence of a gain fluid and hence with air as the upper cladding layer. For this passive characterization, the DFB grating was illuminated through a microscope objective using an external broad band halogen lamp (see Fig. 5.4a). Depending on the angle of incidence and the wavelength, some of the light from the halogen lamp was coupled into the waveguide through the grating. In a next step, the corrugation also led to efficient wavelength and angle dependent outcoupling (according to Eq. 5.2) to the top and to the bottom of the device. A microscope objective together with a $4f$-correlator (see Section 3.2 for details on the experimental setup) was used to image the angle dependent reflection onto an EM-CCD detector connected to a spectrograph. Using this technique with a 40 × microscope objective ($NA = 0.55$), it was possible to image the angle dependent photonic dispersion at an angle range of ±33°. Figure 5.4b shows an example of the recorded angle dependent reflection. The raw data consists of an overlay of the reflected light coming from the DFB grating as well as from the air-substrate interface at the bottom of the device and some direct illumination from the halogen lamp. To clean the data from the reflected light originating from the air-substrate interface and the direct illumination of the EM-CCD detector, a background image was taken on a spot next to the grating and subtracted from the raw image. The result was a clean angle dependent reflection signal.

Similarly, the structure can be actively probed with a laser dye (PM556 dissolved in water at a concentration $c = 5\,\mathrm{mM}$, see Section 3.3 for details) on top of the DFB grating. Here, the fluorescent dye was excited through a microscope objective using an OPO system tuned to the absorption maximum of the dye (wavelength, 480 nm; repetition rate, 20 Hz; pulse length, 5 ns and pulse energy, $< 100\,\mathrm{nJ}$). Using the same microscope objective and a $4f$-correlator, the angle dependent emission was imaged on a EM-CCD detector attached to a spectrograph (see Fig. 5.5a). In contrast to the passive characterization, this experiment relied on light being transmitted through the device rather than reflected. Figure 5.5b shows that the signal after background correction consists of a reduced transmission signal for the photonic modes satisfying the dispersion relation Eq. 5.2. This can be explained by a strong transmission signal since most of the light was not coupled to the waveguide by the grating but directly emitted onto the spectrometer. Only light satisfying Eq. 5.2 was coupled into the waveguide and scattered to the top and bottom by the grating. Hence, the light scattered to the top of the device leads to a reduction in transmission at specific angles and wavelengths.

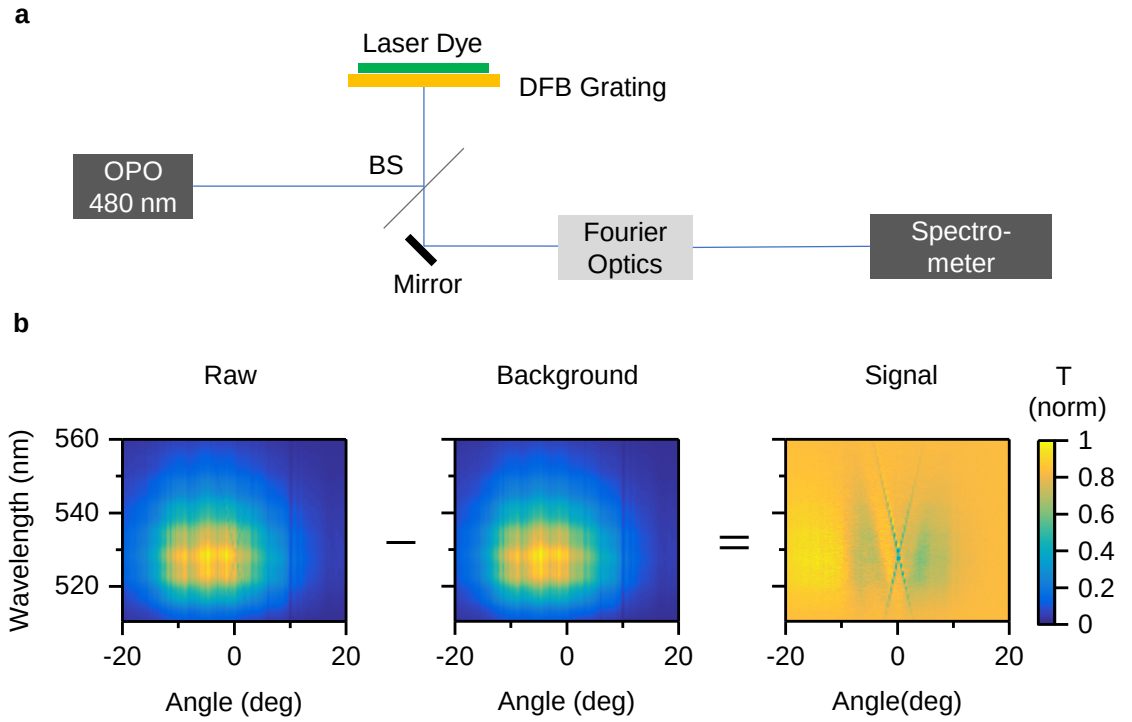

Figure 5.5: Active angluar dispersion characterization of the DFB gratings. **a**, Sketch of the optical characterization set-up used to measure the angle dependent emission from a fluorescent dye on a DFB grating. The emission from an optical parametric oscillator (OPO) at 480 nm was used to excite the laser dye on the DFB grating via a beam splitter (BS) and a microscope objective (not shown). The angle-dependent far-field emission was imaged onto the entrance slit of a spectrometer by the same microscope objective together with a $4f$-correlator (Fourier Optics). **b**, Image data processing steps. The recorded raw data consisted of an overlay of the emission signal originating from the DFB grating and a background signal originating from fluorescence transmitted through the device stack without being coupled to the waveguide. A background image was acquired on a grating free area on the sample and subtracted from the raw image data to obtain the dispersion relation (Signal).

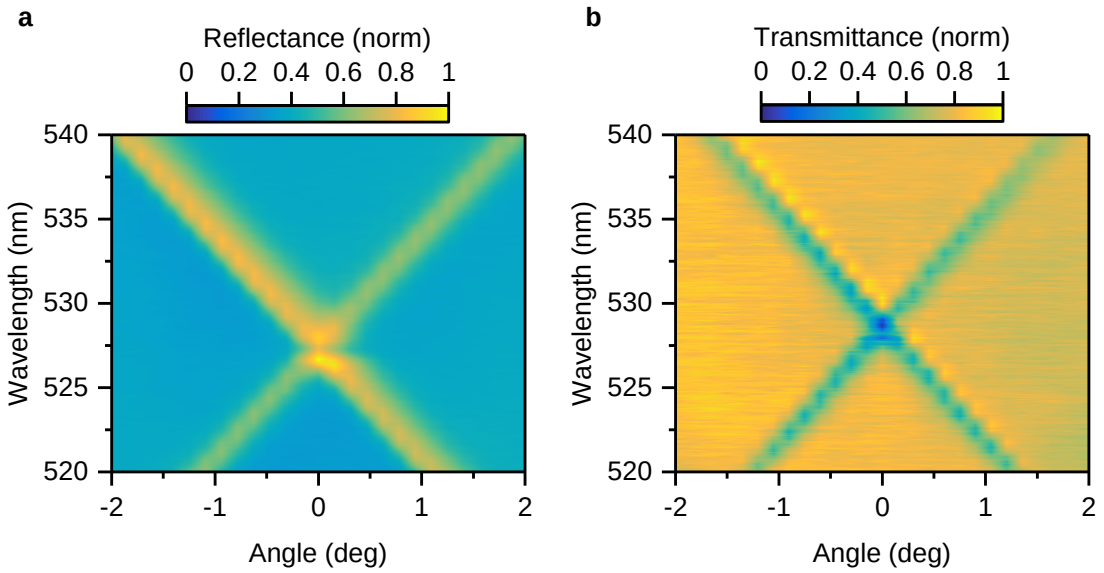

Figure 5.6: Angluar dispersion measurement of a second-order grating. **a**, Background corrected reflection measurement of a SiO_2 substrate based DFB grating with air as the top layer. The grating was illuminated with a broad band halogen lamp. A stop band is opening at 0° angle. **b**, Background corrected transmission measurement of the emission from a fluorescent dye on top of the same DFB grating measured in a. The resonance wavelength λ_B is shifted towards a longer wavelength. The emission data was acquired at pump pulse energies well below the lasing threshold. Adapted from Ref. [182].

Using the passive characterization technique, we firstly investigated a second-order DFB grating device with a grating period $\Lambda = 350\,\text{nm}$ (see Section 3.1.4 for more grating properties) based on a SiO_2 substrate without a fluorescent dye on top. Figure 5.6a shows a close up of the background corrected signal. Fitting Eq. 5.2 to the data yields an effective refractive mode index $n_{\text{eff}} = 1.506$ which can be utilized for solving Eq. 5.1 to determine a core layer thickness $d = (554 \pm 7)\,\text{nm}$ of the structure. This is still below the expected onset for $TE1$ and $TM1$ modes for devices based on SiO_2 substrates (*cf.* Fig. 5.3c). Furthermore, the angle dependent emission shows (Fig. 5.6a) that the characteristic photonic stop band opens at 0° angle and a Bragg wavelength $\lambda_B = (527.7 \pm 0.2)\,\text{nm}$. This is typical for DFB structures operated at the exact Bragg condition where the counterpropagating waves destructively interfere and give rise to a stop band. Hence, within this stop band, no photonic modes are supported and the emission just above and below the stop band at 0° angle can be attributed to the built up of two standing waves with nodes either in the high refractive index or low refractive index material of the DFB structure. Figure 5.6b shows the angle resolved emission from a fluorescent dye on the same DFB grating device excited with an OPO (see Fig. 5.5). The Bragg wavelength $\lambda_B = (528.7 \pm 0.2)\,\text{nm}$ is shifted towards a longer wavelength due to an increased

effective refractive index $n_{\text{eff}} = 1.508$ compared to the situation in Fig. 5.6a. This can be attributed to the higher refractive index of the dye compared to air forming the top cladding layer. Since the the core layer thickness d and the refractive index of the SiO_2 substrate and the grating polymer are known, Eq. 5.1 can be used to find the refractive index of the dye solution $n = 1.342 \pm 0.015$.

5.4 Optofluidic DFB Laser Characterization

After characterizing the photonic properties of the optofluidic DFB lasers below threshold using Fourier imaging, we tested the devices above threshold and analyzed their laser behavior. Firstly, we investigated optofluidc DFB lasers based on mixed-order gratings and a MgF_2 substrate. Due to previous results found on DFB grating structures incorporating a mixture of first- and second-order structures [86] and the higher overlap factor for MgF_2 substrate based devices compared to SiO_2 substrate based devices, we expected the best laser performance for these devices. The mixed-order gratings were excited with a circular pump spot ($\varnothing = 250\,\mu m$) on the first-order and next to the outcoupling (second-order) region using the same pumping scheme as for the active dispersion characterization. The near-field emission was imaged onto the entrance slit of the spectrometer using a microscope objective and a projection lens (see Section 3.2 for details on the characterization setup). The emission spectra obtained for a range of different excitation energies are shown in Fig. 5.7a. At a pump pulse energy of 338 nJ we only observe a broad peak ($\Delta\lambda > 60\,nm$) that can be attributed to the fluorescence of the dye. Increasing the pump pulse energy to 667 nJ leads to the appearance of a single spectrally narrow and weak peak that gains superlinearly in intensity until it dominates the entire spectrum at pump energies of 1400 nJ and above. We attribute the single mode lasing behavior to the thin core layer thickness $d = 250\,nm$ of this device, preventing that higher order modes are supported by the waveguide. Figure 5.7b shows the input-output characteristics of the same optofluidic DFB laser. Above a threshold pump pulse energy of 520 nJ, a superlinear increase in the output signal can be observed. This, together with the narrow band spectrum, is a clear indication for lasing and represents an almost 20-fold reduction in threshold over previous reports on evanescently pumped optofluidic DFB lasers (9.5 µJ [190]). The lasing threshold of our devices is in fact within the same order of magnitude as non-evanescently pumped optofluidic DFB lasers [193]. We attribute this reduction in threshold, compared to other evanescently pumped optofluidic DFB lasers, to the use of a mixed-order grating, the low

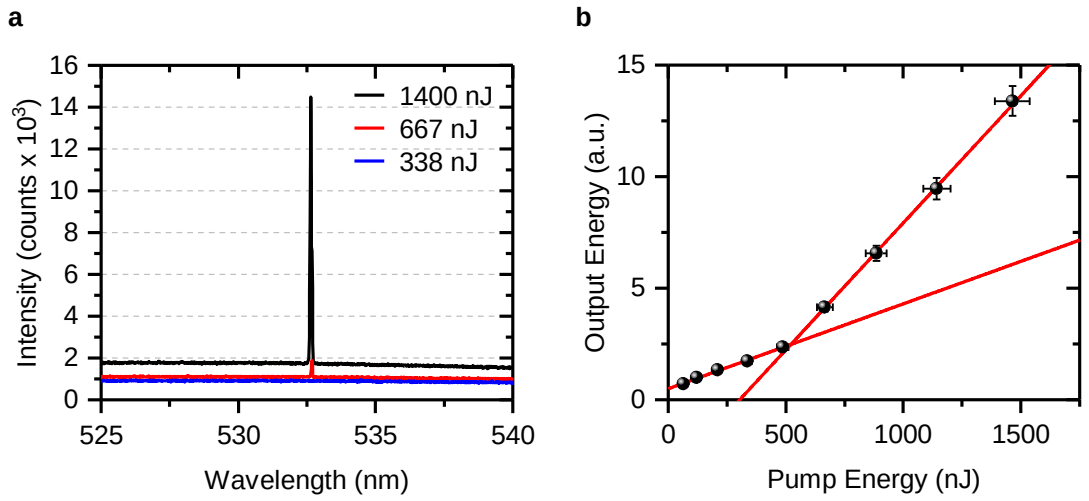

Figure 5.7: a, Emission spectra of an optofluidic DFB laser with a MgF_2 substrate, a core layer thickness $d = 250\,\text{nm}$, a mixed-order grating and a dye concentration of 5 mM. The spectra are shown for pump pulse energies below (blue), at (red) and well above (black) threshold. **b**, Input-output characteristic of the same optofluidic DFB laser. The output energy increases super-linearly above a threshold pump pulse energy of 520 nJ. The red lines represent a linear fit to the data points below and above threshold. Adapted from Ref. [182].

refractive index substrate (MgF_2) and the thin core layer. According to the simulation results (see Fig. 5.3d), a further reduction of the core layer thickness d should lead to an increased overlap factor and hence even lower threshold values. However, the use of the UV curable polymer resist (UVCur06) did not allow to fabricate thinner layers.

Having established lasing emission from our evanescently-pumped optofluidic DFB lasers, we investigated the dependence of the pump threshold on the concentration of the fluorescent dye and the use of different substrate materials. Figure 5.8a shows that for dye concentrations $\geq 2500\,\mu\text{M}$ the required energy to reach the lasing threshold increases slightly with decreasing dye concentration. This can be attributed to a lower fluorophore density and hence a reduction in available gain. For dye concentrations below 2500 µM, the required lasing threshold energy increases drastically since cavity losses are now dominating and the remaining fluorophores are not able to provide sufficient gain. This is particularly apparent for devices based on SiO_2 substrate where lasing operation cannot be reached with fluorescent dyes of concentrations below 2500 µM. Furthermore, the lasing threshold of MgF_2 substrate based devices is always lower compared to those based on SiO_2. This supports the hypothesis that higher mode overlap leads to higher modal gain and hence reduced pump thresholds (*cf.* Fig. 5.3c and d). Figure 5.8b shows the TE and TM polarization dependent near-field emission from

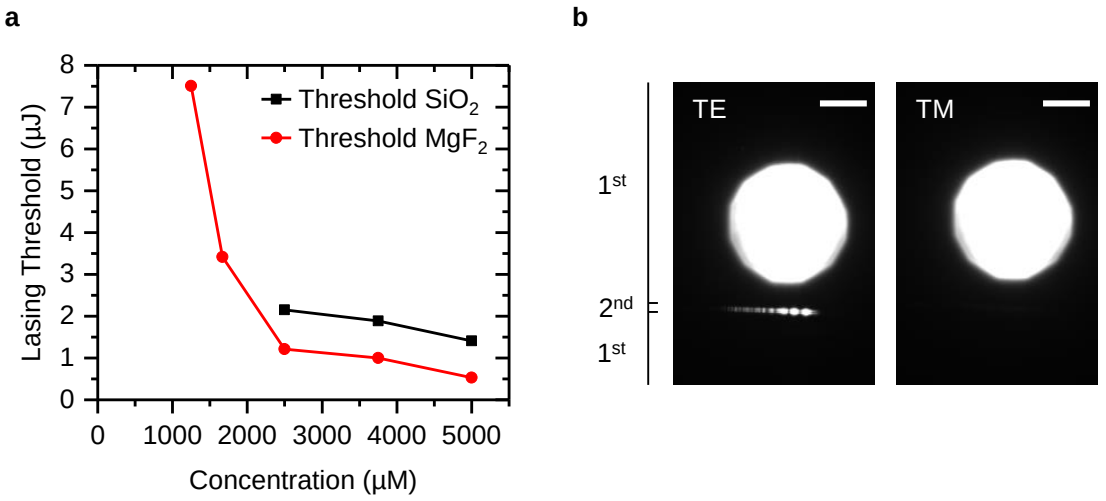

Figure 5.8: **a**, Lasing threshold of SiO_2 (black) and MgF_2 (red) substrate based optofluidic DFB lasers with a core layer thickness of 250 nm and a mixed-order grating for different dye concentrations. The solid lines represent a guide to the eyes. **b**, Polarization dependent (TE and TM) near-field emission image from a mixed-order DFB grating. The circular pump spot is positioned on the first-order section and the emission is originating from the second-order section. The spatial location of the first- and second-order grating regions are indicated on the left-hand side of the near-field emission images. Scale bars, 100 µm. Adapted from Ref. [182].

the mixed-order optofluidic DFB laser. The circular spot is the pump spot which is positioned on the first-order section of the grating and the bright line element is the outcoupled emission originating from the second-order section of the grating. Furthermore, the lasing mode is fully TE polarized with no TM contribution. We attribute this to the higher overlap factor Γ and hence higher modal gain expected for the waveguided TE compared to TM modes (see also Fig. 5.3d). Also, the excitation and emission are spatially separated which can be attributed to the design of the mixed-order grating. More precisely, the grating is pumped on the first-order section where in-plane scattering occurs and feedback is generated and consequently the amplified lasing mode is waveguided within the plane to the second-order structure where scattering perpendicular to the surface takes place.

Lastly, we analyzed the angle dependent lasing emission originating from the second-order section of the mixed-order grating of our optofluidic DFB lasers. Similarly to measuring the angle dependent photonic dispersion of an optofluidic DFB laser with modest pump powers (see also Fig. 5.5), we recorded the angle dependence above threshold using our optical characterization set up in Fourier imaging mode. Figure 5.9a shows a Fourier image of the angle resolved lasing emission from a MgF_2 substrate based device. In contrast to the dispersion

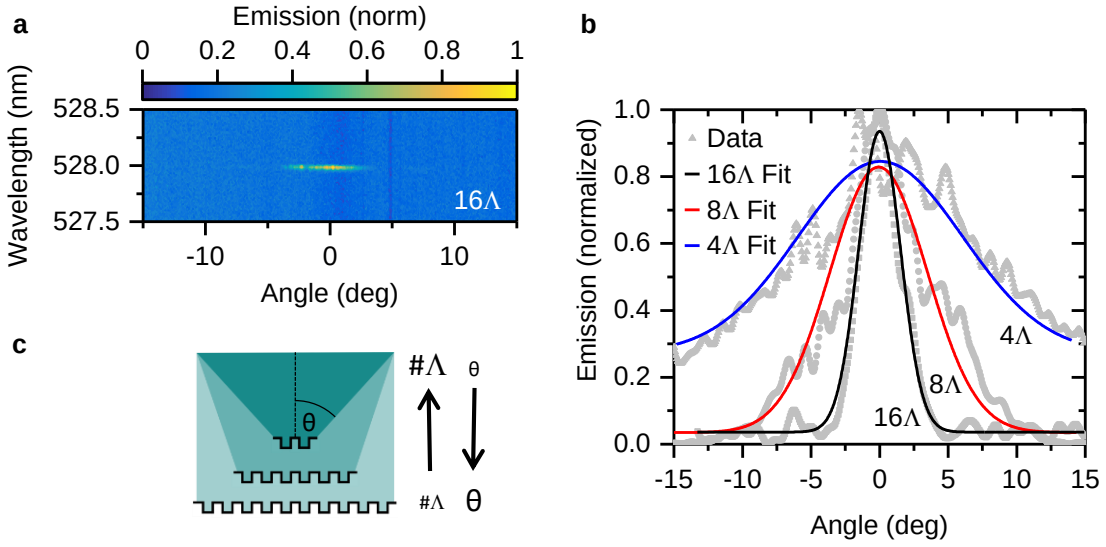

Figure 5.9: **a**, Angle resolved lasing emission from a MgF_2 substrate based optofluidic DFB laser with a mixed-order grating including a second-order section with 16 periods Λ. **b**, Angular divergence of the same optofluidic DFB laser for second-order outcoupling regions with 4, 8 and 16 periods Λ (gray data points). The black, red and blue solid line represent Gaussian fits to the data. **c**, Illustration of the fact that a smaller outcoupling region (small #Λ) leads to an increased angular divergence (large θ) and vice versa. Adapted from Ref. [182].

relation measured below threshold, we now obtain a single spectrally narrow peak with some angular divergence. According to Eq. 5.2, Bragg scattering at a second-order grating should be perpendicular to the surface and hence be emitted at 0°. The disagreement between theory and experimental result can be explained by the finite size of the second-order grating used to couple out the laser mode. Figure 5.9b shows the angular divergence of three different mixed-order gratings containing second-order sections with 4, 8 and 16 periods. The data is extracted from the corresponding Fourier images at the maximum emission wavelength. The laser emission for a second-order grating with 16 periods, for example, diverges with a half angle $\theta = (3.41 \pm 0.32)°$ (FWHM). The emission divergence increases with a reduced number of second-order periods to couple out the light. Since the outcoupling region is the source of the laser emission and hence defines the minimum beam waist, a smaller outcoupling region (small #Λ) leads to an increased angular divergence (large θ) and vice versa (see Fig. 5.9c for an illustration). In fact, this feature can be used to tailor the surface emitted laser beam to the desired angular divergence by changing the number of second-order grating periods.

5.5 Discussion

In conclusion, this chapter presented the development of a water-based optofluidic DFB laser device with a reduced lasing threshold ($E_{\mathrm{th}} = 520\,\mathrm{nJ}$) compared to other evanescently pumped fluidic DFB lasers. This reduction was achieved by using a mixed-order grating and a highly concentrated dye as well as optimizing the modal gain by a using low refractive index substrate and a thin core layer. Especially, the possibility of using water as solvent for the laser gain fluid together with the reduced threshold may pave the way for new biology related sensing application where evanescent pumping is inevitably needed. Furthermore, we could show that specific device parameters such as the core layer thickness d and the refractive index of the gain fluid can be obtained by a combination of passive and active angular dispersion analysis even below threshold. Lastly, the number of second-order grating periods used to couple out the lasing mode can be utilized to tailor the beam divergence.

6

DFB GFP Lasers

Fluorescent proteins have emerged as an attractive gain material for lasers, especially for devices requiring biocompatibility. However, due to their optical properties an integration with distributed feedback (DFB) resonators is not readily achievable.

The advantages of fluorescent proteins as active laser materials and the most important laser devices based on fluorescent proteins are briefly introduced in Section 6.1. Next, in Section 6.2, the optical design challenges for the integration of a green fluorescent protein (GFP) solid-state layer as the active material in a DFB resonator are discussed. Furthermore, it is shown how the introduction of a high refractive index interlayer in the DFB waveguide can help to support lasing modes in a two-dimensional second-order grating. This section is concluded by discussing the fabrication methods and presenting SEM images that reveal the composition and dimensions of our DFB GFP lasers on a nanometer scale. These devices are optically characterized in Section 6.3, and lasing action is confirmed for TE and TM modes. Furthermore, the spectral tuning range and the modal effective refractive index for DFB GFP lasers is analyzed. Section 6.4 discusses, the shape and divergence of the vertically emitted laser beams. Moreover, the effects of finite

coherent in-plane oscillation on the vertically emitted beam is instigated and it is shown that the TE emission is almost diffraction limited. Lastly, in Section 6.5, the results are summarized and possible improvements and applications are discussed.

The SEM and FIB imaging/etching experiments described in this chapter were carried out by David N. Miller.

6.1 Fluorescent Protein Lasers

The green fluorescent protein (GFP), was first discovered and extracted from the jellyfish *Aequorea victoria* in the North Pacific, and is now commonly used as a marker for genes and molecules in biology labs around the world [61, 195]. This wide spread use has also triggered a vivid research field dedicated to finding new and optimizing existing fluorescent proteins [196, 197]. This led to a remarkable library of different fluorescent proteins with spectral bands covering the whole visible spectrum, providing optical gain on par with state-of-the-art fluorescent polymers [29, 198]. Furthermore, their barrel like structure (see Section 2.1) protects the active fluorophore in the center of the protein from self-quenching, which in turn leads to excellent fluorescence properties in solid-state films [29].

Due to their biocompatibility and light emitting properties, fluorescent proteins also received the attention of the laser community and a variety of different laser structures based on fluorescent proteins have been shown. Two remarkable mile stones are the biological single cell laser in which enhanced GFP (eGFP) [33] is used as the gain material and the fabrication of a low threshold polariton laser based on the fluorescent proteins eGFP and tdTomato, emitting laser like radiation from a Bose Einstein condensate [43]. A more thorough analysis of the field can be found in Section 2.5.

However, at the time the work presented in this chapter was carried out, an important resonator structure was missing in the family of lasers based on fluorescent proteins. This was the DFB grating resonator which is an attractive resonator class because they can be operated at low thresholds in a single mode regime and comprise of a planar waveguide structure which can be fabricated on a large scale with relatively little effort and high reproducibility (*cf.* Chapter 2 and 5). Here, we show how eGFP can be used as a solid-state gain material in an optimized DFB resonator structure to obtain lasing emission from different modes over a broad spectral range.

6.2 DFB GFP Laser Design and Fabrication

For a DFB laser to work efficiently, it is important that the lasing mode overlaps sufficiently with the gain material and that the refractive index contrast at the grating interface between gain material and adjacent layer is sufficiently high. This allows for Bragg scattering and consequently the formation of standing waves due to interference of counterpropagating in-plane waves. In Chapter 5, it was shown that the standard design of a DFB grating resonator fabricated using UV nanoimprint lithography relies on a transparent substrate and a UV curable polymer resist defining the grating. In order to build a DFB GFP laser, in a next step, a solid-state eGFP layer acting as the gain material can be fabricated on top of the grating. Depending on the refractive index of the individual layers, there are two possibilities for this structure to support lasing action as depicted in Fig. 6.1. Either the lasing mode is confined in the eGFP gain layer or in the polymer grating. The first option would be more desirable since a maximum modal overlap with the gain region can be achieved and the low refractive index of air (which acts as the top cladding) would further enhance the mode confinement. However, since the eGFP film acts as the waveguide core in this scenario, its thickness must be controlled precisely and a smooth film morphology reducing scattering losses must be achieved. The latter option, in which the mode is confined in the grating layer is similar to the situation discussed in the previous chapter and hence relies on evanescent gain. Naturally, this is the less desirable option since modal gain will be reduced and leaky substrate modes will be present.

In order to decide which design strategy to follow, the refractive index of the individual layers must be determined. Firstly, the refractive index for glass substrates $n_{\text{glass}} = 1.52$ is known [199]. In contrast to the previous chapter, for this work we did not use UVCur06 (e.g. Chapter 5) but the optimized follow up product NIL210 (material properties can be found in Chapter 3.1.4) as the UV curable resist. We performed ellipsometry measurements on NIL210 and eGFP and found the same refractive index ($n_{\text{NIL}} \approx n_{\text{GFP}} \approx 1.55$) within the accuracy of the measurement for the two materials at a wavelength of 530 nm. Since the refractive index of all three materials is similar, one expects that it is not possible to obtain waveguiding nor Bragg scattering. To test this hypothesis, we spin-coated eGFP directly on top of a second-order NIL210 grating and observed that the previously recorded white light reflections on the grating structure indeed disappeared due to refractive index matching of the NIL210 and eGFP.

In order to solve this problem and provide a waveguide structure with sufficient refractive

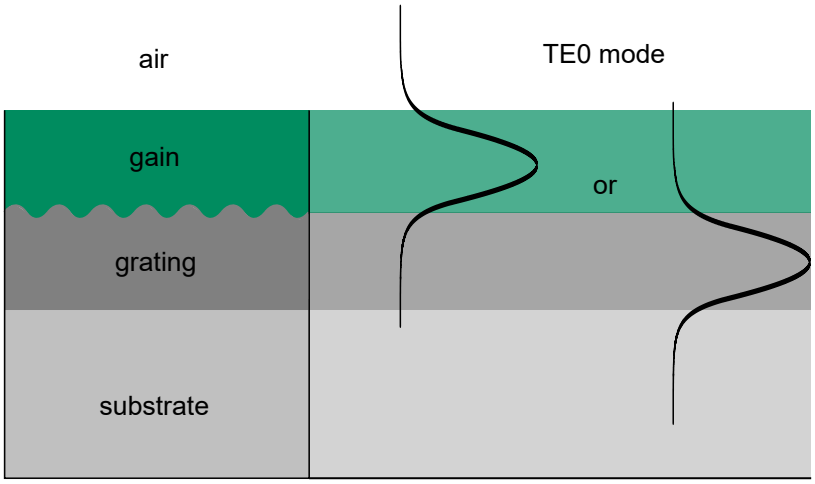

Figure 6.1: Illustration of a DFB waveguide structure consisting of a substrate, a grating layer, a gain layer and air from bottom to top. Depending on the refractive index a photonic mode (e.g. the $TE0$ mode) can either be waveguided in the gain or in the grating layer.

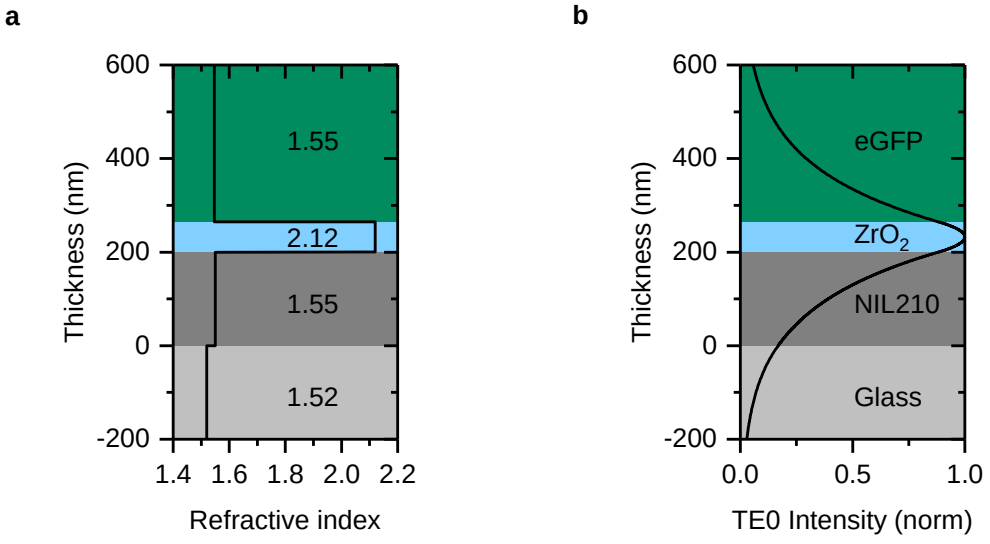

Figure 6.2: **a**, Refractive index profile of the waveguide structure consisting of a glass substrate, a UV curable grating layer, a metal oxide (ZrO_2) core layer and an eGFP gain layer from bottom to top. **b**, $TE0$ mode profile for a laser mode at 530 nm in the same waveguide structure.

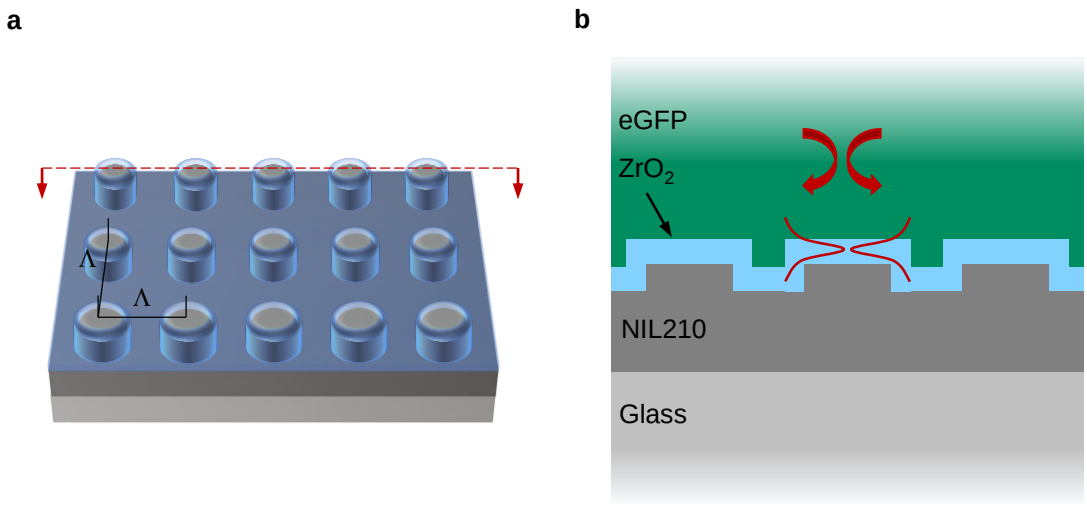

Figure 6.3: **a**, Illustration of a DFB GFP laser based on a two-dimensional second-order grating with a thin metal oxide layer on top. The grating period Λ is defined as the distance between two grating columns. For clarity, the eGFP film is not shown. **b**, Illustration of a cross-section through the DFB GFP laser at a position marked with a red dashed line in a. The photonic modes are confined in the ZrO_2 layer and evanescently extend into the eGFP layer. Mode profile for illustration only; see Fig. 6.2b for actual profile.

index contrast between grating and gain material, we optimized the laser stack by introducing a thin layer of a high refractive index material on the interface between gain material and grating resist. Figure 6a shows the anticipated refractive index landscape within the DFB laser stack consisting of a carrier glass substrate, a UV curable resist defining the grating, a thin layer of high index metal oxide covering the grating and acting as the waveguide core and eGFP as the gain material. Similarly to the design and results introduced in the previous chapter, the nonemissive, high refractive index core layer requires an evanescent pumping scheme. However, when using a small layer thickness $< 100\,\text{nm}$ and a high refractive index material (e.g. ZrO_2 with $n = 2.12$) the modal overlap factor Γ with the gain layer can be $> 30\,\%$. Judging from the findings in Chapter 5, this can be sufficient to support lasing, especially when considering that the refractive index contrast of gain and grating layer is increased in this structure. Figure 6.2b shows the $TE0$ mode profile ($\lambda = 530\,\text{nm}$) in the waveguide stack as described above, with a grating layer (NIL210) thickness of 200 nm and a ZrO_2 layer thickness of 65 nm. The overlap factor Γ for this structure is 31 %.

To fabricate such a grating structure on top of a glass substrate, we used solution processing techniques and UV nanoimprint lithography as described in Chapter 3.1.1 and 3.1.3, respectively. In contrast to Chapter 5, for the following experiments we did not use one-dimensional

gratings but a master grating structure consisting of a two-dimensional second-order square lattice (see Fig. 6.3a for an illustration). One sample contained 35 gratings with grating periods Λ ranging from 250 nm to 425 nm, equally spaced by $\Delta\Lambda = 5$ nm. Using gratings with such a wide tuning range allows to experimentally find the best grating period for a given effective refractive index n_{eff} and gain spectrum so that the Bragg condition $m\lambda = 2n_{\text{eff}}\Lambda$ can be fulfilled. For the high refractive index layer, we choose ZrO_2 which can be deposited using an atomic layer deposition (ALD) process (Ultratech Savanah 200). This process is also used within the group to encapsulate OLEDs and hence did not require much optimization. ALD is a chemical vapor deposition method, in which a thin metal oxide film is grown one atomic layer at a time, making it possible to precisely control the layer thickness [200]. Since ALD relies on chemical reactions, conformal layers can be grown on any substrate including complex grating structures. The process usually relies on the use of two different gaseous materials called precursors. During the process, these materials react with the surface one at a time in a sequential and self limiting manner. The repetitive use and reaction of the two separately present materials slowly grows a thin film. To grow ZrO_2, the two precursors tetrakis(dimethylamino)zirconium (TDMAZr, Pegasus Chemicals) and H_2O were alternatingly purged into the reaction chamber, loaded with substrates already containing gratings in a NIL210 layer [201]. For the process described above, we used a deposition temperature of 100 °C and were able to grow ZrO_2 at a rate of 55 Å h^{-1}. We employed a combination of ellipsometry and profilometer measurements to determine the refractive index ($n = 2.12$) and thickness (65 nm) of the deposited ZrO_2 layer. The thickness and material refractive index data shown in Fig. 6.2a is a representation of the fabricated laser stack. Lastly, we spin-coated an aqueous eGFP solution onto the ZrO_2 layer (spin coating, 1500 rpm for 120 s; concentration, 100 mM; volume, 40 µL), yielding a solid-state eGFP film with a thickness of $\approx 1\,\mu$m. Figure 6.3b shows an illustration of the expected laser stack (cross-section through the grating at a position marked with a red dashed line in Fig. 6.3b). The counterpropagating modes within the thin ZrO_2 layer are indicated by red solid lines.

To asses the quality of the fabricated DFB GFP laser structures, we performed a combined focused ion beam and scanning electron microscope measurement (Scios Dualbeam FIB/SEM). Figure 6.4a shows a top view SEM image of a two-dimensional second-order $\Lambda = 330$ nm grating that was partially covered with eGFP. On the bright left-hand side of the image, it is possible to identify the single grating columns, whereas on the darker right-hand side, these

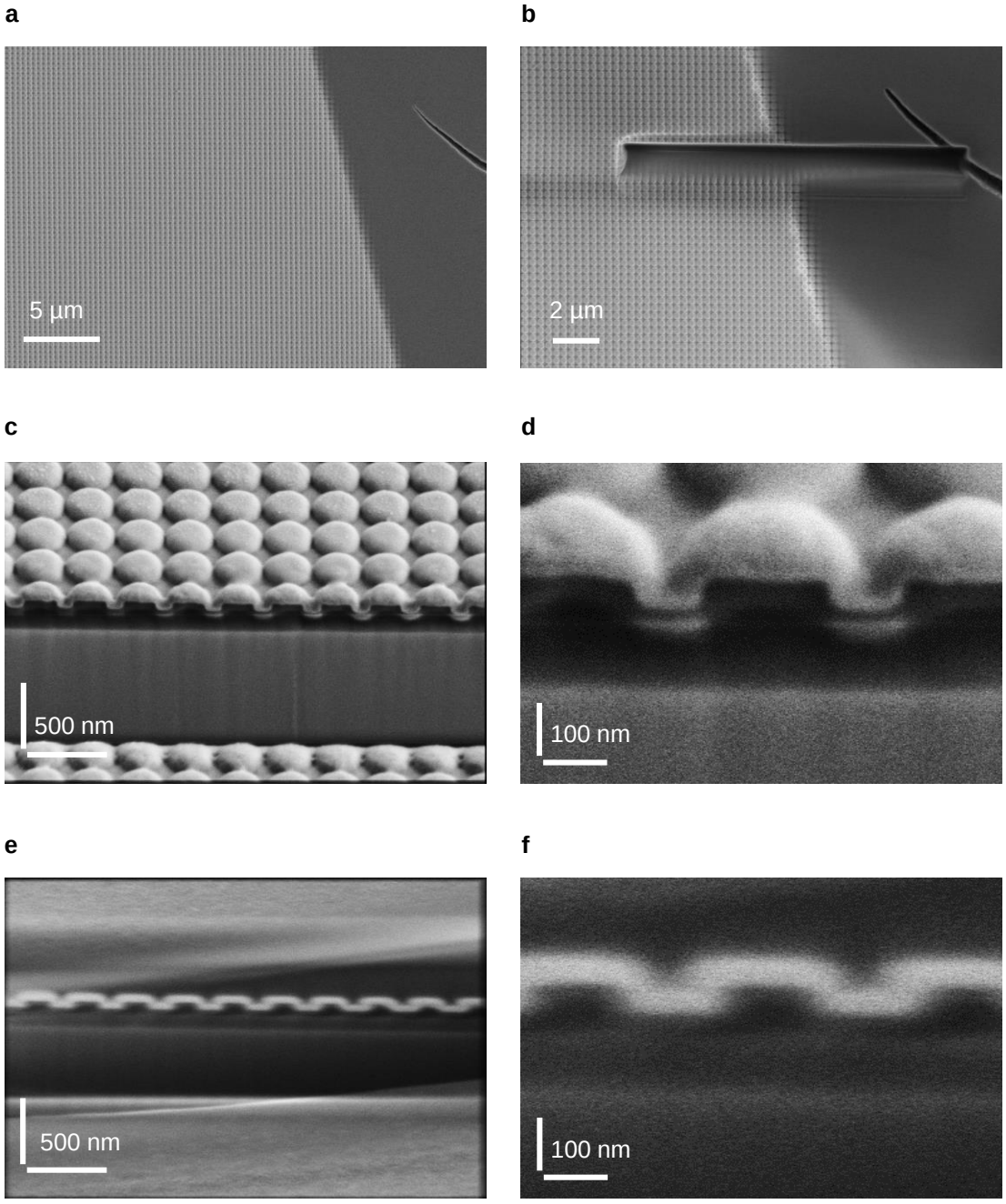

Figure 6.4: SEM images of the DFB GFP laser structure. **a**, Top-view SEM image of a two-dimensional second-order grating partially covered with eGFP. **b**, Top-view SEM image of the same grating structure with trench cut through the individual layers using a focused ion beam. **c**, Glancing incidence SEM image of a grating section not covered with eGFP. The layers can be identified as ZrO_2 (bright), grating polymer (dark) and glass substrate (slightly bright), top to bottom. **d**, Close up of the structure shown in c. **e**, Glancing incidence SEM image of a grating section covered with eGFP (dark top layer). **f**, Close up of the structure shown in e.

domains are covered with a solid-state eGFP film and therefore not visible. Using the focused ion beam consisting of Ga-ions, we cut a trench and removed the eGFP, ZrO_2 and grating polymer layer. Figure 6.4b shows a top-view SEM image of a trench stretching across the uncovered and eGFP covered region of the grating. Ideally, we would have liked to cut a trench at a grating region entirely covered with eGFP. However, in thicker regions of the eGFP film (e.g. in the center of the grating) the ion beam was unstable due to surface charging effects. Figure 6.4c and d (close up) shows a glancing incidence (52°) SEM image of the uncovered grating section. The polymer grating columns can be identified as the dark periodic structure ($\Lambda = (330 \pm 10)$ nm, standard error of mean) sitting on a residual layer with a thickness of (149 ± 6) nm. The grating columns are (198 ± 7) nm by (72 ± 4) nm in size and hence the grating fill factor is (60 ± 5) %. The bright smooth area underneath the polymer grating is the top surface of the carrier glass slide which stopped the milling of the focused ion beam. The bright layer on top of the polymer grating is the ZrO_2 layer and in this image appears to cover the grating columns irregularly forming half domes. However, the glancing incidence SEM images of regions of the grating covered with eGFP reveal that the ZrO_2 layer indeed covers the grating smoothly and regularly and thus, resembles the periodic structure (Fig. 6.4e and f (close up)). This is expected for a layer formed with ALD, where the growth process relies on a chemical reaction (chemical vapor deposition) rather than the condensation of the material (e.g. physical vapor deposition) on the substrate. Here, the ZrO_2 layer appears sharper due to a better contrast between ZrO_2 and eGFP when compared to the out-of-focus signal from ZrO_2 in the background (see Fig. 6.4d). The measured ZrO_2 thickness (67 ± 4) nm is close to the nominal thickness of 65 nm. Hence, the FIB/SEM images reveal that the fabrication of our GFP DFB laser structure worked as anticipated.

6.3 Optical Characterization of DFB GFP Lasers

In addition to the structural characterization, we optically characterized the fabricated DFB GFP lasers using the optical set up introduced in Section 3.2. Figure 6.5a shows the input-output characteristics of our DFB GFP lasers when optically excited with an optical parametric oscillator (OPO) tuned to the absorption maximum of eGFP at 490 nm (pulse duration, 5 ns; repetition rate, 20 Hz). Above a threshold input power fluence of 56.6 kW cm^{-2}, we observe a superlinear increase in output power. This is a first indication for laser action. Figure 6.6b reveals that below this threshold pump fluence only a broad fluorescence background with a

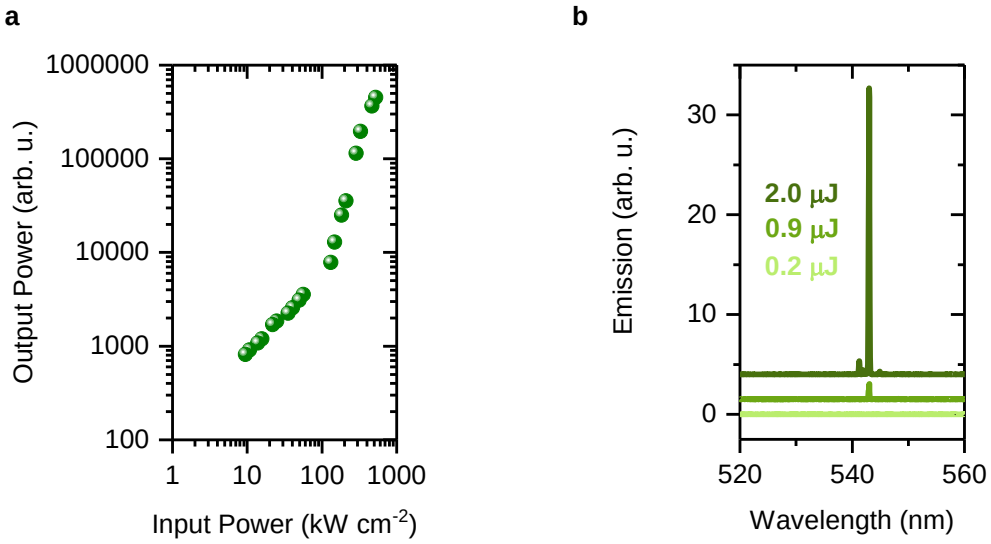

Figure 6.5: **a**, Input-output characteristics of a DFB GFP laser based on a two-dimensional second-order grating with a period $\Lambda = 330\,\text{nm}$ and a thin ZrO_2 layer with a thickness of $(67 \pm 4)\,\text{nm}$. The lasing threshold for this device is $56.6\,\text{kW}\,\text{cm}^{-2}$. **b**, Emission spectra for the same DFB GFP laser for input pump power densities below, just above and well above threshold.

maximum emission wavelength of 510 nm is visible. Just above threshold, at a pump pulse energy of 0.9 µJ, a weak and narrow peak starts to appear on top of the fluorescence background. This peak gained superlinearly in intensity until it dominated the spectrum at input power energies $\geq 2.0\,\mu\text{J}$. This is a further indication for lasing action from the DFB GFP structure. The single mode operation at 543 nm is characteristic for our DFB resonator with a grating period $\Lambda = 330\,\text{nm}$. We also tested the input output characteristics of an eGFP film spin-coated directly on top of a polymer grating. As expected, even at high pump fluences $> 2\,\text{MW}\,\text{cm}^{-2}$ we did not observe any line narrowing associated with lasing but only a broad fluorescence emission, confirming that the refractive index landscape without a high index interlayer does not support lasing modes.

The UV nanoimprint process offers the possibility for transferring large master structures containing severals gratings with different properties onto the sample. As mentioned above, one sample consisted of 35 two-dimensional second-order gratings with grating periods Λ ranging from 250 nm to 425 nm equally spaced by $\Delta\Lambda = 5\,\text{nm}$. Using this wide variety of grating periods offered the possibility of probing the entire eGFP gain spectrum for lasing emission. Figure 6.6 shows that it is possible to continuously achieve eGFP lasing over a wavelengths range from 525.1 nm to 576.7 nm by using gratings with a varying grating pitch. The overall wavelength range available for lasing is thus $\Delta\lambda = 51.6\,\text{nm}$. Even though the maximum

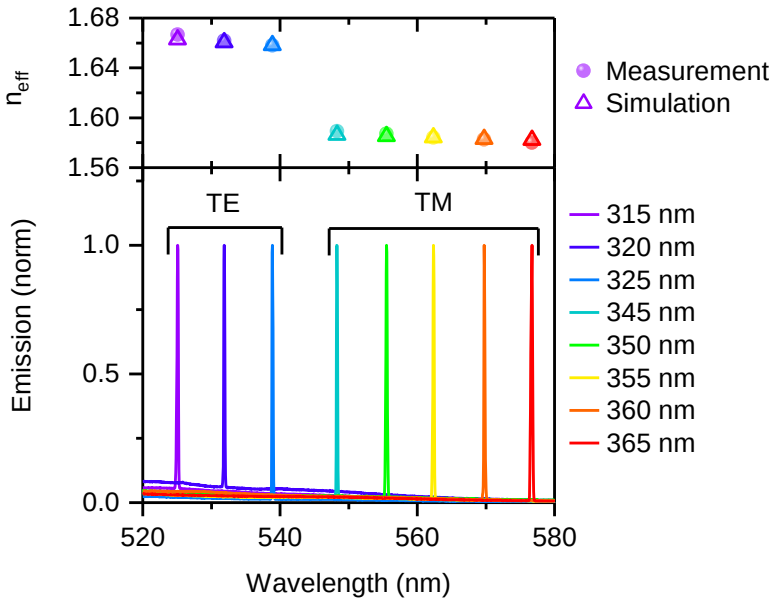

Figure 6.6: Bottom panel: Emission spectra for DFB GFP lasers with different grating periods. The individual lasing modes are labeled with their respective polarization (TE or TM). Top panel: Effective refractive mode index n_{eff} corresponding to the individual lasing modes shown in the bottom panel. The circles represent the measured effective refractive index using the maximum emission wavelength λ_{max} and the corresponding grating period Λ. The triangles represent the simulated effective refractive index using waveguide simulations for the different lasing modes.

emission peak of eGFP is at 510 nm, we do not observe lasing emission at wavelengths smaller than 525.1 nm. We attribute the truncation of lasing at shorter wavelengths to the onset of self absorption in eGFP and hence a reduced stimulated emission rate. In fact, the absorption peak in solid-state eGFP films extends to wavelengths < 525 nm [170]. At longer wavelengths, the lasing emission stops at 576.7 nm, which we attribute to the reduced gain provided by eGFP and hence the domination of cavity losses.

Furthermore, we investigated the polarization of the investigated lasing modes. While all lasing peaks sown in Fig. 6.6 are roughly equally spaced ($\Delta\lambda \approx 7$ nm), the grating periods are not. The first three and last five investigated gratings show a change in period of $\Delta\Lambda = 5$ nm. However, in between, there is a discontinuity with a spacing of $\Delta\Lambda = 20$ nm (from 325 nm to 345 nm). Inserting a linear polarizer into the collection arm of our optical characterization set up revealed that the first three peaks are of TE mode nature whereas the remaining five lasing peaks at longer wavelengths are of TM mode nature (see Chapter 6.4 for details). With the knowledge of the emission peak wavelength λ and the grating period Λ for lasing peaks originating from a DFB resonator it is possible to use the Bragg condition (see Eq. 2.41) to

calculate the effective refractive index n_{eff} of the photonic modes. The circles in the top panel of Fig. 6.6 represent the calculated effective refractive index n_{eff} for the lasing peaks originating from different gratings. Another method to determine the effective refractive index n_{eff} of a mode is by waveguide simulations, taking into account the composition of the waveguide stack, the corresponding layer thicknesses and the expected polarization of the mode (as already shown in Section 5.3). Since the refractive index and thickness of all layers in the laser stack (extracted from the FIB/SEM measurements in Chapter 6.2) as well as the emission wavelength λ and the polarization (TE or TM) are known, we calculated the effective refractive index n_{eff} for each lasing peak (transparent triangles in Fig. 6.6) using a modified version of the code in Appendix A to accommodate an additional layer. Overall, there is a good agreement between the experimentally and computationally obtained effective refractive index for all modes. In fact, the TE lasing mode emitted from the grating with $\Lambda = 315\,\text{nm}$ showed the highest discrepancy in measured and calculated effective refractive index of only $\Delta n_{\text{max}} = 0.004$ amongst all lasing modes. We take this as evidence that we have a correct understanding and description of the different layers of the laser stack at hand. Generally, the effective refractive index n_{eff} for TE modes is higher than the one for TM modes. This can be attributed to the polarization of the electric field of the TE modes, which oscillates in plane of the waveguide and hence mainly experiences the high refractive index of the metal oxide layer. In contrast, the electric field of the TM mode is polarized partially out of plane and hence probes more of the adjacent layers with a lower refractive index which leads to an overall reduction in modal effective refractive index. Having access to TE and TM modes is unusual for DFB lasers based on a polymeric gain material and special to the fluorescent proteins used. Polymer films are strongly anisotropic which means that the long polymer chains are mainly oriented in-plane. In fact, a large optical birefringence of up to $\Delta n = 0.5$ has been reported for some light-emitting polymers [202]. Therefore, the effective refractive index experienced by TE and TM modes in polymer DFB lasers is generally largely different and the Bragg condition cannot be fulfilled for both polarizations. Since the optical dipole orientation of polymers is in-plane, most polymer lasers are optimized for TE mode lasing.

6.4 Laser Beam Properties of DFB GFP Lasers

Next, we analyzed the profile of the beams emitted by our DFB GFP lasers. Similarly to one-dimensional gratings (see Section 5.4), also two-dimensional second-order gratings Bragg-

scatter the light perpendicular to the surface. Figure 6.7 shows the two characteristic TM and TE beams emitted from our DFB GFP laser devices. The emission was recorded using the same set up as before but instead of using an EM-CCD detector attached to a spectrograph, we imaged directly onto a CCD camera using an additional Fourier lens and a projection lens (see Section 3.2 for details). The emission shown in the left and right panel, was collected from gratings with a period of $\Lambda = 345\,\text{nm}$ and $\Lambda = 325\,\text{nm}$, respectively. For both gratings the emission features an annular transverse mode originating from a two-dimensional Bloch resonance [203]. The creation of this resonance can be explained by the two dimensional confinement leading to a superposition of the two orthogonally oriented in-plane grating vectors [204]. The well-defined emission and hence spatial coherence is a further indicator for lasing emission from the DFB GFP lasers. To analyze the properties of the emitted beams further, we imaged both beams through a linear polarizer. As expected, a double lobed beam can be observed. The orientation of the double lobe depends on the orientation of the linear polarizer and is mutually rotated by 90° between the two emitted beams. Hence, the beam emitted from the grating with $\Lambda = 345\,\text{nm}$ is radially polarized which can be attributed to a TM mode. In contrast, the output from the grating with $\Lambda = 325\,\text{nm}$ is azimuthally polarized and hence originating from a TE mode.

Interestingly, in an idealized square grating structure with infinite size and perfectly sharp grating transitions it should not be possible to record any surface emission. This intriguing feature can be physically explained by the electromagnetic field distribution within the device and consequently interference effects occurring between the vertically diffracted waves. The intensity of the surface emission depends on the phase shift between the diffracted waves originating from the in-plane counterpropagating waves. If the Bragg condition is fulfilled and feedback is generated, the induced phase shift between the in-plane counterpropagating waves is exactly π [205]. Hence, the two vertically diffracted waves cancel out due to destructive interference [206]. In contrast, our device has a finite size defined by the pump spot and the optically active grating. Since the mode field is spatially restricted in a finite system, the perfect antisymmetric electromagnetic field distribution is disrupted with respect to the symmetric grating features. The shift of the electromagnetic field due to the spatial confinement is most pronounced at the edges of the device and vanishes in the center. Hence, the vertically radiated field far away from the grating center experiences imperfect destructive interference leading to a detectable emission [203]. This also explains the peculiar annular far-field pattern where

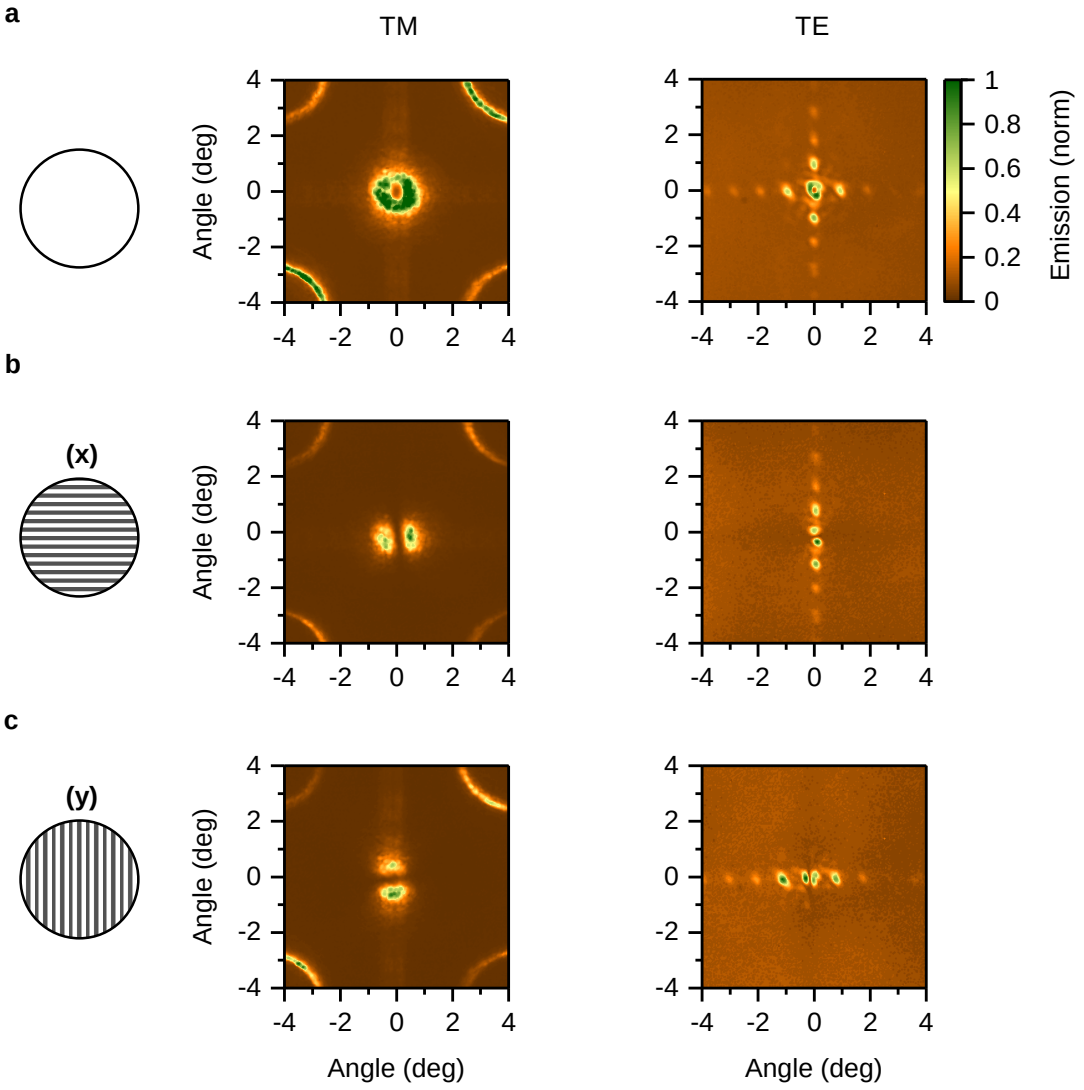

Figure 6.7: Far-field emission of a DFB GFP laser for a TM (left panel) and a TE (right panel) mode with **a**, no polarization filter, **b**, a horizontal polarization filter and **c**, a vertical polarization filter inserted into the collection arm.

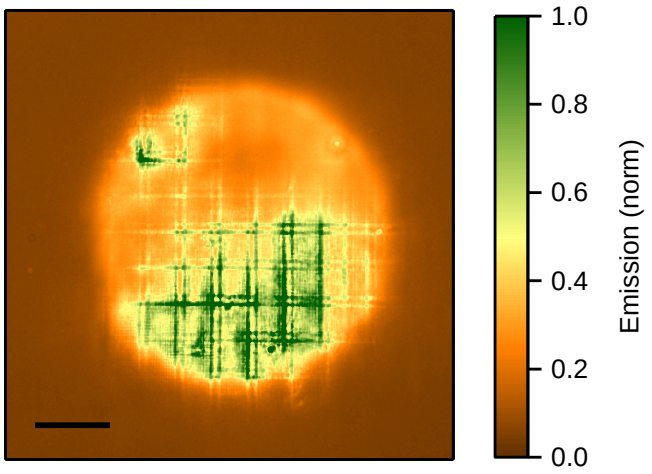

Figure 6.8: Near-field emission from a two-dimensional second-order DFB GFP laser for a TE mode. The bright circular area resembles the pump spot on the grating. Scale bar, 50 µm.

perfect destructive interference only occurs in the center at a divergence angle $\theta \approx 0°$.

The finite size of the optically active grating is furthermore closely related to the divergence angle observed in the far-field emission. As discussed above, if the device would be infinitely large, the surface emission would be exactly in the direction of the surface normal but cancel out due to destructive interference. However, as shown by 3D finite-difference time domain simulations [207, 208], the finite size L allows a wavenumber deviation $\delta k \approx 2\pi/L$. This deviation leads to a variation of the emitted beam with a deflection angle θ from the surface normal. The deflection angle and the wavenumber deviation are related by

$$k_0 \sin(\theta) = \delta k, \tag{6.1}$$

where $k_0 = 2\pi/\lambda$ with λ being the resonance wavelength in vacuum. For the observed emission with $\lambda = 538.8\,\text{nm}$ and $\theta = 0.3°$ this yields an area of coherent oscillation with a length $L = 104\,\mu\text{m}$. Figure 6.8 shows the near-field emission associated to the TE emission shown in the right panel of Figure 6.7. The majority of the emission originated from the bright region at the bottom of the pump spot. The emission area has a diameter $\varnothing = (181 \pm 21)\,\mu\text{m}$ and hence roughly the length calculated above. This suggests, that the emission beam divergence is induced by wavenumber deviation δk due to the finite size of the area of coherent oscillation.

Furthermore, the near-field emission (see Fig. 6.8) reveals that TE outcoupling is predom-

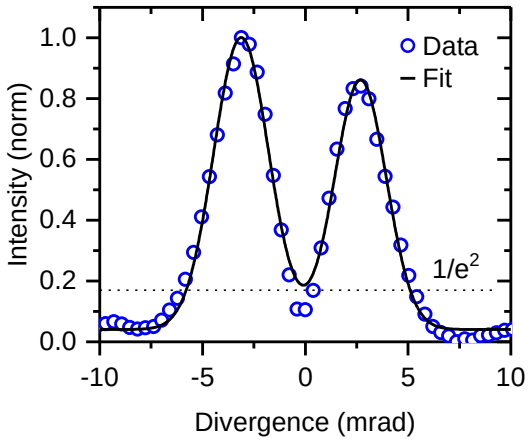

Figure 6.9: Emission intensity cross-section of a TE mode originating from a DFB GFP laser. The blue circles represent the data points extracted from the far-field emission. The black solid line represents a fit with two Gaussian profiles to the data points. The black dotted line marks the position where the intensity dropped by $1/e^2$ of the maximum value.

inantly along line-shaped elements with a spacing of $d = (26.4 \pm 0.5)\,\mu\text{m}$. These line elements can be regarded as a superimposed grating and the corresponding diffraction can be calculated using the diffraction grating equation for light under normal incidence

$$d \sin(\theta_m) = m\lambda; \quad m \in \mathbb{N}, \tag{6.2}$$

where d is the grating period and θ_m the diffraction angle for the m-th diffraction order. Hence, for a grating with a period of $d = (26.4 \pm 0.5)\,\mu\text{m}$ and a wavelength $\lambda = 538.8\,\text{nm}$ we obtain a first ($m = 1$) and second ($m = 2$) order diffraction at an angle $\theta_1 = (1.16 \pm 0.12)^\circ$ and $\theta_2 = (2.34 \pm 0.12)^\circ$, respectively. This is in good agreement with the observed side lobes in the TE far-field emission. The origin of the superimposed grating structure is not known at this stage but may be due to stitching errors during the electron beam fabrication of the Si master structure.

Lastly, we analyzed the beam quality of the emitted TE laser beam. The M^2-factor is the so called beam quality factor and a common measure for the quality of a laser beam. For a diffraction limited Gaussian beam the M^2-factor is defined as

$$\theta = M^2 \frac{\lambda}{\pi w_0}, \tag{6.3}$$

where θ is the half-angle beam divergence, λ the wavelength in vacuum and w_0 the beam radius at the beam waist. Hence, a diffraction limited Gaussian beam has an M^2-factor of 1 and smaller M^2 values are physically not possible. Figure 6.9 shows the contour profile of the TE far-field emission shown in Fig. 6.7. The blue circles represent the data points and the black solid line represents two fits with a Gaussian profile to the data. (The emitted annular profile leads to the occurrence of two peaks in the contour profile and hence $M^2 = 2$ is the best achievable value for the emitted laser beam and would suggest a diffraction limited beam.) A beam waist of $w_0 = (91 \pm 12)\,\mu\text{m}$ was obtained from the pump spot size in the near-field emission. We measured a half angle beam divergence $\theta = 5.36\,\text{mrad}$ at an emission intensity level of $1/e^2$ and thus obtain $M^2 = 2.83$. Hence, the TE emission is almost diffraction limited.

6.5 Discussion

To conclude, this chapter presented a novel waveguide and grating architecture which allows to integrate a solid-state eGFP film as the active material of a DFB laser. By introducing a thin ($\approx 65\,\text{nm}$) and high refractive index ($n = 2.12$) core layer, we optimized the waveguide architecture to overcome the problems originating from an unfavorable refractive index combination of the eGFP film and conventional grating polymers. For the first time to our knowledge, an ALD process has been used to apply a high refractive index layer on top of a DFB grating. The FIB/SEM measurements revealed that the high refractive index ZrO_2 layer was deposited smoothly and regularly with a defined thickness. By optically characterizing a two-dimensional second-order DFB GFP laser, we obtained a pump threshold of $56.6\,\text{kW cm}^{-2}$ and a wavelength tuning range of $\Delta\lambda = 51.65\,\text{nm}$. Furthermore, we showed that in contrast to conventional organic DFB lasers based on polymeric gain materials, both TE and TM modes are accessible and their effective refractive index can be simulated accurately. Far-field imaging of the vertical cavity emission revealed a peculiar annular laser beam profile that can be attributed to the finite-size of the optically active square lattice grating. Lastly, the TE mode emission with a beam quality factor of $M^2 = 2.83$ was found to be almost diffraction limited.

In the future, it may further be interesting to explore strategies for improving the lasing performance and reduce the threshold of DFB GFP lasers. For example, the modal overlap with the gain medium could be further enhanced by using a grating layer with a thinner residual layer in combination with a low refractive index substrate (e.g. MgF_2 as shown in Chapter 5). Furthermore, our two-dimensional grating structures appear to be an excellent model system

to study the coherent emission from vertical-cavity surface emitting lasers. Since the finite size of the pump beam can be used to define the area for coherent in-plane oscillation, they may be used to experimentally investigate the influence of finite-size effects on the emission from square-lattice photonic resonators. Simultaneous access to TE and TM modes as well as their corresponding side lobes is a further unique feature of our DFB GFP lasers.

During the time this chapter was written, work by Dogru *et al.* [209] was published, showing single mode emission from a DFB GFP laser. In this work, a thin layer of the high index metal oxide TiO_2 (deposition method not revealed) is sandwiched between a polymer grating and a gain material based on a mixture of silk and GFP.

7

Organic DFB Membrane Lasers

Optically pumped solid-state lasers based on organic semiconductors have advanced rapidly in the last two decades but applications in real-life scenarios are limited. In contrast to other optoelectronic devices based on organic semiconductors, they are most often produced on rigid substrates with macroscopic thickness not exploiting the inherent flexibilty of organic semiconductors. Here, we show a novel way to fabricate extremely thin and flexible organic lasers and propose their use as versatile security labels.

In Section 7.1, a brief overview of flexible optoelectronic devices based on organic semiconductors is given and the motivation to fabricate membrane-like organic lasers as well as the current limitations are discussed. A possible design for thin ($< 500\,\mathrm{nm}$) membrane lasers based on distributed feeback (DFB) gratings offering a low weight ($m/A \approx 0.5\,\mathrm{g\,m^{-2}}$) is introduced in Section 7.2. Furthermore, a newly developed water based lift-off process to fabricate the aforementioned membrane-like laser devices is shown. Next, in Section 7.3, the optical performance of the fabricated free-standing membrane lasers is assessed on the basis of three different gain materials. The transferability of a membrane laser opens the possibility to apply it to different objects of

complex shape. In Section 7.4, it is shown how membrane lasers can be transfered onto banknotes and be used as barcode-like labels. The laser performance and lifetime on the banknote is further assessed. The results presented in Section 7.5, reveal the influence of structural deformation on the lasing emission of the membrane lasers. Furthermore, the reason for a change in lasing emission and how it influences the application of membrane lasers as a security label on a banknote is investigated. The lightweight and thin design of membrane lasers is utilized in Section 7.6, to show possible applications as wearable security tags to augment biometric authentication. More precisely, the membrane lasers are applied to and operated on a human finger and on contact lenses employed to cow eye balls. In a proof of principle, it is shown that the membrane lasers on contact lenses could be safely operated even on a human eye. Lastly, Section 7.7, summarizes the findings and discusses possible further applications and improvements to the membrane laser design.

The contents of this chapter have in parts been published in Ref. [210].

7.1 Flexible Organic Lasers

The inherent mechanical softness of organic semiconductors allows to fabricate optoelectronic devices in a mechanically flexible and lightweight fashion [211]. Three prominent representatives are organic light emitting diodes (OLEDs) [212, 213], organic solar cells (OSCs) [214–217] and organic field effect transistors (OFETs) [218, 219]. For example, OLEDs and OFETs can be produced on $\approx 1\,\mu$m thick flexible polymer films to be used as wearable optoelectronic sensors and displays directly on the surface of the human skin [211, 220]. In contrast, the majority of organic semiconductor lasers have been produced in a rigid fashion, mainly due to a need for a solid and macroscopic supporting substrate.

Optically pumped organic semiconductor lasers have gained widespread attention as coherent light sources. They are solution processable and, as such, are easy and cheap to fabricate compared to other lasers based on inorganic semiconductors [21]. Furthermore, they can have a biocompatible design [27, 126] and their coherent emission can be tuned over the whole visible spectrum by using light emitting materials with different gain spectra [19] and by altering the resonance condition of the resonator [221]. These properties make organic semiconductor lasers perfect candidates for a range of different applications, including Raman spectroscopy on a single chip level [109], data-communication through LiFi [113], biosensing

on a molecular level [222] and chemosensing for detecting explosive vapors [223, 224]. All of the aforementioned organic semiconductor lasers use DFB gratings as the resonator structure. As discussed in earlier chapters (5 and 6), these resonators support single mode lasing, are easy to fabricate and, most importantly, for the work present in this chapter, are composed of a planar waveguide structure. There are a few examples of flexible organic DFB lasers in the literature, but those either require costly and harmful metal oxide intermediate layers together with femtosecond pumping schemes [225] or are produced on bendable substrates with macroscopic thickness [226–229]. In contrast, the results presented in this chapter show that it is possible to fabricate organic semiconductor lasers offering extreme flexibility without the need for metal oxide intermediate layers. Those membrane-like devices can be operated with nanosecond pumping and have a thickness defined only by the fundamental waveguide comprising the gain layer and the DFB resonator diminishing the need for a supporting substrate [210].

7.2 Membrane Laser Design and Fabrication

The membrane lasers were produced from an organic DFB laser stack with a newly developed water-based lift-off procedure to separate the laser stack from the carrier substrate (Fig. 7.1a). The laser stack shown in Fig. 7.1b was produced using standard solution processing techniques together with UV nanoimprint lithography. A detailed step-by-step fabrication description can be found in Appendix B. Initially, the stack comprised a thick and rigid carrier glass substrate, a water soluble sacrificial layer ($\approx$ 50 nm) consisting of poly(3,4-ethylenedioxytiophene)-polysterene-sulfonate (PEDOT:PSS, Clevios P VP AI4083, Heraeus), a UV curable transparent resist defining the DFB grating (mr-UVCur21-200nm, Micro Resist Technology) and a layer of an organic semiconductor polymer ((180 ± 10) nm, $F8_{0.9}BT_{0.1}$, see Section 3.3.1 for details) as the gain material. By immersing the laser stack into a water bath at 55 °C for 1 h the PEDOT:PSS layer dissolved and a thin membrane containing the DFB resonator and the gain material detached from the carrier substrate. Due to the hydrophobic nature of organic polymers, post lift-off, the membrane spread out on the water surface (Fig. 7.1c and d). The floating membrane was picked up from the water surface using another carrier substrate or was suspended in air (Fig. 7.1e and f). Thus, the membrane design offers the possibility to apply the organic DFB lasers to virtually any surface independent of surface topology or substrate composition.

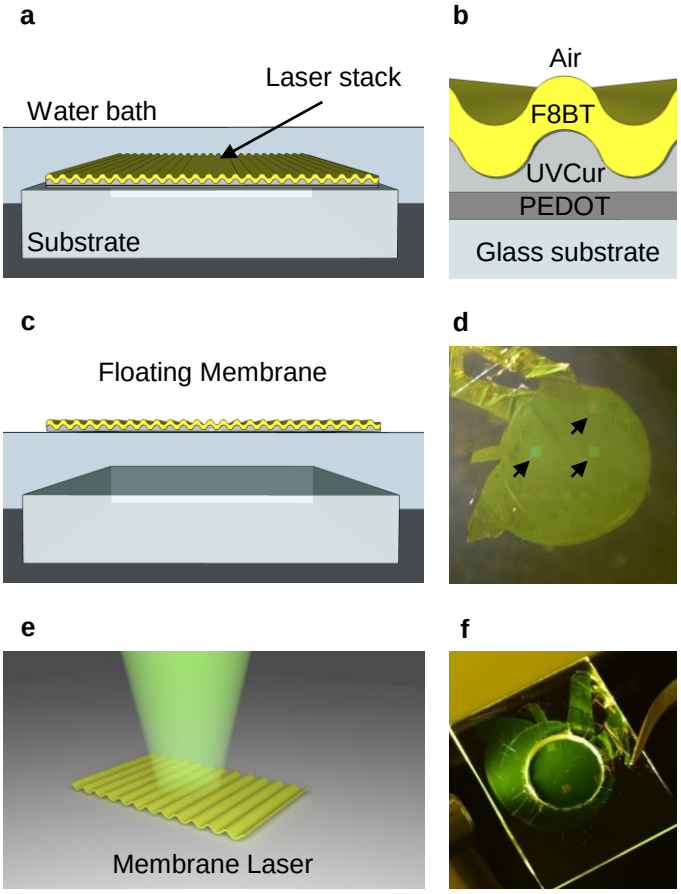

Figure 7.1: Schematic illustrations and photographs of a membrane laser and the fabrication process. **a**, Illustration of the laser stack immersed in a water bath heated to 55 °C. **b**, Illustration of the laser stack composition before lift-off (not to scale). **c**, Illustration of the floating membrane laser post lift-off from the carrier substrate. **d**, Photograph of a floating membrane spread out on the water surface post lift-off. The position of three second-order DFB gratings is indicated by black arrows. **e**, Illustration of the emission from a second-order DFB membrane laser (pump spot not shown). **f**, Photograph of a free standing membrane laser suspended over a hole ($\varnothing \approx 1$ cm) in a glass slide. Adapted from Ref. [210].

Table 7.1: Photoluminescence quantum yield (PLQY) of the conjugated polymers Super Yellow and $F8_{0.9}BT_{0.1}$. Measurements were taken from neat films and membrane laser stacks before and after a water bath at 55 °C for 1 h. The reference samples consisted of a grating layer and a gain layer and were not immersed in water but stored under ambient conditions for 1 h in between measurements.

Sample	PLQY, pre bath	PLQY, post bath
$F8_{0.9}BT_{0.1}$-film (neat)	0.62	0.63
$F8_{0.9}BT_{0.1}$ membrane laser	0.33	0.57
$F8_{0.9}BT_{0.1}$ reference	0.66	0.65
SY-film (neat)	0.43	0.38
SY membrane laser	0.31	0.30
SY reference	0.33	0.29

Furthermore, we found that the lift-off procedure had no detrimental effect on the photoluminescence quantum yield (PLQY) of the organic semiconductor polymer. Table 7.1 shows the PLQY for neat films and membranes of $F8_{0.9}BT_{0.1}$ and Super Yellow neat films as well as membranes before and after the water bath. The PLQY was measured using an integrating sphere (Hamamatsu Photonics C9920-02) at an excitation wavelength of 450 nm. For each material, the PLQY of a neat film and a membrane laser stack (both on a carrier glass substrates) was measured directly after the last fabrication step (spin-coating). A second measurement was performed after both samples had been immersed in water at 55 °C for 1 h. During the water bath, the membrane lasers lifted off the carrier substrate whereas the neat films remained on it. Consequently, the PLQY of the neat film samples was measured directly after the water bath. In contrast, the membrane lasers were first picked up using a carrier substrate on which they were then transfered into the integrating sphere to perform the PLQY measurement. The reference samples, consisting of a polymer grating and the organic gain layer, were not immersed in water but kept under ambient conditions for 1 h between the first and the second measurement. Neither of the two light emitting materials shows a significant reduction in PLQY after the water bath. In fact, the PLQY of the membrane laser consisting of $F8_{0.9}BT_{0.1}$ increased from 0.33 to 0.57 between the two measurements, approaching the PLQY level of the neat film. The lower PLQY of the pre water bath laser stacks is attributed to increased absorption losses in the integrating sphere introduced by the additional PEDT:PSS layer in the laser stack. More precisely, before lift-off, the sacrificial PEDOT:PSS layer causes additional absorption of photons originating from the organic emitter and the excitation source. During the water bath, the PEDOT:PSS layer dissolves and hence in the second PLQY measurement the absorption is reduced, leading to a recovery of the PLQY signal. Furthermore, we can conclude that the DFB grating does not induce significant absorption losses since the PLQY for samples with (membrane laser and reference) and without (neat film) grating is similar.

The membrane design not only offers high flexibility, transferability and lightweight but also improves the waveguiding properties of the laser stack. Figure 7.2 shows the $TE0$ mode profile within an organic DFB laser on a carrier glass substrate (blue dashed line, glass-air cladding, $n = 1.52$) and suspended in air (black solid line, air-air cladding, $n = 1.0$). The membrane design renders the $TE0$ mode more symmetrical and also improves the mode overlap with the organic gain material ($n = 1.7$, thickness 180 nm) from $\Gamma = 36\,\%$ with carrier glass substrate to $\Gamma = 59\,\%$. The thickness of the different layers was measured using a profilometer

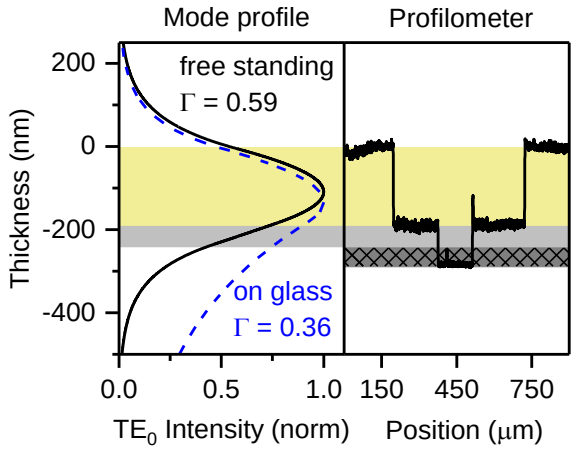

Figure 7.2: $TE0$ mode profile and profilometer measurement of a typical membrane laser stack. Left: The mode profile ($|E_y|^2$) is shown for a membrane laser attached to carrier glass substrate (pre lift-off, blue dashed line) and free standing in air (post lift-off, solid black line). Right: Profilometer measurement of a membrane laser before lift-off. The yellow area indicates the gain layer, the light gray area the polymer grating layer and the patterned dark gray area the sacrificial layer. Adapted from Ref. [210].

(DEKTAK 150 Surface Profilometer, Veeco).

The grating is defined on the boundary between organic gain layer and grating polymer. However, due to the small feature size and limited spatial resolution, the corrugation can not be resolved using a profilometer (grating not visible in right panel of Fig. 7.2). The DFB grating resonators consisted of one-dimensional second-order and mixed-order gratings with periods of 340 nm, 350 nm and 360 nm in second-order. Details on the grating fabrication (ultraviolet nanoimprint lithography) and further grating properties can be found in Section 3.1.3 and 3.1.4, respectively.

7.3 Optical Characterization of Membrane Lasers

The membrane lasers were optically characterized using the optical setup explained in Section 3.2. Devices based on the gain material $F8_{0.9}BT_{0.1}$ and a mixed-order grating as the resonator were investigated while being suspended in air over a hole in a glass cover slide. The DFB membranes showed a super linear increase in output power under optical excitation (wavelength, 450 nm; pulse duration, 5 ns; repetition rate, 5 Hz) above a threshold pump fluence of 3.3 kW cm^{-2} (Fig. 7.3a). This is equivalent to laser thresholds found for state-of-the-art organic DFB lasers on rigid carrier substrates [19, 20]. The emission spectra of the same membrane laser are shown in Fig. 7.3b. At a pump fluence below threshold, only a

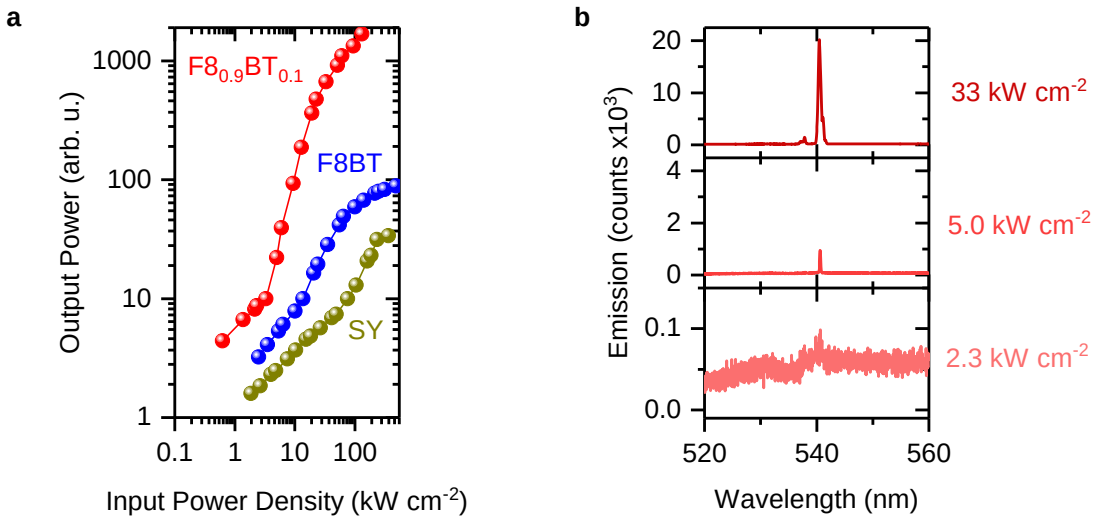

Figure 7.3: **a**, Input-output characteristics for one-dimensional mixed-order DFB membrane lasers based on different gain materials. The lasing threshold for devices with $F8_{0.9}BT_{0.1}$, F8BT and Super Yellow (SY) is 3.3 kW cm^{-2}, 13.8 kW cm^{-2} and 75.6 kW cm^{-2}, respectively. **b**, Emission spectra for the membrane laser device based on $F8_{0.9}BT_{0.1}$ for input pump densities below, just above and well above the lasing threshold. Adapted from Ref. [210].

Bragg mode on top of a broad fluorescence background could be observed. Just above threshold (5.0 kW cm^{-2}), a weak narrow single peak started to appear and gained super linearly in intensity with increasing pump fluence until it dominated the spectrum at a pump fluence well above threshold (e.g. 33 kW cm^{-2}). The spectral line narrowing with increasing pump fluence is shown in more detail in Fig. 7.4. The transition from a rather broad Bragg peak ($\Delta\lambda \approx 2$ to 4 nm) to a narrow peak ($\Delta\lambda \approx 0.1$ to 0.4 nm) happened at the threshold pump fluence identified above. These results are a clear indication for lasing action.

Furthermore, we found that the fabrication of membrane lasers is not limited to a single type of conjugated polymer but compatible with other materials of different molecular weight and chemical structure. Next to $F8_{0.9}BT_{0.1}$, we tested the lasing performance of membrane lasers based on F8BT and Super Yellow and found that $F8_{0.9}BT_{0.1}$ showed the lowest thresholds (see Fig. 7.3a and 7.4). More information on the different conjugated polymers is provided in Section 3.3.1. This is in accordance with earlier findings on rigid carrier substrates and the PLQY measurements [154, 198] (see Table 7.1). Membrane lasers based on the conjugated polymer Super Yellow, however, showed the best device yield post lift-off. The thin nature of our membrane lasers, makes them susceptible to fracture upon contact with sharp objects (e.g. a pair of tweezers during the transfer from the lift-off water bath to a carrier sub-

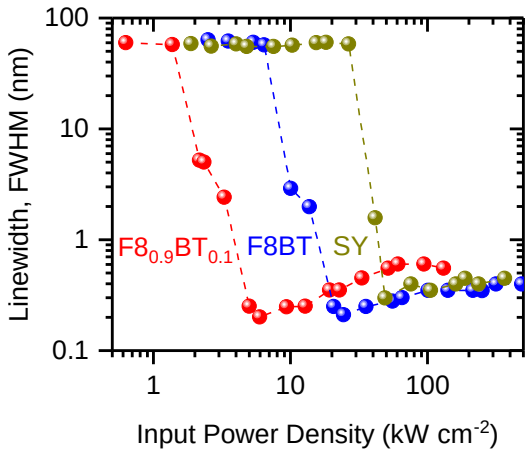

Figure 7.4: Emission peak linewidth for one-dimensional mixed-order DFB membrane lasers based on $F8_{0.9}BT_{0.1}$, F8BT and Super Yellow as the gain material. Adapted from Ref. [210].

strate). For membrane lasers based on F8BT and $F8_{0.9}BT_{0.1}$, we found a fabrication yield of $\approx 70\,\%$ whereas membrane lasers based on Super Yellow with the same layer thickness were more robust and showed a fabrication yield of $\approx 90\,\%$. We attribute the improved robustness and hence better fabrication yield to the higher molecular weight and correspondingly an increased chain branching of the Super Yellow polymer when compared to the fluorene derivates $F8_{0.9}BT_{0.1}$ and F8BT (see Section 3.3.1 for molecular weight information). The longer chain branching enhances the entanglement at branch sites and strengthens the polymer film [230].

A further indicator for lasing emission originating from DFB resonators is a well-defined and hence spatially coherent emission beam. Figure 7.5 shows the near- and far-field emission pattern for a mixed- and a second-order DFB membrane laser structure based on $F8_{0.9}BT_{0.1}$. The near- and far-field emission was measured using the optical characterization set up described in Section 3.2 without and with a Fourier lens inserted into the collection arm, respectively. The near-field emission from a mixed-order grating shows that most of the light is emitted from the narrow second-order region (indicated on the right hand side of the left panel in Fig. 7.5) in the center of the grating. This is in good agreement with our earlier findings on mixed-order DFB gratings on rigid substrates (see Section 5.4). Due to the narrow width of the emission region, the laser beam shows a rather broad divergence of $\pm(2.60 \pm 0.04)^\circ$ (spread of far-field emission at half maximum). As shown in Section 5.4, the emission divergence can be reduced (increased) by increasing (reducing) the number of second-order periods to extract

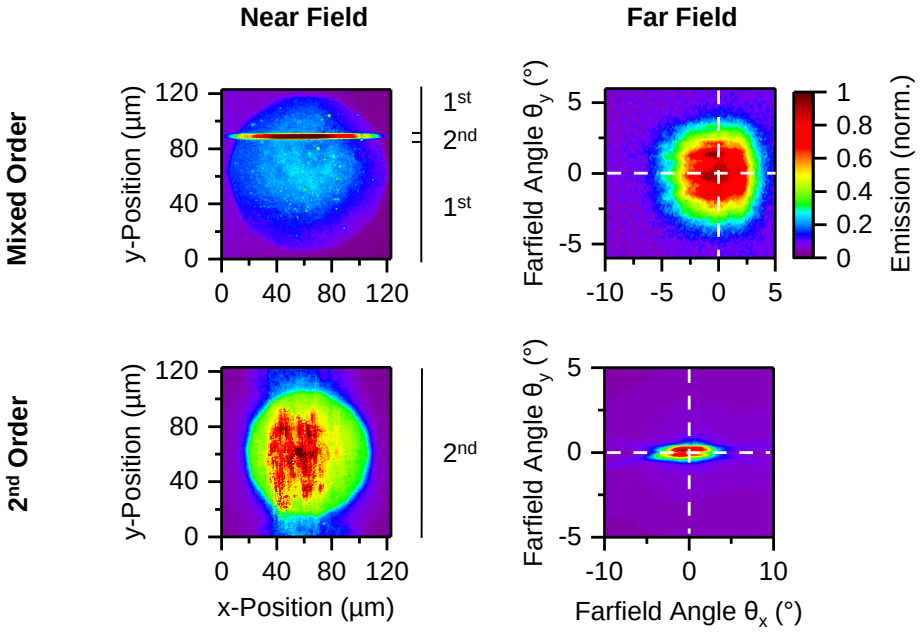

Figure 7.5: Near- and far-field emission of mixed- and second-order DFB membrane lasers based on $F8_{0.9}BT_{0.1}$. The spatial location of the first- and second-order grating regions are indicated on the right-hand side of the near-field emission panels. Adapted from Ref. [210].

the light. In fact, the ultimate limit for this effect can be seen in the emission from the pure second-order grating where the light extracting region is the whole optically active grating structure and hence as big as possible. The near-field emission for the second-order grating resembles the pump spot and proves that the light extraction is enhanced and spread over the the entire available gain area. As shown before, the increase in emission area leads to a less divergent $\pm(0.34 \pm 0.04)°$ and more well defined output beam with a fine double lobe structure in the far-field. However, due to the enhanced light extraction in pure second-order structures, an increased lasing threshold with a required pump fluence $> 60\,\mathrm{kW\,cm^{-2}}$ was observed. The well-defined laser beam is a clear indicator for spatial coherence and hence further evidence for lasing action in our organic DFB membrane lasers.

7.4 Membrane Lasers as Security Feature on Banknotes

The previous results (Section 7.3) clearly show that the membrane lasers emit a well defined, narrow and single mode spectrum which can be attributed to lasing action within the resonator structure. This optical property, together with the excellent transferability resulting from the substrate-less fabrication process, make our DFB membrane lasers a promising candidates for

applications where a unique identifier needs to be applied to an object requiring authentication control (e.g. ID documents, medication, banknotes, etc.). While standard solution processed organic DFB lasers can only be fabricated on very flat surfaces on which spin-coating is possible, the membrane lasers can be applied to any surface independent of shape or composition of the object. Post water lift-off and transfer, the membrane lasers stick tightly to the object after the remaining water has evaporated. The spectral position of the single emission peak of the DFB membrane lasers can be tuned by the grating period Λ, the gain region of the emissive material and the effective refractive index n_{eff} defined by the waveguide design. By using several closely spaced different DFB gratings on one membrane, it is possible to create a well defined emission pattern with multiple narrow peaks similar to a binary barcode, where 1 represents lasing emission at a specific wavelength and 0 otherwise (Figure 7.6a). Similar to a barcode label, the unique emission spectrum of the DFB membrane lasers on the object can be optically read out using a ns-pump and a spectrometer without the need for physical contact. For laser emission peaks with a separation of 1 nm and a typical gain spectrum for conjugated polymers with a width > 50 nm it is possible to encode at least 50 individual channels. The number of possible combinations for a binary code is 2^n where $n \in \mathbb{N}$ represents the number of available 1 and 0 states. Hence, it is possible to generate about $2^{50} \approx 10^{15}$ individual barcode-like labels.

7.4.1 Laser Characterization on Banknotes

The concept introduced above was realized to provide a counterfeit resilient security feature on a banknote. Amongst other reasons, the replacement of cotton with polymer banknotes in many currency unions in recent years is due to their increased counterfeit resilience [231, 232]. Figure 7.6b shows a membrane containing a number of DFB lasers transfered on the transparent window of a polymer banknote. The black arrows in Fig. 7.6b mark the location of two second-order DFB gratings on the membrane laser. Due to the scattering out of plane, the reflection of white light from second-order structures can be easily identified. This is different for mixed-order structures, where the light is only extracted by the narrow second-order section in the center and it is therefore difficult to locate the grating by eye. Similar to the membrane laser suspended in air, we can identify a distinct lasing threshold for membrane lasers transferred onto banknotes 7.6c. For a mixed-order grating DFB membrane laser based on $F8_{0.9}BT_{0.1}$, the required pump fluence to reach lasing action is 38.2 kW cm^{-2} and therefore

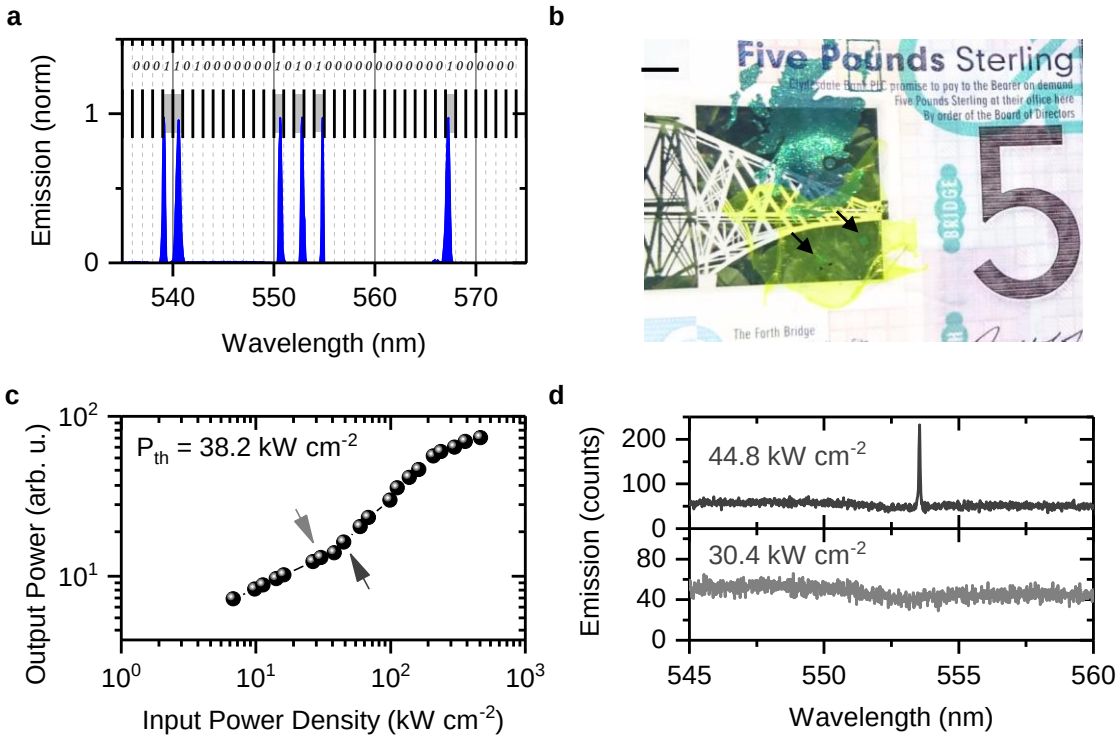

Figure 7.6: **a**, Barcode-like narrow lasing peak emission spectrum from a combination of second-order gratings with periods ranging from 340 to 360 nm. **b**, Photograph of a £5 pound banknote with a membrane laser transferred onto the transparent window. The black arrows indicate the position of two second-order DFB gratings. Scale bar, 5 mm. **c**, Input-output characteristics of a mixed-order DFB membrane laser on a banknote. The light and dark gray arrows indicate the applied pump fluence for the emission spectra recordings shown in d. **d**, Emission spectra just below (bottom) and just above (top) threshold measured on the same membrane laser. Adapted from Ref. [210].

increased compared to the free standing membrane laser. We attribute the threshold difference of more than one order of magnitude to increased absorption and scattering of the mode extending into the banknote. The polymer banknote is a higher refractive index cladding compared to air and consequently changed the waveguiding properties. This reduced the modal overlap with the gain material and gave rise to leaky substrate modes. The field extending into the banknote consequently experienced higher scattering and absorption losses. The spectral properties just below and just above threshold of the DFB membrane laser on a banknote (Fig. 7.6d) agree well with our previous observations on free standing mixed-order DFB membrane lasers. The spectral linewidth of the laser emission from the banknote was measured to be $\Delta\lambda = 0.2$ to 1.2 nm (full width half maximum, FWHM) depending on the grating quality, grating type and pump fluence. However, due to the large signal-to-background ratio it is possible to to localize the maximum spectral position of the lasing peaks to a much higher precision ($\approx \pm 10$ pm) using peak fitting. Hence, the desired 1 nm precision needed to obtain 10^{15} unique labels is readily achievable.

7.4.2 Lifetime of Membrane Lasers on Banknotes

We have shown that a unique and discrete emission spectrum can be readily created on a banknote but the application of this idea is only feasible if the laser shows a stable emission over longer times. A main concern with devices based on organic semiconductor is their stability under ambient conditions. Hence, extensive efforts have been devoted to study the lifetime of OLEDs and OSCs and to find long lasting and well protecting encapsulation strategies for the aforementioned devices [233–235]. For OLEDs or OSCs, it is important that the light emission or light conversion is stable and efficient continuously over long periods of time. For the organic membrane lasers as a security feature on banknotes, in contrast, a continuous emission is not necessary but a stable output while being occasionally probed over the course of several months or years is crucial. Figure 7.7a shows the emission spectrum of a membrane laser on a banknote containing three gratings with a different periodicity. Even after 200 days, we observed a stable emission comprising three distinct and narrow lasing peaks. To analyze the stability of the laser emission, we investigated the spectral peak position at maximum intensity by fitting a Gaussian function to the emission peaks for each spectrum (see Fig. 7.7b). The maximum standard deviation σ of the peak lasing wavelength λ_{max} over the entire test period was only $\sigma(\lambda_{max}) < 65$ nm. In between the emission test cycles, the banknote containing the

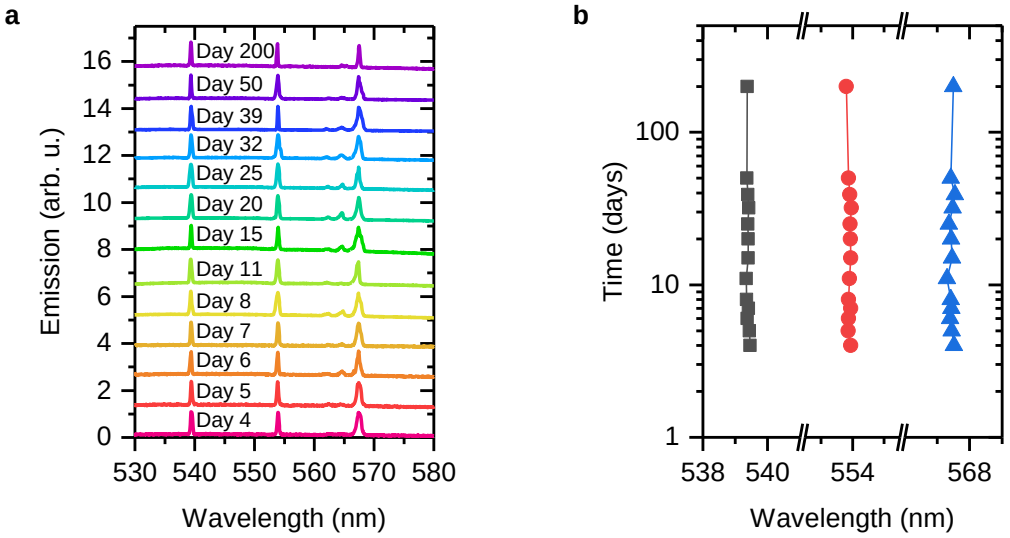

Figure 7.7: **a**, Emission spectra of a DFB membrane laser containing three different gratings measured over a time span of 200 days. **b**, Peak emission wavelengths of the same spectra, accurately extracted by fitting Gaussian functions to the individual lasing peaks. The standard deviation of the peak wavelength is $\sigma_{540} = 33.4\,\text{pm}$, $\sigma_{554} = 33.4\,\text{pm}$ and $\sigma_{568} = 33.4\,\text{pm}$ for the lasing peaks around 540 nm, 554 nm and 568 nm, respectively. Adapted from Ref. [210].

membrane laser was stored under ambient conditions without any encapsulation. To simulate a more realistically environment, during the first 7 days the banknote was even stored in the experimentalists wallet (this was discontinued after 7 days due to fear of mistakenly spending the banknote).

7.5 Bending Characteristics of Membrane Lasers

A banknote made out of a polymer or cotton is by nature flexible and bendable. It was therefore important to investigate the effects of bending on the membrane laser device itself and the spectral emission properties. From the experimental data shown in Fig.7.7, we can confirm that even after 200 days and multiple bending cycles, the membrane laser did not delaminate from the banknote nor did it show any visible damage. As shown in previous studies on organic lasers fabricated on flexible substrates, the emission wavelength can be tuned by gradual bending parallel to the grating grooves [236–238]. The induced radius of curvature leads to a change in grating period and possibly also a change in refractive index due to the compression and extension of the polymer film. According to the Bragg condition (see Eq. 2.41) this leads to a change in resonance wavelength and hence shifts the emission peaks. Figure 7.8a contains photographs and illustrations showing the possible negative and positive bending states

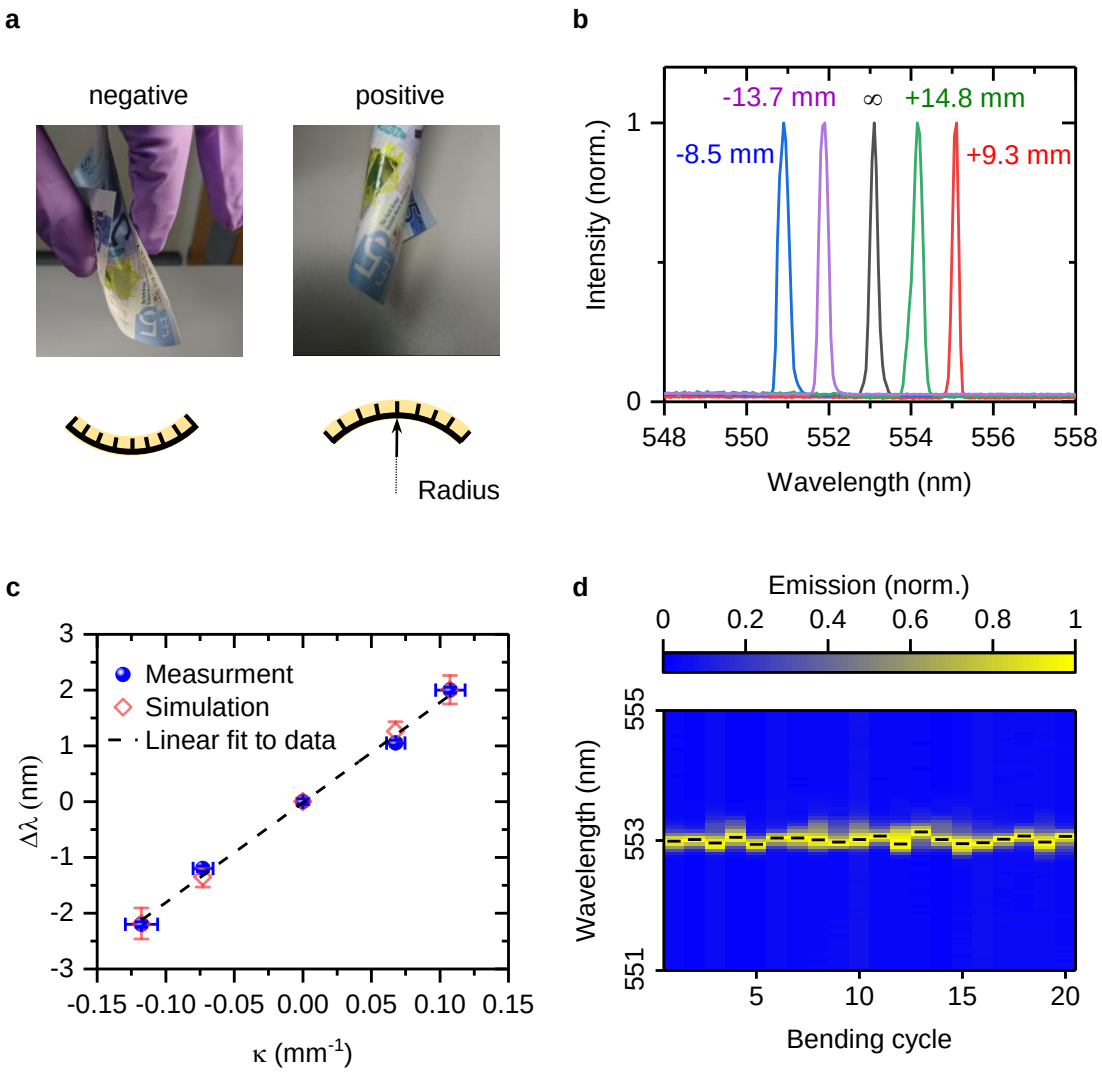

Figure 7.8: **a**, Photographs and illustrations of the negative and positive bending parallel to the grating grooves of a membrane laser attached to a banknote. **b**, Laser emission wavelength depending on the bending radius of the banknote. **c**, Wavelength shift $\Delta\lambda$ upon bending the banknote with a specific curvature κ (inverse of bending radius). The blue circles represent the measured data obtained from b. The red diamonds are calculated values based on the expected displacement of the grating grooves on top of the banknote. The dashed line represents a linear fit to the measured data points. **d**, Lasing emission spectrum of the same membrane laser on a banknote after straightening it out following repetitive bending cycles (bending radius, 8 mm). The black dashed lines represent the peak wavelength determined by fitting Gaussian functions to the spectra. Adapted from Ref. [210].

of a banknote. To study the wavelength shift of the lasing emission upon bending, we used a banknote containing second-order DFB membrane lasers and induced well defined bending radii by wrapping the banknote around different precisely fabricated cylindrical centrifuge tubes. The maximum induced wavelength shift for a negative bending radius of −8.5 mm was −2.2 nm and for a positive bending radius of 9.3 mm was 2.0 nm with respect to the emission from the straightened out and flat membrane laser.

Figure 7.8c shows the measured wavelength shift $\Delta\lambda$ versus the applied bending curvature κ (inverse of radius, blue circles). Also shown, is the expected wavelength shift upon bending by calculating the grating groove displacement on top of the banknote using simple trigonometry. To calculate the expected groove displacement, we measured the thickness of the banknote ($(84.1 \pm 6.1)\,\mu$m) using an optical microscope. In a next step, the Bragg condition was used to determine the expected wavelength shift induced only by the grating groove displacement. The calculated and measured wavelength shift $\Delta\lambda$ agree well and it is hence possible to rule out a significant change in refractive index upon bending. Furthermore, we find a bending sensitivity of the lasing wavelength of $(17.92 \pm 0.69)\,\text{nm} \times \text{mm}$. For using membrane lasers as security features on banknotes, a stable emission spectrum is needed and hence the susceptibility of the emission to bending with a consequent wavelength shift is not desirable. In a real life scenario, however, this may not be a problem since the banknote and hence the membrane laser can always be straightened out before measuring the spectrum and hence obey the same resonance condition leading to a constant lasing emission wavelength. Figure 7.8c shows the emission wavelength after 20 consecutive bending cycles. In one bending cycle the membrane laser on the banknote was bent to a radius of $\approx 8\,$mm and straightened out again. The standard deviation of the laser emission during 20 consecutive bending cycles was only $\sigma(\lambda_{\text{max}}) = 50.7\,$pm, confirming that the initial emission wavelength can be accurately restored.

7.6 Membrane Lasers as Wearable Security Tag

Due to their excellent transferability, the use of membrane lasers as unique labels is not restricted to banknotes or similar paper based documents. In recent years, biometric identification has become increasingly important and is a vivid field for academic and industrial research [239]. A core principle of biometric identification is that the identifier (e.g. read out of finger print or iris scan) is inherent to the owner (e.g. human). This is useful for e.g.

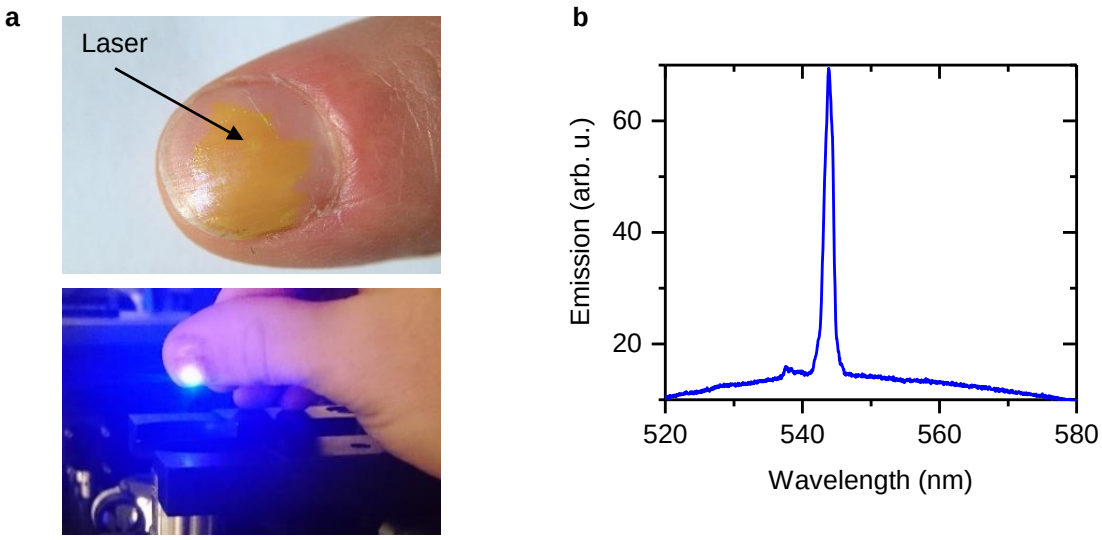

Figure 7.9: **a**, Photographs showing a membrane laser on a finger nail and under optical excitation. **b**, Lasing emission spectra recorded from a membrane laser on a finger nail. Adapted from Ref. [210].

permanent access control and only works with prior knowledge of the identifier. However, if the identifier can not be recorded before or if there is the need to transfer an identifier from one person to the other, the classical biometric identification does not work. In addition, some biometric markers as for example finger prints can be copied and forged. Our DFB membrane lasers may be used as transferable identifiers that can be worn and read out on virtually any body part and as such may complement biometric identification.

7.6.1 Finger Lasers

Figure 7.9a shows a membrane laser transferred onto a finger nail. The small bright square (labeled laser) originates from room light reflections of a second-order DFB grating on the membrane laser. As on the banknote, the membrane sticks tightly to the finger nail after the water from the lift-off process has evaporated. By optically exciting the membrane laser on the finger nail, a narrow emission spectrum from a second-order DFB grating was recorded (Fig. 7.9b). Recording the input-output characteristics of a membrane laser attached to a finger nail reliably, required to have a steady hand for several $\sim 10\,\mathrm{s}$ and was hence not possible. Interestingly, by immersing the finger in water, the hydrophobic nature of the polymer film causes the membrane to delaminate and spread out on the water surface. Consequently, the detached membrane laser can be stored or used on a different object or body part. In the future, these devices may be a possible augmentation basis for biometric finger print scans.

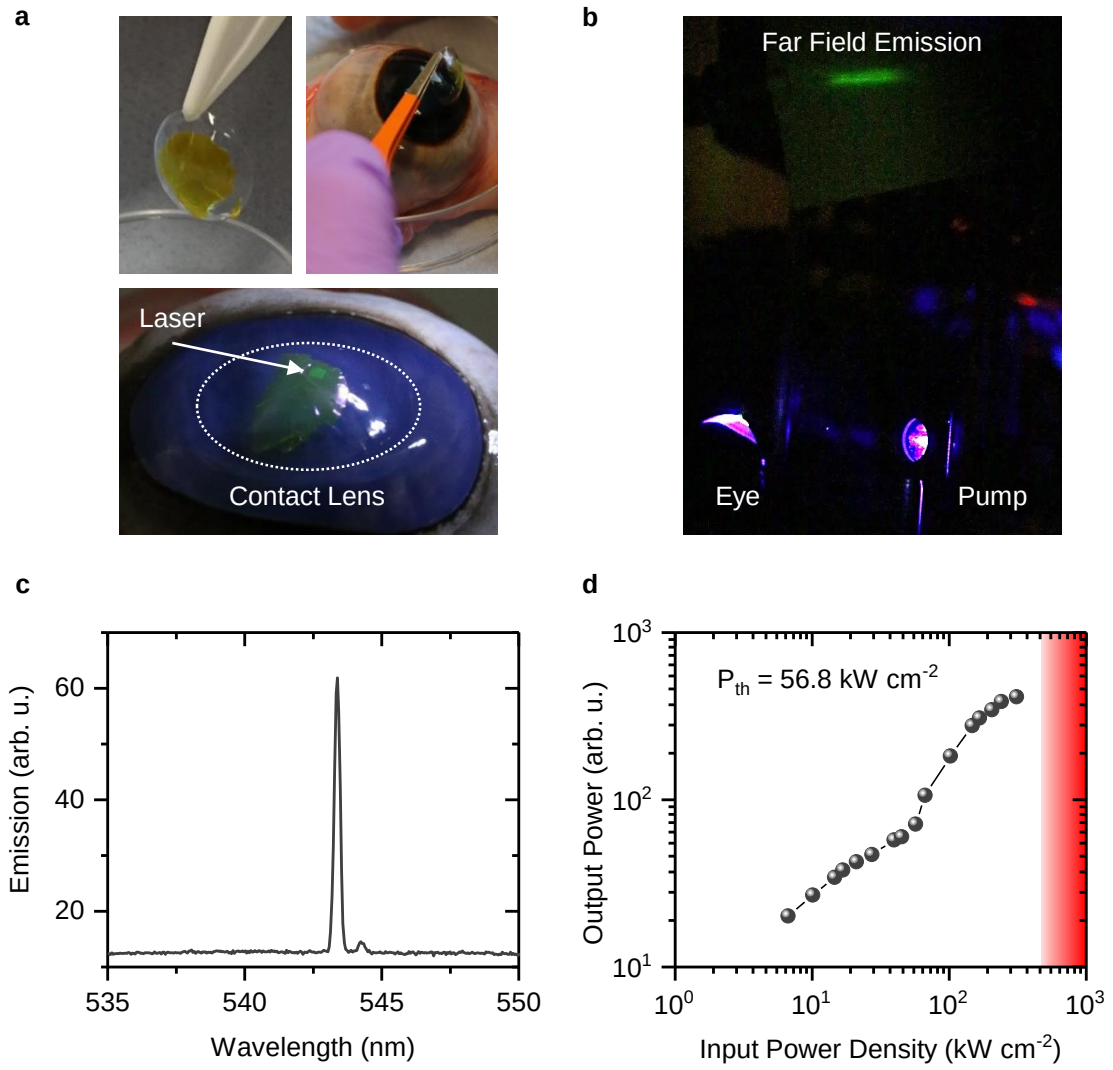

Figure 7.10: **a**, Photographs showing the mounting process of a membrane laser onto a contact lens and subsequently the transfer of the contact lens onto a bovine eye ball. The boundary of the contact lens is highlighted by a white dashed line. **b**, Far-field laser emission from a membrane laser on a bovine eye ball. The emission beam was visualized by placing a screen 50 cm away from the eye ball. The membrane laser was optically pumped from the right-hand side. **c**, Emission spectrum recorded from the bovine eye ball with a contact lens containing a membrane DFB laser. **d**, Input-output characteristics of a mixed-order membrane DFB laser on a bovine eye ball. The red area marks pump power densities that exceed the limit for ocular safety for intentional and repeated use on the human eye. Adapted from Ref. [210].

7.6.2 Contact Lens Lasers

The optical transparency of the membrane lasers in conjunction with the low pump fluence requirements, lightweight and thin design, motivated us to test the feasibility of using them as identification tags on contact lenses where they may complement a biometric iris scan in the

future. After the lift-off process, we mounted a membrane laser on a commercially available contact lens and transferred it on a bovine eye ball. Figure 7.10a shows the fabrication of the contact lens laser as well as the membrane laser on the bovine eye ball. Again, a second-order DFB grating can be identified by the reflected room light as a small bright square. We used bovine eye balls as a model due to their structural similarity and slightly larger size compared to the human eye [240] as well as their general availability (purchased from a local abattoir). Optically exciting a second-order DFB laser on the contact lens, led to the generation of a well-defined green laser beam originating from the eye (see Fig. 7.10b). The double-lobed structure together with the small divergence is similar to the far-field emission shown in Fig. 7.5 and a characteristic of second-order DFB gratings. The spectrum (see Fig. 7.10c) shows that the laser operation on the eye did not hamper the spectrally narrow emission ($\Delta\lambda = 0.25\,\text{nm}$, FWHM) and allows to multiplex the emission from several similar DFB gratings. Figure 7.10d shows the input-output characteristics of a membrane laser based on a mixed-order grating and operated on the eye. The onset for lasing was at a pump fluence of $56.8\,\text{kW}\,\text{cm}^{-2}$ and hence like the threshold of a membrane laser on a banknote (*cf.* Fig. 7.6c) more than one order of magnitude above the lasing threshold for a free standing membrane laser. Again, this can be attributed to the contact lens acting as a higher index cladding compared to air and hence leading to a reduced mode confinement in the gain layer and leaky substrate modes. Interestingly, the required pump fluence to achieve lasing is within the maximum permissible exposure limit for repeated and intentional ocular exposure. This can be assessed by performing calculations based on the ANSI 2000 standard which defines the maximum permissible exposures for ocular safety [241]. The maximum permissible corneal irradiance for a divergent pump beam with a duration of 5 ns, a repetition rate of 5 Hz, a wavelength of 450 nm and a full visual angle of 50° is $505.1\,\text{kW}\,\text{cm}^{-2}$. This is the limit for thermal damage which is dominating for the pump conditions used. Damage to the cornea can thus be expected for a pump fluence one order of magnitude above the onset for lasing in our membrane DFB laser devices (marked as a red area in Fig. 7.10d). Other damage pathways are only important for even shorter pulse durations or longer overall exposure times. For example, photochemical damage is only relevant for exposure times exceeding 1 s at short visible wavelengths. Thus, according to our calculations based on the ANSI 2000 standard, our membrane laser devices - under appropriate optical pumping - may be safely operated on the human eye.

7.7 Discussion

To conclude, this chapter presented a novel water based lift-off procedure to fabricate membrane like DFB lasers with a thickness of $\approx 200\,\mathrm{nm}$ and a weight of only $m/A \approx 0.5\,\mathrm{g\,m^{-2}}$. The hydrophobic nature and flexibility of the polymer film make it possible to repeatedly apply the membrane lasers to arbitrarily shaped objects. This, together with the possibility of creating a unique output spectrum and the low pump power requirements for reaching the onset of lasing, make it possible to apply the membranes to a variety of objects were authentication control is crucial. In this chapter, we have shown that membrane lasers can be successfully and safely be operated as unique labels on banknotes, finger tips and even on an eye if mounted on a contact lens.

The number of unique labels could be further enhanced by combining several conjugated polymers with different spectral gain regions. This would lead to an exponential increase in the number of tags to $(10^{15})^n$, where n is the number of different conjugated polymers. Improving the DFB resonator further may result in even lower threshold values which offers the prospect to use a conventional inorganic LED as a pump source [105] instead of a ns-laser. One strategy to decrease the threshold would be the application of a high refractive index material in order to increase the refractive index contrast in the DFB resonator (similar to the work in Section 6). Another possibility would be to print the grating directly into the polymer film using solvent immersion nanoimprint lithography [242]. This may further enhance the confinement of the optical mode within the gain material and also lead to an increased refractive index contrast in the DFB resonator. With the recent developments of roll-to-roll nanoimprint and organic inkjet printing [114], an economically viable mass production of membrane DFB lasers with high reproducibility may be possible. Furthermore, it would be interesting to explore the applications of membrane DFB lasers in other research fields. The substrate-less design makes the conjugated polymer accessible from both sides and hence maximizes the possible interaction area of the polymer with the environment. This might be especially interesting for increasing the sensitivity in chemosensing applications based on fluorescence quenching and hence gain reduction in organic lasers.

8

Conclusion and Outlook

In this thesis, the generation of laser light within or by biological and biocompatible soft materials has been investigated. The photonic properties of biological laser systems have been studied in order to achieve a better understanding of the optical processes involved and to further enhance and engineer the biointegration and biocompatibility of these devices.

In Chapter 4, the fundamental creation of different lasing modes and their interplay with the biological material in single cell lasers was investigated. Initially, two different intracellular fluorescent materials were examined for their potential to provide sufficient optical gain for single cell laser devices. While the cell produced green fluorescent protein (GFP) offers a better biointegration, the synthetic dye CMFDA is readily introduced to a large fraction of cells within a population and provides a more stable and brighter fluorescence signal. Having established a suitable gain material, we demonstrated that embedding a fluorescent cell into a planar cavity gives rise to 3D photonic confinement. By comparing the single cell laser emission to the emission of a cavity mimicking the refractive index landscape created by the presence of a cell and an unstructured cavity, we concluded that the photonic confinement is due to

the refractive index contrast between cell and surrounding. Furthermore, using Fourier- and hyperspectral-imaging techniques, we investigated the creation of different longitudinal and transversal lasing modes and how their respective mode patterns in Fourier- and real-space are related.

This in depth characterization may provide the basis for developing a single cell laser cytometry platform for sensing intracellular properties. This has in parts been attempted by Chen *et al.* [135] by developing a proof of principle microwell array for single cell lasers. If full biointegration is desired and fluorescent proteins are chosen as intracellular gain material, a more stable and efficient transfection method would be desirable to readily provide enough fluorescent proteins in a large fraction of a cell population. Single cell lasers may further be used for more fundamental photonic research to facilitate strong coupling between cavity photons and material bound excitons and potentially low threshold polariton lasing. A first step towards biological polariton lasing has been achieved by showing the passive light matter coupling and creation of polaritons in a small planar cavity containing the bacterium *Chlorobaculum tepidum* [243]. Here, the small size of the bacterium (roughly, 1 µm) allows a small cavity with reduced mode volume which is beneficial for strong coupling.

In Chapter 5, the development of an evanescently pumped water-based optofluidic DFB laser was presented. While conventional optofluidic DFB dye lasers mainly rely on gain materials dissolved in high refractive index fluids, our optofluidic DFB laser can readily be operated with low refractive index fluids such as water, providing an increased biocompatibility and paving the way for biosensing applications. This was achieved by optimizing the waveguide structure and incorporating a low refractive index substrate as well as using a mixed-order DFB grating. Furthermore, the passive and active photonic dispersion analysis enables a precise measurements of device parameters such as the refractive index of the gain fluid.

Most optofluidic DFB lasers to date rely on optical feedback provided by a whispering gallery mode or a Fabry-Pérot resonator [36], supporting multi-mode emission. In contrast, the single-mode operation of our evanescently pumped DFB laser may allow to more easily detect minute changes in the fluidic and potentially biological gain medium. Furthermore, the possibility of conveniently applying the fluidic gain material as a droplet onto the grating structure diminishes the need for an elaborate microfluidic system. Since the waveguided lasing mode only extends evanescently into the gain material, stimulated emission is expected

to occur only within $\sim$ 300 nm of the gain layer, which may be an interesting feature for experiments involving surface biology [244]. Interestingly, biosensing experiments in a passive corrugated waveguide have already been demonstrated [245]. Another future biological laser device might be a DFB cell laser, in which an evanescently pumped DFB laser may be operated by seeding GFP expressing cells on the grating surface. A change in protein density within the cell, may result in a refractive index change which alters the resonance condition and hence the lasing wavelength. Cellular refractive index measurements have been reported on corrugated waveguides by monitoring shifts in passive resonances [246, 247].

In Chapter 6, the integration of a solid-state GFP film with a DFB resonator for a novel biological laser device was explored. We showed how a high refractive index interlayer can provide sufficient feedback in a DFB resonator structure that otherwise would be refractive index matched. Furthermore, a broad spectral tuning range with precise control of the lasing wavelength by changing the DFB grating period was demonstrated. Lastly, the vertically emitted annular TE and TM beams were investigated.

It is well known that the intermolecular distance in solid-state GFP films and hence the quenching rate depends on the humidity of the environment [29]. In the future, it may be interesting to explore the potential of using the single mode DFB GFP lasers as a humidity sensor. A change in humidity changes the density of the gain material and hence may induce a shift in lasing wavelength, polarization or stop lasing emission entirely due to concentration quenching. The DFB GFP lasers may further be an interesting playground for more fundamental photonic studies since the the finite size of the pump spot can be used to roughly define the area for coherent in-plane oscillation.

Finally, the results presented in Chapter 7 have demonstrated that applications for optically pumped organic lasers are not yet fully exploited and that these lasers if designed in a novel way, for example as membranes, can be used in the context of biocompatible devices. Lasing emission was obtained from membrane like DFB lasers with a thickness < 500 nm and the concept that the emission spectrum constitutes a unique barcode-like label was introduced. In fact, due to the narrow lasing emission, 10^{15} unique labels can be created for one gain material. Due to their excellent transferability, the integration of membrane lasers as security labels on a banknote, a human finger and a contact lens for the use on the eye is readily achievable.

We further envision, that membrane lasers may be used in the context of chemo- or biosens-

ing, where the presence of quenchers reduces the fluorescence signal and hence limits the stimulated emission rate. In contrast to conventional organic laser sensors, the sensitivity may be enhanced due to an increased surface area inherent to the membrane design.

To sum up, this dissertation has mainly explored various ways in which DFB resonators can be operated in the context of lasing from biological and biocompatible soft matter. We have demonstrated that DFB resonators can be utilized as an integral part of optofluidic and various solid-state biological lasers. The modular multi-layer waveguide design and flexible fabrication of DFB resonators offers the possibility of altering the optical properties of certain layers (*cf.* Chapter 5), adding layers (*cf.* Chapter 6) or removing layers (*cf.* Chapter 7), depending on the desired biological application and gain material. Having a tunable and narrow band single mode emission is a further feature of DFB resonators and desired in the context of biological experiments in order to observe minute changes in the emission signal. The enhanced integration of DFB resonators with biological materials may lead to the development of novel on-chip devices for future point-of-care diagnosis. Studying the coherent emission from biological material in general will further enhance our understanding of the interaction between light and living organisms and biological materials. The field of biological lasers is still in its infancy and many concepts and ideas are not yet fully developed, leaving exciting challenges and opportunities for further investigations, both for application driven endeavors but also for fundamental research on the chemical or photonic properties of the biological host materials. In the future, fully integrated biological laser devices may also be used in the human body for a multitude of different sensing and monitoring tasks via contact-less optical readout. This thesis represents an important step towards this future by developing novel biological laser devices, improving their performance and exploring new applications.

A

Waveguide Mode Simulations

```
% Calculates the waveguided modes in an asymmetric 3 layer dielectric slab.
% Input parameters are the refractive indices, the layer thickness of the
% core and the vacuum wavelength. The cut-off wavelength and the number of
% modes and their corresponding refractive index is calculated using a ray-
% optics approach. This is performed for TE and TM modes. The different
% polarization is implemented in all calculations. The mode profile is
% calculated by a wave-field approach utilizing the results from the
% ray-optics approach. Starting of with Maxwell's Eq., solving the
% Helmholtz Eq. in 2 dim. (using the 2 dim. structure of the stack) and
% considering all boundary conditions between the layers gives a system of
% 4 Eq. and 4 unknown coefficients that can be solved.
% Requires InterX.m (available for download on Mathworks File Exchange),
% eqns_te.m and eqns_tm.m (available for download in the associated data
% files to this thesis).
```

```
% Input parameters
na = 1.0;         % Refractive index of the air layer
ng = 1.7;         % Refractive index of the guiding layer
ns = 1.52;        % Refractive index of the substrate layer
d =  500e-9;      % Thickness of the guiding layer
lambda = 530e-9;  % Vacuum wavelength
% Calculation region
x1 = linspace(0, d, 2000);      % Position of the guiding layer
x2 = linspace(-4*d, 0, 2000);   % Position of the substrate layer
x3 = linspace(d, 4*d, 2000);    % Position of the air layer
period = linspace(ns,ng,200);   % Interval for effectiv refractive index ne
% Calculation of the cut off wavelength in nm
lambda_cut_off = (((4*pi*d)/(2*atan(sqrt((ns^2-na^2)/(ng^2-ns^2)))))*sqrt(ng
    ^2-ns^2))*1e9;
% Maximum number of modes for TE and TM
M_max = ceil((1/(2*pi))*(((4*pi*d)/(lambda))*sqrt(ng^2-ns^2)-2*atan(sqrt((ns
    ^2-na^2)/(ng^2-ns^2)))));
i=0;    % Count index
j=0;    % Count index
% Solves the transcendental eq. to calculate the supported TE and TM modes
% plus their effective refractive index
for M = 0:M_max-1;  % Mode number, multiples of 2pi
    j=j+1;          % Start j count at 1
    for ne = linspace(ns,ng,200)    % Every possible refractive index
        i=i+1;      % Start i count at 1
        factor(i) = (4*pi*d/lambda)*sqrt(ng^2-ne^2);
        te(j,i) = 2*atan(sqrt((ne^2-na^2)/(ng^2-ne^2)))+ 2*atan(sqrt((ne^2-
            ns^2)/(ng^2-ne^2)))+2*M*pi;
        tm(j,i) = 2*atan((ng^2/na^2)*sqrt((ne^2-na^2)/(ng^2-ne^2)))+ 2*atan
            ((ng^2/ns^2)*sqrt((ne^2-ns^2)/(ng^2-ne^2)))+2*M*pi;
    end
 i=0;    % Set count to zero
```

```
43      factor_new(1,:) = factor;   % Rearanging to use InterX
44      factor_new(2,:) = period;   % Rearanging to use InterX
45      te_new(1,:) = te(j,:);      % Rearanging to use InterX
46      te_new(2,:) = period;       % Rearanging to use InterX
47      tm_new(1,:) = tm(j,:);      % Rearanging to use InterX
48      tm_new(2,:) = period;       % Rearanging to use InterX
49      te_points(j,:) = InterX(factor_new,te_new) % Find crossing points for TE
50      tm_points(j,:) = InterX(factor_new,tm_new) % Find crossing points for TM
51  end
52  % Calculates the mode profile for all TE modes
53  for r_te = 1:length(te_points(:,1))     % Number of possible modes
54      ne = te_points(r_te,2);             % and corresponding ne
55      k0 = (2*pi)/(lambda);               % Vacuum wavevector
56      kxx = sqrt((-k0^2*ne^2+k0^2*ng^2)); % Wavevector in x direction
57      a = sqrt(k0^2*(ne^2-na^2));         % Def: air factor
58      s = sqrt(k0^2*(ne^2-ns^2));         % Def: substrate factor
59      save('var_te')         % Save workspace to new file 'var_te'
60      guess_te=[1 1 1 1];    % Start guess to solve the system of eq.
61      [result_te,fval_te,exitflag_te,output_te]=fsolve(@eqns_te,guess_te);
            % Solve system of eq. in 'eq_ns' with start guess and workspace
            loaded within the fct.
62      result_te   % Unknown coefficients from system of eq.
63      fval_te     % Solution of the root finding
64      output_te   % Specs of the calculation
65      A_te=result_te(1);  % Unpack coefficients
66      B_te=result_te(2);  % Unpack coefficients
67      C_te=result_te(3);  % Unpack coefficients
68      D_te=result_te(4);  % Unpack coefficients
69      % Calculation of mode profile using determined coefficients
70      Ey1_te = (A_te*exp(1i*kxx*x1)+B_te*exp(-1i*kxx*x1)); % Guide layer
71      Ey2_te = (D_te*exp(sqrt(k0^2*(ne^2-ns^2))*x2));      % Substrate layer
72      Ey3_te = (C_te*exp(-sqrt(k0^2*(ne^2-na^2))*x3));     % Air layer
```

```
73      % Integration of mode overlap with different areas
74      int_part1_te = trapz(x1,abs(Ey1_te).^2);
75      int_part2_te = trapz(x2,abs(Ey2_te).^2);
76      int_part3_te = trapz(x3,abs(Ey3_te).^2);
77      int_full_te = int_part1_te + int_part2_te + int_part3_te;
78      ratio1_te = int_part1_te/int_full_te;
79      ratio2_te = int_part2_te/int_full_te;
80      ratio3_te = int_part3_te/int_full_te;
81  end
82  % Calculates the mode profile for all TM modes
83  for r_tm = 1:length(tm_points(:,1))     % Number of possible modes
84      ne = tm_points(r_tm,2);             % and corresponding ne
85      k0 = (2*pi)/(lambda);               % Vacuum wavevector
86      kxx = sqrt((-k0^2*ne^2+k0^2*ng^2));  % Wavevector in x direction
87      a = sqrt(k0^2*(ne^2-na^2));         % Def: air factor
88      s = sqrt(k0^2*(ne^2-ns^2));         % Def: substrate factor
89      save('var_tm')          % Save workspace to new file 'var_te'
90      guess_tm=[1 1 1 1];     % Start guess to solve the system of eq.
91      [result_tm,fval_tm,exitflag_tm,output_tm]=fsolve(@eqns_tm,guess_tm);
            % Solve system of eq. in 'eq_ns' with start guess and workspace
            loaded within the fct.
92      result_tm   % Unknown coefficients from system of eq.
93      fval_tm     % Solution of the root finding
94      output_tm   % Specs of the calculation
95      A_tm=result_tm(1);  % Unpack coefficients
96      B_tm=result_tm(2);  % Unpack coefficients
97      C_tm=result_tm(3);  % Unpack coefficients
98      D_tm=result_tm(4);  % Unpack coefficients
99      % Calculation of mode profile using determined coefficients
100     Ey1_tm = (A_tm*exp(1i*kxx*x1)+B_tm*exp(-1i*kxx*x1)); % Guide layer
101     Ey2_tm = (D_tm*exp(sqrt(k0^2*(ne^2-ns^2))*x2));      % Substrate layer
102     Ey3_tm = (C_tm*exp(-sqrt(k0^2*(ne^2-na^2))*x3));     % Air layer
```

```
103     % Integration of mode overlap with different areas
104     int_part1_tm = trapz(x1,abs(Ey1_tm).^2);
105     int_part2_tm = trapz(x2,abs(Ey2_tm).^2);
106     int_part3_tm = trapz(x3,abs(Ey3_tm).^2);
107     int_full_tm = int_part1_tm + int_part2_tm + int_part3_tm;
108     ratio1_tm = int_part1_tm/int_full_tm;
109     ratio2_tm = int_part2_tm/int_full_tm;
110     ratio3_tm = int_part3_tm/int_full_tm;
111 end
```

B

Membrane Laser Fabrication

1. Spin coating of a $\sim$ 50 nm thick sacrificial layer of PEDOT:PSS (Clevios P VP AI4083, Heraeus) on an oxygen plasma treated glass substrate at 4000 rpm for 60 s
2. Baking of PEDOT:PSS layer at 100 °C for 10 min
3. Spin coating of a thin ($<$ 10 nm) adhesion promoter (mr-APS1, Micro Resist Technology) at 4000 rpm for 60 s
4. Baking of mr-APS1 layer at 150 °C for 60 s
5. Spin coating of a photo-curable nanoimprint lithography resist (mr-UVCur21-200nm, Micro Resist Technology) at 3000 rpm for 60 s
6. Baking of mr-UVCur21-200nm layer at 100 °C for 20 s
7. Molding a transparent perfluoropolyether soft stamp (comprising a negative of the final grating structure) into the UV curable polymer layer using a UV nanoimprint alignment system (EVG620, EV Group)

8. UV exposure at $\lambda = 365\,\text{nm}$ for 220 s at a constant dose of $56\,\text{mW}\,\text{cm}^{-2}$ (process described in more detail in Section 3.1.3)

9. Removal of the soft stamp

10. Oxygen plasma treatment of the final grating structure to remove organic residues and reduce hydrophobicity

11. Dissolving of light emitting gain materials in Toluene at $25\,\text{mg}\,\text{L}^{-1}$ (for $F8_{0.9}BT_{0.1}$ and F8BT) and $10\,\text{mg}\,\text{L}^{-1}$ (Super Yellow)

12. Spin coating of the required gain materials at 2000 rpm for 60 s (layer thickness, $(180 \pm 10)\,\text{nm}$ for $F8_{0.9}BT_{0.1}$ and F8BT, $(250 \pm 10)\,\text{nm}$ for Super Yellow)

13. Membrane lift-off (dissolving of PEDOT:PSS film) by immersing the sample in deionized water heated to 55 °C for 1 h

14. Picking up membrane from water surface with an intermediate support substrate

C

Transfection Protocols

Lipofection

The lipofection protocol is based on the Lipofectamine 3000 reagent (Thermo Fisher Scientific) and all steps are performed in a safety cabinet with sterile plastics and solutions. The given quantities are optimized for HEK 293 cells in a 6 cm petri dish with a volume of 5 mL. The specifically required materials are Lipofectamine 3000, P3000 reagent and pEAK15 GFP plasmid DNA. The protocol has been optimized by Anja Steude (University of St Andrews).

1. Seed cells to be $70-80\,\%$ confluent at transfection.
2. Change cell medium to the full medium but without antibiotics with a total volume of 4.5 mL.
3. Prepare lipofectamine and DNA solution each in $5\,\%$ ($250\,\mu L$) of the total final volume.
4. Prepare lipofectamine solution with $2\,\mu L$ (per mL medium) of Lipofectamine 3000 to a final volume of $250\,\mu L$ in DMEM.

5. Prepare DNA solution with 1 μg (per mL medium) of DNA to a final volume of 250 μL in DMEM. Hence, 5 μg (22 μL) pEAK 15 GFP plasmid from a stock solution (0.228 $\mu g\,\mu L^{-1}$) were added to 218 μL of DMEM. Lastly, 10 μL of P3000 reagent were added. Pipetting of DNA solution must be done carefully since shear stress could damage DNA.

6. Mix DNA solution to lipofectamine solution.

7. Add transfection mix (500 μL) to cell culture (4.5 mL).

8. Put cell culture in incubator (37 °C, 5 % CO_2).

Nucleofection

The nucleofection protocol is based on the Amaxa Cell Line Nucleofector Kit V (Lonza) and all steps are performed in a safety cabinet with sterile plastics and solutions. The given quantities are optimized for 5×10^6 HEK 293 cells per nucleofection sample. The specifically required materials are a Nucleofector device, Nucleofector cuvettes, Nucleofector solution, Nucleofector supplement and pmaxGFP Vector. The protocol has been optimized by Anja Steude and Andrew Morton (University of St Andrews).

1. Prepare transfection solution (total volume 100 μL) containing 82 μL of Nucleofector solution, 18 μL of Nucleofector supplement and 2 μg (4 μL) pmaxGFP Vector DNA plasmid.

2. Seed cells to be $70-80$ % confluent at transfection.

3. Centrifuge 5×10^6 cells at 1150 rpm for 5 min and remove supernatant completely.

4. Resuspend cell pallet in 100 μL of transfection solution at room temperature.

5. Transfer cell/DNA solution into Nucleofector cuvettes

6. Transfer Nucleofector cuvettes into Nucleofector device

7. Select and execute program. E.g. program A-023 for high viability and G-004 for high expression level.

8. Immediately add 500 μL of cell culture medium and transfer cell solution into cell culture dish and incubator (37 °C, 5 % CO_2).

List of Abbreviations and Nomenclature

List of Abbreviations

AFM	Atomic Force Microscopy
ALD	Atomic Layer Deposition
CCD	Charge Coupled Device
CMFDA	5-chloromethyl-fluorescein diacetate
CW	Contentious Wave
DBR	Distributed Bragg Reflector
DFB	Distributed Feedback
DNA	Deoxyribonucleic Acid
eGFP	Enhanced Green Fluorescent Protein
F8BT	poly(9,9-dioctylfluorene-co-benzothiadiazole)
GFP	Green Fluorescent Protein
HOMO	Highest Occupied Molecular Orbital
LCW	Liquid Core Waveguide
LUMO	Lowest Unoccupied Molecular Orbital
NA	Numerical Aperture
OLED	Organic Light Emitting Diode
OSC	Organic Solar Cell
PDT	Photodynamic Therapy
PM556	Pyrromethene 556, Fluorescent Dye

PPV	Poly(p-phenylene vinylene)
ROI	Region Of Interest
SCW	Solid Core Waveguide
SY	Super Yellow
TE	Transverse Electric
TM	Transverse Magnetic
UV-NIL	Ultraviolet Nanoimprint Lithography
VASE	Variable Angular Spectroscopic Ellipsometry
WGM	Whispering Gallery Modes

Nomenclature

α	Propagation Loss Coefficient
β	Propagation Constant (Coupled Wave Theory)
δ	Detuning Parameter (Coupled Wave Theory)
ϵ, ϵ_0	Electric Permittivity
η	Viscosity Parameter
Γ	Overlap Factor
γ	Complex Propagation Constant (Coupled Wave Theory)
$\hbar$	Reduced Planck constant
κ_{DFB}	Coupling Coefficient (Coupled Wave Theory)
Λ	Grating Period
λ	Wavelength
μ, μ_0	Magnetic Permeability
ν	Vibronic Level Number
ω	Angular Frequency
ϕ	Goos Hänchen Phase Shift
σ	Emission Cross Section
τ	excited State or Photon Lifetime

θ	Angle with respect to Surface Normal
$\vec{B}$	Magnetic Flux Density
$\vec{D}$	Electric Flux Density
$\vec{E}$	Electric Field
$\vec{H}$	Magnetic Field
$\vec{k}$	Wave Vector
A_{21}, B_{21}, B_{12}	Einstein Coefficients
C	Concentration
c, c_0	Speed of Light
d	Waveguide and Layer Thickness
g	Gain Coefficient
G_m	Modal Gain
k_B	Boltzmann Constant
L	Device length
l	Spectral Linewidth
l_c	Planar Cavity Length
m, M	Scattering and Mode Order
N	Population Number
$n, (\kappa)$	Refractive Index; Real Part, (Imaginary Part)
p, q	Transverse Mode Numbers
r	Radius
R, S	Coupled Wave Amplitude
R_1, R_2	Mirror Reflectivity
S	Singlet State
T	Temperature
t	Time
u_ω	Photon Density

References

[1] Einstein, A. Strahlungs-Emission und Absorption nach der Quantentheorie. *Verhandlungen der Deutschen Physikalischen Gesellschaft* **18**, 318–323 (1916).

[2] Einstein, A. Zur Quantentheorie der Strahlung. *Physikalische Zeitschrift* **18**, 121–128 (1917).

[3] Gordon, J. P., Zeiger, H. J. & Townes, C. H. The maser-new type of microwave amplifier, frequency standard, and spectrometer. *Physical Review* **99**, 1264–1274 (1955).

[4] Schawlow, A. L. & Townes, C. H. Infrared and optical masers. *Physical Review* **112**, 1940–1949 (1958).

[5] Maiman, T. H. Stimulated optical radiation in ruby. *Nature* **187**, 493–494 (1960).

[6] Jones, W. D. Keeping cars from crashing. *IEEE Spectrum* **38**, 40–45 (2001).

[7] Sorokin, P. P. & Lankard, J. R. Stimulated Emission Observed from an Organic Dye, Chloro-aluminum Phthalocyanine. *IBM Journal of Research and Development* **10**, 162–163 (1966).

[8] Schäfer, F. P., Schmidt, W. & Volze, J. Organic dye solution laser. *Applied Physics Letters* **9**, 306–309 (1966).

[9] Schäfer, F. P. *Dye Lasers* (Springer-Verlag Berlin Heidelberg, 1990), 3 edn.

[10] Heeger, A. J. Semiconducting and Metallic Polymers: The Fourth Generation of Polymeric Materials (Nobel Lecture). *Angewandte Chemie (International ed.)* **40**, 2591–2611 (2001).

[11] Tang, C. W. & Vanslyke, S. A. Organic electroluminescent diodes. *Applied Physics Letters* **51**, 913–915 (1987).

[12] Geffroy, B., le Roy, P. & Prat, C. Organic light-emitting diode (OLED) technology: Materials, devices and display technologies. *Polymer International* **55**, 572–582 (2006).

[13] Gather, M. C., Köhnen, A. & Meerholz, K. White organic light-emitting diodes. *Advanced Materials* **23**, 233–248 (2011).

[14] Tang, C. W. Two-layer organic photovoltaic cell. *Applied Physics Letters* **48**, 183–185 (1986).

[15] Koezuka, H., Tsumura, A. & Ando, T. Field-effect transistor with polythiophene thin film. *Synthetic Metals* **18**, 699–704 (1987).

[16] Hide, F. *et al.* Semiconducting polymers as a new class of solid-state laser materials. *Science* **273**, 1833–1836 (1996).

[17] Tessler, N., Denton, G. J. & Friend, R. H. Lasing from conjugated-polymer microcavities. *Nature* **382**, 695–697 (1996).

[18] Kozlov, V. G., Bulović, V., Burrows, P. E. & Forrest, S. R. Laser action in organic semiconductor waveguide and double-heterostructure devices. *Nature* **389**, 362–364 (1997).

[19] Samuel, I. D. W. & Turnbull, G. A. Organic semiconductor lasers. *Chemical Reviews* **107**, 1272–1295 (2007).

[20] Kuehne, A. J. C. & Gather, M. C. Organic Lasers: Recent Developments on Materials, Device Geometries, and Fabrication Techniques. *Chemical Reviews* **116**, 12823–12864 (2016).

[21] Chénais, S. & Forget, S. Recent advances in solid-state organic lasers. *Polymer International* **61**, 390–406 (2012).

[22] Dougherty, T. J., Gomer, C. J., Henderson, B. W. & Peng, Q. Photodynamic therapy. *Journal of the National Caner Institute* **90**, 889–905 (1998).

[23] Tanzi, E. L., Lupton, J. R. & Alster, T. S. Lasers in dermatology: Four decades of progress. *Journal of the American Academy of Dermatology* **49**, 1–31 (2003).

[24] Rajadhyaksha, M., Grossman, M., Esterowitz, D., Webb, R. H. & Anderson, R. R. In vivo confocal scanning laser microscopy of human skin: Melanin provides strong contrast. *Journal of Investigative Dermatology* **104**, 946–952 (1995).

[25] Roorda, A. *et al.* Adaptive optics scanning laser ophthalmoscopy. *Optics Express* **10**, 405–412 (2002).

[26] Guck, J. *et al.* Optical deformability as an inherent cell marker for testing malignant transformation and metastatic competence. *Biophysical Journal* **88**, 3689–3698 (2005).

[27] Vannahme, C., Maier-Flaig, F., Lemmer, U. & Kristensen, A. Single-mode biological distributed feedback laser. *Lab on a Chip* **13**, 2675–2678 (2013).

[28] Nizamoglu, S., Gather, M. C. & Yun, S. H. All-biomaterial laser using vitamin and biopolymers. *Advanced Materials* **25**, 5943–5947 (2013).

[29] Gather, M. C. & Yun, S.-H. Bio-optimized energy transfer in densely packed fluorescent protein enables near-maximal luminescence and solid-state lasers. *Nature Communications* **5**, 5722 (2014).

[30] Chen, Q. *et al.* Highly sensitive fluorescent protein FRET detection using optofluidic lasers. *Lab on a Chip* **13**, 2679 (2013).

[31] Jonáš, A. *et al.* In vitro and in vivo biolasing of fluorescent proteins suspended in liquid microdroplet cavities. *Lab on a Chip* **14**, 3093–3100 (2014).

[32] Camposeo, A. *et al.* Physically transient photonics: Random versus distributed feedback lasing based on nanoimprinted DNA. *ACS Nano* **8**, 10893–10898 (2014).

[33] Gather, M. C. & Yun, S.-H. Single-cell biological lasers. *Nature Photonics* **5**, 406–410 (2011).

[34] Gather, M. C. & Yun, S. H. Lasing from Escherichia coli bacteria genetically programmed to express green fluorescent protein. *Optics Letters* **36**, 3299–3301 (2011).

[35] Chen, Y.-C., Chen, Q., Zhang, T., Wang, W. & Fan, X. Versatile tissue lasers based on high-Q Fabry-Pérot microcavities. *Lab on a Chip* **17**, 538–548 (2017).

[36] Fan, X. & Yun, S.-H. The potential of optofluidic biolasers. *Nature Methods* **11**, 141–147 (2014).

[37] Psaltis, D., Quake, S. R. & Yang, C. Developing optofluidic technology through the fusion of microfluidics and optics. *Nature* **442**, 381–386 (2006).

[38] Humar, M., Gather, M. C. & Yun, S.-H. Cellular dye lasers: lasing thresholds and sensing in a planar resonator. *Optics Express* **23**, 27865–27879 (2015).

[39] Chen, Y.-C. *et al.* Laser-emission imaging of nuclear biomarkers for high-contrast cancer screening and immunodiagnosis. *Nature Biomedical Engineering* **1**, 724–735 (2017).

[40] Schubert, M. *et al.* Lasing within Live Cells Containing Intracellular Optical Microresonators for Barcode-Type Cell Tagging and Tracking. *Nano Letters* **15**, 5647–5652 (2015).

[41] Humar, M. & Yun, S.-H. Intracellular microlasers. *Nature Photonics* **9**, 572–576 (2015).

[42] Schubert, M. *et al.* Lasing in Live Mitotic and Non-Phagocytic Cells by Efficient Delivery of Microresonators. *Scientific Reports* **7**, 40877 (2017).

[43] Dietrich, C. P. *et al.* An exciton-polariton laser based on biologically produced fluorescent protein. *Science Advances* **2**, e160666 (2016).

[44] Dietrich, C. P. *et al.* Molding Photonic Boxes into Fluorescent Emitters by Direct Laser Writing. *Advanced Materials* **29**, 1–6 (2017).

[45] Pope, M. & Swenberg, C. E. *Electronic processes in organic crystals and polymers* (Oxford University Press, 1999), 2 edn.

[46] Knupfer, M. Exciton binding energies in organic semiconductors. *Applied Physics A: Materials Science and Processing* **77**, 623–626 (2003).

[47] Müller, J. G. *et al.* Linewidth-limited energy transfer in single conjugated polymer molecules. *Physical Review Letters* **91**, 1–4 (2003).

[48] Liu, X., Klinkhammer, S. & Sudau, K. Ink-jet-printed organic semiconductor distributed feedback laser. *Applied Physics Express* **5**, 3–5 (2012).

[49] Tedde, S. F. *et al.* Fully Spray Coated Organic Photodiodes. *Nano Letters* **9**, 980–983 (2009).

[50] Sirringhaus, H. 25th anniversary article: Organic field-effect transistors: The path beyond amorphous silicon. *Advanced Materials* **26**, 1319–1335 (2014).

[51] Burroughes, J. H. *et al.* Light-emitting diodes based on conjugated polymers. *Nature* **347**, 539–541 (1990).

[52] Halls, J. J. *et al.* Efficient photodiodes from interpenetrating polymer networks. *Nature* **376**, 498–500 (1995).

[53] Feng, G. *et al.* Imaging neuronal sets in transgenic mice expressing multiple spectral variants of GFP. *Neuron* **28**, 41–51 (2000).

[54] Cabantous, S., Terwilliger, T. C. & Waldo, G. S. Protein tagging and detection with engineered self-assembling fragments of green fluorescent protein. *Nature Biotechnology* **23**, 102–107 (2005).

[55] Patterson, G. H. & Lippincott-Schwartz, J. A Photoactivatable GFP for Selective Photolabeling of Proteins and Cells. *Science* **297**, 1873–1877 (2002).

[56] Chalfie, M. & Steven, K. R. *Green fluorescent protein: properties, applications and protocols* (John Wiley & Sons, 2005), 2 edn.

[57] Shimomura, O., Johnson, F. H. & Saiga, Y. Extraction, Purification and Properties of Aequorin, a Bioluminescent Protein from the Luminous Hydromedusan, Aequorea. *Journal of Cellular and Comparative Physiology* **59**, 223–239 (1962).

[58] Phillips, G. N. Structure and dynamics of green fluorescent protein. *Current Opinion in Structural Biology* **7**, 821–827 (1997).

[59] Royant, A. & Noirclerc-Savoye, M. Stabilizing role of glutamic acid 222 in the structure of Enhanced Green Fluorescent Protein. *Journal of Structural Biology* **174**, 385–390 (2011).

[60] Prasher, D. C., Eckenrode, V. K., Ward, W. W., Prendergast, F. G. & Cormier, M. J. Primary structure of the Aequorea victoria green-fluorescent protein. *Gene* **111**, 229–233 (1992).

[61] Chalfie, M., Tu, Y., Euskirchen, G., Ward, W. W. & Prasherf, D. C. Green Fluorescent Protein as a Marker for Gene Expression. *Science* **263**, 802–805 (1992).

[62] Tsien, R. Y. The Green Fluorescent Protein. *Annual Review of Biochemistry* **67**, 509–544 (1998).

[63] Ormö, M. *et al.* Crystal Structure of the Aequorea victoria Green Fluorescent Protein. *Science* **273**, 1392–1395 (1996).

[64] Cormack, B. P., Valdivia, R. H. & Falkow, S. FACS-optimized mutants of the green fluorescent protein (GFP). *Gene* **173**, 33–38 (1996).

[65] Yang, F., Moss, L. G., Phillips, G. N., Phillips Jr., G. N. & Phillips, G. N. The molecular structure of green fluorescent protein. *Nature Biotechnology* **14**, 1246–1251 (1996).

[66] Haldar, S. & Chattopadhyay, A. The green journey. *Journal of Fluorescence* **19**, 1–2 (2009).

[67] Cubitt, A. B. *et al.* Understanding, improving and using green fluorescent proteins. *Trends in Biochemical Sciences* **20**, 448–455 (1995).

[68] Yokoyama, S., Otomo, A. & Mashiko, S. Laser emission from high-gain media of dye-doped dendrimer. *Applied Physics Letters* **80**, 7–9 (2002).

[69] Coolidge, A. S., James, H. M. & Present, R. D. A study of the franck-condon principle. *The Journal of Chemical Physics* **4**, 193–211 (1936).

[70] Born, M. & Oppenheimer, R. Zur Quantentheorie der Molekeln. *Annalen der Physik* **389**, 457–484 (1927).

[71] Planck, M. *The Theory of Heat Radiation (transl.)* (P. Blakiston's Son & Co., 1914), 2 edn.

[72] Xia, R., Heliotis, G., Hou, Y. & Bradley, D. D. Fluorene-based conjugated polymer optical gain media. *Organic Electronics* **4**, 165–177 (2003).

[73] Birnbaum, M., Tucker, A. W. & Fincher, C. L. Laser emission cross section of Nd:YAG at 1064 nm. *Journal of Applied Physics* **52**, 1212–1215 (1980).

[74] Patel, C. K. N. High-Power Carbon Dioxide Lasers. *Scientific American* **219**, 23–28 (1968).

[75] Buckman, A. B. *Guided-wave Photonics* (Saunders College Pub., 1992), 1 edn.

[76] Vahala, K. J. Optical microcavities. *Nature* **424**, 839–846 (2003).

[77] Hill, M. T. & Gather, M. C. Advances in small lasers. *Nature Photonics* **8**, 908–918 (2014).

[78] Foreman, M. R., Swaim, J. D. & Vollmer, F. Whispering gallery mode sensors. *Advances in Optics and Photonics* **7**, 168–240 (2015).

[79] Chiasera, A. *et al.* Spherical whispering-gallery-mode microresonators. *Laser & Photonics Reviews* **4**, 457–482 (2010).

[80] Righini, G. C. *et al.* Whispering Gallery Mode microresonators: Fundamentals and applications. *Rivista del Nuovo Cimento* **34**, 435–488 (2011).

[81] He, L., Özdemir, Å. K. & Yang, L. Whispering gallery microcavity lasers. *Laser & Photonics Reviews* **7**, 60–82 (2013).

[82] Punke, M. *et al.* Organic semiconductor lasers as integrated light sources for optical sensor systems. *Organic-based Chemical and Biological Sensors* **6659**, 665909 (2007).

[83] Vannahme, C. *et al.* Integration of organic semiconductor lasers and single-mode passive waveguides into a PMMA substrate. *Microelectronic Engineering* **87**, 693–695 (2010).

[84] Vannahme, C., Klinkhammer, S., Lemmer, U. & Mappes, T. Plastic lab-on-a-chip for fluorescence excitation with integrated organic semiconductor lasers. *Optics Express* **19**, 8179–8186 (2011).

[85] Baumann, K. *et al.* Organic mixed-order photonic crystal lasers with ultrasmall footprint. *Applied Physics Letters* **91**, 89–92 (2007).

[86] Karnutsch, C. *et al.* Improved organic semiconductor lasers based on a mixed-order distributed feedback resonator design. *Applied Physics Letters* **90**, 131104 (2007).

[87] Kogelnik, H. & Shank, C. V. Coupled-Wave Theory of Distributed Feedback Lasers. *Journal of Applied Physics* **43**, 2327–2335 (1972).

[88] Yariv, A. & Nakamura, M. Periodic structures for integrated optics. *IEEE Journal of Quantum Electronics* **13**, 233–253 (1977).

[89] Kazarinov, R. F. & Henry, C. H. Second-Order Distributed Feedback Lasers with Mode Selection Provided by First-Order Radiation Losses. *IEEE Journal of Quantum Electronics* **21**, 144–150 (1985).

[90] Barnes, W. & Kitson, S. Physical origin of photonic energy gaps in the propagation of surface plasmas on gratings. *Physical Review B* **54**, 6227–6244 (1996).

[91] Turnbull, G. A., Andrew, P., Barnes, W. L. & Samuel, I. D. Photonic mode dispersion of a two-dimensional distributed feedback polymer laser. *Physical Review B* **67**, 165107 (2003).

[92] Peterson, O. G., Tuccio, S. A. & Snavely, B. B. Cw operation of an organic dye solution laser. *Applied Physics Letters* **17**, 245–247 (1970).

[93] Strickland, D. & Mourou, G. Compression of amplified chirped optical pulses. *Optics Communications* **55**, 447–449 (1985).

[94] Xia, Y. & Whitesides, G. M. Soft Lithography. *Annual Review of Materials Science* **28**, 153–184 (1998).

[95] Unger, M. A., Chou, H., Thorsen, T., Scherer, A. & Quake, S. R. Monolithic Microfabricated Valves and Pumps by Multilayer Soft Lithography. *Science* **288**, 113–116 (2000).

[96] Fainman, Y., Lee, L., Psaltis, D. & Yang, C. *Optofluidics: Fundamentals, Devices, and Applications* (McGraw-Hill, Inc., New York, NY, USA, 2010), 1 edn.

[97] Li, Z. & Psaltis, D. Optofluidic dye lasers. *Microfluidics and Nanofluidics* **4**, 145–158 (2008).

[98] Coles, D. M. *et al.* Diffusion-driven continuous-wave-pumped organic dye lasers. *Laser & Photonics Reviews* **9**, 538–544 (2015).

[99] Schauer, S., Liu, X., Worgull, M., Lemmer, U. & Hölscher, H. Shape-memory polymers as flexible resonator substrates for continuously tunable organic DFB lasers. *Optical Materials Express* **5**, 576–584 (2015).

[100] Grossmann, T. *et al.* Strongly confined, low-threshold laser modes in organic semiconductor microgoblets. *Optics Express* **19**, 10009–10016 (2011).

[101] Strangi, G. *et al.* Color-Tunable Organic Microcavity Laser Array Using Distributed Feedback. *Physical Review Letters* **94**, 063903 (2005).

[102] Karnutsch, C. *et al.* Low threshold blue conjugated polymer lasers with first- and second-order distributed feedback. *Applied Physics Letters* **89**, 2004–2007 (2006).

[103] Namdas, E. B. *et al.* Low thresholds in polymer lasers on conductive substrates by distributed feedback nanoimprinting: Progress toward electrically pumped plastic lasers. *Advanced Materials* **21**, 799–802 (2009).

[104] Mischok, A. *et al.* Photonic confinement in laterally structured metal-organic microcavities. *Applied Physics Letters* **105**, 051108 (2014).

[105] Yang, Y., Turnbull, G. A. & Samuel, I. D. W. Hybrid optoelectronics: A polymer laser pumped by a nitride light-emitting diode. *Applied Physics Letters* **92**, 163306 (2008).

[106] Gather, M. C. Continuous lasing for perovskites. *Nature Photonics* **11**, 745–747 (2017).

[107] Sandanayaka, A. S. D. *et al.* Towards continuous-wave operation of organic semiconductor lasers. *Science Advances* **3**, e1602570 (2017).

[108] Jia, Y., Kerner, R. A., Grede, A. J., Rand, B. P. & Giebink, N. C. Continuous-wave lasing in an organic-inorganic lead halide perovskite semiconductor. *Nature Photonics* **11**, 784–788 (2017).

[109] Liu, X. *et al.* Organic semiconductor distributed feedback (DFB) laser as excitation source in Raman spectroscopy. *Optics Express* **21**, 28941–28947 (2013).

[110] Yang, Y., Turnbull, G. A. & Samuel, D. W. Sensitive explosive vapor detection with polyfluorene lasers. *Advanced Functional Materials* **20**, 2093–2097 (2010).

[111] Thomas, S. W., Joly, G. D. & Swager, T. M. Chemical sensors based on amplifying fluorescent conjugated polymers. *Chemical Reviews* **107**, 1339–1386 (2007).

[112] Liao, Q. *et al.* An organic nanowire waveguide exciton-polariton sub-microlaser and its photonic application. *Journal of Materials Chemistry C* **2**, 2773–2778 (2014).

[113] Clark, J. & Lanzani, G. Organic photonics for communications. *Nature Photonics* **4**, 438–446 (2010).

[114] Ahn, S. H. & Guo, L. J. High-speed roll-to-roll nanoimprint lithography on flexible plastic substrates. *Advanced Materials* **20**, 2044–2049 (2008).

[115] Wang, W. *et al.* Optofluidic laser array based on stable high-Q Fabry-Pérot microcavities. *Lab on a Chip* **15**, 3862–3869 (2015).

[116] Wu, X. *et al.* Optofluidic laser for dual-mode sensitive biomolecular detection with a large dynamic range. *Nature Communications* **5**, 3779 (2014).

[117] Chen, Y.-C., Chen, Q. & Fan, X. Optofluidic chlorophyll lasers. *Lab on a Chip* **16**, 2228–2235 (2016).

[118] Heydari, E. *et al.* Label-free biosensor based on an all-polymer DFB laser. *Advanced Optical Materials* **2**, 137–141 (2014).

[119] Mozaffari, M. H., Ebnali-Heidari, M., Abaeiani, G. & Moravvej-Farshi, M. K. Photonic crystal optofluidic biolaser. *Photonics and Nanostructures - Fundamentals and Applications* **26**, 56–61 (2017).

[120] Polson, R. C. & Vardeny, Z. V. Random lasing in human tissues. *Applied Physics Letters* **85**, 1289–1291 (2004).

[121] Song, Q. *et al.* Random lasing in bone tissue. *Optics Letters* **35**, 1425–1427 (2010).

[122] Leupold, D., Mory, S., Konig, R., Hoffmann, P. & Hieke, B. Laser action and excited state absorption of chlorophyll a. *Chemical Physics Letters* **45**, 567–571 (1977).

[123] Wu, X., Chen, Q., Sun, Y. & Fan, X. Bio-inspired optofluidic lasers with luciferin. *Applied Physics Letters* **102**, 2011–2014 (2013).

[124] Shopova, S. I., Farca, G., Rosenberger, A. T., Wickramanayake, W. M. S. & Kotov, N. A. Microsphere whispering-gallery-mode laser using HgTe quantum dots. *Applied Physics Letters* **85**, 6101–6103 (2004).

[125] Chen, Q., Kiraz, A. & Fan, X. Optofluidic FRET lasers using aqueous quantum dots as donors. *Lab on a Chip* **16**, 353–359 (2016).

[126] Choi, Y., Jeon, H. & Kim, S. A fully biocompatible single-mode distributed feedback laser. *Lab Chip* **15**, 642–645 (2015).

[127] Ta, V. D., Caixeiro, S., Fernandes, F. M. & Sapienza, R. Microsphere Solid-State Biolasers. *Advanced Optical Materials* **5**, 1–6 (2017).

[128] Humar, M., Seok, & Yun, H. Whispering-gallery-mode emission from biological luminescent protein microcavity assemblies. *Optica* **4**, 222–228 (2017).

[129] Shopova, S. I. *et al.* Opto-Fluidic Ring Resonator Lasers Based on Highly Efficient Resonant Energy Transfer. *Optics Express* **15**, 12735–12742 (2007).

[130] Zhang, X., Lee, W. & Fan, X. Bio-switchable optofluidic lasers based on DNA Holliday junctions. *Lab on a Chip* **12**, 3673 (2012).

[131] Hänsch, T. W. Edible lasers and other delights of the 1970s. *Optics & Photonics News* **16**, 14–16 (2005).

[132] Chen, Y.-C., Chen, Q. & Fan, X. Lasing in blood. *Optica* **3**, 809–815 (2016).

[133] Siddique, M., Yang, L., Wang, Q. Z. & Alfano, R. R. Mirrorless laser action from optically pumped dye-treated animal tissues. *Optics Communications* **117**, 475–479 (1995).

[134] Nizamoglu, S. *et al.* A Simple Approach to Biological Single-Cell Lasers Via Intracellular Dyes. *Advanced Optical Materials* **3**, 1197–1200 (2015).

[135] Chen, Q. *et al.* An integrated microwell array platform for cell lasing analysis. *Lab on a Chip* **17**, 2814–2820 (2017).

[136] Deegan, R. D. *et al.* Capillary flow as the cause of ring strins from dried liquid drops. *Nature* **389**, 827–829 (1997).

[137] Dietrich, C. P., Höfling, S. & Gather, M. C. Multi-state lasing in self-assembled ring-shaped green fluorescent protein microcavities. *Applied Physics Letters* **105**, 233702 (2014).

[138] Dietrich, C. P. *et al.* Strong Coupling in Fully Tunable Microcavities Filled with Biologically Produced Fluorescent Proteins. *Advanced Optical Materials* **5**, 1–5 (2017).

[139] Oh, H. J., Gather, M. C., Song, J.-J. & Yun, S. H. Lasing from fluorescent protein crystals. *Optics Express* **22**, 31411–31416 (2014).

[140] Baldo, M. *et al.* Organic Vapor Phase Deposition. *Advanced Materials* **10**, 1505–1514 (1998).

[141] Lim, J. A. *et al.* Self-organization of ink-jet-printed triisopropylsilylethynyl pentacene via evaporation-induced flows in a drying droplet. *Advanced Functional Materials* **18**, 229–234 (2008).

[142] Becerril, H. A., Roberts, M. E., Liu, Z., Locklin, J. & Bao, Z. High-performance organic thin-film transistors through solution-sheared deposition of small-molecule organic semiconductors. *Advanced Materials* **20**, 2588–2594 (2008).

[143] Uddin, M. A., Chan, H. P., Chow, C. K. & Chan, Y. C. Effect of Spin Coating on the Curing Rate of Epoxy Adhesive for the Fabrication of a Polymer Optical Waveguide. *Journal of Electronic Materials* **33**, 224–228 (2004).

[144] Meyerhofer, D. Characteristics of resist films produced by spinning. *Journal of Applied Physics* **49**, 3993–3997 (1978).

[145] Meuse, C. W. Infrared spectroscopic ellipsometry of self-assembled monolayers. *Langmuir* **16**, 9483–9487 (2000).

[146] Tompkins, H. & Irene, E. A. *Handbook of ellipsometry* (Springer Berlin Heidelberg, 2005), 1 edn.

[147] Maiti, P., Nam, P. H., Okamoto, M., Hasegawa, N. & Usuki, A. Influence of crystallization on intercalation, morphology, and mechanical properties of polypropylene/clay nanocomposites. *Macromolecules* **35**, 2042–2049 (2002).

[148] Tsiminis, G. *et al.* Nanoimprinted organic semiconductor laser pumped by a light-emitting diode. *Advanced Materials* **25**, 2826–2830 (2013).

[149] Wang, Y. *et al.* Nanoimprinted polymer lasers with threshold below 100 W / cm 2 using mixed-order distributed feedback resonators. *Optics Express* **21**, 14362–14367 (2013).

[150] Graf, A., Tropf, L., Zakharko, Y., Zaumseil, J. & Gather, M. C. Near-infrared exciton-polaritons in strongly coupled single-walled carbon nanotube microcavities. *Nature Communications* **7**, 13078 (2016).

[151] Lai, C. W. *et al.* Coherent zero-state and π-state in an exciton-polariton condensate array. *Nature* **450**, 529–532 (2007).

[152] Savvidis, P. G. *et al.* Asymmetric angular emission in semiconductor microcavities. *Physical Review B* **62**, 278–281 (2000).

[153] Amarasinghe, D., Ruseckas, A., Vasdekis, A. E., Turnbull, G. A. & Samuel, I. D. W. Amplification of optical pulse sequences at a high repetition rate in a polymer slab waveguide. *Applied Physics Letters* **91**, 011105 (2007).

[154] Amarasinghe, D., Ruseckas, A., Vasdekis, A. E., Turnbull, G. A. & Samuel, I. D. W. High-gain broadband solid-state optical amplifier using a semiconducting copolymer. *Advanced Materials* **21**, 107–110 (2009).

[155] Burns, S., Macleod, J., Trang Do, T., Sonar, P. & Yambem, S. D. Effect of thermal annealing Super Yellow emissive layer on efficiency of OLEDs. *Scientific Reports* **7**, 40805 (2017).

[156] Snedden, E. W., Cury, L. A., Bourdakos, K. N. & Monkman, A. P. High photoluminescence quantum yield due to intramolecular energy transfer in the Super Yellow conjugated copolymer. *Chemical Physics Letters* **490**, 76–79 (2010).

[157] López Arbeloa, T., López Arbeloa, F. & López Arbeloa, I. Environmental effects on the photophysics of pyrromethene 556. *Physical Chemistry Chemical Physics* **1**, 791–795 (1999).

[158] Rahn, M. D., King, T. A., Gorman, A. A. & Hamblett, I. Photostability enhancement of Pyrromethene 567 and Perylene Orange in oxygen-free liquid and solid dye lasers. *Applied Optics* **36**, 5862–5871 (1997).

[159] Arbeloa, F. L., Ojeda, P. R. & Arbeloa, I. L. Flourescence self-quenching of the molecular forms of Rhodamine B in aqueous and ethanolic solutions. *Journal of Luminescence* **44**, 105–112 (1989).

[160] Mayr, T. 5-Chloromethylfluorescein (last accessed 2018-03-05). URL `http://www.fluorophores.tugraz.at`.

[161] Sjöback, R., Nygren, J. & Kubista, M. Absorption and fluorescence properties of fluorescein. *Spectrochimica Acta Part A* **51**, 7–21 (1995).

[162] Johnson, I. D. & Spence, M. T. Z. *The Molecular Probes Handbook: A Guide to Fluorescent Probes and Labeling Technologies* (Life Technologies Corporation, 2010), 11 edn.

[163] Christian, W., Johnson, T. J. & Gill, T. J. In vitro and in vivo cell tracking of chondrocytes of different origin by fluorescent PKH 26 and CMFDA. *Journal of Biomedical Science and Engineering* **1**, 163–169 (2008).

[164] Luo, D. & Saltzman, W. M. Synthetic DNA delivery systems. *Nature Biotechnology* **18**, 33–37 (2000).

[165] Pfeifer, A. & Verma, I. M. Gene Therapy : Promises and Problems. *Annual Review of Genomics and Human Genetics* **2**, 177–211 (2001).

[166] Felgner, P. L. *et al.* Lipofection: a highly efficient, lipid-mediated DNA-transfection procedure. *Proceedings of the National Academy of Sciences* **84**, 7413–7417 (1987).

[167] Aluigi, M. *et al.* Nucleofection Is an Efficient Nonviral Transfection Technique for Human Bone Marrow-Derived Mesenchymal Stem Cells. *Stem Cells* **24**, 454–461 (2006).

[168] Alberts, B. *et al. Molecular biology of the cell* (Garland Science, New York, NY, USA, 2002), 5 edn.

[169] Mayr, T. EGFP (Campbell Tsien 2003, last accessed 2018-03-05). URL `http://www.fluorophores.tugraz.at`.

[170] Zajac, J. M. *et al.* Time-Resolved Studies of Energy Transfer in Thin Films of Green and Red Fluorescent Proteins. *Advanced Functional Materials* **1706300**, 1–8 (2018).

[171] Karl, M. *et al.* Single cell induced optical confinement in biological lasers. *Journal of Physics D: Applied Physics* **50**, 084005 (2017).

[172] Reinhardt, C. *et al.* Mode discretization in an organic microcavity including a perforated silver layer. *Applied Physics Letters* **100**, 103306 (2012).

[173] Brückner, R. *et al.* Phase-locked coherent modes in a patterned metal-organic microcavity. *Nature Photonics* **6**, 322–326 (2012).

[174] Thomas, P. & Smart, T. G. HEK293 cell line: A vehicle for the expression of recombinant proteins. *Journal of Pharmacological and Toxicological Methods* **51**, 187–200 (2005).

[175] Siegman, A. E. *Lasers* (Mill Valley, Calif. : University Science Books, 1986).

[176] Shapiro, H. M. *Practical Flow Cytometry* (John Wiley & Sons, Inc., Hoboken, NJ, USA, 2003).

[177] Bonner, W. A., Hulett, H. R., Sweet, R. G. & Herzenberg, L. A. Fluorescence activated cell sorting. *Review of Scientific Instruments* **234**, 108–117 (1976).

[178] Marks, K. M. & Nolan, G. P. Chemical labeling strategies for cell biology. *Nature Methods* **3**, 591–596 (2006).

[179] Kar, A. K., Mackenzie, M. D., Cialowicz, K. I., Saleeb, R. S. & Duncan, R. R. Vitamin C for stabilising biological lasers (Conference Presentation). In *Proc. SPIE, 9711*, 1 (2016).

[180] Beuthan, J., Minet, O., Helfmann, J., Herrig, M. & Müller, G. The spatial variation of the refractive index in biological cells. *Physics in Medicine & Biology* **41**, 369–382 (1996).

[181] Chong, C. & Sarma, J. Lasing mode selection in vertical-cavity surface emitting-laser diodes. *IEEE Photonics Technology Letters* **5**, 761–764 (1993).

[182] Karl, M. *et al.* Optofluidic distributed feedback lasers with evanescent pumping : Reduced threshold and angular dispersion analysis. *Applied Physics Letters* **108**, 261101 (2016).

[183] Hänsch, T. W. Repetitively Pulsed Tunable Dye Laser for High Resolution Spectroscopy. *Applied Optics* **11**, 895–898 (1972).

[184] Li, Z., Zhang, Z., Emery, T., Scherer, A. & Psaltis, D. Single mode optofluidic distributed feedback dye laser. *Optics Express* **14**, 696–701 (2006).

[185] Li, Z., Zhang, Z., Scherer, A. & Psaltis, D. Mechanically tunable optofluidic distributed feedback dye laser. *LEOS Summer Topical Meeting* **14**, 58–59 (2006).

[186] Pang, L., Chen, H. M., Freeman, L. M. & Fainman, Y. Optofluidic devices and applications in photonics, sensing and imaging. *Lab on a Chip* **12**, 3543–3551 (2012).

[187] Wienhold, T. *et al.* Diffusion driven optofluidic dye lasers encapsulated into polymer chips. *Lab on a Chip* **12**, 3734–3739 (2012).

[188] Gersborg-Hansen, M. & Kristensen, A. Tunability of optofluidic distributed feedback dye lasers. *Optics Express* **15**, 137–142 (2007).

[189] Bakal, A., Vannahme, C., Kristensen, A. & Levy, U. Tunable on chip optofluidic laser. *Applied Physics Letters* **107**, 211105 (2015).

[190] Song, W., Vasdekis, A. E., Li, Z. & Psaltis, D. Optofluidic evanescent dye laser based on a distributed feedback circular grating. *Applied Physics Letters* **94**, 161110 (2009).

[191] Galvao, J. *et al.* Unexpected low-dose toxicity of the universal solvent DMSO. *FASEB Journal* **28**, 1317–1330 (2014).

[192] Ippen, E. & Shank, C. Evanescent-field-pumped dye laser. *Applied Physics Letters* **21**, 301 (1972).

[193] Song, W., Vasdekis, A. E., Li, Z. & Psaltis, D. Low-order distributed feedback optofluidic dye laser with reduced threshold. *Applied Physics Letters* **94**, 051117 (2009).

[194] Wang, J. *et al.* A continuously tunable organic DFB laser. *Microelectronic Engineering* **78-79**, 364–368 (2005).

[195] Betzig, E. *et al.* Imaging Intracellular Fluorescent Proteins at Nanometer Resolution. *Science* **313**, 1642–1645 (2006).

[196] Shaner, N. C., Steinbach, P. A. & Tsien, R. Y. A guide to choosing fluorescent proteins. *Nature Methods* **2**, 905–909 (2005).

[197] Shaner, N. C. *et al.* Improved monomeric red, orange and yellow fluorescent proteins derived from Discosoma sp. red fluorescent protein. *Nature Biotechnology* **22**, 1567–1572 (2004).

[198] Xia, R., Heliotis, G. & Bradley, D. D. C. Fluorene-based polymer gain media for solid-state laser emission across the full visible spectrum. *Applied Physics Letters* **82**, 3599–3601 (2003).

[199] Polyanskiy, M. N. Refractive index database (last accessed 2018-02-26). URL `https://refractiveindex.info`.

[200] George, S. M. Atomic Layer Deposition: An Overview. *Chemical Reviews* **110**, 111–131 (2010).

[201] Li, J., Huang, C.-X. & Zhang, J.-H. Tuning the electrical performance and bias stability of a semiconducting SWCNT thin film transistor with an atomic layer deposited AlZrOx composite. *RSC Advances* **7**, 52517–52523 (2017).

[202] Lachut, B. L. *et al.* Large spectral birefringence in photoaddressable polymer films. *Advanced Materials* **16**, 1746–1750 (2004).

[203] Liang, Y., Peng, C., Sakai, K., Iwahashi, S. & Noda, S. Three-dimensional coupled-wave analysis for square-lattice photonic crystal surface emitting lasers with transverse-electric polarization: finite-size effects. *Optics Express* **20**, 15945–15961 (2012).

[204] Harwell, J. R., Whitworth, G. L., Turnbull, G. A. & Samuel, I. D. Green Perovskite Distributed Feedback Lasers. *Scientific Reports* **7**, 11727 (2017).

[205] Miyai, E. & Noda, S. Phase-shift effect on a two-dimensional surface-emitting photonic-crystal laser. *Applied Physics Letters* **86**, 111113 (2005).

[206] Liang, Y., Peng, C., Sakai, K., Iwahashi, S. & Noda, S. Three-dimensional coupled-wave model for square-lattice photonic crystal lasers with transverse electric polarization: A general approach. *Physical Review B* **84**, 195119 (2011).

[207] Ryu, H. Y., Notomi, M. & Lee, Y. H. Finite-difference time-domain investigation of band-edge resonant modes in finite-size two-dimensional photonic crystal slab. *Physical Review B* **68**, 045209 (2003).

[208] Yokoyama, M. & Noda, S. Finite-difference time-domain simulation of two- dimensional photonic crystal surface-emitting laser. *Optics Express* **13**, 2869–2880 (2005).

[209] Dogru, I. B. *et al.* Single transverse mode protein laser. *Applied Physics Letters* **111**, 231103 (2017).

[210] Karl, M. *et al.* Flexible and ultra-lightweight polymer membrane lasers. *Nature Communications* **9**, 1525 (2018).

[211] Yokota, T. *et al.* Ultra-flexible Organic Photonic Skin. *Science Advances* **2**, e1501856 (2016).

[212] Tae-Hee, H. *et al.* Extremely efficient flexible organic light-emitting diodes with modified graphene anode. *Nature Photonics* **6**, 105–110 (2012).

[213] White, M. S. *et al.* Ultrathin, highly flexible and stretchable PLEDs. *Nature Photonics* **7**, 811–816 (2013).

[214] Krebs, F. C., Gevorgyan, S. A. & Alstrup, J. A roll-to-roll process to flexible polymer solar cells: model studies, manufacture and operational stability studies. *Journal of Materials Chemistry* **19**, 5442–5451 (2009).

[215] Pagliaro, M., Ciriminna, R. & Palmisano, G. Flexible solar cells. *ChemSusChem* **1**, 880–891 (2008).

[216] Docampo, P., Ball, J. M., Darwich, M., Eperon, G. E. & Snaith, H. J. Efficient organometal trihalide perovskite planar-heterojunction solar cells on flexible polymer substrates. *Nature Communications* **4**, 2761 (2013).

[217] Kaltenbrunner, M. *et al.* Ultrathin and lightweight organic solar cells with high flexibility. *Nature Communications* **3**, 770 (2012).

[218] Rogers, J. A., Someya, T. & Huang, Y. Materials and Mechanics for Stretchable Electronics. *Science* **327**, 1603–1607 (2010).

[219] Someya, T. *et al.* A large-area, flexible pressure sensor matrix with organic field-effect transistors for artificial skin applications. *Proceedings of the National Academy of Sciences* **101**, 9966–9970 (2004).

[220] Kaltenbrunner, M. *et al.* An ultra-lightweight design for imperceptible plastic electronics. *Nature* **499**, 458–463 (2013).

[221] Schneider, D. *et al.* Ultrawide tuning range in doped organic solid-state lasers. *Applied Physics Letters* **85**, 1886–1888 (2004).

[222] Liu, X. *et al.* Tailored surface-enhanced raman nanopillar arrays fabricated by laser-assisted replication for biomolecular detection using organic semiconductor lasers. *ACS Nano* **9**, 260–270 (2014).

[223] Rose, A., Zhu, Z., Madigan, C. F., Swager, T. M. & Bulović, V. Sensitivity gains in chemosensing by lasing action in organic polymers. *Nature* **434**, 876–879 (2005).

[224] Wang, Y. *et al.* LED pumped polymer laser sensor for explosives. *Laser & Photonics Reviews* **7**, 71–76 (2013).

[225] Zhai, T. *et al.* Free-standing membrane polymer laser on the end of an optical fiber. *Applied Physics Letters* **108**, 041904 (2016).

[226] Kallinger, C. A Flexible Conjugated Polymer Laser. *Advanced Materials* **10**, 920–923 (1998).

[227] Chen, Y. *et al.* Laser action in a surface-structured free-standing membrane based on a pi-conjugated polymer-composite. *Organic Electronics* **12**, 62–69 (2011).

[228] Riechel, S. *et al.* A nearly diffraction limited surface emitting conjugated polymer laser utilizing a two-dimensional photonic band structure. *Applied Physics Letters* **77**, 2310 (2000).

[229] Herrnsdorf, J. *et al.* Flexible blue-emitting encapsulated organic semiconductor DFB laser. *Optics Express* **18**, 25535–25545 (2010).

[230] Perron, P. J. & Lederman, P. B. The effect of molecular weight distribution on polyethylene film properties. *Polymer Engineering and Science* **12**, 340–345 (1972).

[231] Menzies, G. Money to burn, or melt? A cost-benefit analysis of Australian polymer banknotes. *North American Journal of Economics and Finance* **15**, 355–368 (2004).

[232] Hardwick, B., Jackson, W., Wilson, G. & Mau, A. W. H. Advanced materials for banknote applications. *Advanced Materials* **13**, 980–984 (2001).

[233] Park, J. S., Chae, H., Chung, H. K. & Lee, S. I. Thin film encapsulation for flexible AM-OLED: A review. *Semiconductor Science and Technology* **26**, 034001 (2011).

[234] Jørgensen, M., Norrman, K. & Krebs, F. C. Stability/degradation of polymer solar cells. *Solar Energy Materials and Solar Cells* **92**, 686–714 (2008).

[235] Klumbies, H. *et al.* Water ingress into and climate dependent lifetime of organic photovoltaic cells investigated by calcium corrosion tests. *Solar Energy Materials and Solar Cells* **120**, 685–690 (2014).

[236] Foucher, C., Guilhabert, B., Herrnsdorf, J., Laurand, N. & Dawson, M. D. Diode-pumped, mechanically-flexible polymer DFB laser encapsulated by glass membranes. *Optics Express* **22**, 24160 (2014).

[237] Kim, J. H. *et al.* Tunable and flexible solvent-free liquid organic distributed feedback lasers. *Applied Physics Letters* **106**, 053302 (2015).

[238] Guilhabert, B. *et al.* Mechanically-Flexible Organic Semiconductor Laser Array. *IEEE Photonics Journal* **4**, 684–690 (2012).

[239] De Luis-García, R., Alberola-López, C., Aghzout, O. & Ruiz-Alzola, J. Biometric identification systems. *Signal Processing* **83**, 2539–2557 (2003).

[240] Heys, J. & Barocas, V. H. Mechanical characterization of the bovine iris. *Journal of Biomechanics* **32**, 999–1003 (1999).

[241] Delori, F. C., Webb, R. H. & Sliney, D. H. Maximum permissible exposures for ocular safety (ANSI 2000), with emphasis on ophthalmic devices. *Journal of the Optical Society of America A. Optics, Image Science, and Vision* **24**, 1250–1265 (2007).

[242] Whitworth, G. L. *et al.* Solvent immersion nanoimprint lithography of fluorescent conjugated polymers. *Applied Physics Letters* **107**, 163301 (2015).

[243] Coles, D. *et al.* A Nanophotonic Structure Containing Living Photosynthetic Bacteria. *Small* **13**, 1701777 (2017).

[244] Castner, D. G. & Ratner, B. D. Biomedical surface science: Foundations to frontiers. *Surface Science* **500**, 28–60 (2002).

[245] Triggs, G. J. *et al.* Spatial resolution and refractive index contrast of resonant photonic crystal surfaces for biosensing. *IEEE Photonics Journal* **7**, 6801810 (2015).

[246] Nazirizadeh, Y. *et al.* Intensity interrogation near cutoff resonance for label-free cellular profiling. *Scientific Reports* **6**, 24685 (2016).

[247] Nazirizadeh, Y. *et al.* Material-based three-dimensional imaging with nanostructured surfaces. *Applied Physics Letters* **102**, 011116 (2013).